Dissertation
submitted to the
Combined Faculties for the Natural Sciences and for
Mathematics
of the Ruperto-Carola University of Heidelberg, Germany
for the degree of
Doctor of Natural Sciences

presented by
Dipl. Phys. Alexandra Gabriela Herzog
born in
Schorndorf
Oral Examination 21.10.2010

Imaging of Water-sided Gas-Concentration Fields at a Wind-Driven, Wavy Air-Water Interface

Referees: Prof. Dr. Bernd Jähne
Prof. Dr. Ulrich Platt

The aim of this study is to develop improved measurement techniques to determine depth dependent water-sided gas concentration fields under a wind-driven free surface that is strongly wave-influenced. In comparison to previous studies the pH-LIF method was improved by using a novel fluorophore, a more powerful Laser and an optimized optical setup. This configuration allows for the first time high temporal resolution imaging of concentration fields under a strongly wave-influenced surface in two spatial dimensions. Two measurement techniques based on Laser-induced fluorescence have been improved and developed, respectively: On the one hand, the theory of a spectral reconstruction approach was improved, that allows an arbitrary orientation of the illuminated cross section. Here, depth-dependent concentration fields can be estimated by inverse modeling. On the other hand, a novel measurement technique, static pattern LIF (SP-LIF), has been developed from side-LIF by applying a discretized illumination. For the first time, a reliable estimate of the water surface even under a nearly vanishing near surface concentration gradient, has become possible. Now, the found and classified coherent structures in the near surface turbulence under wind shear can be compared to the results of direct numerical simulations to reveal the dominating transport mechanisms under varying conditions.

Ziel der Arbeit ist die Entwicklung einer verbesserten Messtechnik, welche es ermöglicht unter wellenverzerrter Oberfläche das wasserseitige Gaskonzentrationsfeld zu bestimmen. Im Vergleich zu vorherigen Studien wurde die pH-LIF Messtechnik durch einen neuen Fluoreszenzfarbstoff, einen leistungsstärkeren Laser und einen optimierten optischen Aufbau verbessert, was nun erstmals zeitlich hochaufgelöste Messungen unter stark wellenbeeinflußter Grenzschicht in zwei räumlichen Dimensionen erlaubt. Für die Durchführung dieser Experimente wurde ein völlig neuer, chemisch inerter Wind-Wellen Kanal konzipiert, realisiert und weitgehend charakterisiert. Zwei Messtechniken basierend auf Laser-induzierter Fluoreszenz wurden weiter beziehungsweise neu entwickelt: Zum einen wurde die Theorie eines spektralen Ansatzes weiterentwickelt und in numerischen Simulationen getestet, welcher eine beliebige Orientierung des beleuchteten Querschnitts erlaubt. Die tiefenabhängigen Konzentrationsfelder werden hierbei mit Hilfe inverser Modellierung bestimmt. Zum anderen wurde aus der Seiten-LIF Methode durch eine diskretisierte Beleuchtung die neue Messmethode Static Pattern LIF entwickelt. Hierdurch wird nun erstmals eine zuverlässige Detektion der Wasseroberfläche auch in Abwesenheit eines starken Konzentrationsgradienten in der Grenzschicht ermöglicht. Die mit dieser Methode gefundenen und klassifizierten kohärenten Turbulenzstrukturen unter Windscherung können nun mit Ergebnissen der Direkten Numerischen Simulation verglichen werden, um Rückschlüsse auf dominante Transportmechanismen zu ziehen.

Nihil tam difficile est, quin quaerendo investigari possit

Terentius

Contents

I Introduction **17**

1 Introduction **19**

II Theoretical Background **27**

2 Basic Theory of Transport Processes across the Air-Water Boundary Layer **29**

2.1 The Fundamental Transport Mechanisms: Diffusion and Turbulence . . . 30
2.1.1 Diffusive Transport . . . 30
2.1.2 Turbulent Transport . . . 32
2.2 Differential Equations of Transport . . . 34
2.2.1 Conservation of Momentum: The Navier-Stokes Equation 35
2.2.2 Conservation of Mass: Fick's Transport Equation of Mass 36
2.2.3 Transformation to Flux Equations . . . 37
2.2.4 Limits of Validity . . . 37
2.3 Boundary Conditions on Gas Transfer . . . 38
2.3.1 Boundary Conditions due to Flow Regimes: Boundary Layer and Bulk . . . 38
2.3.2 Boundary Condition due to Properties of Trace Gas and Solvent Medium Water . . . 40
2.3.3 Summary of Boundary Conditions . . . 43
2.4 Classification Parameters of Transport across a (free) Interface . 44
2.4.1 Definition of the Boundary Layer Thickness in Transfer Studies . . . 44
2.4.2 Transfer Velocity . . . 46
2.4.3 Transfer Time . . . 47
2.4.4 Summary . . . 47
2.5 Modeling and Simulating Gas Transfer . . . 47
2.5.1 Shear flow . . . 48
2.5.2 Ways of Simplifying the Transport Equations: Linearized 1D-Transport models . . . 49
2.5.3 Full Transport Equations: Direct Numerical Simulation -DNS . . . 55
2.6 Summary and Conclusions . . . 56

III Measurement Technique **57**

3 Method for Visualizing Dissolved Gas in the Water-Phase: Laser-Induced Fluorescence **59**
3.1 Relation to Previous Works 60
3.2 Contribution and Improvements regarding Fluorophore and Tracer Gas in this Study 60
3.3 Introduction to Fluorescence 61
3.4 The pH-Indicator Method: Fluorophore as Tracer for Gas Concentration 64
3.4.1 Indicator Reaction as Basis of Detection of Acid/Alkaline Gases 64
3.4.2 Relation between Intensity of Fluorescence Signal to Concentration of H_3O^+ 65
3.4.3 The Core of the pH-Method: Conservation of Mass Flux . 68
3.4.4 Theoretical Sensitivity of Fluorescence Detection to Concentration Changes 73
3.5 The pH-Method in Comparison to the Oxygen Quenching Technique 74
3.6 Properties of Tracer Hydrogen Chloride 76
3.6.1 Dissociation Reaction of HCl in Water 76
3.6.2 Solubility 76
3.6.3 Partial Pressure over Highly Saturated HCl Solution . . . 78
3.6.4 Diffusion Coefficient 78
3.6.5 Summary 79
3.7 Fluorescent Dye for LIF-Measurements: HPTS 80
3.7.1 Desirable Properties of a Fluorophore used for LIF 80
3.7.2 The fluorophore used for measurements: HPTS 81
3.7.3 Absorption Characteristics of HPTS 84
3.7.4 Fluorescence Characteristics of HPTS 87
3.7.5 Comparison of HPTS to Commonly Used Fluorescein . . 91
3.7.6 Summary 93

4 Realizations of LIF-Setups for Measuring Depth-Dependent Gas Concentration under a Wave-Influenced Water Surface **95**
4.1 Contribution in this Study 96
4.2 The Classic Approach: Tilted Side-Camera Setup 97

5 The Spectral Reconstruction Approach (SPERA) **99**
5.1 Intention of the Method 100
5.2 Relation to Previous Works 100
5.3 Contribution and Improvements in this Study 101
5.4 Basic Principle of the SPERA Technique 102
5.5 Physical Description of Regarded Absorption/ Emission Processes 103
5.6 Discretization of the Emission-Absorption Equation 107
5.6.1 Estimation of the Remaining Rest or Error Term 111

5.6.2 Estimation of the Needed Concentration of the Absorber Dye for a Given Spatial Resolution Δz . . . 113
5.7 Experimental Aspects . . . 114
5.7.1 Fluorophore . . . 114
5.7.2 Absorption Dye . . . 114
5.7.3 Application of the Theoretical Model on Experiments . . 118
5.7.4 Test Measurements: Combination of Fluorophore and Absorption Dye . . . 119
5.8 Parameter Estimation Techniques . . . 121
5.8.1 Statistics of LIF-Signals . . . 121
5.8.2 Numerical Simulation . . . 122
5.8.3 Robust Estimator Used for Simulations . . . 123
5.9 Results of the Numerical Simulations in Spectral Reconstruction Approach . . . 124
5.10 Summary . . . 127

6 Novel Extension for Waves: Static Pattern-LIF (SP-LIF) 129
6.1 Review of Other Approaches for Measuring Concentration Profiles under Wave-Influence Surface Conditions . . . 129
6.2 Main Idea of SP-LIF: Discretization of Illumination . . . 131
6.3 Separating Pattern and Concentration Signal: Basic Ideas of Image Processing . . . 133
6.4 Surface Topology from Refraction of the Static Laser-Pattern . . 136
6.4.1 Surface Orientation from Refraction Angle . . . 136
6.4.2 Determination of Local Angle α_0 of Pattern Structure in Air . . . 138
6.4.3 Inverse: Angle of Refracted Beam γ Calculated from Surface Slope m_s . . . 139
6.5 Experimental Realization . . . 139
6.6 Summary . . . 141

IV Experimental Setup 143

7 Ocean Simulation: The Wind-Wave Tunnel 145
7.1 Main Design Criteria . . . 145
7.2 Design Types of Wind-Wave Tunnels or Reasons for a Linear Wind- Wave-Tunnel . . . 147
7.3 Short Technical Description . . . 149
7.4 Summary . . . 153

8 The Optical Setup 155
8.1 Illumination Setup . . . 155
8.1.1 Light Source . . . 156
8.1.2 Sheet Optics . . . 159
8.2 Detector Setup: The Imaging System . . . 163

8.2.1 Scheimpflug Setup: Significant Improvement of Optical Resolution by Scheimpflug-Arrangement 164
8.3 Summary 167

V Processing of Experimental Data 169

9 Image Processing 171
9.1 Relation to Previous Studies 171
9.2 Improvement and Contribution by SP-LIF for Surface Detection . 172
9.3 Procedures for Analyzing SP-LIF Data 173
9.3.1 Preprocessing: Removal of Dark Current and Scheimpflug Distortion 173
9.3.2 Simple 13-Beam Illumination: Flat and Wavy Interface . . 173
9.3.3 Fine Pattern Illumination 175
9.4 Postprocessing 179
9.5 Outlook 180
9.6 Summary 181

10 Statistical Analysis of the Gained Data Sets 183
10.1 Statistical Analysis for Controlled-Flux Techniques in Comparison to Constant Concentration Techniques 183
10.1.1 Estimation of Water-sided Statistical Quantities for Neumann and Dirichlet-type of Boundary Condition 184

11 Estimation of Systematic Error Sources 187
11.1 Errors Affecting the Concentration Signal 187
11.1.1 Fluorophore 187
11.1.2 Optical Setup 191
11.1.3 Effects of Temperature Variation 194
11.1.4 Errors due to Illumination Refraction Perpendicular to Observation Plane 196
11.2 Disturbances of Flow Regime in the Wind-Wave Tunnel 196
11.2.1 Temperature Flows 196
11.2.2 Secondary Currents 197
11.2.3 Heterogeneous Distribution of HCl Concentration in Air . 197
11.3 Error in Signal Processing 198
11.3.1 Wrong Estimation of Buffer Point 198
11.3.2 Violation of Lambert-Beer Decay by Strong Concentration Variations 199
11.3.3 Errors in Diffusivity of Gaseous Tracer 199
11.4 Discussion of Special Error Sources of SP-LIF 200
11.5 Discussion of Special Error Sources of SPERA 200
11.6 Summary 201

VI Results and Discussion **203**

12 Results: Static-Pattern LIF **205**
12.1 Conducted Measurements 205
12.2 Qualitative Results 207
12.2.1 Identified Coherent Structures in the Surface Vicinity under Wind-Induced Turbulence 207
12.2.2 Statistical Appearance of Different Kinds of Turbulence Events at Varying Turbulence Levels 217
12.2.3 Upwelling (Sweeps/Surface Renewal Events) and Downwelling (Bursts) Events and Surface Renewal dependent on Turbulence Level 218
12.2.4 Wave Slope of Capillary Waves 222
12.2.5 Wave State and Gas Exchange 222
12.2.6 Comparison of Qualitative Results to Model Assumptions and Results of Other Authors 224

13 Discussion and Outlook **227**
13.1 Discussion of the SPERA-Technique 227
13.2 Discussion of Results of the SP-LIF 228
13.3 Outlook 228

VII Appendix **231**

A The Wind-Wave Tunnel **233**
A.1 General Design Rules of a Wind-Wave Flume 233
A.2 Design of the Linear Wind-Wave Tunnel LIZARD 234
A.2.1 General Design Criteria for LIZARD 234
A.2.2 Material of the Tunnel Elements 235
A.2.3 The Individual Elements of the Wind-Wave Tunnel 235
A.3 Characterization of Flow Properties 242
A.3.1 Wave Slope Statistics 245
A.4 Further Technical Characteristics of the Wind-Wave Tunnel . . . 248

B Determining Extinction Coefficients **249**
B.1 General Description of the Technique 249
B.2 Typical Error Sources 250

C Calculation of the pH Value of HPTS in Aqueous Solution **253**
Literatur 271

Symbols

The following list contains the most important symbols and notations used in this study. Subscripts usually refer to a component of a vector (x, y, z, or 1, 2, 3) or to the phase, e.g. air and water (a, w). Derivatives are written in the following way: ∂_x, ∂_{xx} for the first and second partial derivative with respect to x, respectively, and d_t for the total derivative $\partial_t + \mathbf{v} \cdot \nabla$ with respect to time. If the derivative is to be emphasized, the long form $\frac{\partial \diamond}{\partial x}$ is used.

Sign Convention in Coordinate Systems

The normal vector $\mathbf{n}$ on the surface of some volume points outwards. The x-axis points in the main flow direction, while the y-axis marks the horizontal spanwise direction with respect to main flow, see figure 1. The vertical (z) axis points downward, in the direction of the acceleration of gravity. Its origin is typically chosen to be at the water surface. Accordingly, z is called the depth.
If a local coordinate system is used the x-axis marks the surface orientation parallel to main flow, the y-axis marks the surface orientation spanwise to main flow, while the z-axis marks the direction of the perpendicular line with respect to the x-axis, and points towards the fluid bulk. If another convention is used

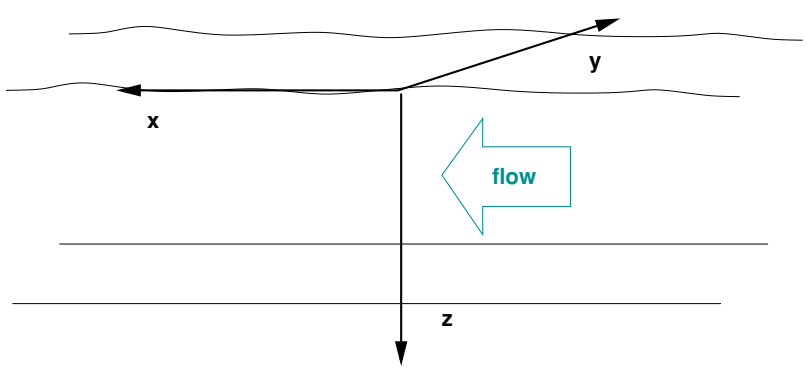

Figure 1: Orientation of standard coordinate system used in this study.

it is noted there explicitly.

The velocity vector components follow the standard notation of fluid dynamics:

$$\mathbf{v} = (v_x, v_y, v_z)^T = (u, v, w)^T,$$

with u as the streamwise component, v as the spanwise component, and w as the vertical velocity component.

Wind-Wave Tunnel

LIZARD	Name of the new Wind-Wave Tunnel: **LI**near **Z**trong **A**cid **R**estistant **D**evice
$\theta = 14.6 \pm 0.3°$	angle of tilt of side-observation window

Mathematical Notation

erf	error function
erfc	complementary error function
$\mathfrak{var}$	variance
ς	standard deviation
μ	mean
d_t	total derivative with respect to time [s^{-1}]
∂_t	partial derivative with respect to time [s^{-1}]
∂_z	partial derivative with respect to vertical coordinate [m^{-1}]
∇	partial derivative with respect to space [m^{-1}]
$\widehat{f}$	Fourier transform of function f
$\mathcal{F}$	Fourier transform
$\mathcal{F}^{-1}$	inverse Fourier transform
$\mathcal{L}$	Laplace transform
$\mathcal{L}^{-1}$	inverse Laplace transform
ϵ	constant $\ll 1$
	a generic argument

Spectroscopy

Φ_q	quantum yield [1]
γ_q	pH-dependent quantum yield [1]
α	absorption coefficient [$1/cm$]
$\mathfrak{e}$	molar extinction coefficient resp. logarithm to base 10 [$1/(\mathrm{mol}\, l^{-1} cm)$]
ε	molar extinction coefficient resp. natural logarithm [$1/(\mathrm{mol}\, l^{-1} cm)$]

$f_b(\lambda)$	normalized fluorescence spectrum [1]
j_Φ	radiant flux $[W]$ or [photons/s]
E	irradiance or incoming radiant flux density $[dj_\Phi/dA] = [W/m^2]$
M	emittance or emitted radiant flux density $[dj_\Phi/dA] = [W/m^2]$
Ω	solid angle of irradiance $[sr]$
L	radiance as radiant intensity for extended sources, describes angular distribution of radiation $\frac{d^2 j_\Phi}{dA\, D\Omega}$ $[Wm^{-2}\, sr^{-1}]$
σ	cross section of scattering or fluorescence and absorption [cm^2]
N_a	Avogadro's constant [mol^{-1}]

Physical Chemistry

K_H	Henry coefficient [mol kg^{-1} Pa^{-1}]
α_{Sol}	Partition coefficient of gas between two phases [1]
pK	negative log. of equilibrium constant [1]
$\mathrm{R}^{-3}\mathrm{OH}$	anion acid of HPTS in aqueous solution [1]
$\mathrm{R}^{-3}\mathrm{O}^-$	anion base of HPTS in aqueous solution [1]
$\wp_{pH}$	ratio of deprotonation of HPTS [1]
$\mathrm{H_3O^+}$	hydronium ion in water [1]
$\mathrm{OH^-}$	hydroxy ion in water [1]
r_{pH}	deprotonation ratio of HPTS component $\mathrm{R}^{-3}\mathrm{O}^-$ at a certain pH compared to total concentration[1]
C	molal concentration [mol kg^{-1}]
$\mathcal{C}$	molar concentration [mol l^{-1}]
$\mathfrak{L}$	specific ion conductivity in solution $[\mu S/cm]$
[HCl]	HCl concentration [mol l^{-1}]

Quantities of Mass Transport

$\mathcal{D}$	diffusion coefficient [cm^2 s^{-1}]
$\mathcal{K}$	turbulent diffusion coefficient [cm^2 s^{-1}]
ν	diffusion coefficient of momentum (kin. viscosity) [cm^2 s^{-1}]
μ	dynamic (shear) viscosity [kg m^{-1} s^{-1}]
$\mathbf{j}$	general flux density of transported value X [X cm^{-2} s^{-1}]
$\mathbf{j}_c$	flux density of mass transport [M cm^{-2} s^{-1}]
$\mathbf{j}_p$	flux density of momentum [g cm^{-2} s^{-1}]

$\mathbf{j}_h$	flux density of heat [J cm^{-2} s^{-1}]
$\mathbf{k}$	transfer velocity [cm s^{-1}]
k_{600}	transfer velocity normalized to Schmidt number of CO_2 in fresh water and T = 20 °C[cm s^{-1}]
R	transfer resistance [s cm^{-1}]
z_c^*	mass boundary layer thickness [m]
z_p^*	viscous boundary layer thickness [m]
z_h^*	thermal boundary layer thickness [m]
τ^*	characteristic time scale of mass transport over boundary layer [s]
ϵ_c	turbulent kinetic energy dissipation
L_{int}	integral length scale [m^{-1}]
L_{Tay}	Taylor micro length scale [m^{-1}]
L_{mic}	Kolmogorov length scale [m^{-1}]
β^s	surface divergence [s^{-1}]
ρ	density [kg m^{-3}]
R	ideal gas constant [Pa m^3 mol^{-1} K^{-1}]
c_p	heat capacity at constant pressure [J kg^{-1} K^{-1}]
$\mathbf{u}_*$	friction velocity [m s^{-2}]
ρ_w	mass density of water [kg m^{-3}]
$\mathbf{g}$	acceleration of gravity [m s^{-2}]
$\mathbf{j}$	flux [X m^{-2}s^{-1}]
k	wave number vector [m^{-1}]
$\widehat{\mathbf{n}}$	unit normal vector
$\mathbf{p}$	momentum [kg m s^{-1}]
p_a	pressure in air phase [hPa]
$d_\mathcal{F}$	fetch length [m]
$\mathbf{v}$	velocity [m s^{-1}]
$\mathbf{x}$	position [m]

Uppercase Latin Symbols

F	force [kg m s^{-2}]
Fr	Froude number
Sc	Schmidt number [1]
Pr	Prandtl number [1]
Re	Reynolds number [1]
Pe	Peclet number [1]
St	Strouhal number [1]

Part I

Introduction

Chapter 1

Introduction

Environmental physics deals with one of the most complex systems known, our planet Earth. Usually, this system is subdivided into the five compartments atmosphere, lithosphere, biosphere, cryosphere, and ocean. One of the special tasks in environmental physics is to gain information about transport processes within and interactions among these compartments. This means trying to find the corresponding transport equations, which are usually highly nonlinear partial differential equations.

Small Scale Air-Sea Interaction as a part of environmental physics tries to find the transport equations of heat, momentum and mass, i.e. gas, especially close to the air-water interface, where the main resistance of transport for low soluble gases like oxygen and carbon dioxide is located. The first being of interest to biochemical processes for example with respect to re-aeration of lakes and rivers, and the latter being one of the most important gases for natural and, recently also human-induced greenhouse warming of our planet. Good estimates of gas transport velocities under various conditions are of great interest for climate modeling as they allow to predict how much gases are transported from the atmosphere into the oceans and vice versa, as well as the fraction of gas remaining dissolved in the ocean.

Important to note is, that the ocean acts as the largest sink of the greenhouse gas carbon dioxide. Up to 30-40% of man-made CO_2 is estimated to be transferred into the oceans according to Donelan and Wanninkhof [2002].

Yet, even under decades of laborious studies the uncertainties in global gas transfer are still outstandingly large: Jähne [2009] speaks of uncertainties of a factor of two, while Banerjee et al. [2004] speak of variations up to a factor of three. All estimates of global gas transfer depend on the chosen parametrization of gas transfer on different variables like wind speed or mean sea surface slope, that can be accessed by remote sensing from satellites. Widely used are for example the parametrization of Liss and Merlivat [1986], a piecewise linear parametrization based on wind speed which estimates the global gas transfer to be in the order of 1.1 PgC/year, and the parabolic parametrization of Wanninkhof and McGillis [1999], which estimates global gas transfer to be in the order of 3.3 PgC/year, according to Banerjee et al. [2004].

The difficulties in finding a suitable parametrization are wide spread: One problem is that the interaction of ocean and atmosphere is a highly dynamic process. Moreover, the interaction of wind and wave field is highly nonlinear, i.e. wind is generating waves, waves interact with themselves and with the wind field and vice versa. Momentum induced on the water body by wind shear is only partially transferred to shear of the interface but also to waves and finally shear is dissipated by decay of waves to large and low scale turbulence. So far, the relative strength of the different ways of momentum transfer is still unknown.

So far accepted knowledge is, that gas transfer rapidly increases with the onset of waves as pointed out by Jähne [2009], Csanady [2001] Bannerjee and MacIntyre [2004] and others. Already Jähne [1980] reported an increase of factor of three up to ten depending on the wind speed. This increase is modelled by every proposed parametrization up to the onset of waves. However, the situation is quite different after the onset of waves, here the predictions vary widely. Unfortunately, especially at high wind speed reliable gas transfer rates have been rarly determined.

Generally, wind-induced shear stress fluid motion is usually divided into three different regimes as shown in figure 1.1 based on the parameter wind speed and surface condition: Regime I is the regime of a flat interface without waves. The regime II, the regime of waves and including the onset of regular microscale wave breaking, is found to be the most widespread in the oceans as the estimated mean wind velocity at a height of 10 m over the ocean is 7.5 m/s according to Donelan and Wanninkhof [2002]. Microscale wave breaking is characterized by strong downwelling motions at the wave crests and strong upwelling in the wave troughs according to Banerjee et al. [2004] but without bubble entrainment. Most authors define microscale-wave breaking as the local downwelling of the whole thermal sublayer, which is visible in IR-imaging of the water surface, see for example Jessup et al. [1997] for a definition of microscale wave breakings. Finally, regime III is accociated with wave breaking with bubble entrainment called whitecap breaking (i.e. Ebuchi et al. [1993]).

The three regime assumption has been the base for the empirical Liss-Merlivat parametrization of gas transfer, see Liss and Merlivat [1986]. The parametrization consists of a piecewise linear increase with wind speed with a change of slope whenever the borders of a regime are crossed. This piecewise parametrization is plotted in the lower part of figure 1.1. It is assumed that micro-scale wave breaking might be one of the causes of the enhanced gas transfer rates after the onset of waves, but a direct experimental proof is still missing. The same is true for the influence of white cap breaking. Wanninkhof et al. [2009] put in their conclusions that '.. The role of breaking waves at high wind speeds is recognized as important, but as yet there remains no reliable way to accurately quantify the effect of breaking waves on gas exchange.' Summarizing, waves are identified to effect gas exchange but the details and the quantity is still unknown.

Furthermore, the simple Liss-Merlivat relation does not respect the dependency

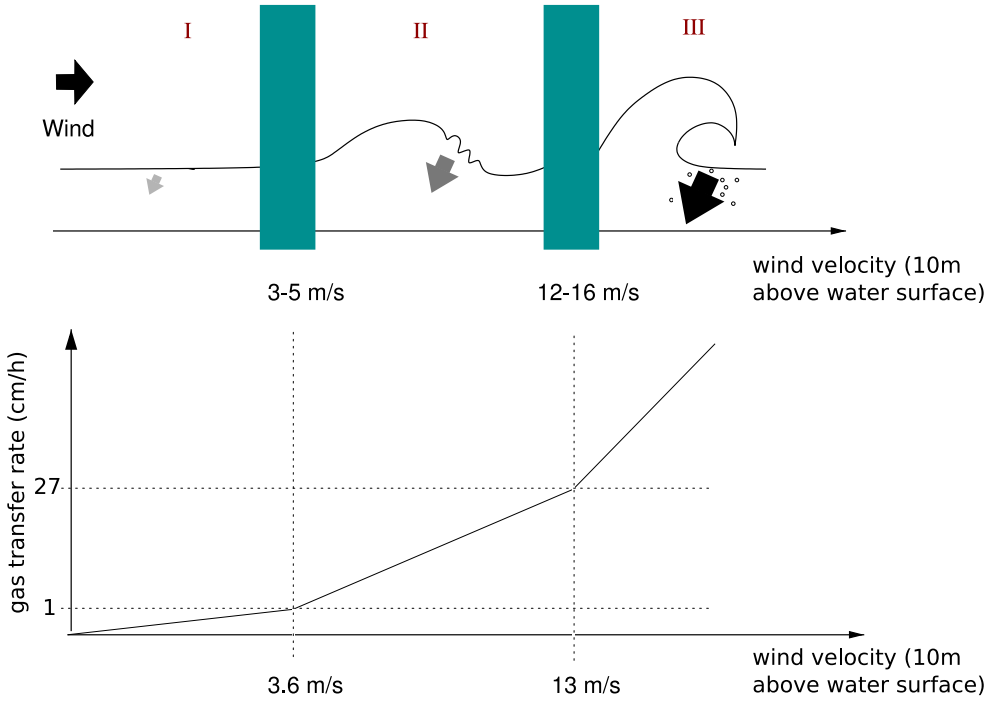

Figure 1.1: Classification of free surface at an air-water interface in three physical regimes, adapted from Jähne [2009] and Bannerjee and MacIntyre [2004]
Upper Part:
I : smooth - pure shear stress regime, smooth and flat interface
II : wave-influenced - micro-scale wave breaking without bubble entrainment
III: bubble-influenced- whitecap breaking with bubble entrainment
The dashed areas mark the transition regimes
Lower Part:
Empirical parametrization of Liss and Merlivat [1986] based on the three regime assumption.

of gas transfer on other parameters beside wind speed: The surface topology, represented in the three regimes, does not only depend on wind speed but more on the characteristics of the wave field, which itself depends also on surface conditions like films, that suppress wave formation and others. See for example figure 1.2 and for details the review of Wanninkhof et al. [2009].

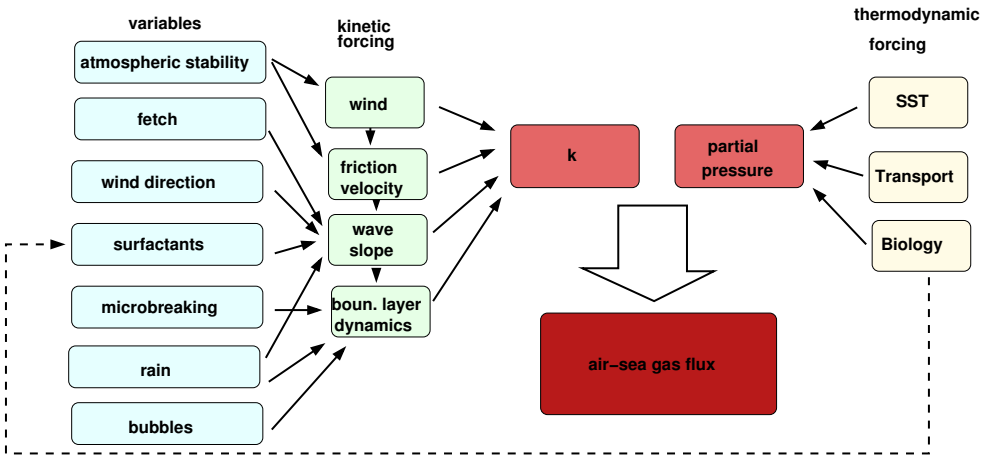

Figure 1.2: Sketch of parameters influencing gas transfer, that are identified to some extent beside their relative individual influence on gas transfer rates. Graph adapted from Wanninkhof et al. [2009].

In more detail it is expected that gas transfer may vary with the wave field including the local slope and the state of the wave (crest, falling/rising limb, trough), which is indicated in the measurements of Walker and Peirson [2008]. They made first efforts to verify this assumption, and related the transfer rates to the state of the gravity wave at a constant fetch [1] position in their wind-wave tunnel. In linear wind-wave tunnels the wave field depends on the fetch and therefore gas transfer rates should show a dependency on fetch, if they were related to the characteristics of the wave field. Surprisingly, Walker and Peirson [2008] reported lowest transfer rates at the wave crest and the rising limb where the strongest downwelling is located and therefore the highest gas transfer rates should be expected. This contradicts the assumption that micro-scale wave breaking, that is associated with the location between rising limb and wave crest, would cause the enhanced transfer rates. So the dependency of gas transfer on wave state demands a more detailed investigation.

A detailed study of the solution dynamics of gases in liquid including gas transfer rates at higher wind speeds and in combination with the local wave state is a demanding challenge for experimental investigation. Besides the desired local gas transfer rates, also the local surface topology has to be monitored. What is needed is the estimation of local gas transfer velocities directly in combination with local slope to characterize the surface condition as well.

The demands on spatio-temporal resolution are extremely high as the main resistance of transport for low-soluble gases lies in the first 20-200 micrometers beneath the air-water interface. So the processes happen on an extremely small scale at a surface that moves with approximately two percent of the wind speed.

[1] fetch: the distance over which wind shear has been exposed to the water surface in wind-wave tunnels

Two processes determine gas exchange in this very thin layer: On the one hand molecular diffusion and on the other hand turbulent transport. The interaction of both determines the size of the mass boundary layer, the layer where diffusive transport exceeds turbulent transport and where main resistance of transport is located.
Different models exist how viscous and turbulent processes interact in this layer, but until now measurements have not been able to prove or dismiss them.
Yet, all theories predict that in the topmost layer only molecular diffusion occurs. Furthermore, they all claim, the more turbulent the water phase becomes the thinner the boundary layer becomes. The equilibrium concentrations in gaseous and liquid phase are known as they are determined by the partition coefficient of Henry's law, but the intermediate states are still not well examined.

Three methods are available to determine gas transfer rates in the demanded high local and temporal resolution: First, heat is often used as a proxy tracer to gain knowledge about concentration fields and gas transfer rates. Heat is assumed to be a good tracer for gas transport as it is similar distributed by molecular and turbulent diffusion. Heat flux measurements are done by IR-imaging and are successfully used in laboratory Haußecker et al. [2002] and in field measurements Schimpf et al. [2004]. Heat as a substitute of gas transfer is regarded critically by Atmane et al. [2004], since the analogy between heat and gas transport is limited due to the strongly varying diffusivities in water. Jähne [1991] pointed out that heat cannot resolve fine structures of gas transfer also due to the higher molecular diffusivity of heat.

In the last two decades, a more theoretical approach to gain knowledge about water-sided concentration fields has been evolved in numerical simulations called Direct Numerical Simulation or DNS for short. Representatives of DNS are Magnaudet and Calmet [2006] and Tsai and Hung [2007], all of whom lack knowledge of the full concentration and velocity fields as initial conditions for their simulation. They assume that the partial differential equations once started with an initial guess lead finally to a result, that is describing a realistic situation. Whether these solutions correspond to situations typically encountered in nature is still not clear. Therefore, to prove the results of Direct Numerical Simulations concentration and velocity fields in high spatio-temporal resolution are needed for comparison.
The third approach is again a measurement technique - Laser-induced fluorescence - that allows to visualize water-sided concentration fields by a change in fluorescence of an excited dye solution dependent on the concentration of the dissolved gaseous tracer. Gas transfer rates can be readily calculated once the concentration field next to the surface is known. Laser-induced fluorescence is the most direct method of the three mentioned here. Yet, wave-influenced surfaces disturb Laser-induced fluorescence measurements in many ways, summarizing, the limit of the LIF technique is linked to a robust detection of the water surface. Therefore, studies of concentration fields under a strongly wave-influenced interface are rare. Up to now concentration fields have mainly been studied in bottom-induced turbulence setups where the surface remains flat.

Examples are here the work of Jirka and Ho [1990], Herlina and Jirka [2004], Herlina and Jirka [2008], Variano and Cowen [2007] and Asher and Litchendorf [2009]. Only a few studies under wind-induced turbulence and a free interface are available: Münsterer and Jähne [1998] and Falkenroth [2007] measured mainly under surfactants that suppressed waves and under a midly wave-influenced surface. Only Walker and Peirson [2008] had been successful so far to study gas transfer rates under waves with a LIF technique, yet without a full spatial 2D information on the concentration field that would allow to identify different types of turbulence.
The aim of this study is to deliver needed high-resolution measurements of the water-sided gas concentration field under a strongly wave-influenced free water surface. Non-intrusive Laser-induced fluorescence technique (LIF) is used to visualize an acidic gas penetrating the water mass boundary layer through changing the intensity of fluorescent light depending on the instantaneous concentration of the examined gas.

Concentration fields gained by the LIF-technique shall be compared to the heat distribution fields gained at the surface with active or passive IR-tomographie of heat transfer. The LIF-technique with its direct visualization of gas transport could act as a complementary technique for verifying or denying of the IR-approach.
This study should be a continuation of the work of Jähne [1991] and Münsterer and Jähne [1998] based on planar Laser-induced fluorescence of a pH indicator and the tracer HCl with a better suited fluorophore, a more powerful Laser and an optimized optical setup, which allows measuring in temporal and two spatial dimensions (xzt, 3D).
To achieve the above mentioned aims a novel measurement technique has been developed in this study for LIF-measurements under a strongly wave-influenced water surface: The Static-Pattern LIF technique (SP-LIF), which allows for the first time reliable measurements under rough surface conditions, because in this technique a robust surface detection can be guaranteed due to a discretized illumination light source. With this technique even measurements of water-sided gas concentration fields in capillary wave trains have become possible.
SP-LIF is used in combination with a novel fluorophore-gaseous tracer combination: the pH-indicator HPTS with gaseous tracer HCl. HCl can be shown to work as a suitable substitute for transport of carbon dioxide. Being an air-side controlled tracer HCl shows also some similarities to heat transport. This dye-tracer pair allowed to increase the sensitivity in detecting concentration variations remarkably compared to previous visualizations. Furthermore, this high sensitiviy compared with a large illumination area of the SP-LIF gave an insight into coherent structures of turbulent mass transport happening in the first centimeter below the interface. The turbulent vortices could be visualized without using an additional Particle Image Velocitmetry technique.

A further technique, the Spectral Reconstruction Approach (SPERA) has been theoretically deduced and tested for usage with the aim of achieving concentration profiles spanwise to the main flow direction. This tomographic tech-

nique combines a measurement technique with parameter estimation from inverse modeling to determine depth dependent concentration profiles from the spectral composition of the integral spectra that can be detected at the surface.

In the next section a short overview is given about the contents of this study.

Short Outline of the Thesis

In part II the theoretical background is presented including the current knowledge of gas transport and modeling of the processes.

In part III the measurement techniques are discussed in detail. The basic theory of Laser-induced fluorescence is presented as well as the special LIF-variation, the pH-indicator method, that is used here as main principle of measurement. This section is followed by a detailed descripton of both the fluorescent indicator HPTS and the gaseous tracer HCl.
In this study two different approaches have been used for measurements: on the one hand the Spectral Reconstruction Approach and on the other hand the novel Static Pattern LIF: The Spectral Reconstruction Approach is analysed theoretically in chapter 5. Only test measurements were done besides that. The SP-LIF has been developed by the author for usage under complex surface topology of the wave field like capillary wave trains. It is desribed in chapter 6.

Moreover, the experimental setup is presented in part IV, including the details of the wind-wave tunnel LIZARD, **LI**near **Z**(S)trong **A**cid **R**estistant **D**evice.
Part V deals with the post-processing of the actual measurements including image and statistical analysis. This part finishes with a detailed presentation of the systematic errors of both measurement techniques in chapter 11.

Finally, part VI deals with the results gained by the measurements and theoretical considerations, including an outlook.

Part II

Theoretical Background

Chapter 2

Basic Theory of Transport Processes across the Air-Water Boundary Layer

Gas transfer across the air-water interface is determined by two mechanisms: diffusive and turbulent transport. In a non-moving fluid pure diffusive transport would determine gas transfer. Yet, in nature, gas transfer under wind-induced shear flow is common: The solar radiation as main source of energy leads to wind as motion in the gaseous phase which accelerates the water phase and transports in that way momentum from the air into the water phase. A typical measure for this momentum transfer is the friction velocity u_*. This momentum transfer influences mass transfer by creating additional turbulent transport. The most simple situation is regarded here theoretically: Wind-induced turbulence under stable wind conditions in the absence of surfactants, rain, biological influences, and any other noise sources as sketched in the introduction in figure 1.2. Effects of temperature gradients are discussed as even under best experimental conditions small temperature variations (± 0.5 K) can often not be prevented.

Even under such restricted conditions further variables influence gas transfer besides momentum transport. Csanady [2001] mentions

- the solubility of the trace gas in the water-phase,
- the diffusivity of the dissolved gas in water, and the
- surface divergence.

The first two variables are physical-chemical properties of solute-solvent that mark the dissolution aspect of gas transport. The last one - surface divergence - is a property of the surface movement and of surface topology, a property that is linked to wave formation.

In this study the interaction between wind-induced turbulence, especially waves, and gas transfer across the air-water boundary layer should be analyzed. For

such an analysis pre-knowledge of the transport mechanisms involved is mandatory.

However, the interaction of the two transport mechanisms - molecular diffusive and turbulent transport - especially near the phase boundary between air and water in the case of surface-induced turbulence by wind shear is not well understood. The proportion of turbulent transport in the mass boundary layer (where diffusion is assumed to be the domination process, see 2.4.1 has to be taken into account compared to diffusive transport. The proportion of the turbulent transport depends on the shear stress applied to the surface by wind and appears to be specially linked to the onset of waves, where gas transfer rapidly increases, as shown by Jähne [1985].

In this section an overview of the current knowledge about transport processes at and in the direct vicinity of the phase boundary between air and water including the fundamental transport equations - the Navier-Stokes momentum transport equation and Fick's diffusion relation is given. The theoretical aspects are outlined as far as it is possible in the circumstances and as far as they are necessary for the evaluation of experiments in the later parts of this study. The boundary conditions imposed by physical and chemical effects like solubility of the trace gas will be given a special emphasis, as they determine the statistical analysis of the conducted experiments, see section 10.1. Furthermore, a short overview of the transport models that are currently in use is given, since the results of this study will be compared to their predictions.

2.1 The Fundamental Transport Mechanisms: Diffusion and Turbulence

Momentum, mass (dissolved gas) and heat are transported across a gaseous-liquid boundary layer by interaction of two different transport mechanisms: molecular diffusive transport and turbulent transport.

2.1.1 Diffusive Transport

The molecular diffusion is most effective on small scales (i.e. $\leq$ mm-scale depending on the transported quantity). It transports molecules via the uncorrelated stochastic motion of the individual molecules - the Brownian motion-driven by a gradient in concentration. Molecular diffusion is in that way also independent of the velocity of the regarded fluid element i - it works also for $\mathbf{u_i} = \mathbf{0}$. For an isotropic medium Fick [1855] formulated the corresponding linear equation for the mass flux $\mathbf{j_c}$ of concentration c to:

$$\mathbf{j}_c = -\mathcal{D} \cdot \nabla c. \tag{2.1}$$

For a steady state condition the resulting concentration profile is linear.
Diffusion leads to a broadening of the original distribution with time until a uniform distribution is reached in the long time limit.

The constant of proportionality in equation 2.1.1 is the diffusion coefficient $\mathcal{D}$ that depends both on the physical properties of the medium and the transported gas tracer. Typical values in liquids are in the order $\sim 10^{-5}\mathrm{cm}^2/\mathrm{s}$, while in gases values lie between $0.1 - 1\,\mathrm{cm}^2/\mathrm{s}$ at 293.15 K and a pressure of 1013 hPa.

Equivalence of Mass, Heat and Momentum Transport Diffusion coefficients can also be defined for the transport of momentum and heat using the related transport equations:

$$\mathbf{j}_p = \mathbf{j}_{\mathbf{xy}} = -\nu \frac{\partial \rho \mathbf{u}}{\partial z}, \tag{2.2}$$

$$\mathbf{j}_h = -\frac{k_h}{\rho c_p} \frac{\partial \rho T}{\partial z}. \tag{2.3}$$

with ν as the kinematic viscosity, ρ as the medium density, c_p as the heat capacity at constant pressure, T as temperature and k_h as the heat conductivity coefficient.
In comparison with 2.1.1 the diffusion coefficients for heat and momentum are therefore,

$$\mathcal{D}_h := \frac{k_h}{\rho c_p}, \tag{2.4}$$

$$\mathcal{D}_p := \nu. \tag{2.5}$$

This analogy is the reason that heat is supposed to can be used as a proxy for mass transfer.
Important for the transport is the difference between diffusion in air and water of mass, heat and momentum expressed by the ratio of their respective diffusion coefficients $\mathcal{D}_c$, $\mathcal{D}_h$ and $\mathcal{D}_p$:

$$\mathcal{D}_c^{\mathrm{air}} \approx \mathcal{D}_h^{\mathrm{air}} \approx \mathcal{D}_p^{\mathrm{air}}, \tag{2.6}$$

while in water the following relation is found

$$\mathcal{D}_c^{\mathrm{water}} \approx \frac{1}{100}\mathcal{D}_h^{\mathrm{water}} \approx \frac{1}{1000}\mathcal{D}_p^{\mathrm{water}}. \tag{2.7}$$

This difference is the reason for different thicknesses of the mass boundary layers - where diffusion dominates over turbulence- for the different quantities. This implies that transport for these quantities in water could show significant differences.
The free path length can be estimated to $\sigma^{\mathrm{path}} = \sqrt{2\,\mathcal{D}\,t}$. This argument is one of those given by authors who see the usage of heat as a proxy for mass transfer

rather critically like e.g. Atmane et al. [2004]. In that context Jähne [1991] pointed out that heat due to its higher molecular diffusivity cannot resolve fine structures of gas transfer.

Temperature Dependence The mass diffusion coefficient shows a strong temperature dependence: in liquids it strongly increases with temperature according to an exponential function,

$$\mathcal{D}_{liquid}(T) \;=\; \mathcal{D}(T_{ref}) \exp \frac{-\Delta\, E_{\text{position change}}}{kT}, \tag{2.8}$$

where k is the Boltzmann constant, $\Delta\, E_{\text{position change}}$ the amount of energy needed for a change in position of the molecule, see Jähne [2008]. In the temperature range from 20-25 ℃, this leads to an increase of 2-3% per Kelvin. The kinematic viscosity, however, decreases with a temperature increase exponentially. That is one of the reasons why temperature has to be constant during the measurements. Also local heating for example by optical heating by absorption of Laser light could effect a change of the diffusion constant and thereby the gas transport.
In air the increase of the diffusion coefficient with temperature is moderate with

$$\mathcal{D}_{gas}(T) \;\propto\; \mathcal{D}(T_{ref}) T^{1.5}, \tag{2.9}$$

approximately 0.15 % per Kelvin at a range from 20-25 ℃, Roedel [2000].
An additional difficulty for theoretical description of transfer in water is that mass diffusion coefficients in liquids are not well known, often with inaccuracies of more than 40%, Cussler [1997].
A thorough introduction to diffusion including diffusion in heterogeneous systems is given in Cussler [1997]. As coupled diffusion of ions is fundamental for the transport of the fluorophore in the Laser-induced fluorescence measurement technique used here. It will be separately discussed in section 3.4.3.

2.1.2 Turbulent Transport

Turbulent transport is difficult to define, usually turbulence is described by characteristics. Turbulent transport of mass depends on momentum transport and therefore a non-zero velocity field. Turbulence can be an overlay of a convective flow, it appears as a statistical temporal and spatial non-stationary random motion, Roedel [2000]
Turbulent transport will appear if statistical disturbances in the flow - for example vorticity induced by high shear stress, see figure 2.1- can no longer be suppressed by molecular viscosity of the medium: turbulent motion appears.
In contrast to diffusion turbulent transport is anisotropic even in a isotropic medium. Every spatial direction has its own turbulent diffusion coefficient. Moreover, this coefficient also depends on time and or the distance from the

position of separation of two velocity fluctuations, Sagaut et al. [2006].
Furthermore, turbulent flows are highly nonlinear, small perturbations can grow creating new perturbations until the flow reaches a chaotic behavior, Kundu [2007]. Yet, the structures are not fully random as coherent structures can occur, that imply the existence of finite characteristic scales of spatial correlation. Coherent structures show a peculiar spatial organization or pattern that appears repeatedly and have a lifetime much higher than the characteristic turn over times of turbulent fluctuations, Sagaut et al. [2006]. In that context different characteristic length and time scales of turbulence are defined: The integral length scale L_{int} characterizes the distance over which velocities are detectably correlated, see e. g. Kundu [2007]. This scale can be associated with the diameter of the largest eddies. The corresponding time scale T gives the timescale over which velocities are correlated and can be associated with the turn over time of the largest eddies. Sagaut et al. [2006] pointed out that the integral length scale and velocity scale in experiments are in general one order of magnitude smaller than the characteristics of the flow (e.g. depth of water, mean flow velocity).
For the smallest scales Kolmogorov [1941] derived a typical scale of

$$L_{mic} = \left(\frac{\nu^3}{\epsilon}\right)^{1/4},$$

with ν as the kinematic viscosity and ϵ as the rate of dissipation. The Kolmogorov micro scale L_{mic} characterizes the size of the eddies, in which energy is dissipated to heat. In turbulence sometimes long thin tubes appear, regions of high strain. The diameter of these tubes is typically of the order of the Kolmogorov length scale according to Brethouwer [2000] citing Jiménez and Wray [1998]. So identifying such structures would allow an estimate of the Kolmogorov scale. The smallest length scale of the turbulent concentration field is the so called Batchelor length scale L_B. The Batchelor length scale is related to the Kolmogorov scale by the following equation, see e.g. Tennekes and Lumley [1992]:

$$L_B = \frac{1}{\sqrt{(\nu/\mathcal{D})}} \cdot L_{mic}. \tag{2.10}$$

The ratio $\nu/\mathcal{D}$ is the so called Schmidt number Sc that will be discussed in more detail in section 2.3.2. For the used tracer HCl Sc $\gg 1$ is valid, which implies that the scalar concentration field will be wrapped around turbulent velocity vortices and in that way allowing to visualize flow fields, Brethouwer [2000]. Turbulent motion is characterized by high vorticity over a large range of scales: eddies of various sizes ranging from the dimensions of the system to the sub micron range can be found, leading to a transport of mass, heat and momentum from the macroscopic to the microscopic range. So turbulence is a multi-scale phenomena. Energy is transported uni-directionally from large eddies that are produced by the driving mechanism of the flow, in this study wind shear, over smaller to smaller scales where it is finally dissipated by viscosity to heat. The smaller the eddies or vortices the steeper the velocity gradients and therefore the more effective diffusion. This is the so called spectral energy cascade, proposed

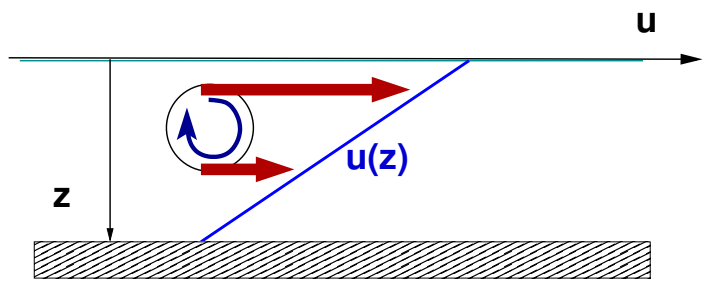

Figure 2.1: Vorticity creation by shear stress. The velocity gradient induces a rotational movement in the liquid

by Richardson [1920]. The cascade is in principal unidirectional. Energy is mainly transferred from larger to smaller structures but interscale interactions of different scales can happen as well. According to Sagaut et al. [2006] this so called distant interactions between scales of very different sizes can make up to 25 % of the total energy transfer.
To analyze turbulence under certain conditions either the energy power spectra are recorded to find frequencies of the dominating eddies, which is done e.g. in the work of Herlina and Jirka [2008] or the auto-correlation function, which contains the same information, has to be determined.
The quantity describing the ratio of inertial forces and viscous forces is the Reynolds number:

$$\mathrm{Re} := \frac{|\mathbf{u}|_{char} \cdot L_{char}}{\nu}, \tag{2.11}$$

with $|\mathbf{u}|_{char}$ and L_{char} being a characteristic velocity and a characteristic length scale, respectively.
At higher Reynolds numbers, $\mathrm{Re} \gg 1$ turbulent transport is by far more effective than diffusive transport except directly at the phase boundaries: Diffusion is the only way of transport as turbulent eddies cannot penetrate the boundary layer. The ratio of the small structure of the Kolmogorov scale to large structures of the integral length scale can be expressed in terms of the Reynolds number:

$$\frac{L_{int}}{L_{mic}} = \mathrm{Re}^{\frac{3}{4}} \tag{2.12}$$

This relations implies that the higher the Reynolds number the broader the range of turbulent scales. As turbulence is linked to high shear stress it is also linked to wave formation. Before a further discussion of these relations is done, the theoretical description of transport phenomena will be given.

2.2 Differential Equations of Transport

Transport of a trace gas is linked to the potentially turbulent velocity field as presented in the previous sections. Two partial differential equations describe transport of mass in a viscous fluid:
On the one hand, transport of momentum is described by the Navier-Stokes

equation and on the other hand, mass transport is described by Fick's second law. Both can be deduced from conservation considerations.

2.2.1 Conservation of Momentum: The Navier-Stokes Equation

The work of Navier [1827] and Stokes [1849] lead to the description of momentum transport by the Navier-Stokes equation. The Navier-Stokes equation can be deduced from the conservation of momentum in a fluid system. The equation is here written for a fluid with isotropic shear and volumetric viscosity in the advective form, according to Schlichting and Gersten [2006]:

$$\frac{d\mathbf{u}}{dt} = \frac{\partial \mathbf{u}}{\partial t} + (\mathbf{u}\nabla)\,\mathbf{u} \tag{2.13}$$

$$= \rho \sum \mathbf{f} - \frac{1}{\rho}\nabla p + \nu\Delta\mathbf{u} + (\frac{\zeta}{\rho} + \frac{\nu}{3})\nabla(\nabla\mathbf{u}), \tag{2.14}$$

with

ρ	density of medium
$\rho\sum\mathbf{f}$	sum of all external volume forces
$\frac{1}{\rho}\nabla p$	volume pressure force
ν	kinematic shear viscosity
ζ	volume viscosity
$\nu\Delta\mathbf{u}$	viscous shear volume forces
$(\frac{\zeta}{\rho} + \frac{\nu}{3})\nabla(\nabla\mathbf{u})$	volumetric shear volume forces.

For transport of momentum in an incompressible viscous liquid, $\nabla\mathbf{u} = \mathbf{0}$, (and constant density $\rho > 0$ and viscosity $\nu > 0$) [1] the Navier-Stokes equation reduces to

$$\frac{d\mathbf{u}}{dt} = \frac{\partial \mathbf{u}}{\partial t} + (\mathbf{u}\nabla)\,\mathbf{u} = \rho\sum\mathbf{f} - \frac{1}{\rho}\nabla p + \nu\Delta\mathbf{u}, \tag{2.15}$$

with f as density of external forces, $\frac{1}{\rho}\nabla p$ the density of the pressure forces and $\nu\Delta\mathbf{u}$ as density of viscous forces.
The solution of the elliptic partial differential equation has to fulfill the following conditions:

$\nabla\mathbf{u} = \mathbf{0}$	for incompressibility,
$\mathbf{u} = \mathbf{0}\,\vert_{\mathbf{z}=\infty}$	no-slip at bottom and
$\mathbf{u}\vert_{\mathbf{0}} = \mathbf{u}(t = 0)$	as initial velocity field and
$\int p(\mathbf{x}, t)\mathbf{dx} = p_0(t)$	for medium pressure.

Especially, the demand of knowledge of the full initial flow field is a problem in solving this equation as it is tried in Direct Numerical Simulation of flows, see 2.5.3.
Unfortunately, this equation is also nonlinear trough the term $\mathbf{u}\nabla\mathbf{u}$ of field

[1] These assumptions are fulfilled for water at constant temperature.

acceleration, also called convective term, as the transported quantity momentum is transported by itself. The velocity gradient tensor $\nabla\mathbf{u}$ can be separated into the vorticity and the rate of strain tensor:

$$\mathbf{u}\nabla\mathbf{u} = \mathbf{u}\left[\frac{\mathbf{1}}{\mathbf{2}}\left(\nabla\mathbf{u} - (\nabla\mathbf{u})^{\mathbf{T}}\right) + \frac{\mathbf{1}}{\mathbf{2}}\left(\nabla\mathbf{u} + (\nabla\mathbf{u})^{\mathbf{T}}\right)\right], \tag{2.16}$$

$$\mathbf{u}\nabla\mathbf{u} = \mathbf{u}\left[\mathsf{W} + \mathsf{S}\right], \tag{2.17}$$

with W as the antisymmetric vorticity tensor, describing the local vorticity of the fluid, and S as the symmetric rate of strain tensor, describing the local deformation of the flow field. Vorticity and Deformation are the two local characteristics of a flow field. With equation 2.17 the momentum equation can be rearranged to the rotation form of the Navier Stokes equation, see Zang [1991]:

$$\frac{\partial\mathbf{u}}{\partial t} + \left(\nabla\frac{||\mathbf{u}||^2}{2}\right) + (\nabla\times\mathbf{u})\times\mathbf{u} = \rho\sum\mathbf{f} - \frac{1}{\rho}\nabla p + \nu\Delta\mathbf{u}, \tag{2.18}$$

with $\omega := (\nabla\times\mathbf{u})$ as the vorticity. In an irrotational flow the vorticity would be zero and therefore this term would vanish. The existence of unique solutions of the Navier Stokes equation could not be proven in $\mathbb{R}^3$ for all times $t \geq 0$ while such a global uniqueness and existence is proven in $\mathbb{R}^2$. The uniqueness could only be proven if an additional constraint of smoothness of the solution is fulfilled according to Temam [1988]. For a short review on the theoretical solution aspects of the Navier-Stokes equation see for example Taylor [1997].
In order to solve the Navier-Stokes equation several assumptions are fed into them to simplify this system in the transport models that will be described in section 2.5.

2.2.2 Conservation of Mass: Fick's Transport Equation of Mass

Under a known velocity field Fick's second law describes mass transport for diffusive processes in an isotropic medium and can be deduced from conservation of mass in fluid system:

$$\frac{dc}{dt} = \frac{\partial c}{\partial t} + \mathbf{u}\nabla c \tag{2.19}$$

$$= \nabla\mathbf{j_c} + S(c) \tag{2.20}$$

$$= \nabla(\mathcal{D}\nabla c) + S(c), \tag{2.21}$$

with

c	concentration
$\mathbf{j}_c$	mass flux density
$\mathcal{D}$	diffusion coefficient
$S(c)$	source/sink term

Fick's transport equation in the above formulation is valid for a medium with sinks and sources. This is fulfilled for dissolution of the acid gas CO_2. CO_2 can be produced from H_2CO_3 by chemical reaction in neutral and basic range above

a pH of 6.5, the typical pH range of fresh and seawater, see Stumm and Morgan [1996] for further details. For a second order reaction,

$$A + B \rightarrow P. \tag{2.22}$$

The sink/source term can be expressed in the following form according to Brethouwer [2000]:

$$S(c_A, c_B) = -K_1 \exp(-\frac{R}{K_2 T}) c_A c_B, \tag{2.23}$$

with c_i as the concentration of species i, K_1, K_2 as constants, R as the activation energy and T as the temperature. This is one of the reasons why HCl has been chosen as a tracer. As it dissociates completely in water, there is just one source at the surface, and the production of HCl molecules in water can be neglected. The sink-source term can therefore be excluded from the considerations in the bulk for this gaseous tracer.

Though the diffusive mass flux equation is linear in concentration, the turbulence comes in through the turbulent velocity field $\mathbf{u}$, so turbulent transport of mass is described by the convection term $\mathbf{u}\nabla c$.
In the case of pure diffusive transport, if Re << Re_{crit} [2] and under the assumption of a constant diffusivity $\mathcal{D}$, which is justified in dilute solutions, Fick's second law 2.19 can be simplified to

$$\frac{dc}{dt} = \nabla(\mathcal{D}\nabla c) + S(c) = \mathcal{D}\Delta c + S(c).$$

2.2.3 Transformation to Flux Equations

Both transport equations can be transformed into flux equations. This is handy regarding cases of steady state flux with $\mathbf{j}$ = constant. In the case of momentum, the kinematic viscosity ν is interpreted as the diffusivity of momentum. To simplify notation, only z-component is regarded in the following

$$\frac{d\mathbf{u}}{dt} = \nu\Delta\mathbf{u} + \sum_{\mathbf{i}} \mathbf{f_i} + \frac{1}{\rho}\nabla p \tag{2.24}$$

$$\frac{dc}{dt} = \frac{dj_{cz}}{dz} \tag{2.25}$$

2.2.4 Limits of Validity

The above described system of transport equations - the Navier-Stokes equation together with Fick's transport equation of mass - describes flow of a Newtonian viscous fluid.

[2] The Reynolds number is a measure for the ratio of total transport to diffusive transport, see equation 2.11; above a critical Reynolds number turbulent transport dominates.

Yet, both equations are only sufficient for describing transport if other environmental conditions remain unchanged. This includes that temperature changes, pressure changes, as well as spatio-temporal changes in density and salinity must be prevented.
This implies special demands on experimental investigations, under which these environmental conditions have to be kept constant. A lot of afford has been spent on the design of the experimental setup to minimize uncontrolled changes in the environmental parameters.

2.3 Boundary Conditions on Gas Transfer

The boundary conditions on the transport equations are presented in this section: Firstly, the boundary conditions implied by the regimes of diffusive and turbulent transport, the boundary layer and the bulk, respectively. Secondly, the properties of solute and solvent and their influence on gas transfer: diffusivity and solubility of the trace gas in the respective fluid of interest, here water.

The diffusivity is usually included in a dimensionless quantity, the Schmidt number Sc (equation 2.32), which characterize the strength of diffusive momentum transport with respect to diffusive mass transport. These quantity allows to relate results of transport for different trace gases or media to the results of the widely used reference tracer CO_2 in water by simple scaling.

The solubility of a trace gas determines where the main resistance of transport is located, for highly soluble gases in the air-side mass boundary layer and for slightly soluble gases in the water-sided mass boundary layer. It also determines whether a constant concentration or a constant flux can be assumed at the air-water interface.

2.3.1 Boundary Conditions due to Flow Regimes: Boundary Layer and Bulk

In this subsection the two flow regimes are presented which have the boundary layer, where diffusive transport dominates and the bulk, where turbulent transport dominates.
While the regimes where turbulence dominates can be easily shown, the existence of a boundary layer can not be proven strictly mathematical. Yet, its existence can be deduced theoretically by using conservation of vorticity as described in Goldstein [1965].

Classification of Transport Regimes

The transport mechanisms themselves define two different layers: a layer where diffusive and turbulent transport are of the same magnitude, and a layer where turbulent transport dominates. These layers are introduced in the following paragraphs.

Dominating Diffusive Transport: Estimation of the Thickness of the Boundary Layer Directly at the interface gas molecules can be exchange between gas and liquid side only by diffusion as turbulent eddies cannot penetrate the interface. So on either side of the interface there must be at least a skin layer where

$$j_z = j_{diff} = -\mathcal{D} \cdot \left.\frac{\mathrm{dc}}{\mathrm{dz}}\right|_{\mathrm{z=0}}, \tag{2.26}$$

is valid. This equation forms one of the boundary conditions of the transport. In fluid dynamics, the thickness of the layer where the influence of diffusion still exceeds influence of turbulence is estimated with the depth where diffusive and turbulent transport are of the same order of magnitude as proposed by Jeffreys [1925]. Kundu [2007]used approximations of the terms of the Navier-Stokes equation for steady state and negligible pressure gradient to estimate the thickness of the viscous boundary layer:

$$\underbrace{u \cdot \frac{\partial u}{\partial x}} \sim \underbrace{\nu \frac{\partial^2 u}{\partial x^2}} \tag{2.27}$$

$$\frac{u_{char}^2}{L_{char}} \sim \nu \frac{u_{char}}{\delta_{diff}^2} \tag{2.28}$$

$$\Rightarrow \delta_{diff} \sim \sqrt{\frac{\nu L_{char}}{u_{char}}}. \tag{2.29}$$

By dividing the last formulation by L_{char} the dependence on the Reynolds number Re (see equation 2.11) becomes obvious:

$$\frac{\delta_{Diff}}{L_{char}} \sim \frac{1}{\sqrt{\mathrm{Re}}}. \tag{2.30}$$

From this simple consideration some important properties of the layer thickness can be already deduced: The thickness decreases with increasing velocity. That corresponds to the measurements by Jähne [1991] who showed an experimentally layer thicknesses in the range of 20 μm for high wind speeds and about 200 μm for low wind speed.

Dominating Turbulent Transport: Bulk Region The boundary layer is followed by the so called bulk. The bulk is the region where turbulent transport is the dominating process. In this region measured mean concentrations of transported scalar components are constant as the water body is well mixed, which gives another boundary condition on the transport equations:

$$\lim_{z \mapsto \infty} c_X(z) = < c_X > = \text{ constant}. \tag{2.31}$$

tracer	Schmidt number Sc			source
	10 ℃	20 ℃	30 ℃	
CO_2	1036	600	367	[Jähne, 2009]
Heat	9.46	7.02	5.42	[Jähne, 2009]

Table 2.1: Schmidt number dependency on temperature for different trace gases in fresh water.

2.3.2 Boundary Condition due to Properties of Trace Gas and Solvent Medium Water

Schmidt Number: Influence of Viscosity of Solvent Medium and Diffusivity of Trace Gas

The viscosity of the medium determines transport in two ways: on the one hand, it determines the wave formation of capillary waves and on the other hand, the medium viscosity determines the value of the diffusion coefficient of the dissolved trace gas. Both diffusion coefficient and viscosity of the medium are therefore strongly related in their influence on transport. In fluid dynamics a dimensionless quantity, the Schmidt number Sc, is used to characterize their combined influence on transport.

The Schmidt number Sc itself is defined as the ratio of kinematic viscosity ν to diffusion coefficient $\mathcal{D}$:

$$\mathrm{Sc} := \frac{\nu}{\mathcal{D}}\,. \tag{2.32}$$

The Schmidt number is a measure how much faster momentum is transported in comparison to diffusive mass transport.
Its analogue for heat transport is the Prandtl number with $\mathrm{Pr} := \nu/\mathcal{D}_H$. The Schmidt number is normally used to discriminate between the behavior of different dissolved gases: While in air typical values are $\mathrm{Sc} \approx 1$, in water the Schmidt numbers are of order 1000 and vary widely as do the diffusion coefficients.
In water, transport of every trace gas is related to the transport of CO_2 by doing a Schmidt number scaling:

$$r(T) = \frac{\mathrm{Sc}(\mathrm{CO_2}, T)}{\mathrm{Sc}(\mathrm{tracer}, T)}. \tag{2.33}$$

Schmidt number of CO_2 at 20 ℃ is $\mathrm{Sc} = 600$ in fresh water, so with the Schmidt number of the here used fluorophore HPTS at 20 ℃, $\mathrm{Sc}(HPTS) = (2.172 \pm 0.420) \cdot 10^3$, see section 3.7.2, this leads to the scaling factor

$$r(20\ ℃) \approx \frac{600}{2172}, \tag{2.34}$$

$$\approx 0.276 \pm 0.05. \tag{2.35}$$

Furthermore, the Schmidt number depends strongly on the temperature.In table 2.1 the Schmidt number dependency on temperature for different tracers is shown.
As a scaling factor it is part of many models describing gas transfer, see the following sections 2.4 and 2.5.

Solubility of a Trace Gas

The solubility of a trace gas determines, where the main resistance of transport is located and whether a constant concentration or a constant flux can be assumed at the air-water interface. These relations will be presented in this subsection.

The solubility is a quantity that is based on equilibrium between the gaseous and liquid phase: In equilibrium, the concentration of a trace gas in water and the corresponding air phase reaches equilibrium in the two phases. The equilibrium concentration in both phase normally differ.

A partition coefficient α_{Sol}, sometimes called Ostwald's solubility, gives the ratio of the volumetric concentration in the liquid c_{ls} to the one in the gaseous c_{gs} phase,

$$c_{ls} = \alpha_{Sol} \cdot c_{gs}. \tag{2.36}$$

The Ostwald solubility is a dimensionless quantity and is mainly used in the air-sea- interaction science. There are several other definitions of solubility in use dependent on the scientific community. Most commonly used is the formulation of the solubility equilibrium as Henry's law of solubility:

$$c_w = \mathrm{K}_H \cdot p_a, \tag{2.37}$$

with c_w as the tracer concentration in water and p_a as the partial pressure of the trace gas in the air phase.
Henry's coefficient can be found in common encyclopedias like NIST Standard Reference Database. The SI units are $[\mathrm{K}_H]$ =mol kg^{-1} Pa^{-1}, with $[p_a]$ = Pa and $[c_w]$ = mol kg^{-1}.
For unit conversion from Henry coefficient in SI units to Ostwald's solubility Schwartz [2003] gave the following relation,

$$\alpha_{Sol} = \mathrm{K}_H \cdot \rho_{solvent} \cdot \mathsf{R} \cdot T. \tag{2.38}$$

with $[\rho_{solvent}]$ =kg m^3, $[\mathsf{R}]$ = 8.3143 J K^{-1} mol^{-1} and $[T]$ = K.
For a detailed discussion of varying definitions and conversion of units see [Schwartz, 2003].
Like the Schmidt number, the solubility also shows a strong temperature dependence, here given for Henry's coefficient,

$$\mathrm{K}_H = \exp(-\Delta G^\circ / RT), \tag{2.39}$$

with ΔG° as the change in Gibb's free energy of dissolution. For highly soluble gases like HCl, whose equilibrium concentration $[HCl]_l \approx 0$ the linear relation given in Henry's law is no longer valid and has to be replaced (for a more detailed discussion see 3.6.2).

Solubility allows to classify trace gases in three categories: slightly soluble gases with $\alpha_{Sol} << 1$, intermediate soluble gases with $\alpha_{Sol} \approx 1$, and highly soluble gases with $\alpha_{Sol} >> 1$. These three classes are sketched in figure 2.2 for the case of an invasion experiment where the tracer concentration in the

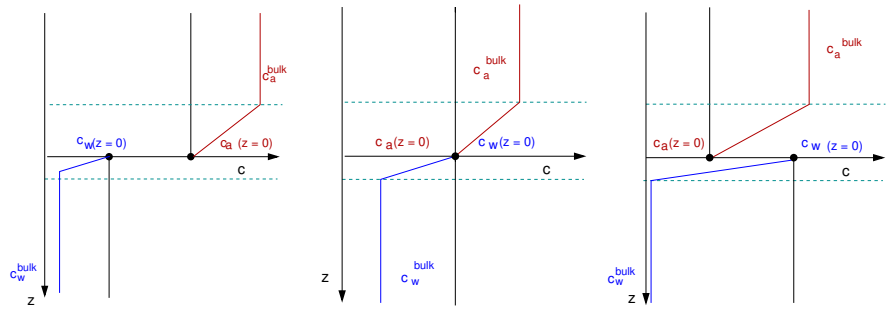

(a) $\alpha_{Sol} < 1$ (b) $\alpha_{Sol} \approx 1$ (c) $\alpha_{Sol} > 1$

Figure 2.2: Effect of different solubilities α_{Sol} on gas tracer invasion experiment. The gas concentration is discontinuous at the water surface and is plotted red in the air phase and blue in the water phase. The air side and water side concentrations right at the interface differ by the factor α_{Sol}, here marked as black circles. The dashed lines mark the corresponding mass boundary layer thicknesses. (a) the tracer is low soluble, (b) tracer is as well soluble in air as in water, (c) tracer is more soluble in water.

water $c_w = 0$ for $t = 0$. CO_2 and O_2 are low-soluble gases like most trace gases, reactive gases like HCl however are highly soluble.
This classification of solubility has also effects on gas transfer:

For low-soluble gases the main resistance of transport lies on the waterside, the process of dissolution hinders a rapid transfer. Furthermore, it is generally assumed in gas transfer studies, that equilibrium concentration directly at the interface are reached for both phases instantaneously. Therefore, low-soluble gases are assumed to follow the boundary condition of constant concentration at the air-water interface, called a Dirichlet boundary condition:

$$c_w\big|_{z=0} = \alpha_{Sol} \cdot c_a\big|_{z=0}. \tag{2.40}$$

However, there are studies of Mühlfriedel and Baumann [2000] and Wothe [2006] showing that equilibrium concentrations at the interface of a liquid-liquid system do not reach instantaneously the equilibrium concentrations of Henry's law. However, they measured a continuous concentration gradient over the interface instead of the discontinuity at the interface predicted by Henry's law. Equilibrium concentrations at the interface were only reached in the long time limit when equilibrium in the bulk was reached, see figure 2.3. This might indicate that the assumption of equilibrium concentration at an air-water interface may not be valid under all conditions and need further investigation. First steps in that direction are done by Winter [2011].

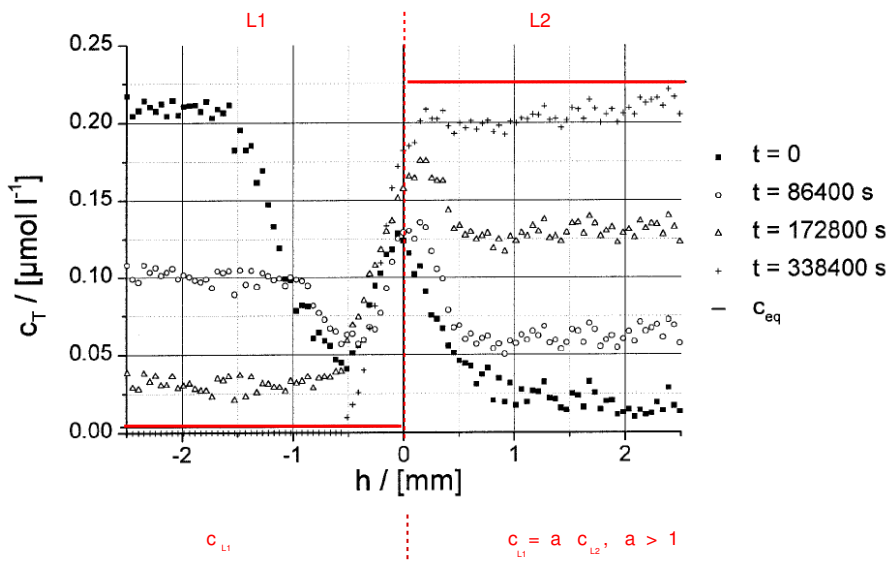

(a)

Figure 2.3: Measurements by Bäumler and Mühlfriedl [2001] and Wothe [2006] showing that concentrations at fluid-fluid interfaces of immiscible fluids (1-butanol and water) do not correspond to the assumption of instantaneous equilibrium concentrations. The interface is plotted in dashed red line, while the equilibrium concentrations predicted by Henry's law are plotted in red in each liquid phase L1 an L2. The direction of mass transfer is from fluid L1 to L2. Graphics adapted from Bäumler and Mühlfriedl [2001].

For highly-soluble gases the main resistance of transport lies on the air-side. Especially in invasion experiments for gases with solubilities $\alpha_{Sol} >> 1$ it can be assumed that equilibrium concentration in the water-phase will not be reached, but instead the mass flux will be constant - given that the concentration in the air side is constant. Therefore, the boundary condition at the interface is now a flux boundary condition or Neumann boundary condition:

$$\left.\frac{\partial c}{\partial t}\right|_{z=0} = \text{constant}. \tag{2.41}$$

2.3.3 Summary of Boundary Conditions

The boundary conditions of transport processes that have been presented in this section are the following:

- The diffusion coefficient of the trace gas has great influence of its transport in the media. This dependency is expressed by the Schmidt number, an individual scaling factor.

- The concentration of low-soluble gases at the liquid surface follows the relation:

$$c_a\Big|_{z=0} = \alpha_{Sol} \cdot c_w\Big|_{z=0},$$

  and gives therefore a Dirichlet boundary condition.

- Transport of high-soluble gases in an invasion experiment is subject to a flux boundary condition:

$$\frac{\partial c}{\partial t}\Big|_{z=0} = \text{constant}.$$

- Inside the boundary layer diffusive transport dominates:

$$j_{z0} = -\mathcal{D}\frac{\partial c}{\partial z}\Big|_{c=0}.$$

- In the bulk the concentration of a scalar tracer is constant as the water body is well mixed, giving the boundary condition:

$$\lim_{z\mapsto\infty} c_X(z) = < c_X > = \text{constant}.$$

2.4 Classification Parameters of Transport across a (free) Interface

In this section the three model-independent characteristic quantities of gas transfer will be introduced: the transfer velocity k, the boundary layer thickness z^* and the characteristic time constant τ all of whom are linked to diffusivity and solubility of the corresponding trace gas. The three quantities can be transformed in one another if the diffusivity of the trace gas is known.
These characteristic quantities are usually used for model descriptions presented in section 2.5 and contain equivalent information on the fluid-tracer system.

2.4.1 Definition of the Boundary Layer Thickness in Transfer Studies

In gas exchange studies a different measure for the thickness of the boundary layer is used than the above given equation 2.27 which is mainly used in fluid dynamics.
The boundary layer thickness z^*_X is defined as that depth, where the gradient of the profile of the regarded quantity $X \in$ (heat,mass,momentum) directly at the surface $\frac{\partial X}{\partial z}\Big|_{z=0}$ intersects with the line fitted to the concentration of the

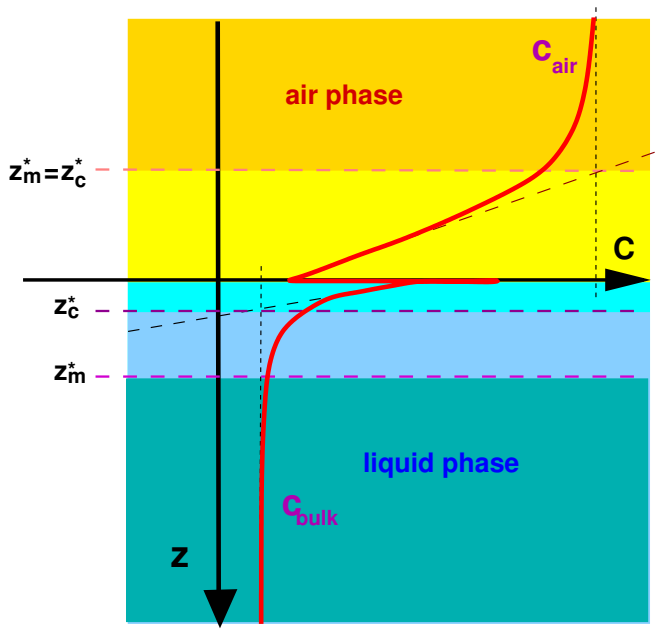

Figure 2.4: Sketch of the mass (c) and momentum (m) boundary layers in air and water at an air-water interface, plotted for a trace gas with solubility $\alpha_{Sol} > 1$. The mean gas concentration profile is plotted in red.

quantity in the bulk.

$$\frac{\Delta X}{\Delta z} \doteq \left.\frac{\partial X}{\partial z}\right|_{z=0} \tag{2.42}$$

$$\Longrightarrow z^*_X := \Delta z \doteq \frac{\Delta X}{\left.\frac{\partial X}{\partial z}\right|_{z=0}} \tag{2.43}$$

$$= \left|\mathcal{D}_X \cdot \frac{\Delta X}{j_X}\right|. \tag{2.44}$$

In the following, the subscript 'a' refers to air-side and 'w' to water side. Together with the influence of solubility on the concentration at the interface the thickness of the mass boundary layer then is given by:

$$z^*_c := \frac{c_a|_{z=0} \cdot \alpha_{Sol} - c_{bulk}}{\left.\frac{\partial c}{\partial z}\right|_{z=0}} \tag{2.45}$$

$$= \frac{c_w|_{z=0} - c_{bulk}}{\left.\frac{\partial c}{\partial z}\right|_{z=0}} \tag{2.46}$$

$$= \frac{\Delta c}{\frac{\partial c}{\partial z}|_{z=0}} \tag{2.47}$$

$$= \left|\mathcal{D} \cdot \frac{\Delta c}{j}\right|. \tag{2.48}$$

As in air all diffusion coefficients approximately the same value $\mathcal{D} \approx \mathcal{D}_m \approx \mathcal{D}_h \approx 0.1$ cm^{2}s^{-1}, the boundary layer thicknesses are also of the same size, approximately 1 mm - 1 cm.
In water, the three boundary layer thicknesses differ significantly. The aqueous mass boundary layer is extremely thin, e.g. has a thickness of approximately 20- 200 μm for low-soluble gases (i.e. O_2, CO_2) depending on the strength of turbulence, [Jähne, 1991]. While the viscous boundary layer has a thicknesses in the range 600-2000 μm. The higher the turbulent motion the thinner is this layer found to be.
The proportion of boundary layer thicknesses of different trace gases can be estimated using a scaling according to

$$\mathsf{z}_\mathsf{c}^*(gas1) = \left(\frac{\mathcal{D}(gas1)}{\mathcal{D}(gas2)}\right)^{n-1} \cdot \mathsf{z}_\mathsf{c}^*(gas2). \tag{2.49}$$

The exponent n - the so called Schmidt number exponent- accounts here for different situations: $n = 3/2$ for a flat surface and a reduction to $n = 1/2$ for a wave-undulated interface (for more details see for example [Jähne, 1990])

2.4.2 Transfer Velocity

The transfer velocity is a quantity that describes how fast the regarded concentration is moving through a certain distance Δz in the fluid, sometimes it is therefore called 'piston velocity'.
The transfer velocity is defined as the flux density over the interface divided by the concentration difference of the regarded quantity X (heat, mass or momentum) over a distance Δz, normally the distance between bulk and interface:

$$\mathbf{k} := \frac{\mathbf{j}_X}{\Delta X} = \frac{\mathbf{j}_X}{X_{z=0} - X_{bulk}}. \tag{2.50}$$

This definition takes into account that a passive tracer like mass is transported linearly according to the partial differential equation of mass transport (see 2.2). Transfer velocities are added reciprocally, as they are the inverse of a kind of resistance of transfer $R := 1/|\mathbf{k}|$. As the concentration difference in the case of mass transport has to respect the solubility relation at the interface, the value of the transfer velocity changes whether it is regarded as air-sided or water-sided. Regarded from a water-sided point of view, the total transfer velocity of the overall transport process over the gas-liquid interface is therefore described as:

$$\frac{1}{|\mathbf{k}_{tot}|} := \frac{\alpha_{Sol}}{|\mathbf{k}_a|(\Delta c^a_{bulk-surface})} + \frac{1}{|\mathbf{k}_w|(\Delta c^w_{bulk-surface})} = \alpha_{Sol} \cdot R_a + R_w. \tag{2.51}$$

The solubility α_{Sol} accounts for the discontinuity of concentration over the interface as presented above. Important to stress again is, that the transfer velocity is only valid when defined on a certain interval, i. e. Δz, distance from surface (z=0) to bulk.

The transfer velocity is related to the boundary layer thickness by a simple relation:

$$\begin{aligned} |\mathbf{k}| &= \frac{|\mathbf{j}_X|}{X_{z=0} - X_{bulk}} \\ &= \frac{\mathcal{D}_X \cdot \frac{\partial X}{\partial z}\big|_{z=0}}{X_{z=0} - X_{bulk}} \\ \Rightarrow |\mathbf{k}| &= \frac{\mathcal{D}_X}{z_X^*}. \end{aligned} \tag{2.52}$$

If experimental knowledge about the gradient of the concentration profile directly at the interface is given and the diffusion coefficient is known, this relation allows to calculate the transfer velocity.

2.4.3 Transfer Time

The third characteristic of transport over the boundary layer is the characteristic transport time τ^*

$$\tau^* := \frac{z^*}{|\mathbf{k}|} = \frac{\mathcal{D}}{|\mathbf{k}|^2}. \tag{2.53}$$

Typical values are 0.04-4.0 s according to Jähne [2009].

2.4.4 Summary

All three characteristic quantities contain the same information. If one of them is known the other two can be deduced - if and only if the diffusion coefficient of the transported component is known.

$$z_x^* = \frac{\mathcal{D}_X}{|\mathbf{k}_X|} = \tau_X^* \cdot |\mathbf{k}_X|. \tag{2.54}$$

As typical errors for diffusion coefficients are of 20 % the wish to achieve a higher accuracy in gas transfer measurements is often limited by the poor knowledge of the last.
With these characteristic quantities the basis is given to make the next step and go on to modeling the transport equations.

2.5 Modeling and Simulating Gas Transfer

In this section approaches are presented, which try to solve the transport equations by using different models for transport.
Important to note is that usually the transport equations have to be solved in a local coordinate system attached to the water surface. These local coordinate systems usually change with time like the free moving water surface. This is implicitly contained. Every measurement technique has therefore not only to record the desired measurement values but also the position of the local coordinate system for further analysis of the transport. At the beginning a short

overview over shear flow will be given, as it represents the most basic model for momentum transfer over a gas-liquid interface and allows to illustrate the influence of waves on gas transfer, which is usually included in the various models only in the Schmidt number exponent n: $n = 2/3$ for a flat and $n = 1/2$ for a wavy interface.

The next model to discuss is the surface divergence model, currently regarded as one of the most promising models. Models for a simplified 1D-transport, which are the models whose validity can be tested with the measurement technique used in this study are presented.
The most demanding approach is currently the Direct Numerical Simulation, which will be summarized in section 2.5.3. It tries to solve the full 3D-transport equations.

2.5.1 Shear flow

In wind-induced turbulence setups, momentum is imposed through shear on the water surface. The friction velocity u_* characterizes the amount of horizontal shear stress τ_{horiz} induced on the water-surface. The formulation is given according to Weber [1999]

$$\begin{aligned} \tau_{horiz} &= \rho\sqrt{\overline{u'w'}^2 + \overline{v'w'}^2} && (2.55)\\ \Rightarrow u_* &:= \sqrt{|\tau_{horiz}|/\rho}, && (2.56)\\ & && (2.57) \end{aligned}$$

with ρ as the density of the medium. With the assumption of Prandtl that the main flow fluctuations dominate over the spanwise components in a linear wind wave tunnel, the friction velocity reduces to :

$$\begin{aligned} u_* &= \left(\overline{u'w'}^2 + \underbrace{\overline{v'w'}^2}\right)^{1/4} && (2.58)\\ &= \left(\overline{u'w'}^2 + 0\right)^{1/4} \\ &= \left(\overline{u'w'}\right)^{1/2}. \end{aligned}$$

The relation between air-sided friction velocity and water-sided friction velocity is given by:

$$u_*^w = \sqrt{\rho^w/\rho^a} \cdot u_*^a. \qquad (2.59)$$

If the shear is low enough the water surface will remain flat, although the water-sided flow may already be turbulent.
At higher wind shear a complex wave-field evolves that is characteristic for different wind speeds and characteristic for fetch, the distance the wind has exercised shear on the fluid.

2.5.2 Ways of Simplifying the Transport Equations: Linearized 1D-Transport models

All models presented here follow a general description of transfer velocity:

$$|\mathbf{k}_w| = u_{*w} \cdot \frac{1}{\mathfrak{b}(s)} \cdot \mathrm{Sc}^{-n(s)}, \tag{2.60}$$

with u_w^* as the water-sided friction velocity, $\mathfrak{b}$ as a model parameter dependent on s and s as a collection of parameters describing surface conditions, for example mean square slope and others.
Following this equation the relation between the transfer velocities of two different tracers can be determined:

$$\frac{|\mathbf{k}_1|}{|\mathbf{k}_2|} = \left(\frac{\mathrm{Sc}_2}{\mathrm{Sc}_1}\right)^n. \tag{2.61}$$

Flat Surface: Schmidt Number Exponent $n = 2/3$

A flat surface is usually encountered below wind velocities of 3 m/s Wanninkhof [2007]. In the most simple model wind can be treated as a kind of solid plate that is in contact with the fluid and accelerates the fluid molecules directly in contact with it by shears. As the molecules are bound in the liquid by intermolecular bonds, momentum is transported into the liquid as the faster molecules are transported into the liquid by diffusion, as it is described for example in Roedel [2000]. Shear flow implicitly produces in that way vorticity whose rotational energy is finally transported into eddies.
In the laminar case viscosity damps the upcoming turbulent eddy motion. But when velocity is too high, viscosity is no longer able to dissipate the energy in the inertial subrange. Energy is stored in bigger eddies that can no longer be suppressed. The initial linear velocity profile is transformed into a logarithmic one.
For a more detailed discussion on energy storage, see [Kundu, 2007].
A coordinate system fixed to the water surface remains stationary in space and time, which simplifies the calculation of transport equations as they can be solved on a constant mesh.

Wave-influenced Surface: Schmidt Number Exponent $n = 1/2$

In the case of a free moving water surface in three dimensions everything said about turbulence production is still valid but here an additional influence comes up in the spatio-temporal changing of the topology of the water surface-waves: Energy and momentum of the wind field can now not only be stored in shear stress but also in waves.
In that context Jähne [1985] distinguished three energy fluxes: first turbulent air flow, second nonlinear wind-wave interaction and third decay of waves to turbulence and wave-breaking.
More detailed, the wave-field itself acts on the wind-field as it appears as surface roughness, especially in the case of capillary waves, where it effectively increases

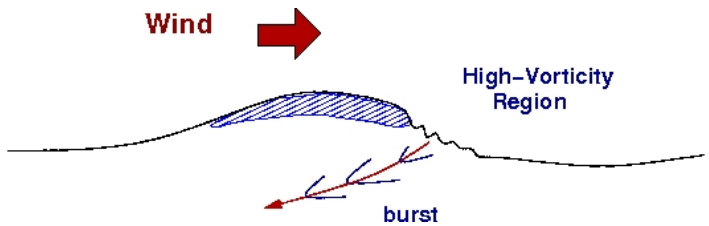

Figure 2.5: Burst at wave crest according to Ebuchi et al. [1993]

momentum transfer from the wind-field into the water body. Waves of high amplitude can also block the wind-field and lead to flow separation.Also, wave-wave interaction can lead to an exchange of energy between waves of different length. All in all, these effects lead to a highly complex interaction of wind- and wave-field.
Therefore, Csanady [2001] adds to his listing in the turbulent case some quantities that are suspected to influence the gas transfer in addition

- short waves
- wave dependent transfer velocities
- surface tension in the presence of bubbles
- local surfactant concentration

All these quantities are directly or indirectly linked to wave formation. So in the case of a free moving water surface there is shear flow from viscous shear and wave breaking, Csanady [2001].
Toba et al. [1975] and Ebuchi et al. [1993] pointed out in their studies a coupling of creation of large eddies to the location of the wave crest. In the capillary waves at the crest the surface converges which induces a flow towards the water bulk ('forced convection'), which they called 'burst' in contrast to 'sweeps' when fluid is transported out of the bulk towards the surface.
Also two wave regimes are acknowledged, the micro-scale wave breaking regime and the white-cap breaking regime. Micro-scale wave breaking is characterized by Banerjee et al. [2004] as 'plunging motions without air entrainment' and white-cap breaking as 'plunging motion with air entrainment'.
Yet, the gas transfer in the presence of waves is still not well understood, which is demonstrated quite plane in the usage of the Schmidt number exponent in the models to distinguish only two cases - no waves and waves, while measurements by Nielsen [2004] indicated a smooth transition of the Schmidt number exponent.

Reynolds Fluctuational Approach

Reynolds fluctuational approach models turbulence as fluctuations (') around a mean ($\mathbf{U}$ or C) in velocity $\mathbf{u}$ and concentration c:

$$\mathbf{u} = \mathbf{U} + \mathbf{u}' \tag{2.62}$$

$$c = C + c'. \tag{2.63}$$

This is the so called concept of 'correlated fluctuations' or 'eddy correlation'. This concept is included into the partial differential equations, that describe mass transport in a fluid.

To differ between turbulent and diffusive part of transport the fluxes are separated respectively

$$j = j_{diff} + j_{turb}. \tag{2.64}$$

Using the concept of correlated fluctuations as mentioned and taking means of the fluxes (mean of fluctuations is assumed to be zero) one finally comes to the following expressions: For the momentum p

$$\overline{\mathbf{j^p}} = \overline{\mathbf{j^p_{diff}}} + \overline{\mathbf{j^p_{turb}}} \tag{2.65}$$

$$\text{e.g.:} \quad \overline{j^p_{xz}} = -\nu \frac{\partial U_x}{\partial z} + \overline{u'w'}. \tag{2.66}$$

and accordingly for mass fluxes:

$$\overline{j^c} = -\mathcal{D}\frac{\partial \overline{c}}{\partial z} + \overline{c'w'} \tag{2.67}$$

$$\overline{j^c} = \overline{j^c_{diff}} + \overline{j^c_{turb}}. \tag{2.68}$$

1D-turbulent transport models differ mainly in how they describe the turbulent part of the regarded fluxes.
All models predict different concentration profiles in the mass boundary layer. Their applicability to different conditions has been tried to examine but still the results allow not a definite evaluation.
In the following subsections different models are presented that use this approach to set up 1D transport equations.

Turbulent diffusion models

In turbulent diffusion models the turbulent part of the flux is modeled by introducing a turbulent diffusivity that is depth-dependent $\mathcal{K} = \mathcal{K}(z)$ in contrast to the molecular diffusivity $\mathcal{D}$.

$$\overline{j^p_{turb}} = \overline{u'w'} = -\mathcal{K}_p(z)\frac{\partial U_x}{\partial z}, \tag{2.69}$$

$$\overline{j^c_{turb}} = \overline{c'w'} = -\mathcal{K}_m(z)\frac{\partial C}{\partial z}. \tag{2.70}$$

Film Model The film model is the oldest and simplest model in use and was introduced by Lewis and Whitman [1924]. Though being a oversimplification the film model still serves as a lower limit for estimation of transfer velocities. It assumes two flow regimes: Just molecular diffusion is responsible for transport in the aqueous mass boundary layer reducing the flux equation in the whole layer to

$$\overline{j^c} = -\mathcal{D}\nabla C, \tag{2.71}$$

while pure turbulent transport is assumed in the well-mixed bulk.
Under steady state conditions it predicts a linearly changing concentration in the boundary layer while in the well-mixed bulk the concentration is constant, Cussler [1997]. The turbulent diffusion coefficient is zero in the boundary layer and a constant in the bulk. The transfer velocity in the boundary layer is therefore given by:

$$|\mathbf{k}| = \frac{\mathcal{D}}{z^*}. \tag{2.72}$$

The transfer rates predicted by the film model are far too low, as the influence of turbulence in the boundary layer cannot be neglected in reality.

Interesting for the present study is the mean concentration profile predicted by each model.
For a more general characterization of individual situations a dimensionless depth z^+, a dimensionless transport time t^+ and concentration $\bar{c}^+$ are introduced:

$$z_+ := \frac{z}{z^*}, \quad t^+ := \frac{t}{t^*} \quad \text{and} \quad \bar{c}^+ := \frac{\bar{c}}{C_{bulk} - C_{surface}}. \tag{2.73}$$

For tracer invasion and both a flat and a wavy-free surface, the predicted mean concentration profile by the film model is given by

$$c^+(z^+) = \begin{cases} 1 - z^+, & \text{if } z^+ \leq 1; \\ 0, & \text{if } z^+ > 1. \end{cases} \tag{2.74}$$

Large and Small Eddy Models In the small and large eddy models turbulent eddies of different sizes are assumed to dominate transport. Theofanus [1984] assumed them to be valid for low turbulence in the case of the large eddy model and for high turbulence in the case of the small eddy model.
Fortescue and Pearson [1967] developed the so called large eddy model, here large eddies of the integral length scale are assumed to dominate transport.

In the small eddy model, introduced by Banerjee et al. [1968], Deacon [1977] and Lamont and Scott [1970], small eddies nearing Kolmogorov length scale the nearer the come to the surface are supposed to influence transport in the aqueous mass boundary layer. Their size should decrease the nearer they are located to the surface from simple geometric argumentation. In that way directly at the surface, no turbulent eddies are present, therefore only diffusive transport is encountered at the interface. The main idea is that transport into the bulk is achieved by a cascade of eddies increasing in size towards the bulk. Generally,

the influence of turbulence in the small eddy model is modeled as a turbulent diffusivity $\mathcal{K}$,

$$\overline{j_z^c} = -(\mathcal{D} + \mathcal{K}_m(z))\frac{\partial C}{\partial z}, \tag{2.75}$$

with $\mathcal{K}_m(z) = \alpha_i z^i$ with i ≥ 2. For a rigid surface, $i = 3$ is chosen, while for a free surface $i = 2$. Jähne and Münnich [1980] gave an approximation for the transfer velocity at a rigid interface to

$$|k_w| \;=\; \frac{|\mathbf{u}_{*\mathbf{w}}|}{12.2} \cdot \mathrm{Sc}^{-2/3} \text{ for Sc} > 60, \tag{2.76}$$

Coantic [1986] gives for a free interface

$$|k_w| \;=\; \text{constant} \cdot |\mathbf{u}_{*\mathbf{w}}| \cdot \mathrm{Sc}^{-1/2}. \tag{2.77}$$

The corresponding mean concentration profiles were calculated by Münsterer [1996] for the case of free mobile interface, (Schmidt number exponent $n = 1/2$) and a smooth interface (Schmidt number exponent $n = 2/3$).
Falkenroth [2007] also calculated an estimated mean concentration for a Schmidt number exponent of $n = 4/3$ for the case of thermal convection. A free mobile interface corresponds to the case i= 2 for the exponent of the defining polynomial of the turbulent diffusivity $\mathcal{K}$ leading to the following concentration profile:

$$c^+(z^+) \;=\; 1 - \frac{2}{\pi}\arctan(\frac{\pi}{2}z^+). \tag{2.78}$$

A smooth or rigid interface is described by an exponent i= 3, thus yielding

$$\begin{aligned} c^+(z^+) \quad = \quad & \frac{3}{4} + \frac{3}{2\pi}\arctan\left(\frac{1}{\sqrt{3}} - \frac{4\pi}{9z^+}\right) - \frac{\sqrt{3}}{2\pi}\ln\left(9 + \pi\sqrt{12}z^+\right) + \\ & \frac{\sqrt{3}}{4\pi}\ln\left(81 - 18\sqrt{3}\pi z^+ + 12(\pi z^+)^2\right). \end{aligned} \tag{2.79}$$

Surface Renewal Models

Surface renewal models assume that parts of the boundary layer are statistically exchanged with the bulk. The turbulent flux is modeled by

$$\frac{\partial}{\partial z}\overline{j_{zturb}^c} = \lambda z^p \cdot C \tag{2.80}$$

leading to

$$\frac{\partial}{\partial z}\overline{j_z^c} = -\frac{\partial}{\partial z}(\mathcal{D}\frac{\partial C}{\partial z}) + \lambda z^d \cdot C \text{ with } d \geq 0 \tag{2.81}$$

λ is the so called 'renewal rate', $< \tau >$ the residence time, that may increase with depth and also vary statistically.
There are a few modifications regarding the most effective eddy size. Surface renewal models were introduced by Higbie [1935] for a constant renewal rate, and modified to the statistically varying rate by Danckwerts [1951]. Short renewal times are in that model associated with strong renewals and long times with

weak ones. This relation is sketched in figure 2.6. The transfer velocity in the boundary layer is given by:

$$k_w = \sqrt{\frac{\mathcal{D}}{<\tau>}} = \sqrt{\frac{\nu}{<\tau>}} \cdot \mathrm{Sc}^{-1/2}. \tag{2.82}$$

The mean concentration profiles predicted by the surface renewal model were

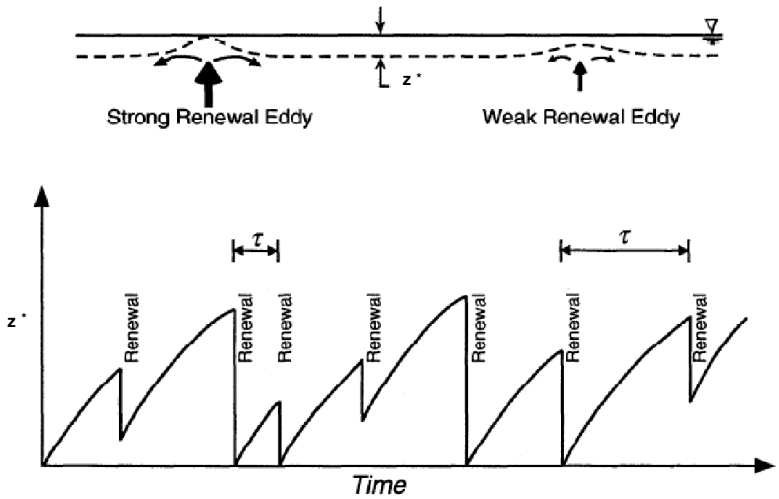

Figure 2.6: Sketch of theory of surface renewal model for statistically varying renewal time. In the upper part the strong and weak renewal events are sketched. A strong renewal is associated with a short renewal time, while a weak renewal is associated with a long one. Image adapted from Falkenroth [2007].

calculated by Münsterer [1996] and Falkenroth [2007] for a smooth and a wavy free interface For a free interface (d=0) this yields an exponential profile:

$$c^+(z^+) = \exp(-z^+). \tag{2.83}$$

For the smooth interface (d=1) the mean profile is based on Airy functions

$$c^+(z^+) = \frac{1}{\mathrm{Ai}(0)}\mathrm{Ai}\left(-\frac{\mathrm{Ai}(0)}{\mathrm{Ai'}(0)z^+}\right). \tag{2.84}$$

Surface Divergence Model

The surface divergence model was the first to combine hydrodynamical properties of the surface, local convergence and divergence in the local coordinate system at the water surface, to transport of heat, mass and momentum. At the interface the continuity equation yields for the velocity fluctuations

$$\left(\frac{\partial u'}{\partial x} + \frac{\partial v'}{\partial y}\right)\Big|_{z=0} = -\frac{\partial w'}{\partial z}\Big|_{z=0}. \tag{2.85}$$

That changes in the horizontal components must equal the transport towards the bulk. In that way the vertical velocity w can be estimated from the surface divergence which is defined as

$$\beta^s(x,y,t) := \left(\frac{\partial u'}{\partial x} + \frac{\partial v'}{\partial y}\right)\Big|_{z=0}. \tag{2.86}$$

The surface divergence has been introduced by McCready et al. [1986]. At the beginning it was developed to describe effects at an unsheared interface, but has been adapted to wind sheared surfaces.
Here, convergence and divergence effects induced by waves are assumed to have great influence on mass transport, see the sketch in figure 2.5, where in the area before the wave crest a high surface convergence is given, and therefore transport towards the bulk is suspected, as reported by Ebuchi et al. [1993]. In the area of the trough a high divergence is given and therefore increased transport towards the surface is assumed. For a free sheared water surface, the transfer velocity is predicted to follow this relation according to Banerjee et al. [2004]:

$$|\mathbf{k}_w| = \text{constant} \cdot \sqrt{\mathcal{D}\beta^s_{RMS}}, \tag{2.87}$$

$$= \text{constant} \cdot \sqrt{\nu\beta^s_{RMS}} \cdot \mathrm{Sc}^{-1/2}, \tag{2.88}$$

with $\beta^s_{RMS} = \sqrt{\left(\frac{\partial u'}{\partial x} + \frac{\partial v'}{\partial y}\right)^2\Big|_{z=0}}$.

2.5.3 Full Transport Equations: Direct Numerical Simulation -DNS

In Direct Numerical Simulation, abbreviated by DNS, the transport equations are directly solved in numerical computer experiments using finite volume and finite-difference approaches for solving the partial differential equations. The whole range of turbulence from Kolmogorov microscale up to the integral length scale have to be resolved in the computation mesh by solving the Navier-Stokes-equation without using any model assumptions for turbulence.
The simulations are very demanding regarding computer resources and very time consuming according to Hung [2009]. The PDE-system is usually solved as an initial value problem starting with an initial guess of the full 3D-flow fields of momentum, heat and mass. As these fields are not known in such a high spatial resolution demanded by the simulations from measurements, they are substituted by simplified fields, like a Stokes gravity wave (see Tsai and Hung [2007]) for momentum and constant temperature and concentration fields. The results are therefore extrapolations of these initial fields, that are assumed to resemble natural conditions. The results seem promising, see for example Tsai and Hung [2007], but without experimental validation they remain hypotheses. An illustration for the drawbacks of solving initial value problems (possible loss of efficiency and of stability by elimination of state variables) is given by Bock [1985]: He showed that initial value problem cannot be solved numerically for a test problem.

To overcome these drawbacks Bock [1985] proposed so called multiple-shooting methods, which allow to incorporate measurement values at different control times, which do not need to contain full field information. These multiple-shooting approaches are widely used, and may be a suitable way to incorporate incomplete measurements, for example gained by LIF experiments conducted in this study, in the solvers of Direct Numerical Simulations and make their results more reliable.

2.6 Summary and Conclusions

In figure 2.7 the mentioned dimensionless mean concentration profiles are plotted that are predicted by the different transport models presented in the last section. These mean concentration profiles can be compared to those obtained

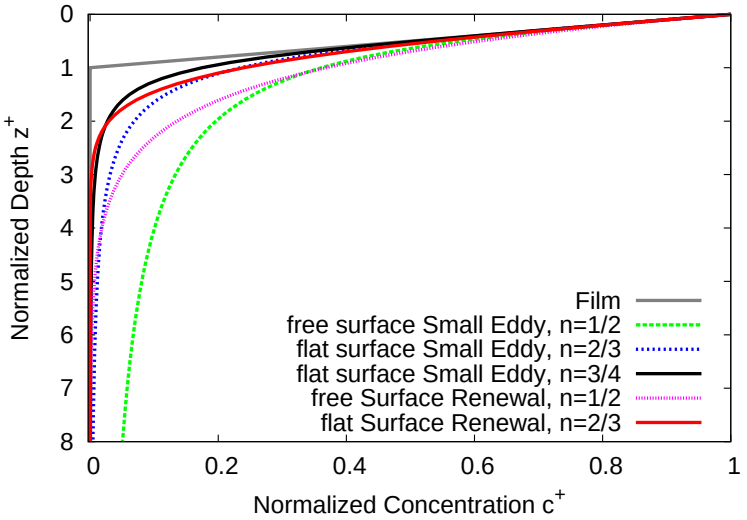

Figure 2.7: Model predictions for mean gas concentration profiles. Image based on calculations by Falkenroth [2007] and Münsterer [1996].

in LIF-measurements of concentration fields, like they are done in this study. Therefore, a model discrimination may be done by such a comparison.
In laboratory measurements the gained mean gas concentrations profiles seem to support in many cases the surface renewal approach in the case of lower turbulence; for example the studies of Münsterer and Jähne [1998], Falkenroth [2007], and Herlina and Jirka [2008]. Herlina and Jirka [2008], who also measured at high bottom induced turbulence, gained gas concentration profiles in a grid stirred tank that 'fall between the two theoretical profiles based on the model with dominant large scale assumption and the small-eddy turbulent diffusion'.

Part III

Measurement Technique

Chapter 3

Method for Visualizing Dissolved Gas in the Water-Phase: Laser-Induced Fluorescence

In small-scale air-sea interaction solution dynamics of different gases in the water phase can be studied with a high spatio-temporal resolution by Laser-induced fluorescence, abbreviated as LIF.
In Laser-induced fluorescence techniques the water volume to be analyzed is dyed with a fluorophore and fluorescence is stimulated by illumination with a laser light sheet. This fluorophore changes the intensity of its fluorescent emission depending on the local concentration of the dissolved gaseous tracer. From that change in intensity, the local concentration of the dissolved gas can be determined. Therefore, the core of the LIF-technique is the combination of the fluorophore and the gaseous tracer used for experiments.

The non-invasive LIF-technique allows to map water-sided gas concentration fields in up to three spatial dimensions without disturbances of the flow. The concentration of the fluorophore is kept so low, that surface activity of the dye can be neglected. The main difficulty of the technique is the detection of the water surface. However, with the novel Static-Pattern LIF technique presented here, a reliable detection is achieved. This technique is presented in detail in section 6.

In this chapter the basic theoretic principle of the LIF-technique is described, before any detailed setup is discussed, which will be the task of chapter 4. In the following sections an introduction to Laser-induced fluorescence techniques is presented by a short recapitulation of previous and related works in 3.1 and a small section mentioning the contribution done in this work in 3.2. An overview of the process of fluorescence follows in 3.3 including a theoretical description of the encountered absorption and emission processes, that is needed for analyzing the obtained signals. After that the actual kind of LIF approach used in this

study is described in its theoretical principles in 3.4, including preconditions for usability and sensitivity to the gaseous tracer HCl. Furthermore, the presented pH-indicator method will be compared to the oxygen quenching method used by many authors in 3.5.
A more detailed description of the gaseous tracer HCl, the solution dynamics of which are to be examined in invasion or evasion experiments, is presented in section 3.6. In section 3.7 the properties of a suitable fluorophore for LIF are discussed, followed by a detailed description of the fluorophore 1-Hydroxypyrene-$3, 6, 8$-trisulfonic acid trisodium salt, abbreviated by HPTS, used in this study.

3.1 Relation to Previous Works

Hiby et al. [1967] was the first to use the LIF-technique for visualizing gas transport in falling films to determine mean concentration and fluctuations at one point.
Later it was adapted for measurements under the condition of a flat water surface, by Pankow and Asher [1984] in a grid-stirred tank. Jähne [1991] successfully applied the LIF technique for 2D-measurements of concentration profiles in the water-sided mass boundary layer in a wind-wave tunnel.

Up to now the LIF-technique is widely and successfully used in studies of dissolution of various gaseous tracers. Generally, two categories of LIF measurements have been evolved: On the one hand, the method of oxygen quenching, for example the works of Duke and Hanratty [1995], Falkenroth [2007],Walker and Peirson [2008] and Herlina and Jirka [2008], and on the other hand, the pH-indicator method using acid or alkaline gases as tracers. Examples here are the studies of Münsterer and Jähne [1998] with tracer HCl,Variano and Cowen [2007] and Asher and Litchendorf [2009], both with CO_2 as gaseous tracer. The pH-indicator method is discussed detailed in 3.4.
The oxygen quenching method allows only the study of the low-soluble gas oxygen, while the pH-method is more versatile and can be used for detection of both low-soluble gases like CO_2 and highly-soluble gases as well as HCl.

3.2 Contribution and Improvements regarding Fluorophore and Tracer Gas in this Study

Up to now, fluorescein and its derivates like dichlorofluorescein have been used for visualizing acid gases, while in this thesis the novel fluorescent pH-indicator HPTS, 1-hydroxypyrene-$3, 6, 8$-trisulfonic acid trisodium salt, is used for studies of invasion of HCl.

HPTS offers several advantages over fluorescein. The most important one is a larger Stokes shift of approximately 53 nm compared to 25 nm of fluorescein. Therefore the probability of reabsorption of emitted fluorescence by the dye itself is reduced drastically. The optical properties of HPTS regarding absorption

and fluorescent emission are characterized in aqueous solution. For further details on the fluorescent dye see 3.7.

Furthermore, HCl has been chosen as gaseous tracer because of its high solubility, which can be approximated to be close to infinity. HCl induces a constant flux boundary condition at the water surface independent of its concentration in solution.
A constant flux boundary condition instead of an assumed constant concentration directly at the interface, which would be the case for low soluble gases, seemed to be a more robust choice, since Mühlfriedel and Baumann [2000] showed in their measurements at fluid-fluid interfaces that the common assumption of equilibrium concentrations in air and water at the interface according to Henry's law of solubility might not be valid. In addition transport of the tracer CO_2 is complex, because of its slow hydration reaction. A far more demanding modeling of its reaction chemistry is needed as shown for example by Eichkorn [1997].

In our research group Jähne [1991] and Münsterer and Jähne [1998] used HCl as tracer for measurements in a wind-wave tunnel, but the resolution of these early studies was limited so that only mean vertical concentration could be evaluated in their temporal evolution (zt, 2D).
This study will be a continuation of their work with a better suited fluorophore, a more powerful laser and an optimized optical setup, which allows measuring in temporal and two spatial dimensions (xzt, 3D).

3.3 Introduction to Fluorescence

Best suited for non-invasive measurement techniques is the analysis of optical properties of absorption and fluorescence of dyes solved in the water volume of interest.
In principle, absorption and fluorescence spectroscopy offer the same information of the observed tracer molecule as Kirchhoff's law shows, see Schmidt [2000] for more details. Absorption and fluorescence have timescales in the nano second range which allow to measure changes in the fluorophore and its surroundings with a high optical and temporal resolution. Fluorescence offers one advantage over absorption as it can be measured in an illuminated cross section of the probe of interest. So one plane can be picked out of a large volume. Furthermore, the distance between detector and measurement plane can be of greater distance, as the emitted light can be detected relatively far away - say outside of the probe to measure which allows a non-disturbed flow regime- given that reabsorption can be neglected. Even whole volumes can be measured by scanning a whole volume with a 2D-laser sheet like it is done by Van Vliet et al. [2004].
Fluorescence appears if an electron relaxates from the vibrational levels of usually the first excited singlet state S_1 to the the vibrational levels of the electronic

ground state S_0 under photon emission, Haken and Wolf [1992].
Excitations to higher states normally relaxate without photon emission to the S_1 state, Schmidt [2000].
The ground state can be reached by several mechanisms:

- fluorescence,
- chemical reaction (an example is photosynthesis),
- internal energy transfer via
  - internal conversion (energy is transferred to rotational/vibrational energy by conversion), or
  - inter-system crossing (energy transfer from the singlet to the triplet state),
- energy transfer to other molecules (quencher molecules) via
  - collision, or
  - resonance transfer.

A measure for the amount of energy transferred from the absorbed photon to fluorescence is the quantum yield defined as the ratio of the number of emitted photons N_{em} and the number of absorbed photons N_{abs}:

$$\Phi_q := \frac{N_{em}}{N_{abs}} \tag{3.1}$$

The quantum yield ranges from zero to one. If this quantity equals one the whole energy is transferred to emission and not into other kinds of energy like heat (rotational/vibrational excitation).
Fluorescence emission band is always shifted towards larger wavelengths with respect to the absorption bands, see figure 3.1.
In that context the Stokes shift is defined as the distance in wavelength between the wavelength of maximum absorption and the wavelength of maximum fluorescence emission. The higher the Stokes shift the less important are reabsorption effects of fluorescence photons by the dye itself, which is also important for the LIF measurement technique used here.

Fluorescence emission or radiance L_{em} is directly proportional to the absorbed irradiance E_{abs} as

$$L_{em} = \Phi_q \cdot E_{abs} \tag{3.2}$$

given that the dye solution dilute. Schmidt [2000] stated as a typical upper limit an absorption of approximately 0.05. The maximum concentration can be estimated via the law of Lambert-Beer with:

$$L_{em} = \Phi_q \cdot E_0 \cdot (1 - \exp(-\varepsilon \cdot cz)), \tag{3.3}$$

with ε as the extinction coefficient of the fluorophore, E_0 as the initial irradiance emitted by the laser and c as concentration of the fluorophore. Linearity is given

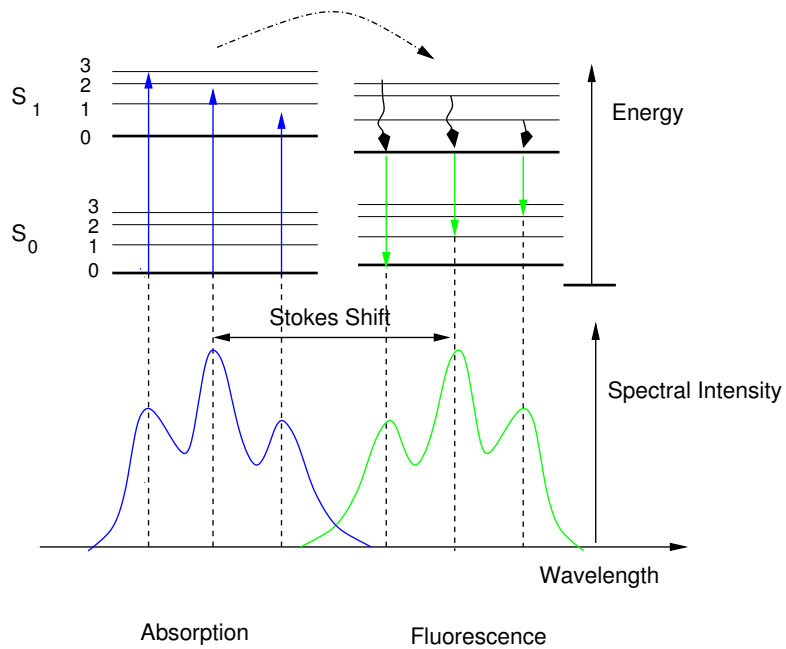

Figure 3.1: Absorption and emission spectra plotted with respect to the energy diagram of a typical fluorophore in the upper part of the spectra (Jablonski-diagram). Photon absorption shifts the electrons to the vibrational levels of the first excited singlet state S_1, relaxation to the ground level of the excited state is followed by photon emission to the vibrational levels of the ground state S_0.

if the exponential term can be approximated by the first two elements of the Taylor series:

$$\exp(-\varepsilon \cdot cz) \;=\; 1 - \varepsilon \cdot cz + O(|\varepsilon \cdot cz|^2).$$

If $\varepsilon \cdot cz \ll 1$ then the higher order terms can be neglected.

This leads to the following simplified relation that forms the basis for all later calculations:

$$L_{em} \;=\; \Phi_q \cdot E_0 \cdot \varepsilon \cdot c \cdot z \;+\; O(|\varepsilon \cdot cz|^2). \tag{3.4}$$

If the above condition of a dilute solution is fulfilled, this relation states that the intensity of fluorescence radiance is proportional to the concentration of the fluorophore because absorption is proportional to concentration. In this relation the equivalence of fluorescence and absorption in their information becomes evident. Important for the LIF-technique is: If the local concentration of the fluorophore changes then it can be detected by a decrease of the fluorescence intensity.
This relation is the basis of all concentration measurements in the experiments based on Laser-induced fluorescence.

3.4 The pH-Indicator Method: Fluorophore as Tracer for Gas Concentration

The basic idea of the measurement techniques presented in the scope of this work is that the presence of a highly reactive gas in the water body can be made visible by changes in emission of a fluorescent pH-indicator dye.
The main arguments against the usage of highly reactive and therefore highly soluble gases are, that the main resistance of transport lies in the air-side instead in the water side which is the case for oxygen and carbon dioxide and that H_3O^+ tunneling effects may occur.
However, for the dissolution of HCl in water, where a pH-indicator dye is present, the transport phenomena are altered significantly due to electromagnetic interaction of the dissolved ions. Cl^- and H_3O^+-ions together with the dye form a kind of ion cluster that is transported like an inert gas.
In the following passages the fluxes of gas molecules and ionic fluorophore components are regarded and quantitatively deduced. Followed by considerations regarding the sensitivity of the experimental techniques regarding local gas concentrations.

3.4.1 Indicator Reaction as Basis of Detection of Acid/Alkaline Gases

For studying of the transport dynamics of acid or alkaline gases the gaseous tracer must dissociate to its ions instantaneously at the surface. Only dissolution processes that take place faster than a few microseconds are favorable. There the reaction is much faster than the diffusion step. These processes are called diffusion-controlled, Cussler [1997]. Acid-base reactions are the common example. For the gaseous tracer HCl whose reaction rate Graedel and Mandich [1986] reported to be $2.7 \cdot 10^{10}$M s^{-1} this assumption is valid.
The same demand is set on the fluorescent pH-indicator. An indicator is needed, the reaction time constant of which is much faster than the time constant for transport trough the mass boundary layer which is of the order of magnitude of 0.04-4 seconds according to Jähne [2009].

A reaction of a pH-indicator IH is a reversible acid-base reaction:

$$\mathrm{IH} + \mathrm{H_2O} \rightleftharpoons \mathrm{I^-} + \mathrm{H_3O^+}. \tag{3.5}$$

I^- is the deprotonated version of the fluorophore or base component, while IH is the acid component. The deprotonation is the reaction from left to right, while protonation runs from right to left. The time constants for acid-base reactions are typically in the range of nano seconds according to Cussler [1997] and therefore fulfill the above stated demand.
The individual concentrations of the constituents are linked via the law of mass action:

$$K = \frac{[\mathrm{I^-}][\mathrm{H_3O^+}]}{[\mathrm{IH}]}, \tag{3.6}$$

where the brackets indicate the concentrations and K is the equilibrium constant of the reaction. The equilibrium constant depends on temperature, according to

$$\ln K = -\frac{\Delta H^0}{RT} + \text{constant}, \tag{3.7}$$

with ΔH^0 as the standard enthalpy change of the reaction, R as the gas constant and T as temperature in Kelvin, see Stumm and Morgan [1996]. At standard atmospheric conditions the pressure dependence of K can be neglected.
Both components of the indicator IH and I^- do have the same concentration if the pH value (pH :=$-\log([H_3O^+])$) of the solvent (water, in all measurements conducted in this work) is equal to the pK value of the reaction, which is the negative logarithm of the equilibrium constant K of the reaction. If pK = pH is in the dye solution the solution is called to be at its buffer point.

The indicator dye is present in the solutions in two components: the acid component IH and the base component I^-. One component is fluorescing at the given excitation wavelength λ_L, the other one not. So concentration changes in the two components of the fluorophore lead to a decrease or increase of induced fluorescence.
In the case of the used pH-indicator HPTS (see 3.7 for details on the fluorophore), the base component is excited to fluorescence by the laser while the acid component is not. Since dissolved HPTS is in both components negatively charged, the acid component is called anion acid and the base component anion base. The anion acid of HPTS will be abbreviated as $R^{-3}OH$, which corresponds to the IH, and the anion base as $R^{-3}O^-$, which corresponds to I^-. R stands here for 'rest' of the chemical formula of HPTS.

If an acid gas is dissolved in the fluorophore solution the concentrations of two fluorophore components adjust in a way that the relation 3.6 is fulfilled.

3.4.2 Relation between Intensity of Fluorescence Signal to Concentration of H_3O^+

Equation 3.6 allows to calculate the concentration of the dye components at a given concentration of H_3O^+ ions.
Additionally needed is mass conservation, the initial concentration of the indicator C_0 at a time $t = 0$ must equal the sum of both components

$$C_0 = [I^-] + [IH] \tag{3.8}$$

Combining mass conservation and equation 3.6, the following relation can be deduced

$$[I^-] = \frac{C_0}{[H_3O^+]/K + 1} \tag{3.9}$$

A plot of this sigmoid function is shown in figure 3.2, with pH $= -\log([H_3O^+])$. Expanding the relation into a Taylor series around the buffer point condi-

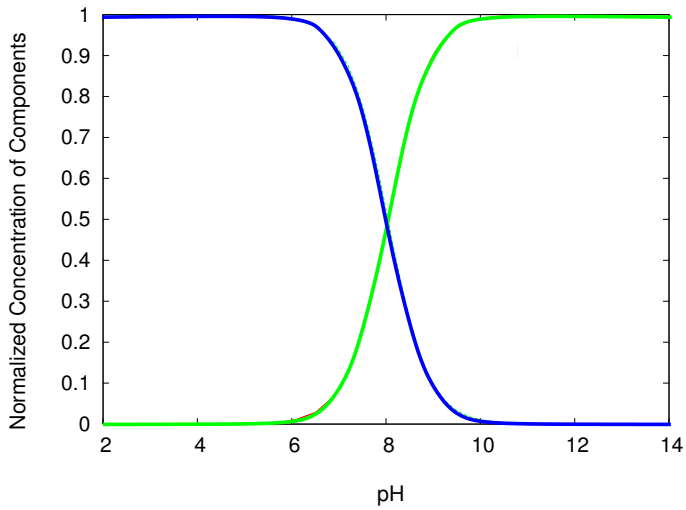

Figure 3.2: Concentrations of the two components of the pH indicator HPTS $R^{-3}OH$ (blue) and $R^{-3}O^{-}$ (green) dependent on pH $= -\log(H_3O^+)$ normalized with the start concentration of HPTS. $R^{-3}O^{-}$ corresponds to I^{-}. At the buffer point pH = pK (here pK = 8.04), the fluorophore components have the same concentration.

tion, where the concentration of the H_3O^+-ions equals the equilibrium constant $[H_3O^+] = K$, yields:

$$[I^-] = \frac{C_0}{2} - \frac{C_0}{4 \cdot K}([H_3O^+] - K) + O\left(([H_3O^+] - K)^2\right). \tag{3.10}$$

If $([H_3O^+] - K) \ll 1$ this approximation is valid.
Therefore, given that the concentration of H_3O^+-ions in the solution is close to the K-value of the fluorescent indicator, the change in fluorescence is proportional to the H_3O^+ concentration and hence the local concentration of dissolved HCl. At the buffer point the fluorophore is most sensitive to changes in concentration of H_3O^+. It could therefore be expected that the best contrast will be reached in images taken of gas penetration events at the buffer point. An example of this best contrast compared to an image of gas penetration less than 0.5 pH units away from the buffer point is shown in figure 3.4.

This relation states that the transport of HCl in water can only be studied in the direct vicinity of the buffer point, because only there this approximation can be made:

$$\Delta[I^-] \propto \Delta[H_3O^+] \tag{3.11}$$

As figure 3.3 shows concentration changes can also be visualized at a larger range $\Delta_{max} = (\text{pK} - \text{pH}) \lesssim 1$ around the buffer point. On the whole range $[\text{pK}-\Delta_{max}, \text{pK}+\Delta_{max}]$ the relation between concentration of fluorescing base component I^- and pH can be approximated to be linear. However, the relation

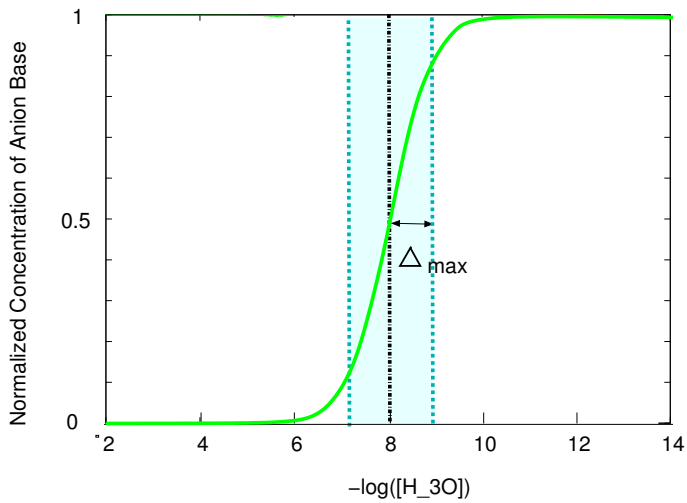

Figure 3.3: Concentration of the $R^{-3}O^{-}$ component. The light blue area marks the concentration range of $pK \pm \Delta_{max}$, where the fluorophore indicates concentration changes visibly. The black dashed line marks the position of the buffer point. The buffer point is reached in this plot at pH = pK = 8.04.

to the concentration of the H_3O^+ is not linear, but logarithmic.

$$[\mathrm{I}^-] = \frac{C_0}{2} + \frac{C_0 \ln 10}{4}(\mathrm{pH} - \mathrm{pK}) + O\left((\mathrm{pH} - \mathrm{pK})^3\right) \tag{3.12}$$

$$\Delta[\mathrm{I}^-] \propto \Delta \log[\mathrm{H_3O^+}] \tag{3.13}$$

In experiments it is therefore crucial to search for best contrast directly in the images to ensure that the buffer point is also locally reached. Just looking at bulk pH does not suffice as conditions may vary over the whole water volume. So far, the above stated has not revealed anything about the transfer velocity of the dissolved ions of HCl in the dye solution. In the next subsection this should be regarded.

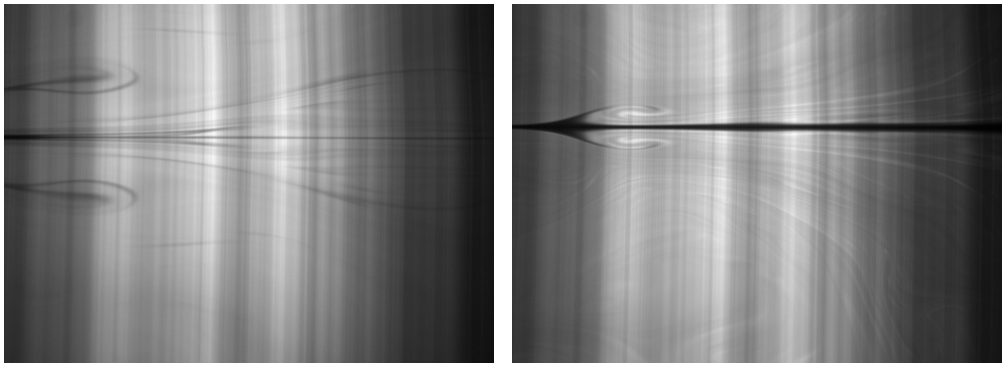

(a) (b)

Figure 3.4: Measurements taken with pH-Indicator method: (a) LIF-image taken away from the buffer point.(b) LIF-image taken at the buffer point. The contrast is significantly increased. Please note, the two images are taken with a time lag of 10 minutes and the same HCl flux. In the experiments, the buffer point condition was usually kept over a period of less than 10 minutes depending on the turbulence level.

3.4.3 The Core of the pH-Method: Conservation of Mass Flux

Besides the careful adjustment of the fluorophore solution to be at its buffer point during experiments, great care has to be taken that the flux of the gaseous tracer HCl does not exceed the maximum flux the fluorophore can handle or in other words that the concentration in the boundary layer does not locally violates the buffer point condition. So two cases will occur: A tracer flux below and above the maximum flux suitable for the fluorophore. These two cases will be regarded separately in this subsection.

In this section that deals with the fluxes the properties of the gaseous tracer can no longer be ignored. In contrast to water-side controlled gaseous tracer CO_2, HCl as an extremely high soluble gas is air-side controlled. Therefore, HCl transport is subject to a flux boundary condition flux. As HCl dissociates completely at the water surface the concentration of HCl at the interface equals zero, $\mathsf{C}_{air}^{HCl}\big|_0 \equiv 0$, and so the air-sided flux density j_{air} reduces to

$$\begin{aligned}
\mathbf{j}_{\mathbf{air}}^{\mathbf{HCl}} &= \mathbf{k}_{air}\Delta[\mathrm{HCl}] && (3.14)\\
&= \mathbf{k}_{air}\left([\mathrm{HCl}]_{air}\big|_{bulk} - [\mathrm{HCl}]_{air}\big|_0\right) && (3.15)\\
&= \mathbf{k}_{air}\left([\mathrm{HCl}]_{air}\big|_{bulk}\right). && (3.16)
\end{aligned}$$

Note, that this complete dissociation is crucial for the following considerations. This is quite different for instance for CO_2, which does not dissociate completely. The aqueous concentration of such a tracer has to be regarded additionally, see for example Asher and Litchendorf [2009].
HCl is also a highly reactive gas: It dissociates instantaneously [1] and completely

[1] with respect to transport times

at the water surface into its two ions H_3O^+ and Cl^-. The concentration of undissociated HCl in water is therefore almost zero, $[HCl]_{aqueous} \approx 0$. Now, the case of a water phase without an additional fluorophore is regarded: The diffusion of H_3O^+-ions in water is highly increased by the possibility of tunneling from water molecule to water molecule, see for example Hamann and Vielstich [1975]. Yet, the dissolved ions of HCl, H_3O^+ and Cl^-, cannot diffuse individually through the liquid without creating electrostatic fields. These electrostatic forces couple the ions together and force them to diffuse as a electronically neutral ion cluster, Cussler [1997]. The diffusion coefficient of HCl in water can be calculated as the harmonic mean of the individual diffusion coefficients of the ions to

$$\mathcal{D}_{HCl} = \frac{1}{1/\mathcal{D}_{H^+} + 1/\mathcal{D}_{Cl^-}} \tag{3.17}$$

$$\approx 3.3 \cdot 10^{-5}\ \mathrm{cm}^2/\mathrm{s} \text{ at } 25\ ^\circ\mathrm{C} \tag{3.18}$$

For further details see 3.6. In the presence of dye ions, the diffusion of the ions H_3O^+ and Cl^- in aqueous solution is also coupled to the dye ions and is no longer the harmonic mean of the individual HCl ion diffusion coefficients alone.

Here, two cases must be regarded separately: In the first case, the flux of the gaseous tracer should be so low that the concentration of the H_3O^+-ions in the mass boundary layer remains next to the buffer point. In the second case the flux of the tracer exceeds this limit. So the concentration of the H_3O^+-ions will become so high that it exceeds even the maximum indicator range Δ_{max} where concentration changes are visible in a detectable change in fluorescence intensity.
In the experiments conducted in this study the conditions of case I were fulfilled.

Case I: Low Concentration of Gaseous Tracer HCl - Flux Detection

The dissociated HCl ions react with the fluorophore components IH and I^- that are of equal concentration in the water phase: the H_3O^+-ions in the water phase react in an extremely fast acid-base reaction with the fluorescing base component of the fluorophore I^- to the acid component IH. So the concentration of the fluorescing base component drops and the concentration of the acid component is increased in the boundary layer - a concentration gradient is evolved - and both indicator ions start diffusing to each other - IH towards the bulk and I^- towards the surface to guarantee electric neutrality. An illustration of this can be found in figure 3.5. The transport of the IH is now what can be tracked: Every area in the illuminated sheet where IH is to be found fluorescence intensity decreases, which appears as darker structures in the LIF images. Summarizing, the transport of HCl is exchanged by transport of the IH component of the fluorophore, a species that is formed at the interface with a completely different diffusivity. Intensity of emitted fluorescence in the whole range Δ_{max} is proportional to the concentration of the I^- component and therefore to $C_0 - \mathrm{IH} = I^-$ component.

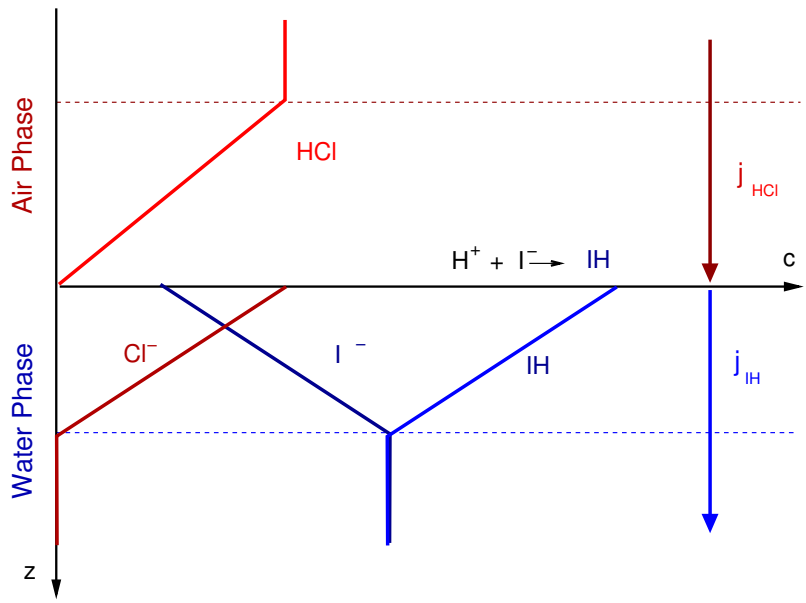

Figure 3.5: Invasion of HCl: Sketch of HCl dissolution in water and corresponding concentrations of dissociation products and indicator components. The horizontal dashed lines mark the mass boundary layers in air and water respectively. Flux of IH equals the flux of HCl into the water body. Graphic adapted from Jähne [1991].

In terms of diffusion coefficients the ions of dissociated HCl and the fluorophore components couple to clusters that are transported together trough the fluid. The combined diffusion coefficient of the coupled cluster is now deduced for the fluorophore HPTS.

HPTS in solutions is present in its two components, the three-fold-charged anion acid of HPTS and the four-fold-charged anion base of HPTS together with three Na^+ ions per HPTS molecule. The Na^+ ions are assumed to be equally distributed in the solution and do not effect the pH value further.

If HCl dissolves at the surface the pH value is shifted towards acid conditions and therefore a surplus of the anion acid $R^{-3}OH$ occurs. While the anion base ions $R^{-3}O^-$ are reduced, the remaining Cl^- ions start diffusing into the bulk as the surplus of anion acid ions does. The reduction of the $R^{-3}O^-$ ions leads to a concentration gradient of this ion type over the mass boundary layer and therefore to transport towards the bulk. The Cl^- ions couple with the three-fold-charged anion acid of HPTS $R^{-3}OH$ to a new cluster $R^{-3}OH\text{-}Cl^-$ that is transported as a whole in the water bulk, as electroneutrality has to be maintained. This cluster has a different (lower) diffusion coefficient than HCl ions alone, but is found in the same concentration as dissolved HCl. Thus, the transport velocity of HCl in the bulk is slowed down.

The diffusion coefficients of the cluster can be theoretically approximated to be:

$$\mathcal{D}_{cluster} = \frac{|3| + |1|}{|3|/\mathcal{D}_{\mathrm{R^{-3}OH}} + |1|/\mathcal{D}_{Cl^-}} \tag{3.19}$$

$$= (6.03 \pm 1.2) \cdot 10^{-6}\mathrm{cm^2s^{-1}} \tag{3.20}$$

With $D_{\mathrm{R^{-3}OH}} \approx D_{\mathrm{R^{-3}O^-}} = (4.6 \pm 0.9) \cdot 10^{-6}\mathrm{cm^2sec^{-1}}$ at 298.15 Kelvin as the diffusion coefficient of HPTS anion acid and $D_{Cl^-} \approx 9.31 \cdot 10^{-5}\,\mathrm{cm^2sec^{-1}}$. For details see 3.7. As this construct from physical chemistry appears to react like one molecule of moderate to low diffusivity, the ion cluster can be regarded as a dissolved inert gas. Münsterer and Jähne [1998] proved this cluster forming experimentally for the fluorescent pH-indicator fluorescein. Therefore, the concentration profiles of the dye component $\mathrm{R^{-3}OH}$ can also be treated as the concentration profiles of an inert gas. The source of this 'species' is the water surface where the cluster is formed.
As mentioned above this considerations are only valid if the protonation and deprotonation reactions of the fluorophore are fast. Förster [1950] and Weller [1958] were the first to investigate the extremely fast reaction rate of HPTS deprotonation. Spry et al. [2007] mentioned the reason for this 'because of the enhanced Coulombic attraction of the HPTS anion's fourfold negative charge, the reaction is nearly twice as fast as the self-neutralization of water'. Since conservation of mass has to be maintained over the air-water interface the flux density of the newly formed ion cluster $\mathrm{R^{-3}O(H+)\text{-}Cl^-}$ equals the flux of HCl into the water body.

$$\mathbf{j_{air}^{HCl}} = \mathbf{j_{water}^{cluster}} \equiv \mathbf{j_{water}} \tag{3.21}$$

In the water, the ion cluster including the anion acid of HPTS diffuses down into the water bulk, where both HPTS ion species have the same concentration if the buffer point condition is valid with $[\mathrm{R^{-3}O^-}] = [\mathrm{R^{-3}OH}] = \frac{C_0}{2}$. Therefore due to this concentration gradient the counter-ion in form of the anion base $\mathrm{R^{-3}O^-}$ of HPTS diffuses with the same flux from the water bulk up to the surface:

$$\mathbf{j_{water}} = \mathbf{k}_{water}\left([\mathrm{R^{-3}OH}]_{water}\big|_{surface} - [\mathrm{R^{-3}OH}]_{water}\big|_{bulk}\right) \tag{3.22}$$

$$= -\,\mathbf{k}_{water}\left([\mathrm{R^{-3}O^-}]_{water}\big|_{bulk} - [\mathrm{R^{-3}O^-}]_{water}\big|_{surface}\right) \tag{3.23}$$

For simplification the following definition will be used in the next sections:

$$\Delta[\mathrm{R^{-3}OH}] := [\mathrm{R^{-3}OH}]_{water}\big|_{surface} - [\mathrm{R^{-3}OH}]_{water}\big|_{bulk} \tag{3.24}$$

$$\Delta[\mathrm{R^{-3}O^-}] := [\mathrm{R^{-3}O^-}]_{water}\big|_{surface} - [\mathrm{R^{-3}O^-}]_{water}\big|_{bulk} \tag{3.25}$$

To summarize: In the case of a low tracer flux the transport of the highly soluble tracer HCl equals transport of the newly formed ion cluster. Tunnel effects will not detectably occur as $\mathrm{H_3O^+}$ ions are immediately bound to the fluorophore to form IH. To guarantee this, the tracer concentration must fulfill the buffer point condition at all times. Please note, the above derived relations are not valid for a tracer that does dissociate completely to its ions in the water phase. The next paragraph will describe what happens if the demand is violated and the flux becomes to high.

Case II: High Concentration of Gaseous Tracer HCl - Visualizing Mass Boundary Layer Thickness

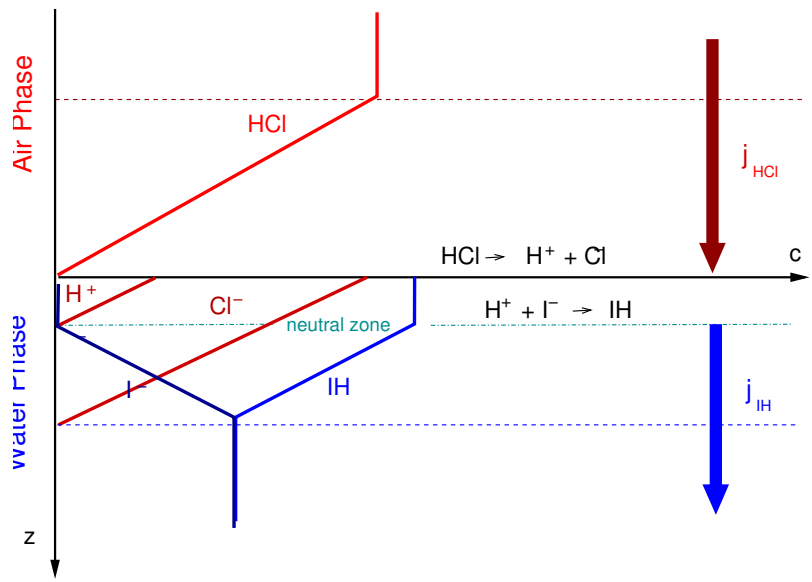

Figure 3.6: Invasion of HCl for high tracer flux: Sketch of HCl dissolution in water and corresponding ions concentration of tracer ions and indicator components. The horizontal dashed lines mark the mass boundary layers in air and water respectively, while the dashed-dotted line marks the neutral zone. Graphic adapted from Jähne [1991].

Here, we come to case number II, sketched in figure 3.6. We still have an instantaneous dissolution of HCl to its ions at the surface. But now the H_3O^+ concentration exceeds the maximum concentration the dye can handle: Not all H_3O^+ are bound to a fluorophore molecule. So a partition of the H_3O^+ ions are diffusing freely but coupled to Cl^- electromagnetically. Yet, this combined diffusion coefficient as shown at the beginning of this subsection is much higher than that of the fluorophore component So in the topmost part of the mass boundary layer a very fast diffusion occurs towards the so called neutral zone, the depth where the concentration of the hydronium ions has dropped to a value the fluorophore can compete again with. The detectable reaction of the tracer ions with the fluorophore components happens here. The neutral zone appears as dark layer. The thickness of the neutral zone corresponds to the thickness of the mass boundary layer, as in that depth turbulent transport from the bulk brings enough non-acid liquid. Here starts the reduced part of the boundary layer in which a concentration profile can still be resolved. Yet, the remaining part of the mass boundary layer may be too thin to extract a profile. Hiby et al. [1967] used exactly the here described technique for measuring the thickness of the mass boundary layer by measuring the thickness of the neutral zone.

For determining the thickness of the mass boundary layer this technique works

but for resolving concentration profiles within the mass boundary layer case II has to be avoided at all cost.

3.4.4 Theoretical Sensitivity of Fluorescence Detection to Concentration Changes

To conduct the experiments it is necessary to estimate the air-sided concentration of the HCl $[\mathrm{HCl}]_{air}$.
First it has to be checked with what kind of ions the dissolved HCl mainly reacts: The concentration of the dye has to be compared to the other ion-concentrations present in the aquas fluorophore solution.
At a temperature of 22 ℃ the ion product describing the self-ionization of water yields:

$$[\mathrm{OH}^-] \cdot [\mathrm{H_3O}^+] \quad = \quad 1 \cdot 10^{-14}\mathrm{M}^2 \tag{3.26}$$

At the buffer point where the pH equals the pK value of the fluorophore HPTS (pK= 7.5 in water, see section 3.7) and a dye concentration of $2 \cdot 10^{-5}$M, this leads to the following ion concentration:

$$[\mathrm{H_3O}^+] = 10^{-7.5}\mathrm{M},\ [\mathrm{OH}^-] = 10^{-6.5}\mathrm{M},\ \text{and}[\mathrm{R}^{-3}\mathrm{O}^-] = [\mathrm{R}^{-3}\mathrm{OH}] = 10^{-5.0}\mathrm{M},$$

Regarding the orders of magnitude, the dye ion concentration exceeds the dissociated water ions by 1.5 orders of magnitude. Therefore, reactions of dissolved HCl ions with the water ions can be neglected.
Increasing the dye concentration for a better signal to noise ratio may increase the surface activity of the dye solution, thus affecting gas transport.

As the images of concentration gradients of the dissolved gas are detected via a digital camera, the gray value resolution of the camera sets the limit for difference detection:
A 8-bit camera offers 256 gray values, given that a difference of 2 gray values can be detected and the buffer point condition is reached, a 1% change in concentration can be detected ($p_8 = 0.01$).
For a 10-bit camera with 1024 gray values, a 0.2% change in concentration may be possible to detect ($p_{10} = 0.002$).

$$p_i = \frac{\Delta[\mathrm{R}^{-3}\mathrm{O}^-]}{[\mathrm{R}^{-3}\mathrm{O}^-]} \tag{3.27}$$

$$= \frac{\Delta[\mathrm{HCl}]}{[\mathrm{HCl}]} \tag{3.28}$$

The typical relation for the transfer velocity of HCl in air and water is according to Jähne [1985]:

$$\frac{|\mathbf{k}_{air}|}{|\mathbf{k}_{water}|} \approx \frac{1}{500} \tag{3.29}$$

Together with this estimation the following concentration change can be estimated

$$\Delta[\mathrm{HCl}] \approx \frac{|\mathbf{k}_{air}|}{|\mathbf{k}_{water}|}\,\Delta[\mathrm{R}^{-3}\mathrm{O}^{-}] \tag{3.30}$$

$$\approx \frac{|\mathbf{k}_{air}|}{|\mathbf{k}_{water}|}\,p_i\,\frac{C_0}{2} \tag{3.31}$$

This leads to the following detection limits for the different numbers of gray values in image and a total HPTS concentration of $2 \cdot 10^{-5}$M:

$$\Delta[\mathrm{HCl}]_{8bit} \approx 4 \cdot 10^{-10}\mathrm{M} \tag{3.32}$$

$$\Delta[\mathrm{HCl}]_{10bit} \approx 0.8 \cdot 10^{-10}\mathrm{M} \tag{3.33}$$

$$\tag{3.34}$$

These values will be the basis for the conducted experiments.

3.5 The pH-Method in Comparison to the Oxygen Quenching Technique

An alternative method to the pH-method is oxygen quenching.

The quenching of luminescence intensity is described by the Stern-Vollmer equation

$$L(c_{quencher}) = \frac{L_0}{1 + K_{dye}c_{quencher}} \tag{3.35}$$

with $c_{quencher}$ as the concentration of the quenching molecule - the molecule that suppresses the luminescence of the dye with increasing concentration - and K_{dye} the quenching constant of the used luminescent dye.
A typical quencher is oxygen.
The relation 3.35 is nonlinear. Due to this, for an increased contrast either a dye with a higher quenching constant has to be chosen or a higher concentration gradient of the quenching molecule has to be used.
The commonly used pyrenebutric acid PBA has several significant disadvantages for measurements as Falkenroth [2007] showed, including wavelength for excitation in the UV, a small Stokes shift of 38nm with high self-absorption, a small quenching constant $K = 648 \pm 80\mathrm{M}^{-1}$ reported by Vaughan and Weber [1970], and an extremely low solubility. Falkenroth [2007] therefore used sodium tris(4,7-diphenyl-1,10-phenanthroline disulfonic acid)ruthenate(II)complex (Na4[Ru(dpp ds)3]) as luminescent dye for measurements to overcome these drawbacks.
This dye improves the oxygen quenching technique significantly.

Summarizing, oxygen quenching is a suitable complementary measurement technique compared to the pH-technique with respect to low soluble gases.
In future a comparison of the two techniques in one experiment is planned but could not be conducted in this study as the ruthenium complex has not been available for financial reasons. For the above stated reasons PBA was not regarded as a usable alternative.

3.6 Properties of Tracer Hydrogen Chloride

In the following section the properties of the tracer gas hydrogen chloride are presented as far as they are of importance to the pH-method presented in section 3.4. HCl is used as tracer gas in all the experiments conducted in this study.

3.6.1 Dissociation Reaction of HCl in Water

The dissociation reaction of HCl in water can be described by

$$\mathrm{HCl} + \mathrm{H_2O} \rightleftharpoons \mathrm{H_3O^+} + \mathrm{Cl^-} \tag{3.36}$$

HCl in aqueous solution is a strong acid. The equilibrium constant or acid ionization constant of the above presented reaction is "too large to be measured accurately", stated Mortimer [2008]. Values in literature vary therefore widely between 10^3-10^9 M, [Sigg and Stumm, 1994] and [Mortimer, 2008], respectively. Therefore, the amount of undissociated HCl is approximately zero and can be neglected in mass balance considerations, which is one of the essential assumptions for the pH-method to be applicable:

$$K_a = \frac{[\mathrm{H_3O^+}][Cl^-]}{[HCl]}, \tag{3.37}$$

$$\Rightarrow [HCl] = \frac{[\mathrm{H_3O^+}][Cl^-]}{K_a}, \tag{3.38}$$

$$\approx 0,$$

$$\Rightarrow [\mathrm{HCl}]|_a = [H_3O^+] = [Cl^-]. \tag{3.39}$$

According to Graedel and Mandich [1986] the rate constant of this dissociation reaction for HCl in water is $2.7 \cdot 10^{10}$ $\mathrm{M\,s^{-1}}$. This value is so high, that the reaction is much faster than any transport phenomenon in water, which has already been stated in section 3.4.1.

3.6.2 Solubility

HCl as a highly reactive gas dissociates almost entirely in the water phase, as mentioned above. The solubility of such a tracer gas differs widely from that of other gases. The most severe difference is, that HCl does not follow Henry's law of solubility.

Henry's Coefficient for highly reactive gases like HCl

For highly reactive gases, the partial pressure depends no longer linearly on the concentration of dissociated [HCl], as Henry's law states for low soluble gases, but quadratically instead:

$$p_{\mathrm{HCl}} = K_{eq}^{-1}[\mathrm{HCl}]^2. \tag{3.40}$$

In the case of highly reactive gases, Henry's law is not valid so to gain the effective Henry's law coefficient $\mathrm{K}_H^\dagger$ for physical solubility the equilibrium constant

of the overall reaction K_{eq} has to be scaled by the acid dissociation constant leading to an effective Henry's coefficient, as Schwartz [2003] calls it,

$$\mathrm{K}_H^{\dagger} = \frac{\mathrm{K}_H}{K_a^{\mathrm{HCl}}}, \tag{3.41}$$

in units of $\mathrm{mol}^2\ \mathrm{kg}^{-2}\ \mathrm{Pa}^{-1}$. Sometimes the effective coefficient is also called 'combined coefficient', i.e. Sigg and Stumm [1994]. In table 3.1 Henry's coefficients for different tracer gases are listed for a comparison. It can be seen that

tracer gas	**Henry's coefficient** $\cdot(1.01325 \cdot 10^5)^{-1}$ **[mol kg^{-1}Pa^{-1}]**
CO_2	3.1-4.5 $\cdot 10^{-2}$
O_2	1.2-1.3 $\cdot 10^{-3}$
NH_3	0.19-7.8 $\cdot 10^{2}$
HCl	0.019 - 2.5 $\cdot 10^{3}$

Table 3.1: Henry's coefficient for different tracer gases at 298.15 K . Values taken from NIST Standard Reference Database.

the coefficient of HCl exceeds the commonly used tracer gases CO_2 and O_2 by two to six orders of magnitude. It even exceeds the solubility of ammonia, the alkaline tracer gas tested by Münsterer [1996].
Currently, one of the most reliable estimate of effective solubility seemed to be given in the study of [Clegg and Brimblecombe, 1986] with

$$K_H^{\dagger} = 2.04 \cdot 10^6 \mathrm{mol}^2\ \mathrm{kg}^{-2}\mathrm{atm}/K_a(HCl). \tag{3.42}$$

With extremely low air-sided tracer gas concentrations in the pH-method, see section 3.4.4 and A.4, equilibrium will never be reached under the given experimental conditions.
Solubility of HCl in water is so large that its "reactivity prevents establishment of the solubility equilibrium at measurable concentrations and partial pressures" as stated by [Schwartz, 2003]. Ostwald's solubility for HCl can therefore be approximated to be infinity for practical calculations: $\alpha_{Sol} \approx \infty$.
As the solubility can be estimated to be infinity and nothing prevents further solution of HCl except variations in the air-sided gas flux itself, this leads to a constant flux of HCl from the air phase into the water phase.
With $\alpha_{Sol} \approx \infty$ HCl is the prototype of an air-side controlled tracer gas, see figure 2.2.

Temperature Dependence of Solubility

Solubility decreases with increasing temperature. But as water temperature was kept constant during all experiments these effects can be neglected.
An approximation formula for temperature dependent effective Henry's coefficient $\mathrm{K}_H^{\dagger}$ can be found in Fogg [2003] for a reference temperature of $T_{ref} =$

298.15 K:

$$\ln(\mathrm{K}_H^\dagger) = 6.4822 - 90027^3[1/T_{ref} - 1/T] - 65.346[T_{ref}/T - 1 \quad (3.43)$$
$$+ \ln(T/T_{ref})] + 0.078178[T_{ref}(T_{ref}/T - 1) + T + T_{ref}[\quad (3.44)$$

This equation delivers $\mathrm{K}_H = 65.3$ bar^{-1} at 298.15 K which corresponds to $2.013 \cdot 10^6$ mol^2 kg^{-2} bar^{-1}. Accuracy in the temperature range 289.4-250 K is said to be about 3%.

3.6.3 Partial Pressure over Highly Saturated HCl Solution

In the measuring section A.4 the partial pressure of HCl over 32% hydrochloric acid is needed. For that reason it is given in figure 3.7.

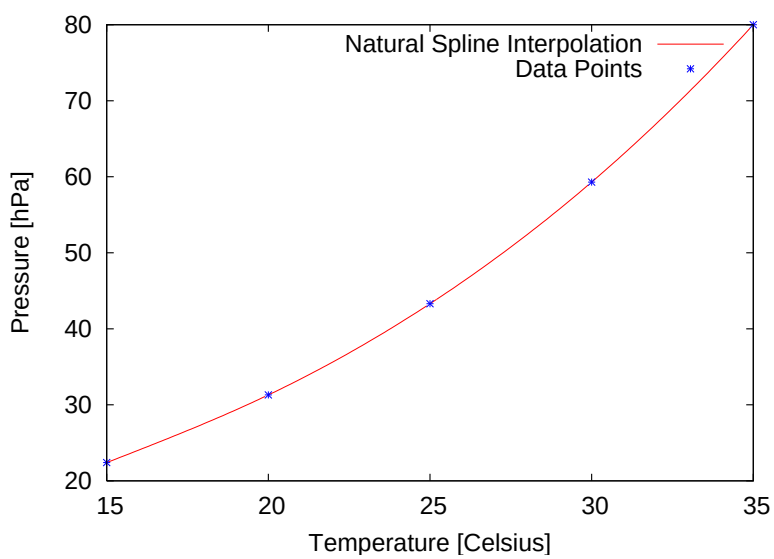

Figure 3.7: Partial pressure of HCl over 32% hydrogen chloride acid according to Perry and Green [2008].

3.6.4 Diffusion Coefficient

The diffusion coefficients of HCl, both in air and in water, are needed for the experiments conducted in this study. The first to estimate after which time an isotropic distribution can be assumed and the second to estimate the combined diffusion coefficient of the fluorophore and HCl in the pH-method.

Diffusion Coefficient in Air Dimmock and Marshall [1987] reported the diffusion coefficient of HCl to be after Hidy and Brock [1970]:

$$\mathcal{D}^a_{\mathrm{HCl}} \approx 1.6 \cdot 10^{-5}\mathrm{m}^2\mathrm{s}^{-1} \quad (3.45)$$
$$\approx 1.6 \cdot 10^{-5}\mathrm{m}^2\mathrm{s}^{-1} \quad (3.46)$$

Diffusion Coefficient in Aqueous Solution

For a dilute solution of HCl in water Cussler [1997] gives a diffusion coefficient of as the harmonic mean of the diffusion coefficient of its ion species

$$\mathcal{D}_{\mathrm{HCl}} = \frac{2}{1/\mathcal{D}_{H^+} + 1/\mathcal{D}_{Cl^-}} \approx 3.3 \cdot 10^{-5}\ \mathrm{cm}^2\ \mathrm{s}^{-1} \tag{3.47}$$

at 25 degree Celsius with $\mathcal{D}_{H^+} = 9.31 \cdot 10^{-5}$ cm^2/sec and $\mathcal{D}_{Cl^-} = 2.03 \cdot 10^{-5}$ cm^2/sec Compared to diffusion coefficients of different gases at 25 degree Celsius in aqueous solution it is rather high: oxygen $\mathcal{D}_{O_2} = 2.1 \cdot 10^{-5}$ cm^2/sec, for carbon dioxide $\mathcal{D}_{CO_2} = 1.92 \cdot 10^{-5}$ cm^2/sec, Acetone $\mathcal{D} = 1.16 \cdot 10^{-5}$ cm^2/sec (values from Cussler [1997]).

3.6.5 Summary

In this section it could be shown that the tracer gas HCl fulfills all demands of the pH-method, presented in section 3.4, that is used in this study. Furthermore, the diffusion coefficients of HCl are listed that are needed for estimates of tracer transport.

3.7 Fluorescent Dye for LIF-Measurements: HPTS

The core of LIF-studies lies in the properties of the used fluorescent gas indicator.
For the detection of certain gases via laser-induced fluorescence several fluorophores have been explored with regard to their possibilities of usage by various researchers. An overview of suitable fluorophores for small molecule sensing can be found in [Geddes and Lakowicz, 2005].
In fluid dynamics, fluorescein is the most commonly used fluorophore for the detection of acid gases like CO_2 and HCl with the pH-method and PBA for the detection of O_2 with the oxygen quenching method, e.g.[Münsterer and Jähne, 1998] for studies with fluorescein, and [Herlina and Jirka, 2008] for PBA.

In this section a novel fluorescent pH-indicator is presented for studying transfer dynamics of dissolved acid or alkaline gases in aqueous solution: 1-Hydroxypyrene-$3, 6, 8$-trisulfonic acid trisodium salt, called HPTS or pyranine.

First, the selection criteria are described that have been used to determine the most suitable dye for LIF-application in 3.7.1.
A detailed description of the properties of the chosen fluorophore HPTS is given in subsection 3.7.2, including absorption and fluorescence characteristics as well as chemical properties like diffusion and equilibrium constant of deprotonation reaction.

3.7.1 Desirable Properties of a Fluorophore used for LIF

In his review of the planar Laser-induced fluorescence method for applications in fluid dynamics Crimaldi [2008] listed desirable properties of a fluorescent dye. The most-suitable fluorophore should have:

- an absorption maximum suitable for available Laser lines,
- a large Stokes shift to reduce probability of self-absorption,
- a high quantum yield to maximize signal intensity,
- the dye should be insensitive to photobleaching,
- show a linear change in fluorescence intensity to concentration of dissolved gas,
- and its fluorescence should be insensitive to temperature changes.

Further desirable properties would be, especially for usage with the pH-method for gas transfer in wind-wave tunnel facilities:

- an insensitivity to quenching effects by oxygen,

- little to non-existent surface activity in solvent water to prevent an influence on gas transition at the interface,
- only a low percentage of absorbed energy should go into heat (intersystem crossing or vibrational excitation),
- buffer point near neutral with respect to equal ion concentrations of OH^- and H_3O^+,
- and non-toxicity or at least low toxicity of the dye to prevent problems of disposal for large amounts of water.

For financial reasons, the costs of the dye should not exceed 1 Euro per liter solution sufficient for measuring.
This criterion excludes almost every of the newly available fluorophores with excellent photostability and fluorescent properties like the Alexa Fluoro -, Hilyte- and DyLight-series, with prizes of 300 euros per mg and more.

Most of these desired properties could be fulfilled by the fluorophore HPTS, which will be presented in the following subsection.

3.7.2 The fluorophore used for measurements: HPTS

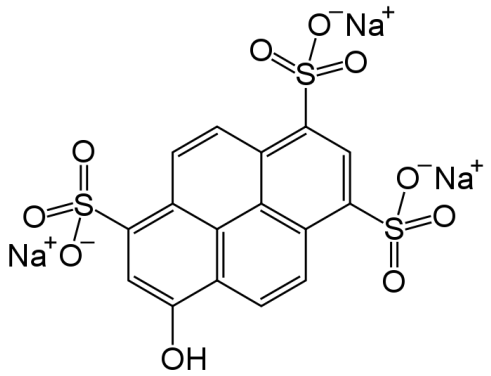

Figure 3.8: Plot of the HPTS molecule. HPTS is a fourfold charged anion, that emits 3 Na^+ in aqueous solution. Image from Wikipedia - the Online Reference.

HPTS is the fluorescent pH-indicator that is used in all experiments conducted in this study. It has been presented for possible usage in planar LIF by Coppeta and Rogers [1998] and proposed for measurements of small scale mass transfer in air-water interaction by Falkenroth et al. [2006].
This study is the first, where HPTS is actually used for LIF-measurements in the side setup in small scale mass transfer between a gas and a liquid phase.

HPTS is the abbreviate name of 1-hydroxypyrene-3, 6, 8-trisulfonic acid trisodium salt (C_{16} H_7 Na_3 O_{10} S_3), sometimes also called 'Pyranine' or 'Solvent Green 7'

and it belongs to the group of aromatic alcohols, [O'Neil, 2006].

With a molecular weight of 524.39± g/mol (source: O'Neil [2006]) and a diameter in main axis of 9.2 Å according to Haar et al. [1977] it belongs to the rather large molecules.
HPTS fulfills several of the above described desirable properties of a fluorophore usable for LIF:
The anion base of HPTS has excellent optical properties like an absorption maximum at 455 nm suitable for commercial lasers, a large Stokes shift of ≈ 58 nm, a high quantum of 0.986 and a low sensitivity to photobleaching. These fluorescence properties are discussed in detail in 3.7.4.
Furthermore, HPTS is almost insensitive to oxygen; due to decay times of fluorescence in the ns-range quenching effects are extremely small. Wolfbeis et al. [1983] reported that fluorescence decreases from saturated nitrogen solute to saturated oxygen solute by approximately 5%. Similar results are reported by Zhujun and Seitz [1984] who claim to see no change in fluorescence intensity by changing from normal to nitrogen atmosphere for immobilized HPTS.
Temperature dependence of fluorescence is low (about -0.2 ± 0.03 percent change per Kelvin in intensity with increasing temperature), when excited at 445 nm. For further details see 3.7.4.
At low concentrations ($< 10^{-4}$M) HPTS shows little surface activity in the solvent water.
The buffer point of HPTS is reported to be between 7.29 and 8.04, depending on the present concentration of salts, see for further details.
Finally, HPTS has a very low toxicity for humans according to Lutty [1978] but is classified to be dangerous to water resources (class 3, [Sigma Aldrich])

Acid-Base Reaction

Now the indicator reaction of HPTS shall be regarded, that can be formulated as

$$\mathrm{R^{-3}OH} + \mathrm{H_2O} \rightleftharpoons \mathrm{R^{-3}O^-} + \mathrm{H_3O^+}, \tag{3.48}$$

The protonation is very fast (direction left to right), and exceeds the self-neutralization of water by a factor of 2 according to Spry et al. [2007]. This reaction of proton and hydroxide,

$$\mathrm{H^+} + \mathrm{OH^-} \rightleftharpoons \mathrm{H_2O}, \tag{3.49}$$

has a reaction rate of $K_1 = 1.4 \cdot 10^{11}$l/(mol s) Cussler [1997] and therefore the acid-base reaction of HPTS with water is diffusion-controlled. It has a protonation time of approximately 5.6 ns, which is much shorter than the upper limit of the fluorophore reaction set by typical resident times in the mass boundary layer, see section 3.4. The equilibrium constant of this reaction is reported to lie in the range of $10^{7.3} - 10^{8.04}$M dependent on the concentration of additional ions in the solvent, as it can be expected for a weak acid:

pK	concentration [mol/l]	buffer	source
7.3	10^{-4}	borat-citrate	[Förster, 1950]
8.04 ± 0.07	$6.6 \cdot 10^{-3}$	ultra pure water	[Wolfbeis et al., 1983]
7.51 ± 0.03	$6.6 \cdot 10^{-3}$	phosphate buffer	[Wolfbeis et al., 1983]
7.29 ± 0.02	$66 \cdot 10^{-3}$	phosphate buffer	[Wolfbeis et al., 1983]
7.8 ± 0.1	n.m.	n.m.	[Förster, 1950]
7.7	n.m.	n.m.	[Pines and Huppert, 1986]
8.1 ± 0.1	n.m.	n.m.	[Goldberg et al., 1992]
7.3 – 8.0	n.m.	n.m.	[Geddes and Lakowicz, 2005]
7.5 ± 0.1	$5 \cdot 10^{-5}$	-	[Prayer, 1997]
7.4 ± 0.2	$10^{-5} - 10^{-3}$	borat-citrate	own measurements

Table 3.2: pK values of HPTS reported in Literature. Notation: n.m. stands for not mentioned. Own measurements were done by fitting a sigmoid curve to the extinction coefficients determined at different pH.

At highly purified water a pK_a of 8.04±0.07 is given according to table 3.2, while at $6.6 \cdot 10^{-3}$mol of phosphate buffer pK reaches a value of 7.51 ± 0.03. Avnir and Barenholz [2005] found that pK_a decreases with increasing ion concentration in a nonlinear dependency. An explicit dependency was not given. Yet, their plots implied a kind of square-root dependency. For NaCl they measured a change of pK_a of $\Delta pK_a/(10^{-3}S)$ for salt concentrations around a molality of 0.201. Yet, 'at low ionic strength ($\sim$ 0.01 molal)' the ratio of 'ΔpK_a/ionic strength is higher with $\sim$ 6. for Na^+.
Barnadas-Rodríguez and Estelrich [2008] continued the work on salt effects and reported also a shift of the pK-value of the excited state of HPTS.
In this study salt concentration in solution will change due to the absorption of HCl and the following back titration to the buffer point of the solution. Therefor a measurement of the pH value to find the buffer point is impossible as the value of the buffer point shifts. For that reason, the ratio of absorption of the two ion species of HPTS - the anion base $R^{-3}O^-$ and the anion acid $R^{-3}OH$ is used to determine the buffer point in the wind-wave tunnel in an absorption cell added to one of the cycles, see chapter 7.

Furthermore, Barnadas-Rodríguez and Estelrich [2008] reported at pH >1 the three sulfonate groups were completely ionized, emitting in total three Na^+ion. In the measurements conducted in this study the pH value will be around the pK-value of HPTS. For this reason a 'background' concentration of Na^+ions is given.

Diffusion Coefficient and Schmidt Number

For the pH-method the diffusion constant of the dye used is needed.
In literature, no values for the diffusion coefficient of HPTS were found by the

author.
For this reason the diffusion coefficient was estimated by using the Debye-Stokes Einstein equation,

$$\mathcal{D} = \frac{k_B\,T}{6\,\Pi\,\mu\,R_0}. \tag{3.50}$$

with k_B as the Boltzmann constant, T as temperature of solvent in Kelvin, μ as the dynamic viscosity of the solvent and R_0 as the radius of the regarded molecule. The estimated accuracy of the diffusion coefficient for a spherical molecule is approximately $\pm\,20$ percent according to Cussler [1997].

Haar et al. [1977] determined the HPTS molecule's gyration radius R_0 from rotation times to 4.6 Å. Furthermore, Haar et al. [1977] estimated that about ten water molecules rotate together with the HPTS anion. HPTS anion and water molecules form a sphere.
With these values and assumptions the diffusion coefficient of HPTS can be estimated to

$$D_{\mathrm{R}^{-3}\mathrm{O}^{-}} \approx 4.62 \cdot 10^{-6} \pm 0.9\mathrm{cm}^2\mathrm{sec}^{-1} \text{ at 298.15 Kelvin.}$$

The relative error 20 % is extremely high. The only values available in literature, were relative diffusion coefficients for proton transport defined as the sum of cationic and anionic diffusion coefficients.
From data of Cornish and Speedy [1984], Leiderman et al. [2006] calculated these relative diffusion coefficients of HPTS and proton transfer rates at different temperatures. The relative diffusion coefficients are in the range of the diffusion of the H_3O^+-ion and have not much in common with the diffusion of the whole molecule in a medium needed for mass transport.

The above deduced diffusion coefficient for HPTS allows to estimate the Schmidt number of the fluorophore at 293.15 K with $\nu_{H_2O} = 1.004 \cdot 10^{-6}$ m^{2}s^{-1} to,

$$\mathrm{Sc}_{HPTS} = \frac{\nu_{H_2O}}{D_{HPTS}}, \tag{3.51}$$

$$= (2.172 \pm 0.420) \cdot 10^3. \tag{3.52}$$

This value is even lower than that of the fluorophore fluorescein, calculated by Münsterer and Jähne [1998] to Sc $\approx$ 2440. The scaling to the Schmidt number of CO_2 at 20 ℃, Sc = 600, leads to the scaling factor r for HPTS

$$r(20\,℃) \approx \frac{600}{2172}, \tag{3.53}$$

$$\approx 0.276 \pm 0.05. \tag{3.54}$$

3.7.3 Absorption Characteristics of HPTS

The absorption characteristics of the two ion species of HPTS, the anion acid $\mathrm{R}^{3-}\mathrm{OH}$ and the anion base $\mathrm{R}^{3-}\mathrm{O}^{-}$, will be presented in this subsection. The ratio of the two species depends on the pH of the solvent.

Maxima of HPTS-absorption in nm				
Source	$R^{3-}OH$	$R^{3-}O^-$	$R^{3-}OH^*$	$R^{3-}O^{-*}$
[Avnir and Barenholz, 2005]	-	460	-	-
[Pines and Huppert, 1986]	-	-	450	-
[Wolfbeis et al., 1983]	∼403	∼454	-	-
[Tran-Thi et al., 2000]	403.6	460.8	450.0	484
O'Neil [2006]	403	454	-	-
[Prayer, 1997]	403.5 ± 0.5	454.5 ± 0.5	-	-
own measurements	404 ± 1	455 ± 1	-	-

Table 3.3: Maxima of HPTS-absorption reported in literature.

For ground state absorption the maximum for $R^{3-}OH$ is found at $403.4, \pm 0.4$ nm while the anion base maximum is found at 456 ± 3 nm in aqueous solution. The values and errors are estimated from deviation of values in literature, shown in table 3.3.

The isosbestic wavelength, at which both anion base and anion acid have the same absorption, is reported in [Avnir and Barenholz, 2005] and [Wolfbeis et al., 1983] at 415 nm. Own measurements gave a value of 416 $\pm$ 1 nm.
The absorption measurements are the basis for determination of the extinction coefficients.

Extinction Coefficients of HPTS

From the absorption, measured spectroscopically at different concentrations of the fluorophore, the extinction coefficients can be determined. Details of these measurements can be found in appendix B.

Prayer [1997] reported a molar extinction coefficient to the base of 10 of

$$\mathfrak{e}(403.5\text{nm}) \;=\; 2.32 \cdot 10^4 \text{M}^{-1}\text{cm}^{-1},$$

for the anion acid and a molar extinction coefficient of

$$\mathfrak{e}(454.5\text{nm}) \;=\; 2.44 \cdot 10^4 \text{M}^{-1}\text{cm}^{-1},$$

for the anion base. These values corresponded well to the values obtained by own measurements shown in figure 3.10 if a pK of 7.4 is assumed for the fluorophore solution.

Extinction Coefficient in the Range of Laser Modes The extinction coefficient of HPTS at the Laser excitation wavelength range $\overline{\lambda}_L$ of 440-446 nm is needed for all calculations regarding fluorescence in this study.

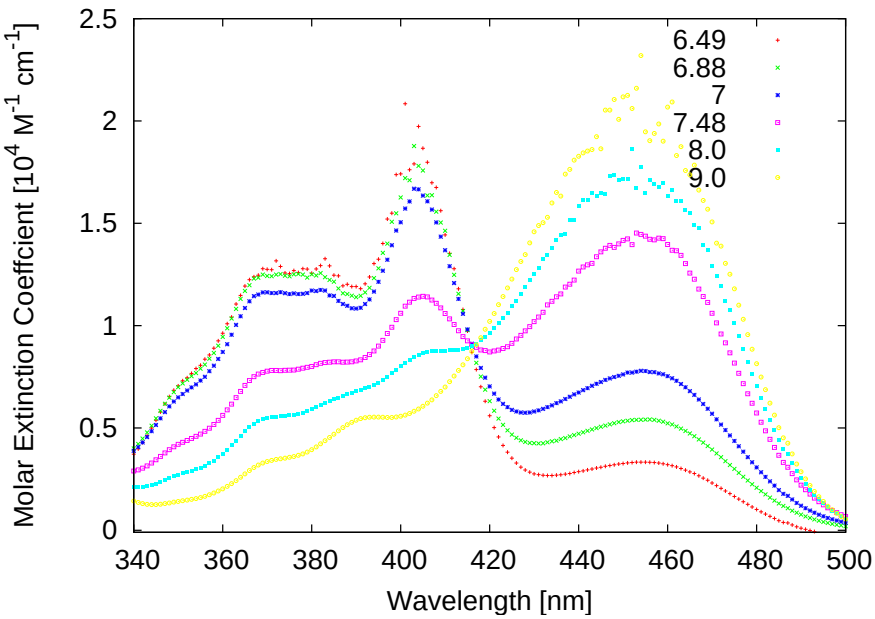

Figure 3.9: Wavelength dependent extinction coefficients of HPTS for different pH of solution based on measurements with an optical multichannel analyzer HP 8453 (Temperature = 24.0 ±0.5°C).

At the wavelength range of the laser modes (440-446 nm), see 8.1.1, only the anion base component of HPTS absorbs significantly [Prayer, 1997] and Wolfbeis et al. [1983]), so the total extinction coefficient can be approximated by

$$\varepsilon_{tot}(\overline{\lambda}_L)\, C^0_{HPTS} \approx \varepsilon_{\mathrm{R^{-3}O^-}}(\overline{\lambda}_L)\, [\mathrm{R^{-3}O^-}] \tag{3.55}$$

$$\varepsilon_{tot}(\overline{\lambda}_L)\, C^0_{HPTS} \approx r_{\mathrm{pH}}\, \varepsilon_{\mathrm{R^{-3}O^-}}(\overline{\lambda}_L)\, C^0_{HPTS}. \tag{3.56}$$

Therefore, the total extinction coefficient of HPTS is linearly dependent on the concentration of the anion base form, and a nonlinear function of pH and therefore of concentration of the hydronium H_3O^+, see 3.4.
Own measurements, see B, yield the following values for the extinction coefficients:

$$\mathfrak{e}(440\mathrm{nm}) = 2.07 \cdot 10^4 \pm 0.08\,\mathrm{M^{-1}cm^{-1}}, \tag{3.57}$$

$$\mathfrak{e}(442\mathrm{nm}) = 2.15 \cdot 10^4 \pm 0.08\,\mathrm{M^{-1}cm^{-1}}, \tag{3.58}$$

$$\mathfrak{e}(445\mathrm{nm}) = 2.25 \cdot 10^4 \pm 0.08\,\mathrm{M^{-1}cm^{-1}} \tag{3.59}$$

The variation of the extinction coefficient in the range of the laser modes can then be estimated to 8%.

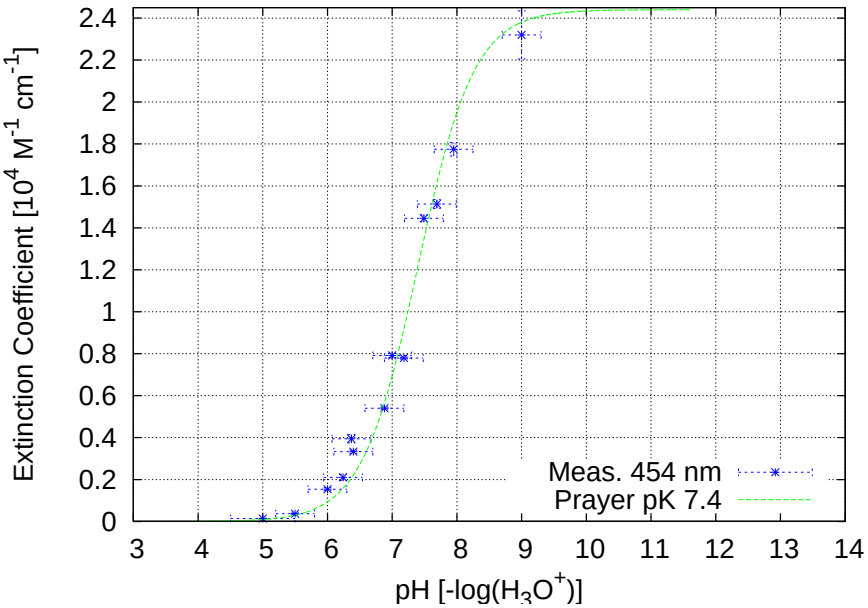

Figure 3.10: pH dependent extinction coefficient at 454 nm of HPTS based on measurements with an optical multichannel analyzer HP 8453 (Temperature = 24.0 ±0.5°C). The green curve marks the extinction coefficients based on the values of Prayer [1997].

3.7.4 Fluorescence Characteristics of HPTS

Maxima of fluorescence

The anion acid and anion base can be excited to fluorescence both in the ground state and also in the excited state. Yet, the proportion of molecules in the excited state is so low, $< 10^{-5}$, see 11, the fluorescence of the excited molecules can be neglected.

A comparison between fluorescence of excited and ground state is given by Tran-Thi et al. [2000].In table 3.4 values from literature are compared to own measurements and yield that the maximum of emission is in the range of 511-515 nm. The mean value of the literature values and of own measurements gave a maximum emission wavelength of $\lambda_{em}^{max} = 513 \pm 1.4\,\text{nm}$ which was used to calculate the Stokes shift.

The fluorescence spectrum is plotted in figure 3.7.4 as normalized spectrum, gained by two different spectrometer setups, one a commercial, a Varian Eclipse Carrier, that delivered corrected spectra and a simple fiber spectrometer, a Ocean Optics USB 4000, that delivered uncorrected spectra. Both spectra do not differ significantly, which implies that uncorrected spectra can be used in experiments without increasing the error.

Maxima of HPTS-Emission in nm		
Source	$R^{3-}OH$	$R^{3-}O^{-}$
[O'Neil, 2006]	-	511
[Green, 1990]	-	514
[Wolfbeis et al., 1983]	-	∼515
[Tran-Thi et al., 2000]	442.5	514.1
[Geddes and Lakowicz, 2005]	435	512
[Prayer, 1997]	-	512
own measurements	-	513 ± 1

Table 3.4: Maxima of HPTS-fluorescence reported in literature.

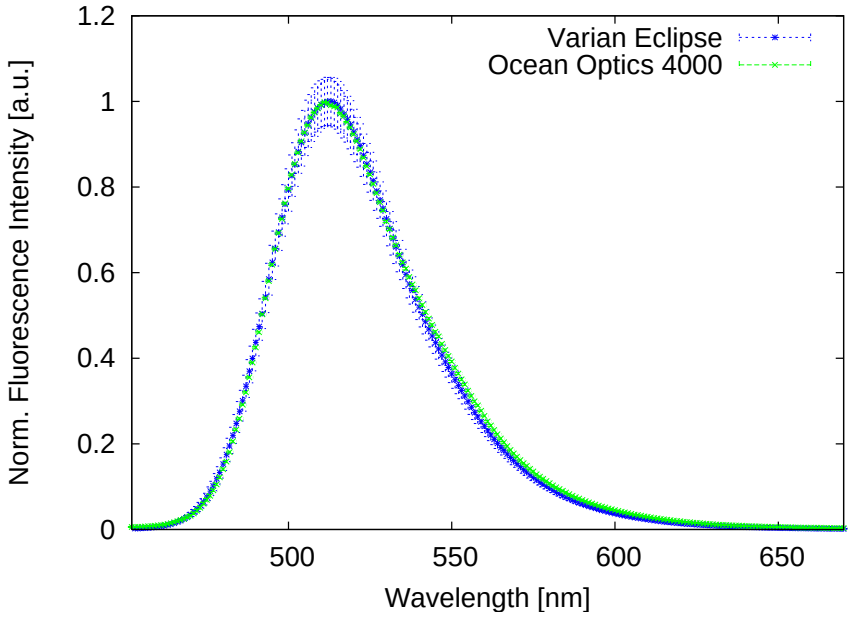

Figure 3.11: Fluorescence Spectrum of the HPTS anion base normalized by maximum intensity. The fluorescence spectra were recorded with a Varian Eclipse fluorescence spectrometer (Temperature 20 ±0.2°C) and a Ocean Optics 4000 spectrometer (Temperature 22 ±1.0°C), the first with an excitation wavelength of 445 nm ± 5 nm, and the second with excitation by the Laser nano-440-450 used for experiments.

Stokes shift

The Stokes shift is defined as the distance between the peak of maximum absorption to maximum of fluorescence in wavelength, O'Neil [2006] found the maximum of emitted fluorescence spectrum at 511 nm, reporting a Stokes shift of 57 nm. Values of Tran-Thi et al. [2000] differed to them. They reported a Stokes shift of the anion acid (ground state) of 38.9 nm, and of 53.3 nm for the anion base in ground state. Here, the Stokes shift is calculated from the above calculated mean values of maximum of emission and absorption yielding a value of $57 \pm \pm 2$ nm. This large Stokes shift implies a low probability of reabsorption.

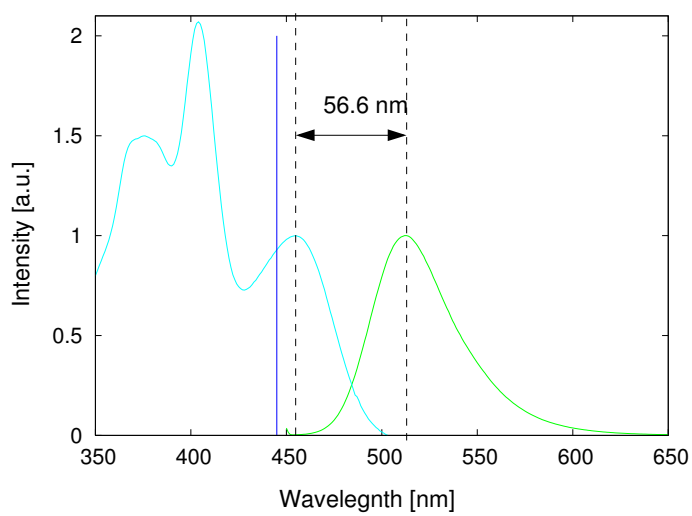

Figure 3.12: Stokes shift of the anion base of HPTS, based on own data. The blue line marks the wavelength of Laser excitation.

According to Spry et al. [2007] concentrations of less than 10^{-4} M reabsorption effects are negligible. As measurement concentrations are in the order of 10^{-5} M reabsorption effects were neglected in this work.

Quantum efficiency/Quantum yield According to Wolfbeis et al. [1983] quantum efficiency is 'nearly one'.
Tran-Thi et al. (Tran-Thi et al. [2000]) report a quantum efficiency of 0.99 $\pm$ 0.01 at a pH of 11 and an excitation wavelength of 394nm in aqueous solution. Prayer [1997] reported a value of $\Phi_q^{abase} = 0.986 \pm 0.01$ for the deprotonated form of the anion base and a value of $\Phi_q^{abase} \approx 1$ for the protonated form or the anion acid.
Both quantum yields are very high as the quantum yield is in the range of zero to one. This implies that almost the whole absorbed energy is transferred into fluorescence emission and almost nothing transferred to other energy forms like heat.

Lifetime

Lifetime of HPTS Components			
Reference	$R^{-3}OH$ [ns]	$R^{-3}O^{-}$ [ns]	environment
[Weller, 1958]	6.4	5.7	water
[Wolfbeis et al., 1983]	4.8	-	water
[Pines and Huppert, 1991]	5.15	5.5	water
[Pines and Pines, 2001]	5.15	5.3 ± 0.03	water

Table 3.5: Literature values of lifetime of the two HPTS components $R^{-3}OH$ and $R^{-3}O^{-}$.

Fluorescence decay time is said to be 5.3 ns in a pH-range from 2 to 13 according to Pines and Pines [2001] and 5.7 ns according to Weller [1958]. Geddes and Lakowicz [2005] reports an excited state lifetime of 5.3 ns for the anion base and 4.8 ns for the anion acid, citing works of Wolfbeis et al. [1983] and Mills and Chang [1993]. Though these reported values differ, but they all are below 6 ns, which is short enough for the reaction to be faster than any transport process.

Temperature dependence

In literature reports about temperature dependence of fluorescence intensity differ widely:
Temperature dependence of fluorescence is reported by Kermis et al. [2002] for immobilized HPTS. According to their work HPTS fluorescence increases with increasing temperature. This is in contrast to the work of Zhujun and Seitz [1984] who report the ratio to be not effected. They measured temperature dependence to be $1.1\%/K$ at 298 K (25C) and $1.7\%/K$ at 308 K. Coppeta and Rogers [1998] reported a shift in absorption band towards longer wavelengths and decreasing absorption with temperature increase. They measured absorption for an excitation wavelength of 488 nm and a pH of 11 an increase in fluorescence intensity of 1.21% per Kelvin with an inaccuracy of 15 %. They indicated however, an expected decrease in intensity with increasing temperature for excitation wavelengths below 450 nm in a graphical illustration of measurements.
In experiments performed by the author at a fluorescence spectrometer from Varian, Type Eclipse [2] a change in fluorescence was determined to be of $-0.25 \pm 0.03\%$ per Kelvin in the temperature range from 10 - 35 degrees Celsius at an excitation wavelength of 445 nm and pH 8. Measurement volume $1.4 \cdot 10^{-3}$ l; no correction for photobleaching. The result was gained as harmonic mean of five slopes, fitted with weighted total-least squares solver of Krystek and Anton [2007].

[2] We greatly acknowledge the support by the group of Dr. D. P. Herten

Photobleaching

Photobleaching of HPTS is very low according to Wolfbeis et al. [1983], though detailed values were not given. An estimate of the photobleaching of HPTS in combination of values from HPTS and fluorescein, for lacking HPTS values is given in chapter 11.

Quenching

Due to decay times of fluorescence in the ns-range quenching effects are extremely small. According to Wolfbeis et al. [1983] fluorescence decreases from saturated nitrogen solute to saturated oxygen solute by approximately 5%.
In the measurements conducted here these effects can be neglected.

3.7.5 Comparison of HPTS to Commonly Used Fluorescein

The chosen fluorophore HPTS has to compete with the commonly used fluorescein. After the detailed description of the properties of HPTS, in this subsection they will be compared to those of fluorescein.
HPTS has been chosen for mainly two reasons: On the hand HPTS offers a much larger Stokes shift of 57 nm compared to the Stokes shift of 25 nm of fluorescein, see figure 3.13. This larger Stokes shift indicates a much lower overlap of the emission-absorption spectra and thus a significantly reduced probability of reabsorption of the fluorescent light when traveling trough the medium towards the detector. On the other hand, HPTS offers an even higher quantum yield in its anion base form of 0.98, according to Prayer [1997] compared to 0.93 of the dianion of fluorescein as reported by Sjöback et al. [1995]. These two main criteria are also summarized in table 3.6.

	Fluorescein	HPTS
Abs. max.	490 nm	456 nm
Fluo. max.	515 nm	513 nm
Stokes shift	25 nm	57 nm
Quant. yield	0.93	0.99

Table 3.6: Comparison of Stokes shift and quantum yield of both HPTS and fluorescein.

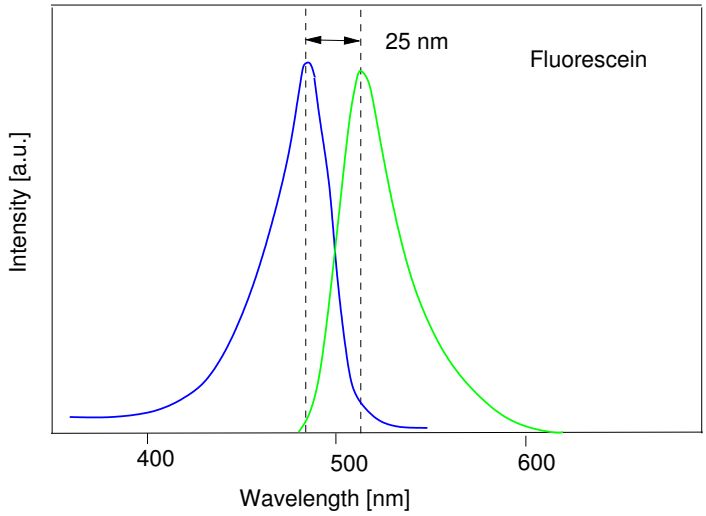

(a)

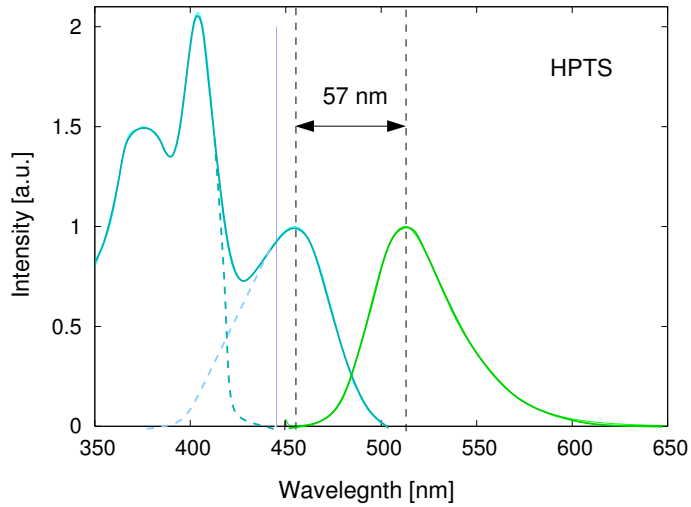

(b)

Figure 3.13: Absorption (blue) and fluorescence (green) spectra of (a) fluorescein, adapted from Sjöback et al. [1995] and (b) HPTS. Remarkably is the more than doubled Stokes shift of HPTS compared to fluorescein.

3.7.6 Summary

Summarizing, HPTS offers all the demanded properties of a fluorophore suited for LIF and can therefore be used for measurements. HPTS even exceeds the commonly used fluorescein in its positive characteristics of a high Stokes shift and a high quantum yield. Furthermore, the protonation time of the acid-base reaction of HPTS of 5.6 ns is much shorter than the typical timescale of mass transport, which fulfills together with a pK next to the neutral range the main demands of the pH-method on a suitable fluorophore as described in 3.4.

Chapter 4

Realizations of LIF-Setups for Measuring Depth-Dependent Gas Concentration under a Wave-Influenced Water Surface

Although undulated water surfaces are common in oceanic environments, laboratory measurements of water-sided gas concentration profiles under a wave-influenced water surface are rare.

Laser-induced fluorescence studies of gas transfer with wave amplitudes in the mm-range and a water depth of 11 mm were done by Duke and Hanratty [1995] and Woodrow and Duke [2001].
Takehara and Etoh [2002] made qualitative measurements of turbulent motion under a wavy interface.
Münsterer and Jähne [1998], Falkenroth [2007] and Walker and Peirson [2008] measured mean concentration profiles under higher wave amplitudes in the cm-range to determine gas transfer velocities under wave-influenced surface conditions.

However, Münsterer and Jähne [1998] and Falkenroth [2007] suppressed waves by a surfactant to be able to measure at higher wind speeds. Walker and Peirson [2008] measured in combination with a wave follower at four positions of the wave (crest, falling and rising limb and trough).

The aim of this study was to develop a Laser-induced fluorescence setup that could be used for measuring under a strongly wave-influenced water surface.

4.1 Contribution in this Study

Two different techniques are presented in this study that allow measuring concentration profiles under a complex surface topology: the Spectral Reconstruction Approach (SPERA) and the Static-Pattern LIF technique (SP-LIF).

The Spectral Reconstruction Approach - SPERA - is based on the LIF-technique but analyzes the integral fluorescence spectrum measured on top of the water surface. The lost depth information of gas concentrations is reconstructed from the spectral information via inverse parameter estimation, where the depth-dependent concentrations are the parameters to be determined.
The theory of the Spectral Reconstruction Approach (SPERA) is presented and analyzed regarding the possibilities of solving the inverse problem.
The inverse problem is tested in computer experiments on artificial data sets with a variety of different combination of non-Gaussian noise and model response. Experimental data is not available since during the realization studies of this theoretical approach, it turned out that no suitable fluorophore-absorber dye pair was available to allow high-resolution measurements in the thin mass-boundary layer thicknesses under high wind-induced turbulence.
One of the most important advantages of the SPERA technique is, that it allows arbitrary orientation of the illumination light sheet and therefore the search of turbulence structures in spanwise direction like micro-Langmuir circulations.
In more detail the spectral reconstruction technique is presented in section 5.

The Static-Pattern LIF Technique - SP-LIF - is a novel extension of the classic LIF-technique that allows the simultaneous measurement of the local gas concentration and the local surface slope within the measurement plane.
Convergence and divergence effects induced by the passing of waves change the local intensity of the illuminating Laser sheet. These intensity variations lead to a wrong identification of local gas concentration. The SP-LIF allows to correct for these effects as it additionally measures surface slope. The additional information on surface slope increases the knowledge on surface topology, thus leading to more reliable identification of the surface results even under a strongly wave influenced surface where estimates of surface position by symmetry filtering fail.
The Static Pattern LIF technique has been developed within this project. It will be presented in more detail in section 6.

Before these two used measurement techniques will be presented in more detail, an introduction to the common used side-setup for LIF is given in the next section. This side-setup has been the basis on which the new techniques have been developed.

4.2 The Classic Approach: Tilted Side-Camera Setup

For investigating transport of dissolved gases one kind of LIF setup has been most widely used: the tilted side-camera setup. The tilted side-camera setup has been used for grid-stirred tanks by Herlina and Jirka [2008] and Schulz and Janzen [2009] as well as wind-wave tunnels by Münsterer and Jähne [1998] and Falkenroth [2007] and Walker and Peirson [2008]. Generally, the plane of fluorescence emission is oriented parallel to main flow direction. In the side- setup images of this are taken with a camera positioned at a side-window. In figure 4.1 a typical side-setup is shown together with an image taken with it.

As transport processes in the mass boundary layer are of special interest, see chapter 2, the water-sided mass boundary layer should be part of the imaged area. For this reason the viewpoint of the camera in a LIF-setup has been tilted to allow taking images of the illuminated plane up to its total reflection on the water surface. This angle has to be made steeper the higher the wave amplitudes get, as deep wave troughs may block the view to the surface of the camera.

Images taken with the side setup include the plane of emission as well as its

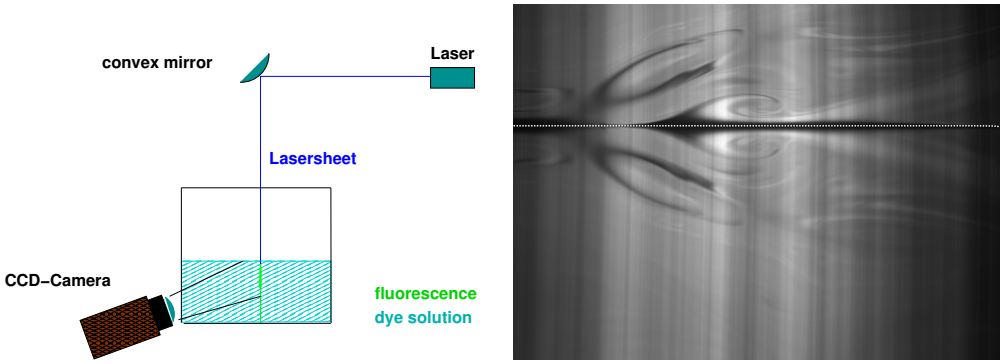

(a) (b)

Figure 4.1: (a)Sketch of side-camera LIF setup at a wind-wave tunnel.(b) Image taken in Static Pattern LIF-setup with illuminating light sheet generated by a widened laser beam. Areas of increased local gas concentration appear as areas of decreased local intensity. The water surface is marked by the white -dashed line. The imaged area above the surface is the total reflexion of the plane of emission at the water surface.

total reflection at the water surface, see figure 4.1.

For an estimation of depth dependent gas concentration the position of the surface has to be determined in the images. Furthermore,if the laser illumination comes from the top the local slope of the surface has to be determined: Divergence and convergence effects due to waves (see figures 4.2 and 6.2) lead to a spatio-temporal changing distortion of the laser sheet, so called lens effects. These lens effects of local intensity will lead to a wrong concentration reconstruction from the local gray values if they are not corrected.

For details on possible illumination setups see sections 8.1 and 9 for reconstruction of dissolved gas concentration from local gray value.

Improvements of the Side Setup in this Study

Optical resolution in the LIF-side setup could be significantly improved by using a Scheimpflug arrangement in combination with the side-Setup. The Scheimpflug arrangement is discussed together with the optical measurement components in section 8.2.1, as a special feature of the here used wind-wave tunnel - a tilted side window - is part of the arrangement.

Although optical resolution can be improved, the problems of determining the position of the water surface and lens effects due to wave motion remain.
In the following section an extension of the side-setup is presented that allows to detect the water surface and to correct for lens effects directly in the LIF-images without further technical equipment like wave followers.

Chapter 5

The Spectral Reconstruction Approach (SPERA)

In the present work concentration gradients of dissolved gases in the aqueous mass boundary layer will be detected above the water surface by analyzing the emitted integral fluorescence spectrally. The depth information is lost in the recorded image as the spectrometer only sees a fluorescent line at the water surface.
The lost depth information has to be extracted from the emitted spectrum via an inverse parameter estimation. The depth-dependent concentrations appear as the parameters of the inverse problem to solves.
The method used is actually a tomographic method but with one significant alteration: the position of the detector is fixed and is not varied over a whole range of radial positions. Here, the integral fluorescent spectrum is detected only at one position above the water surface with a spectrometer. The integral spectrum is the overlay of spectra emitted at every depth layer in the water probe below.
From that integral spectrum the individual spectra coming from different depth layers can be reconstructed:
In the structure of each spectrum is the local concentration at the corresponding depth z and the depth information z itself coded like a fingerprint, so each depth and each concentration has its own uniquely formed fluorescence spectrum. This depth and concentration coding is done by the combined usage of a fluorophore and a second dye that absorbs in the emission band of the fluorophore. In that way the depth information can be regained by extracting the individual depth spectra from the integral spectrum like a vector function is expanded in its basis vectors.

In the next sections the reasons for developing the Spectral Reconstruction Approach (abbreviated SPERA) are presented, followed by a recapitulation of previous and related works, and a section mentioning the contribution done in this work. After that the actual approach is described in its theoretical principles, followed by a mathematical verification/analysis of the possibilities to reconstruct the desired parameters.

5.1 Intention of the Method

The side-setup techniques described in section 4.2 are characterized by the following attributes:
One advantage of the side-setup is the large depth range that can be visualized from micrometer to several centimeters depending on the experimenters' demands and the optical possibilities. The Laser-sheet orientation is usually chosen to be parallel to main flow in a linear wind wave tunnel. This allows only detection of structures that are also oriented parallel to main flow. Other orientations of the sheet are rarely chosen as the optical distortion is too large for quantitative measurements without special adaptions to the tunnel; the angle of observation is much steeper than in the parallel side-setup and therefore the problems with tilted optical components regarding astigmatism and refraction at a tilted phase boundary are further increased. Only Takehara and Etoh [2002] visualized flow structures spanwise to main flow qualitatively. They reported streaky structure and interpreted them as a kind of Micro-Langmuir circulation. So the question came up whether an alternative technique might give better resolution of spanwise concentration fields where Side-LIF has difficulties.
The here presented Spectral Reconstruction Approach SPERA offers the possibility of an arbitrary orientation of the Laser light-sheet, so structures parallel to main flow like Micro-Langmuir should be detectable. As the method is based on light absorption, the coordinated system is automatically coupled to the current local topology of the water surface as light follows refraction. Problems appear only at singular points when local slope, especially in a capillary wave train, comes near the limit of infinity, see section 12.2.4 for details. So apart from such singular events the Spectral Reconstruction Approach is usable under rough surface conditions.
The depth range however is limited to the topmost 1 mm of the water phase, where difference in light ray path and local perpendicular z-axes can be neglected.

5.2 Relation to Previous Works

Already in the 1980's, Asher and Pankow [1989] presented an experimental approach in which a fluorophore was used in combination with a dye that absorbs broadly in the main emission band of the fluorophore to ensure that fluorescence is only recorded down to a cut-off depth. At this cut-off depth the emitted fluorescent light is damped to 1% of its initial intensity when having reached the surface. The dye pair used there were 2,7.dichlorofluorescein and Orange G.
A recent work by Asher and Litchendorf [2009] uses the same technique to determine concentration fluctuations in the topmost 100μm beneath the water surface by recording the integral intensity of that layer in CCD-detector without a spatial 2D resolution. Concentration was determined in this whole layer and no further effort was made to use the spectral information.

The spectral reconstruction technique was introduced in the work of Lode [1998],

theoretically based on an idea of B. Jähne. Also a first experimental test setup was build. Yet, the inversion method had only been tested on the reconstruction of artificial data sets. The pair of fluorophore and absorber dye used there consisted of fluorescein and bromphenol blue.
Reinmuth [2000] investigated the characteristics of a suitable absorber dye for the technique and developed a setup for the extension of the method to 3D. Later, Schwarz [2005] tried to analyze the model regarding convergence properties, now with the dye pair HPTS and Violamine R. Additionally, depth-dependent spectra were measured with a confocal microscope.
The acquired spectra, however, suffered from strong noise as intensity of the used laser was much to low with a total power of 30 mW. Therefore, a verification of the model with real depth spectra was not possible.
Even with the diode laser used in this work with a power of 450 mW, the intensity was much to low for taking real time spectra with a commercial multi channel analyzer, Ocean Optics 4000, see section 5.7 for details.

In all three works, discrepancies between the measured integral spectra and depth spectra with respect to the theoretical prediction could not be detected. In experiments conducted later with higher Laser intensities a mismatch between theory and experiments lead to the conclusion that the theoretical model needed to be revised.

5.3 Contribution and Improvements in this Study

In this work an improved theoretical model is presented to account for the discrepancies detected among theoretical predictions and experimental results.
Furthermore, mathematical conditions were formulated that the integral spectrum could be expanded in the vector space of the individual depth spectra including that the functions of the depth spectra form a basis of the regarded vector space.

Additionally, the design matrix of the linearized model was analyzed for finding the conditions for full rank and these results were related to the properties of the pair of dyes. In that way an evaluation system for choosing the best fitted pair of dyes could be set up.
It turned out, that the crucial parameter is in fact a strong gradient in extinction coefficient of the absorber in the emission band of the fluorophore to ensure non-singularity of the matrix and therefore invertibility.

Moreover, the high noise level in spectral data sets was analyzed statistically. It turned out that the Poisson-characteristic of the fluorescence was a significant component in the combined statistics of the emitter-detector system (illuminated area and optical system with CCD-camera).

Knowledge of the errors of the experimental data was used to choose a suit-

able solver for the inverse problem: instead of the standard l_2 norm used in least-squares solver, robust fitting routines based on non-Gaussian error distribution assumptions were tested, which led to encouraging results.
Even if stronger non-Gaussian noise was added, the inversion routine could regain the undisturbed concentration for up to three layers, which is a significant improvement to everything achieved before.

The experiments conducted could not be analyzed within this work, as the noise level due to low detector sensitivity was still to high. For that reason a new spectrometer setup was constructed by F. Friedl in which a combination of a prism and a CCD-camera was used to ensure a high dynamic resolution even at low total radiance intensities.

5.4 Basic Principle of the SPERA Technique

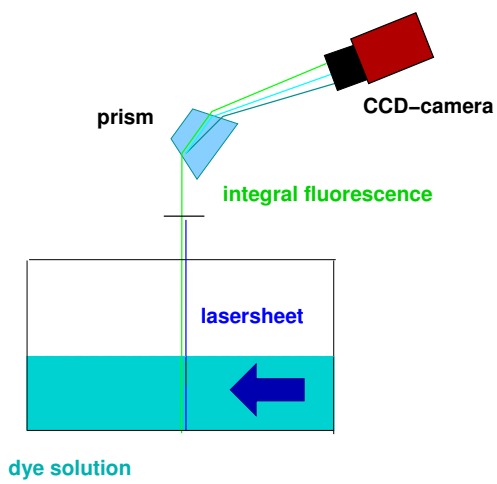

Figure 5.1: Sketch of the spectral setup in side view needed in SPERA. The direction of flow is perpendicular to the sheet orientation, see orientation of the arrow.

In the SPERA setup, the aqueous phase consists of a dilute solution of a pH-sensitive fluorophore and a non-fluorescent dye in H_2O. This solution is illuminated by Laser light-sheet from above, so that a 2D cross-section is obtained. A sketch of the experimental setup is shown in figure 5.1.
The intensity of emission of this fluorophore is directly linked to the concentration of the investigated gaseous tracer. In the present case of the pH-indicator HPTS, the intensity of the emitted light either increases with an increasing concentration of dissolved gas molecules in the case of alkaline gases or decreases with increasing concentration in the case of acid gases like HCl, see section 3.7 for details on the fluorophore and the demanded properties.
The aim of the technique is to gain depth-dependent concentration fields or the

gas concentration at every desired water depth z_i .
As fluorescent emission cannot be easily excited in the setup at just a single depth z_i of interest, the technique has to make sure that every depth z_i produces a unique emission spectrum. This is achieved by adding a second non-fluorescent dye that must not react in any way in the presence of the gaseous tracer:
The second dye absorbs in the emission band of the fluorophore, but is (nearly) transparent to the Laser wavelength λ_L. As absorption depends non-linearly on the thickness of the transversed layer, the fluorescence signal is also altered in a nonlinear way leading to unique depth-dependent fluorescence spectra under the assumption that both dyes are equally distributed in the solution. Summarizing, every depth z has in this way its own unique spectrum, which will be called the basis spectrum $\mathfrak{B}(z, \lambda)$ of the corresponding depth. Within each depth the basis spectrum is altered by the local concentration of the anion base $R^{-3}O^{-}$. So for every depth and every concentration a unique spectrum is produced.
What we measure at the surface is therefore the integral over these basis spectra $\mathfrak{B}$:

$$L(\lambda) \quad = \quad \int_0^z c(z')\mathfrak{B}\left(z';\lambda\right)dz'. \tag{5.1}$$

So the integral fluorescence spectrum has to be decomposed into its basis spectra to gain the information of depth-dependent concentrations. This is achieved via an inverse modeling approach.
In the following subsections the mathematical formulation that finally leads to the desired depth-dependent ion concentrations is described. From ion concentrations gas concentration can be derived.
The next subsection will give a more detailed look on the theoretical description of absorption/emission processes involved.

5.5 Physical Description of Regarded Absorption/ Emission Processes

In the following, a theoretical description of the mixed absorption/emission of the fluorescent pH-indicator and the second dye is given. The second dye will be called absorber dye from here on. First, we start with the absorption of Laser light by the fluorescent pH-indicator. The concentration of the anion base of HPTS, $R^{-3}O^{-}$ (see section 3.7), is abbreviated with c_b; the concentration of the anion acid with c_a. The anion base is the HPTS species that significantly absorbs at the used Laser wavelength spectrum [440-445 nm] at a pH greater than 6. The concentration of these ions equal the concentration of the observed gas, see section 3.4 for explanations.

Absorption of Laser Light The incoming Laser light, the irradiance E_L, is depth-dependently diminished according to the law of Bouguer-Lambert-Beer

when traversing a layer of thickness z. This leads to a transmitted irradiance E_{trans} ($[E] = \mathrm{W/m^2}$) described by Bouguer-Lambert-Beers' law

$$\begin{aligned} E_{trans}(z, \lambda_L) &= E_L \cdot e^{-\alpha(\lambda_L; c(z))z} \\ &= E_L \cdot e^{-\varepsilon(\lambda_L)\cdot c(z)\cdot z}, \end{aligned} \tag{5.2}$$

with E_L as the unreduced Laser intensity or irradiance, α as the absorption coefficient of the used dye, c as dye concentration, z as the depth in water ($z = 0$ corresponds to the surface), and λ_L as the wavelength of absorbed (Laser) light. The extinction coefficient ε describes the linear dependency of the absorption coefficient α on the concentration.
Important for the following considerations is the fact, that the dye concentration c is a function of depth and not a constant value. In this context the validity of Bouguer-Lambert-Beers' law has to be verified. Schmidt [2000] formulated conditions under which the validity is guaranteed:

- Scattering and reflexion have to be insignificant.
- The dye should be homogeneously distributed.
- Not all intensity should be absorbed at the regarded depth, this means that the solution has to be dilute.
- The temperature has to be kept constant, as optical properties depend strongly on temperature.
- The same solvent should be used for all measurements as the optical properties are solvent dependent.

In the present case these demands are fulfilled. For a more detailed discussion of error sources see section 11. The extinction coefficient of the fluorophore HPTS is pH dependent, and therefore a function of the hydronium concentration $[H_3O^+]$[1]. The reason for this is that dissolved HPTS consists of two components, the anion base $\mathrm{R^{-3}O^-}$ and the anion acid $\mathrm{R^{-3}OH}$, see section 3.4. A rearrangement of the law of mass action by using continuity of mass of the indicator dye leads to the so called Henderson-Hasselbach equation, e.g. Bliefert [1978], again under the assumption that the solution is dilute[2],

$$\mathrm{pH} - \mathrm{pK}_H = \log\left(\frac{c_b}{c_a}\right). \tag{5.3}$$

The extinction coefficient for each of the HPTS components is a constant. The extinction coefficient ε_{HPTS} of the whole solution, however, varies with pH as the ratio c_b/c_a varies with pH following the Henderson-Hasselbach equation, (5.3),

$$\varepsilon_{HPTS}(\lambda) \cdot c_{HPTS} = \varepsilon_b(\lambda) \cdot c_b + \varepsilon_a(\lambda) \cdot c_a. \tag{5.4}$$

In the case of an excitation wavelength $\lambda_L \geqslant 440$ nm only the anion base of HPTS can absorb the Laser light. Therefore the absorption coefficient of

[1] $pH = -log\left([H_3O^+]\right)$, $[H_3O^+]$ the concentration of H_3O^+-ions
[2] activity coefficients are approximately one

HPTS only depends on the concentration c_b of the anion base $R^{-3}O^-$ and the corresponding extinction coefficient ε_b. This extinction coefficient is a constant for all pH values as said above, in contrast to ε_{HPTS} of the whole solution.
With this restriction, we get a simplified formulation for the total extinction coefficient ε_{HPTS}, because $\varepsilon_b(\lambda_L) \gg \varepsilon_{acid}(\lambda_L)$,

$$\varepsilon_{HPTS}(\lambda_L)\, c_{HPTS} \doteq \varepsilon_b(\lambda_L) \cdot c_b. \tag{5.5}$$

As mentioned at the beginning of this section, the absorption of the added absorber dye $\alpha_A = \varepsilon_A \cdot c_A$ also has to be negligible with respect to the absorption of the anion base component of the fluorophore $\varepsilon_b(\lambda_L) \cdot c_b$,

$$\varepsilon_b(\lambda_L) \cdot c_b \gg \varepsilon_A(\lambda_L) \cdot c_A. \tag{5.6}$$

All properties of the second absorber dye are marked by the subscript 'A' for absorber. With these assumptions the integral absorbance is found to be

$$\alpha_{HPTS} \cdot z = \varepsilon_b(\lambda_L) \int_0^z c_b(z')dz'. \tag{5.7}$$

The transmitted irradiance is then described by

$$E_{trans}(z, \lambda_L) \doteq E_L \cdot \exp\left(-\varepsilon_b(\lambda_L) \int_0^z c_b(z')dz'\right). \tag{5.8}$$

Not only the integral transmitted intensity is of interest in a certain depth but also the intensity absorbed in an infinitesimal layer dz at depth z. The incident irradiance changes with depth z, so that the absorbed irradiance in this layer equals the derivative of E_{trans}:

$$\begin{aligned} \Delta E_{abs}(z_i) &= \left.\frac{\partial E_{trans}}{\partial z}\right|_{z_i} \Delta z, \\ \Rightarrow \frac{\partial E_{trans}}{\partial z} &= -\varepsilon_b(\lambda_L) \cdot c_b(z) \cdot E_L \cdot \exp\left(-\varepsilon_b(\lambda_L) \int_0^z c_b(z')dz'\right). \end{aligned} \tag{5.9}$$

This proportion of irradiance $\frac{dE_{trans}}{dz}$ absorbed in the depth layer dz is the intensity that is used for exciting fluorescence within this layer.

Emission of Fluorescence The absorbed irradiance of the Laser light induces emission of fluorescence. This emission itself is proportional to the absorbed irradiance, given that the dye-solution is dilute (verified by experiment up to a concentration of 35 mgl^{-1} or $0.67 \cdot 10^{-4}$ mol/l for 1 cm as length of absorption of the fluorophore). The function η describes the fluorescence spectrum that is emitted by the fluorophore. This function η consists of two parts $\eta(\lambda) = \Phi_q \cdot f_b(\lambda)$ with $f_b(\lambda)$ as the wavelength-characteristics of emission spectrum of the fluorophore or the normalized fluorescence spectrum and Φ_q as the wavelength independent constant called quantum efficiency or quantum yield. The quantum yield describes the efficiency of the fluorescence emission. Quantum yields are tabulated for many fluorophores and therefore allow to compare the different fluorophores.

The determination of quantum yields is an experimentally demanding task, which contains many error sources for the inexperienced. For a detailed description of measuring quantum yields see for example Lakowicz [2006]. The absorbed light at a depth z_i induces fluorescence. This change of emittance M with depth can be mathematically described by the following formulae,

$$\begin{aligned}
\frac{\partial M_{em}(z;\lambda)}{\partial z} &= \tilde{\eta}_b(\lambda) \left| \frac{\partial E_{trans}}{\partial z} \right| \\
&= \eta_b(\lambda)\, \varepsilon_b(\lambda_L) \cdot c_b(z) \cdot E_L \exp\left(-\varepsilon_b(\lambda_L) \int_0^z c_b(z')dz' \right) \quad (5.10) \\
&= \Phi_{q_b}\, f_b(\lambda)\, \varepsilon_b(\lambda_L)\, c_b(z)\, E_L \exp\left(-\varepsilon_b(\lambda_L) \int_0^z c_b(z')dz' \right).
\end{aligned}$$

with Φ_q^{abase} as the quantum yield of the anion base, ε as the extinction coefficient of the anion base. Yet, fluorescence is homogeneously emitted in all directions; this has to be taken into account: A camera sees just a cone of spatial angular distribution. Using the above formulation we arrive at this description for the depth-dependent radiance of fluorescent emission $\partial L_{em}(z;\lambda) \,/\, \partial z$ ([L] $=$ [W/(m^2 sr)]) normalized to the full spatial angle $\Omega = 4\pi$:

$$\begin{aligned}
\frac{\partial L_{em}(z;\lambda)}{\partial z \partial \Omega} &= \frac{\partial M_{em}(z;\lambda)}{\partial z \partial \Omega} \quad (5.11) \\
\frac{\partial L_{em}(z;\lambda)}{\partial z} &= \frac{1}{4\pi} \cdot \frac{\partial M_{em}(z;\lambda)}{\partial z} \quad (5.12) \\
&= \frac{1}{4\pi} \Phi_{q_b}\, f_b(\lambda)\, \varepsilon_b(\lambda_L)\, c_b(z)\, E_L \exp\left(-\varepsilon_b(\lambda_L) \int_0^z c_b(z')dz' \right) \\
&\approx \frac{1}{4\pi}\, \Phi_{q_b}\, f_b(\lambda)\, \varepsilon_b(\lambda_L)\, c_b(z)\, E_L + O(\left[\varepsilon_b(\lambda_L) \int_0^z c_b(z')dz' \right]^2).
\end{aligned}$$

The last approximation is only valid for

$$\varepsilon_b(\lambda_L) \int_0^z c_b(z')dz' \ll 1, \quad (5.13)$$

because the approximation of the exponential function with the constant term is only valid in that case. A dye concentration that fulfills this condition guarantees a linear relation between fluorescence intensity and absorption. In fluorescence spectroscopy most dyes follow this approximation up to a absorption of 0.05 according to Schmidt [2000].

Alteration of Intensity due to Absorption by Second Dye In the last paragraph the depth and concentration dependent radiance has been deduced. These formulae tell that a lower intensity due to lower concentration of the anionic dye form or due to a greater depth z cannot be distinguished in the value of intensity without knowledge of $c(z)$ and the current position z.
So if it shall be distinguished between a loss due to depth or due to concentration without prior knowledge of depth, a second information source is needed or is to be coded into the intensity formulation.

This is achieved by adding a second dye that absorbs in the main emission band of the fluorophore used and alters in that way the fluorescent spectra depth-dependently.

In contrast to local pH-dependent fluorophore concentration the concentration of the absorber is supposed to be homogeneously distributed in the whole solution, so $c_A =$ constant. The second dye gets the radiance of the fluorophore as input and reduces the fluorescence according to Lambert-Beer-Bouguers' Law:

$$\begin{aligned} L_{absem}(z,\lambda) &= \int_0^z \frac{dL_{em}(z';\lambda)}{dz'} \exp(-\varepsilon_A(\lambda)c_A z')dz' \\ &\doteq \frac{1}{4\pi}\,\Phi_{q_b}\, f_b(\lambda)\,\varepsilon_b(\lambda_L)\; E_L \cdot \int_0^z c_b(z')\exp(-\varepsilon_A(\lambda)c_A z')dz' \\ &\doteq \mathcal{C}\cdot f_b(\lambda)\cdot \int_0^z c_b(z')\exp(-\varepsilon_A(\lambda)c_A z')dz'. \end{aligned} \tag{5.14}$$

with $\mathcal{C} := \frac{1}{4\pi}\,\Phi_{q_b}\;\varepsilon_b(\lambda_L)\;E_L$ as summarizing constant and the maximum water depth is assumed to be infinity, $\lim z = \infty$.

5.6 Discretization of the Emission-Absorption Equation

The integral equation in the previous paragraph can be discretized to take account of the discrete detector resolution. In a discretized form the integral is changed into a sum, with N as the number of regarded depth layers,

$$\begin{aligned} L_{em}(z,\lambda) &\doteq \mathscr{C} f_b(\lambda)\cdot \int_0^{z=\infty} c_b(z')\exp(-\varepsilon_A(\lambda)c_A z')dz' \\ &\doteq \mathscr{C} f_b(\lambda)\cdot \sum_{i=0}^{N-1} c_b(z_i)\exp(-\varepsilon_A(\lambda)c_A z_i)\Delta z_i \\ &\quad \text{with: } \lim N = \infty, \quad N\in\mathbb{N}. \end{aligned} \tag{5.15}$$

Rearrangement of the components of this sum leads to

$$\begin{aligned} L_{em}(z,\lambda) &\doteq \sum_{i=0}^{N} c_b(z_i)\mathscr{C} f_b(\lambda)\exp(-\varepsilon_A(\lambda)c_A z_i)\Delta z_i \\ &\doteq \sum_{i=0}^{N} c_b(z_i)\mathfrak{B}(z_i,\lambda) \end{aligned} \tag{5.16}$$

The depth-dependent concentrations $c_b(z_i)$ are the weighting factors of the basis functions $\mathfrak{B}(z_i,\lambda,)$.

Setting up the Model Matrix of the Linearized Problem The integral radiance L_{em}^{int} can be reformulated as a linear problem and so it is possible to formulate it in matrix form. For convenience reasons the formulation of

$L_{em}^{int}(\lambda_m) = \sum_{n=0}^{N-1} L_{em}(z_n, \lambda_m)\Delta z_n$ and $c_j = c(z_j)$ is used. We have to solve the following linear equation system:

$$\begin{pmatrix} L_{em}^{disc}(\lambda_0) \\ \vdots \\ L_{em}^{disc}(\lambda_{M-1}) \end{pmatrix} = \begin{pmatrix} \mathfrak{B}(z_0, \lambda_0) & \cdots & \mathfrak{B}(z_{N-1}, \lambda_0) \\ \vdots & & \vdots \\ \mathfrak{B}(z_0, \lambda_{M-1}) & \cdots & \mathfrak{B}(z_{N-1}, \lambda_{M-1}) \end{pmatrix} \begin{pmatrix} c_0 \\ \vdots \\ c_{N-1} \end{pmatrix}. \quad (5.17)$$

For an easier investigation of the conditions under which this matrix has full rank and allows a unique reconstruction of the integral intensities from the basis functions $\mathfrak{B}$ the model matrix is divided into the factor $\mathcal{C}$ and three submatrices:

$$B = \begin{pmatrix} \mathfrak{B}(z_0, \lambda_0) & \cdots & \mathfrak{B}(z_{N-1}, \lambda_0) \\ \vdots & & \vdots \\ \mathfrak{B}(z_0, \lambda_{M-1}) & \cdots & \mathfrak{B}(z_{N-1}, \lambda_{M-1}) \end{pmatrix} = \mathcal{C}FEZ, \quad (5.18)$$

with

$$F = \begin{pmatrix} f(\lambda_0) & & 0 \\ & \ddots & \\ 0 & & f(\lambda_{M-1}) \end{pmatrix}, \quad (5.19)$$

$$E = \begin{pmatrix} e^{-\alpha_0 z_0} & \cdots & e^{-\alpha_0 z_{N-1}} \\ \vdots & & \vdots \\ e^{-\alpha_{M-1} z_0} & \cdots & e^{-\alpha_{M-1} z_{N-1}} \end{pmatrix}, \; Z = \begin{pmatrix} \Delta z_0 & & 0 \\ & \ddots & \\ 0 & & \Delta z_{N-1} \end{pmatrix}, \quad (5.20)$$

where the notation $\alpha_i = \varepsilon_A(\lambda_i)c_A$ is used. Therefore, the model matrix can be divided into three matrices F and E and Z, where F is the diagonal matrix of the fluorescence intensities, Z the diagonal matrix of the depth layer thicknesses, and E the matrix containing the exponential decay terms of absorption. In the diagonal of F the norm fluorescence spectrum is coded, see figure 5.2 for the spectrum of HPTS. Given that the spectrum is non-zero in the regarded wavelength range, and $M \geq N$ measurements are available F has full rank. Z contains the chosen thicknesses of the individual layers and has full rank given that every layer is non-zero. E is the most important submatrix of the three because it mainly decides on invertibility of the problem: In each row of E the elements decrease exponentially with the parameter z that increases with column number. Furthermore, in each column the elements follow the absorption characteristic of the absorber dye, with low values for large absorption coefficients $\alpha(\lambda_i)$. Typically, the absorption coefficients have a range of two to three orders of magnitude. Summarizing these two behaviors, the elements of the matrix E vary over several orders of magnitude due to the exponential nature, especially if depth layers of a wide range will be regarded.

This behavior also shows up in the singular values of the complete model matrix as the influence of E is vast. The singular values are the eigenvalues of the product of the design matrix and its transpose; for further details and algorithms for calculation see Golub and van Loan [2002] and Nocedal and Wright [1999]. In table 5.1, the singular values are calculated as an illustrating example for 5 and 10 equally distributed depth layers z. Assumed is a homogeneous concentration of the tracer fluorophore and a homogeneous concentration of the absorber dye.

No. Layers	λ_{Max}	λ_{Min}	Condition number (spectral norm)
5	$0.78\ 10^9$	$1.3 \cdot 10^4$	$6.0 \cdot 10^4$
10	$1.03\ 10^9$	$0.65 \cdot 10^{-5}$	$1.6 \cdot 10^{13}$

Table 5.1: Maximal and minimal singular values λ_{Max} and λ_{Min} are listed together with the spectral norm of the design matrix for the case of 5 and 10 equally distributed depth layers, with $\Delta z = 10\mu m$ and range of the fluorescence spectrum [490 nm, 630 nm].

Values are calculated for the fluorophore HPTS and the absorber Violamine R. The wide range of the singular values also illustrates the bad condition number of the design matrix, here calculated from the more convenient spectral norm instead of the Frobenius norm used by Schwarz [2005] if singular values are already calculated.
The matrix being ill-conditioned will be of importance when choosing a suitable solver algorithm for the inverse problem that is finally to be solved. For moderate cases the condition number in the spectral norm ranges from 1 to 100.

The integral spectrum, the spectrum that can be recorded on top of the water surface, is a linear overlay of all these basis functions in the above derived approximation. If the basis functions were known, the integral spectrum could be decomposed for the individual concentrations $c_b(z_i)$ of the fluorophore component $R^{-3}O^-$, but if and only if the basis functions $\mathfrak{B}(\lambda, z_i)$ form a linear independent subset of $\mathbb{C}^{(N-1)}(-\infty, \infty)$, the space of (N-1) times smoothly differentiable functions (see for example Fischer [2003]) with respect to depth z. Before setting up the model matrix of the problem this has to be tested in the next paragraph.

Testing the functions $\mathfrak{B}(\lambda, z_i)$ to be a Basis of the Vector Space Even if matrix E has full rank, it still has to be tested whether the functions $\mathfrak{B}(\lambda, z_i)$ form a basis of the corresponding vector space, see for example Fischer [2003]. The number of the basis functions is equal to the dimension of the vector space of the basis function and represents the number of depth layers that can be resolved. What has to be shown is the linear independence. This holds if the determinant of the Wronskian-matrix W of the basis function system is not zero, det $W \neq 0$, with

$$\begin{bmatrix} \mathfrak{B}(\lambda_0, z) & \dots & \mathfrak{B}(\lambda_M, z) \\ \vdots & \ddots & \vdots \\ \mathfrak{B}^{(N-1)}(\lambda_0, z) & \dots & \mathfrak{B}^{(N-1)}(\lambda_M, z) \end{bmatrix} =: W. \tag{5.21}$$

For resolving N depth layers at least $M = N$ different wavelengths for independent measurements are needed. For the case $M = N$ it will be tested under which conditions full rank of the matrix W is given and therefore the functions $\mathfrak{B}(\lambda, z_i)$ form a basis of the regarded vector space.

To simplify the calculations, the matrix W is factorized into two sub matrices,

$$W = F_1 \cdot W_2. \tag{5.22}$$

These two matrix are defined as:

$$F_1 := \begin{bmatrix} \mathscr{C} f_b(\lambda_0) \cdot \Delta z_0 & \dots & 0 \\ \vdots & \ddots & \vdots \\ 0 & \dots & \mathscr{C} f_b(\lambda_M) \cdot \Delta z_N \end{bmatrix}, \tag{5.23}$$

and

$$W_2 := \begin{bmatrix} \exp(-\alpha_0 z) & \dots & \exp(-\alpha_N z) \\ (-\alpha_0)\exp(-\alpha_0 z) & \dots & (-\alpha_N)\exp(-\alpha_N z) \\ \vdots & \ddots & \vdots \\ (-\alpha_0)^{(N-1)}\exp(-\alpha_0 z) & \dots & (-\alpha_N)^{(N-1)}\exp(-\alpha_N z) \end{bmatrix}. \tag{5.24}$$

The factors $\mathscr{C} f_b(\lambda) \cdot \Delta z_i$ of the first diagonal submatrix F_1 are non-zero resulting from experimental demands. A diagonal with non-zero main diagonal elements has full rank. So testing of full rank is simplified to the task of testing full rank of the second submatrix W_2.
The important Wronskian-matrix W_2 can be transformed using matrix equivalence steps in

$$W_2 = \begin{bmatrix} 1 & \dots & 1 \\ (-\alpha_0) & \dots & (-\alpha_N) \\ \vdots & \ddots & \vdots \\ (-\alpha_0)^{(N-1)} & \dots & (-\alpha_N)^{(N-1)} \end{bmatrix} \tag{5.25}$$

The last simplification of the matrix W_2 shows that the submatrix W_2 of is equivalent to the transpose of the Vandermonde matrix V. The determinant of the Vandermonde matrix can be calculated to

$$\det(V) = \prod_{1 \le i < j \le N} (\alpha_j - \alpha_i) \tag{5.26}$$

$$= \prod_{1 \le i < j \le N} (\alpha(\lambda_j) - \alpha(\lambda_i)) \tag{5.27}$$

and as $\det A = \det A^T$ this gives also a non-zero determinant of the Wronskian determinant of the system. So it is shown that given $\alpha_j \neq \alpha_i$ and $\alpha_j - \alpha_i \neq 0 \, \forall \, i, j, \, i \neq j$ the Wronskian determinant is non-zero and the system therefore forms a linear base of the vector space as demanded.

In reality, this demands that the absorber dye's absorption coefficient α differs strongly in the regarded wavelength range, so a high gradient in the absorption spectra of the absorber dye- say a peak or dip- is necessary in the emission band of the fluorophore. For more details on the absorber dye see section 5.7.2.

Having ensured that the system forms a basis of the vector space and given that the model can be formulated as a linear problem, solving the inverse problem seems possible. In the next subsection a more detailed analysis is done on the errors of the SPERA method under varying conditions.

5.6.1 Estimation of the Remaining Rest or Error Term

The discretization of the emission-absorption equations has been introduced in the last subsection 5.6. Now this subsection deals with the error of the integral sum when the infinite discretized sum is only calculated up to a certain term $\hat{\imath}$

$$L_{em}(\lambda) = \int_0^{\hat{z}} \frac{\partial L}{\partial z}(\lambda; z)\, dz + \int_{\hat{z}}^{\infty} \frac{\partial L}{\partial z}(\lambda; z)\, dz, \tag{5.28}$$

$$\doteq \sum_{i=0}^{\hat{\imath}} \frac{\Delta L}{\Delta z}(\lambda; z_i)\, \Delta z + \sum_{i=\hat{\imath}}^{\infty} \frac{\Delta L}{\Delta z}(\lambda; z_i)\, \Delta z. \tag{5.29}$$

Now the question remains from which discretized depth z_i with $i = \hat{\imath}$ the rest term can be neglected, or in other words, which depth no longer significantly contributes to the integral spectrum. This is equivalent to the fact that the corresponding depth layer can no longer be resolved.

The usual limit for influence on the result is a proportion of the term of approximately 1 %, with respect to the value of the total sum.
An estimation of the error term is done here for an equal discretization of the depth layers with $\Delta z_i = \Delta z =$ constant and $z_i = i \cdot \Delta z$. Furthermore, a homogeneous distribution of the anion base component c_b of the fluorescent dye is assumed for estimation: $c_b =$ constant. As concentration changes are assumed to be small, this approximation is acceptable for a rough estimation of the error term. All constant terms are collected in the expression $\mathscr{K} := f_b(\lambda) c_b \mathscr{C} \Delta z$. For calculation of the error term the discretized infinite sum is rearranged. Herein the expression $x(\lambda) := \exp(-\varepsilon_A(\lambda) c_A \Delta z)$ is used,

$$L_{em}(z, \lambda) \doteq \sum_{i=0}^{\infty} c_b(z_i) \mathscr{C} f_b(\lambda) \exp(-\varepsilon_A(\lambda) c_A z_i) \Delta z_i \tag{5.30}$$

$$\doteq \mathscr{K} \cdot \sum_{i=0}^{\infty} \exp(-\varepsilon_A(\lambda) c_A \Delta z)^i \tag{5.31}$$

$$\doteq \mathscr{K} \cdot \sum_{i=0}^{\infty} x(\lambda)^i. \tag{5.32}$$

For $|x(\lambda)| < 1 \,\forall\, \lambda$ this infinite series is convergent (see for example Forster [2001]). The assumption is fulfilled as it was one of the demands on fluorescence. The exponential term can be approximated by the constant term described in (5.13). It follows that

$$\sum_{i=0}^{\infty} x(\lambda)^i = \frac{1}{1 - x(\lambda)}. \tag{5.33}$$

Furthermore, for the finite geometric series it is found that

$$\sum_{i=0}^{L} x(\lambda)^i = \frac{1 - x(\lambda)^{L+1}}{1 - x(\lambda)} \quad \forall\, L \in \mathbb{N}. \tag{5.34}$$

With these two equations an estimation of the error or rest term can be made:

$$\sum_{i=0}^{\infty} x(\lambda)^i = \sum_{i=0}^{L-1} x(\lambda)^i + \sum_{i=L}^{\infty} x(\lambda)^i, \tag{5.35}$$

$$\frac{1}{1-x(\lambda)} = \frac{1-x(\lambda)^L}{1-x(\lambda)} + \sum_{i=L}^{\infty} x(\lambda)^i \tag{5.36}$$

$$= \frac{1-x(\lambda)^L}{1-x(\lambda)} + \text{error term.}$$

The error term R in that notation is then defined as

$$R := \sum_{i=L}^{\infty} x(\lambda)^i \tag{5.37}$$

As said above, the error term R should be less than p=1% of the value of the infinite sum, so R can be estimated to

$$R \leq p \cdot \sum_{i=0}^{\infty} x(\lambda)^i, \tag{5.38}$$

$$R \leq p \cdot \frac{1}{1-x(\lambda)}. \tag{5.39}$$

With this substitute and (5.36) and the additional knowledge that $x(\lambda)$ is positive and $|x(\lambda)| < 1$ due to equation 5.13, the following inequality holds, $0 < (1 - x(\lambda)) < 1$, and therefore the following relation can be deduced,

$$p \cdot \frac{1}{1-x(\lambda)} \geq \frac{1}{1-x(\lambda)} - \frac{1-x(\lambda)^L}{1-x(\lambda)} \tag{5.40}$$

$$\Rightarrow p \geq 1 - 1 + x(\lambda)^L \tag{5.41}$$

$$\Rightarrow p \geq x(\lambda)^L \tag{5.42}$$

$$\Rightarrow L \leq \frac{\ln(p)}{\ln(x(\lambda))}. \tag{5.43}$$

Since the absolute value of both p and $x(\lambda)$ is smaller than 1 and both are positive values, the logarithm of both is negative and therefore L is always positive.
With this expression the optimal absorber dye concentration can be estimated, which determines the layer that can still be resolved for a given wavelength λ:

$$x(\lambda) := \exp(-\varepsilon_A(\lambda) c_A \Delta z).$$

What is shown here theoretically, is the description that the absolute intensity is determined by the concentration of the fluorophore, in the case of HPTS the anion base component of the fluorophore, while the absorber dye defines the layer from which any measurable influence on the integral spectrum is lost.

The mean concentration of the anion base component before the acid tracer

gas is added into the wind-tunnel gas phase can be regarded as the upper limit of the concentration of the anion base. The reason for this is that in this work invasion experiments of acid tracer are conducted. Invasion of an acid gas reduces the concentration of the anion base component and therefore intensity.
Analyzing the results of this subsection yields:
With a bit of rearrangement of (5.43), the necessary concentration of the absorber dye can be calculated for a given depth resolution Δz and a given maximum depth z_{max} which should be the last layer to be evaluated, which is done in the following subsection.
Important to note here is that every wavelength has another penetration depth, so every wavelength has a different z_{max} than its neighbors.

5.6.2 Estimation of the Needed Concentration of the Absorber Dye for a Given Spatial Resolution Δz

As said at the end of the last subsection, (5.43) allows to calculate the necessary concentration of the absorber dye c_A^* for a desired depth resolution Δz_{des} and a given maximum depth z_{max}.
The corresponding L can be readily calculated to

$$L_{des} = \frac{z_{max}}{\Delta z_{des}}, \tag{5.44}$$

with the difference that now equality is regarded in (5.43),

$$\begin{aligned} L_{des} &= \frac{\ln(p)}{\ln x(\lambda)} \\ &= \frac{\ln(p)}{\ln \exp(-\varepsilon_A(\lambda) c_A^* \Delta z_{des})} && (5.45) \\ \Rightarrow \ln(p) &= -\varepsilon_A(\lambda) c_A^* \Delta z_{des} \cdot L_{des} && (5.46) \\ \Rightarrow c_A^* &= \frac{\ln(p)}{-\varepsilon_A(\lambda) \Delta z_{des} L_{des}} && (5.47) \\ &= \frac{\ln(p)}{-\varepsilon_A(\lambda) z_{max}}. \end{aligned}$$

The last expression is equivalent to the calculation of a penetration depth after rearrangement with $p \hat{=} E/E_0$, where E/E_0 is the ratio of irradiance in the regarded layer to the incident irradiance:

$$\begin{aligned} z_{max}(\lambda) &= \frac{\ln(p)}{-\varepsilon_A(\lambda) c_A^*} && (5.48) \\ &= \frac{\ln(\frac{E}{E_0})}{-\varepsilon_A(\lambda) c_A^*}. && (5.49) \end{aligned}$$

This is not a surprising result and indicates the correct deduction of the equations above.

5.7 Experimental Aspects

In the present section the experimental aspects of the Spectral Reconstruction Approach will be presented with respect to a practical applicability.

5.7.1 Fluorophore

The fluorophore for SPERA is the same that is used in SP-LIF, named HPTS. Its properties have been discussed in 3.7. Important in the context of SPERA is mainly the normalized fluorescence spectrum of the used fluorophore, that is shown in figure 5.2, together with the wavelength range used for reconstruction to ensure a non-singular diagonal submatrix Z of the design matrix. For more

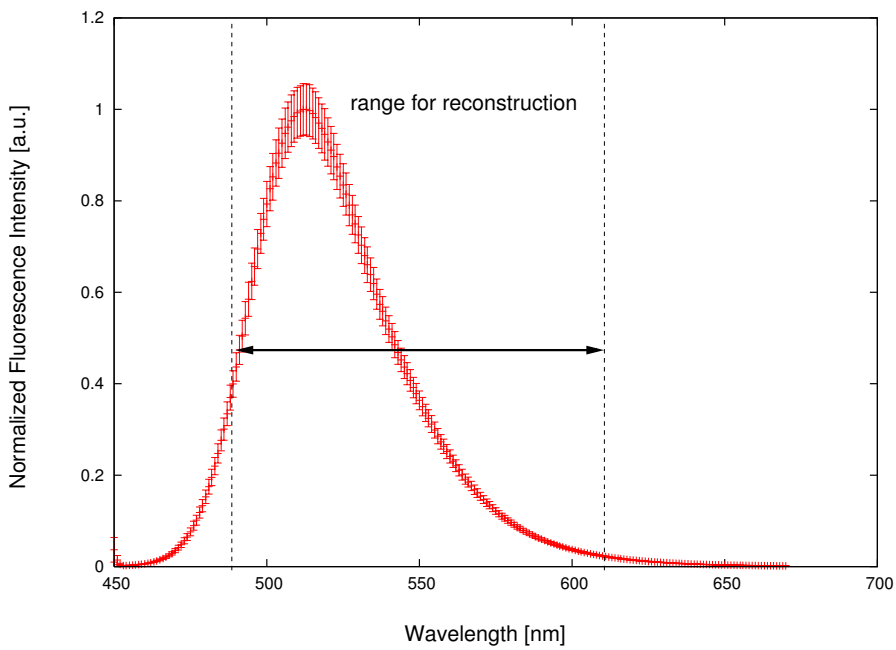

Figure 5.2: Fluorescence Spectrum of the HPTS anion base normalized by maximum intensity. Plotted in black is the wavelength range used for inverse modeling, with the dashed lines marking the limits of the range. The fluorescence spectrum was recorded with a Varian Eclipse fluorescence spectrometer (Temperature 20 $\pm$ 0.2°C).

details on the fluorophore properties see section 3.7.

5.7.2 Absorption Dye

In section 5.4 the theoretical demands on the absorber dye have been presented. In this subsection the way is described how the best matching absorption dye to the fluorophore could be practically identified.

Desired properties of the Absorber Dye

The theoretical demands on the absorber dye can be summarized in the following sentences:

- The **absorption** of the absorber should be **strong in the emission band of the fluorophore**, and should especially have a strong gradient in the extinction coefficient, to ensure non-singularity of the design matrix.
- Additionally, the dye should have a **negligible absorption at the laser wavelength** to ensure validity of assumptions for the simplified model, see (5.6).
- Furthermore, the absorber must be **insensitive to the gaseous tracer**; especially change of the optical properties must not occur.
- Moreover, the absorber must **not interact physio-chemically with the fluorophore and the solvent**: Especially no energy transfer from the excited state of the fluorophore to the absorber due to similar energy levels should be possible, which may lead to quenching of fluorescence. Furthermore, surface activity should be negligible to avoid effects on gas exchange.
- And finally, the absorber dye should also be **insensitive to photobleaching**.

From practical reasons the following desirable properties should also be mentioned

- The dye should be non-toxic for humans.
- The dye should be available as pure substance to avoid time-consuming cleaning procedures.

Beginning with these formulated properties suitable dyes were searched for combined usage with the fluorophore HPTS (emission 500-700 nm, maximum at 513.0 $\pm$ 1.4 nm, see table 3.4 for more details).
The results of this pre-scan are presented in the following table:

Name	CAS	Absorbance Maximum [nm]	Abs. 440-450 nm [a.u.]	Fluorescence	Solubility Water [mg/g]	Solubility Ethanol [mg/g]	Dangers
Chromotrope 2R	4197-07-3	510 (broad peak,∼0.8,c=15.0)	∼ 0.15	n.m.	200	20	n.m.
Eosin Y	548-26-5	514 (peak,∼0.8,c=6.8)	∼ 0.05	Yes	40	10	n.m.
New Fuchsin	3248-91-7	553 (1.0,c=5.1)	0.07-0.1	n.m.	20	20	n.m.
Acid Fuchsin	3244-88-0	545(broad peak,0.6,c=10.2)	0.07-0.1	No	100	1	n.m.
Basic Fuchsin	569-61-9	544(0.8, c=3.1)	0.07-0.1	No	20	50	poisonous
Violamine R	6252-76-2	529 (peak, 0.6, c=9.8)	∼ 0.05	No	100	20	WGK 3

Table 5.2: Absorption and other properties of suitable dyes for combination measurements. Notation: c stands for concentration. the number in front gives the relative absorption. n.m. stands for not mentioned. WGK refers to the German 'Wassergefeährdungsklasse', describing the danger level if the dye is deposited in water; 3 is the highest level.

From these suitable dyes the five most convincing ones were tested for their usage in combination with the fluorophore HPTS. They were: Acid Fuchsin, Eosin Y, Chromotrope 2R, and Violamine R.

Summary of the Results of Test Measurements of Combined HPTS-Absorber Solutions under Laser illumination

The actual experiments with the above chosen dyes were done by Felix Friedl. His results are shown here in brief.

Acid Fuchsin Acid Fuchsin turned out to be strongly sensitive to photobleaching. Within minutes the dye was destroyed under laser illumination.

Eosin Y Eosin strongly absorbs at the desired 514 nm. Yet, the fluorescence of Eosin was very strong, even higher than the fluorescence maximum of HPTS. So energy transfer without radiation emission from HPTS to Eosin seems to occur.

Chromotrope 2R Though the dye absorbs at the desired 514 nm, it absorbs too much of the exciting laser light and is so easily destroyed by laser illumination.

Violamine R/ Violamine A2R Violamine turned out to be the best suitable dye found during this work. Purity of 100 percent is needed as at lower purity the dye is mixed with hardly water soluble substances. One drawback of Violamine R is its relatively high surface activity at higher concentrations, which set an upper limit to the usable dye concentration far below the maximum solubility limit.

The Dye of Choice: Violamine R

Properties of Violamine R Violamine R (CAS 6252-76-2) has a molar weight of 612.64 g/mol and was obtained as pure substance from manufacturer Waldeck GmbH, Division Chroma. Its chemical sum formula is $C_{34}H_{25}N_2NaO_6S$. It is declared as strongly hazardous to organisms living in water (German water hazardous class 3) Violamine R was now tested for its spectral properties, especially its extinction coefficients had to be measured in detail for a successful reconstruction, see the system of equations in section 5.6.

Determination of Extinction Coefficients of Violamine R The method used is described in detail in the appendix, seeB. Here only the results for Violamine R are presented in figure 5.3.

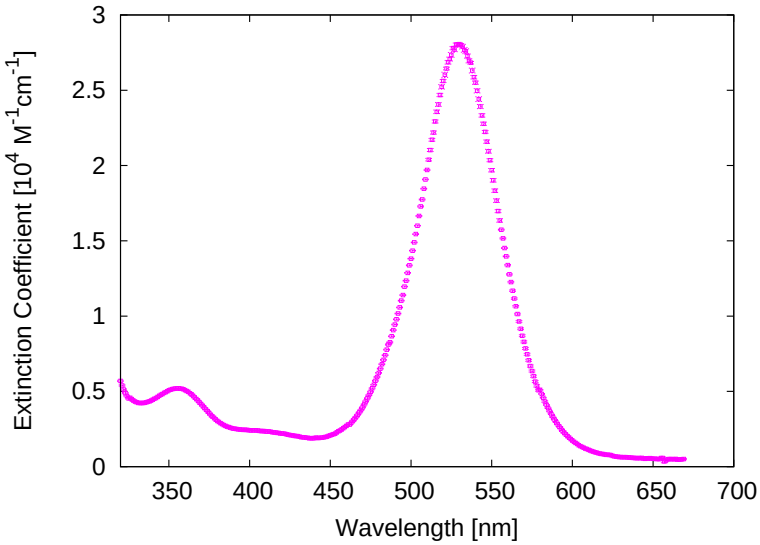

Figure 5.3: Extinction coefficients of Violamine R in the range of 320-700 nm. Measurements taken with an Optical Multichannel Analyzer (OMA) from Hewlett Packard (HP 8453)

The extinction coefficient of Violamine R in the Laser wavelength range is about one order of magnitude below the extinction coefficient of the HPTS anion base:

$$\mathfrak{e}(445\text{nm}) = (0.19 \cdot 10^4 \pm 0.08)\,\text{M}^{-1}\text{cm}^{-1}. \tag{5.50}$$

The extinction coefficient in the HPTS emission band has its maximum at a wavelength of 529 nm according to Sigma Aldrich and 530 nm according to own measurements:

$$\mathfrak{e}(530\text{nm}) = (2.81 \cdot 10^4 \pm 0.02)\,\text{M}^{-1}\text{cm}^{-1}. \tag{5.51}$$

5.7.3 Application of the Theoretical Model on Experiments

Calculation of the Concentration of the Used Absorber Violamine R

As the water-sided mass boundary layer z^* has a thickness of $10 - 100$ μm depending on the wind speed as described in section 2.4.1, a desired resolution would be $\Delta z = 1\mu$m with a z_{max} of 100μm.
The needed concentration of Violamine R for this desired maximum depth equation 5.47 can be calculated as:

$$c_A^* = \frac{\ln(p)}{-\varepsilon_A(\lambda) z_{max}} \tag{5.52}$$

$$= \frac{-\ln(0.01)}{2.81 \cdot 10^4 \cdot \ln(10)\ 100 \cdot 10^{-4}}\,\text{M} \tag{5.53}$$

$$\approx 7.12 \cdot 10^{-3}\,\text{M} \tag{5.54}$$

This value exceeds the maximum solubility of Violamine R in water with 100 mg/g $\widehat{=} 0.16 \cdot 10^{-3}$M/g by a factor of approximately 44, which explicitly shows that a resolution of the mass boundary layer under high wind speeds cannot be achieved with this absorber dye and the desired precision. With this dye only thick layers can be resolved, for example encountered in thermal convection. For the thin mass boundary layers an alternative dye has not been found so far.

5.7.4 Test Measurements: Combination of Fluorophore and Absorption Dye

Although, the concentration of the absorber dye needed to measure in the mass boundary layer exceeds the dye's solubility limit, test measurements can be performed if layers in the mm-range are to be explored. In figures 5.4 and 5.5 individual layer spectra are plotted as well as the integral fluorescence intensity measured above the water surface. The concentration of the absorber dye was arbitrary, but adjusted for visible contrast in the individual depth-layer spectra. The signal intensity achieved by the available spectrometer was very low so that a new camera-spectrometer as plotted in figure 5.1 had to be built for a better signal to noise ratio. Due to that, it was not possible to make measurements with varying depth-dependent concentrations, as they changed too fast in the test section for the spectrometer to follow without averaging them away. Ground truth of the concentration profiles was gained by parallel P-LIF measurements of the illuminated area.

These measurements, however, gave hints about the statistical distribution of noise. Even in the high averaged images of the spectra, noise was dependent on intensity, as can be seen in for example in figure 5.2. The noise distribution influences the choice of the best-suited estimator for the inverse problem. This is discussed in more detail in the section 5.8.1.

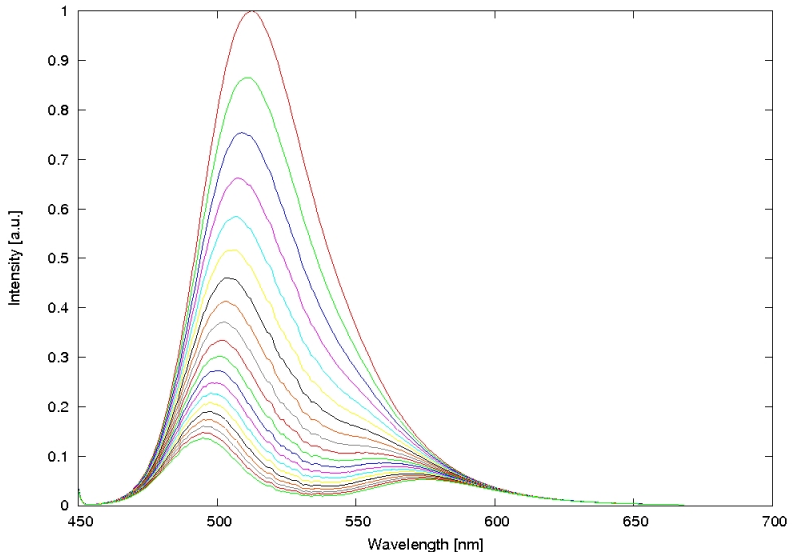

Figure 5.4: Fluorescence Spectrum of the HPTS anion base altered by the absorber dye Violamine R dependent on depth of the excitation light source in the water for 19 individual depth layers. The maximum intensity measured by illumination directly at the water interface is set to one, all other intensities are measured relative to this value. Measurements done by F. Friedl.

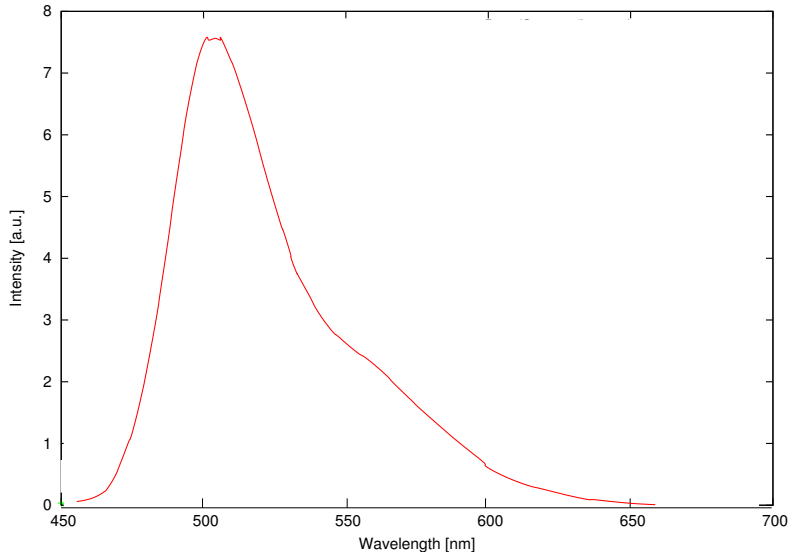

Figure 5.5: Averaged integral fluorescence intensity of HPTS-Violamine R combination measured above the water surface by illumination with a single Laser beam. Measurements done by F. Friedl.

5.8 Parameter Estimation Techniques

In this section the corresponding optimization problem to determine the desired depth-dependent concentration c_i is described as:

$$\min_{c_i} \qquad \left|\left| [1/\sigma] \left(L_{em}^{model}(\lambda, c) \; - \; L_{em}^{meas}(\lambda) \right) \right|\right|_p$$

subject to the following boundary conditions:

- $\left.\frac{\partial c}{\partial z}\right|_{c=0} = \frac{\mathbf{j_{diffusion}}}{\mathcal{D}}$
- c_{gas}^{bulk} =const.

One important aspect of the optimization problem however has not been investigated yet: the statistical distribution that describes the data distribution. Knowledge of the statistical distribution allows a more suitable choice of the optimization routine to estimate the desired parameters.
Here, a high spatio-temporal resolution is requested. Due to that each state is described by only one measured spectrum or one single data set. This is in contrast to many spectroscopy applications where stacks of one hundred and more spectra are at hand for the same situation. As Jähne [2005] states in his book 'Image processing" the variation of the mean decreases with $1/\sqrt{N}$, where N is the number of images over which is averaged. So already averaging over only 16 images decrease the error by a factor of 4, making the assumption of a Gaussian statistic more realistic. If only one spectroscopic image is to be evaluated, a heavy-tailed statistic cannot be improved by averaging and the basic statistics remains unchanged. In Least-Squares estimators a Gaussian distribution is assumed for the errors of measurement values. However, there are estimators available that support other error distributions with heavier tails. One of this class are the robust estimators defined by Huber [1981], who define robustness as 'insensitivity to small deviations from the assumptions', here a normal distribution of errors. They can handle outliers due to heavier tails. Though their robustness to outliers they are widely unknown by users and software is only rarely found. Here MATLAB 2009 offers with the routine 'robustfit' now a commercially available package. and finished "while long-tailed data appear to be far more typical than most researchers would like to believe.".

5.8.1 Statistics of LIF-Signals

Fluorescence spectral data is assumed to be Poisson distributed. The analysis of Dimarcq et al. [1994] showed that the actual distribution in LIF-signals is an overlay of the statistics of all processes involved in the LIF-technique:

- the statistical fluctuations of the Laser illumination,
- the statistics of fluorescence emission, and
- the statistics associated with the detector sensor system.

Own measurements, see figure 5.2, supported this assumptions. Here, even after averaging the variance of the measured value depends on the absolute measured value and is not independent. This behavior seems to be a result of the Poisson-characteristic of fluorescence.
Without statistical analysis of the signals themselves the most suitable distribution could not be chosen. For this reason, two distributions with heavy tails were randomly chosen, a Gamma distribution and a log-normal distribution.

5.8.2 Numerical Simulation

To account for the lack of experimental data, artificial data sets were created using the theoretical model presented in section 5.4. The noise distributions are most probably be heavy-tailed non-Gaussian distributions, as shown in the previous subsection. Three numerical simulations have been conducted with:

1. a concentration profile consisting of three depth layers and a decreasing concentration in the mass boundary layer

2. a concentration profile consisting of three depth layers and a increasing concentration in the mass boundary layer

3. a concentration profile consisting of five depth layers and a decreasing concentration in the mass boundary layer

Since concentration profiles in the boundary layer are regarded, the assumed profiles follow a linear relationship, concentration per layer is set constant.
The fluorophore concentration was $c_F = 2 \cdot 10^{-5}$ M and the absorber dye concentration was chosen to be $1.71 \cdot 10^{-4}$ M, maximum depth $z_{max} = 0.1\,\mathrm{mm}$.

Case I: Invasion and three depth layers The first simulation contained the following depth-dependent concentrations:

$$z(0.0\,\mathrm{mm}) = 10^{-5}\mathrm{M}, \tag{5.55}$$
$$z(0.05\,\mathrm{mm}) = 0.5 \cdot 10^{-5}\mathrm{M}, \tag{5.56}$$
$$z(0.1\,\mathrm{mm}) = 10^{-7}\mathrm{M}. \tag{5.57}$$

Case II: Evasion and three depth layers The second simulation contained the following depth dependent concentrations:

$$z(0.0\,\mathrm{mm}) = 10^{-7}\mathrm{M}, \tag{5.58}$$
$$z(0.05\,\mathrm{mm}) = 0.5 \cdot 10^{-5}\mathrm{M}, \tag{5.59}$$
$$z(0.1\,\mathrm{mm}) = 10^{-5}\mathrm{M}. \tag{5.60}$$

Case III: Invasion and five depth layers The simulation contained the following depth dependent concentrations:

$$
\begin{aligned}
z(0.0\,\mathrm{mm}) &= 10^{-5}\mathrm{M}, && (5.61)\\
z(0.025\,\mathrm{mm}) &= 7.5\cdot 10^{-6}\mathrm{M}, && (5.62)\\
z(0.05\,\mathrm{mm}) &= 5.0\cdot 10^{-6}\mathrm{M}, && (5.63)\\
z(0.075\,\mathrm{mm}) &= 2.5\cdot 10^{-6}\mathrm{M}, && (5.64)\\
z(0.1\,\mathrm{mm}) &= 10^{-7}\mathrm{M}. && (5.65)
\end{aligned}
$$

Chosen Statistical Distribution for Noise in Data

The error functions used were a Gamma distribution and a log-normal distribution. With these choices the error on the measurement data could rise up to the same order of magnitude as the measurement value itself. The distributions are defined by their probability density functions:

Gamma Distribution

$$
\begin{aligned}
\mathrm{pdf}_{\Gamma}(p) &= \frac{\theta^p\, x^{p-1}\, e^{-\theta\, x}}{\Gamma(p)} \quad \forall\, x \geq 0, && (5.66)\\
\Gamma(p) &= \int_0^\infty u^{p-1} e^{-u} du \quad \forall\, p > 0, && (5.67)\\
&\text{with } \theta\, =\, 1\,,\, p\, =\, \text{measured value}, && (5.68)
\end{aligned}
$$

Log-normal Distribution

$$
\begin{aligned}
\mathrm{pdf}_{LN}(p) &= \frac{1}{\sqrt{2\pi\sigma^2\, x^2}} e^{\frac{(\ln(x)-\mu)^2}{2\sigma^2}} \quad \forall\, x\, <\, \infty, && (5.69)\\
&\text{with } \sigma\, =\, 1 \;\; \mu 2 = \text{measured value}, && (5.70)
\end{aligned}
$$

5.8.3 Robust Estimator Used for Simulations

In this subsection the basics of robust estimators are briefly reviewed including the routines that are actually used in estimating the parameters of the simulations, the routines of available in MATLAB *robustfit* (Version 2009A and later). For more details on the estimator see Binder et al. [2010].

Here, the standard regression model $y = X\beta + \varepsilon$ is regarded, with β as the parameters to estimate and ε as the noise. $y - X\beta = \varepsilon$ is the function that is to be minimized. A robust estimator for the location parameter $\hat{\beta}$ is given here by

$$
\min_{\beta} \sum_{i=1}^{n} \rho\left(\frac{y_i - x_i\beta}{\sigma}\right), \tag{5.71}
$$

where x_i denotes the i-th row of the matrix X and ρ is a robust loss function while the factor σ is a scaling parameter.

By defining $\psi = \frac{\partial \rho}{\partial \beta}$, a necessary condition for β to be a minimizer of (5.71) can be formulated as

$$\sum_{i=1}^{n} x_{ij} \psi \left(\frac{y_i - x_i \beta}{\sigma} \right) = 0 \quad \text{for all } j. \tag{5.72}$$

Now $w(r)$ is defined as a weight function $w(r) := \psi(r)/r$. The notation $\mathrm{diag}(v)$ is used for a diagonal matrix with entries from the vector v. Let the initial value $\hat{\beta}_0$ be given. Then the iteration scheme for reweighed least squares, as promoted by Beaton and Tukey [1974], is written as

$$\hat{\beta}_{i+1} = \hat{\beta}_i + \left[X^T \mathrm{diag} \left(w(\frac{y - X\hat{\beta}}{\sigma}) \right) X \right] X^T \mathrm{diag} \left(w(\frac{y - X\hat{\beta}_i}{\sigma}) \right) (y - X\hat{\beta}_i). \tag{5.73}$$

It must be emphasized that for non-convex functions ρ there is no guarantee that the method will converge. This is one reason why a good starting value is important. Holland and Welsch [1977] recommend the use of the least absolute residuals (LAR) estimator $\hat{\beta}_L$ which minimizes $\sum_{i=1}^{n} |y_i - x_i\beta|$. Algorithms for its computation are described, e.g., by Barrodale and Roberts [1973] and Bartels et al. [1978].

For the Huber estimator, which is defined via the so-called Huber function Huber [1981]

$$\rho_\gamma(r) = \begin{cases} \frac{1}{2} r^2 \,, & |r| \leq \gamma, \\ \gamma |r| - \frac{1}{2}\gamma^2 \,, & |r| > \gamma, \end{cases} \tag{5.74}$$

the tuning constant γ relates to the expected ratio of errors in the measurement data. A value of 1.345 corresponds to an asymptotic efficiency of 95% in case of Gaussian errors. The Huber estimator can be written equivalently as a combination of least squares and LAR estimators. The scaling parameter σ is estimated once before the actual iterations are started by the equation

$$\sigma = 1.48 \left(\operatorname*{med}_i |(y_i - x_i\hat{\beta}_0) - \operatorname*{med}_i (y_i - x_i\hat{\beta}_0)| \right). \tag{5.75}$$

The factor 1.48 is included to achieve an almost unbiased estimator of scale in case of a Gaussian error model.

5.9 Results of the Numerical Simulations in Spectral Reconstruction Approach

Results of the numerical simulations are summarized in table 5.3. This results in a total of six different data sets, one for each combination of concentration profiles and error distributions.

The results of the parameter estimations with Huber's M-estimator and least squares are summarized in table 5.3.

The reconstruction results of Huber estimator in the case of three depth layers (four test cases) correspond well to the true values. Three out of four parameter sets could be estimated and matched the true values on which simulations were based. Least-Squares estimates failed to reconstruct the true data in three out of four test cases.
Both estimators had difficulties in reconstruction of the two five-layer test cases. Least squares could not find one single parameter, while Huber managed to estimate at least the concentration at the surface.

Comparison of estimators for simulated data with errors from gamma distribution.						
Profile	Estimator	c_0	c_1	c_2	c_3	c_4
(I)	true values	10^{-5}	$5.0 \cdot 10^{-6}$	10^{-7}	—	—
	Huber	1.000014 10^{-5}	4.999718 10^{-6}	1.001047 10^{-7}	—	—
	LS	-8.824528 10^{-4}	2.515347 10^{-3}	-1.717656 10^{-3}	—	—
(II)	true values	10^{-7}	$5.0 \cdot 10^{-6}$	10^{-5}	—	—
	Huber	1.000459 10^{-7}	5.000034 10^{-6}	9.999845 10^{-6}	—	—
	LS	7.716606 10^{-4}	-1.994890 10^{-3}	1.282866 10^{-3}	—	—
(III)	true values	10^{-5}	$7.5 \cdot 10^{-6}$	$5.0 \cdot 10^{-6}$	$2.5 \cdot 10^{-6}$	10^{-6}
	Huber	1.019416 10^{-5}	6.637964 10^{-6}	6.426011 10^{-6}	1.458348 10^{-6}	3.834845 10^{-7}
	LS	4.414422 10^{-1}	-2.112778	3.774575	-2.983306	8.802230 10^{-1}
Comparison of estimators for simulated data with errors from log-normal distribution.						
Profile	Estimator	c_0	c_1	c_2	c_3	c_4
(I)	true values	10^{-5}	$5.0 \cdot 10^{-6}$	10^{-7}	—	—
	Huber	6.083482 10^{-6}	6.640487 10^{-6}	-1.784732 10^{-7}	—	—
	LS	5.895890 10^{-5}	-1.601342 10^{-4}	1.236267 10^{-4}	—	—
(II)	true values	10^{-7}	$5.0 \cdot 10^{-6}$	10^{-5}	—	—
	Huber	9.940238 10^{-8}	5.001823 10^{-6}	9.998663 10^{-6}	—	—
	LS	1.011999 10^{-7}	5.014798 10^{-6}	9.980614 10^{-6}	—	—
(III)	true values	10^{-5}	$7.5 \cdot 10^{-6}$	$5.0 \cdot 10^{-6}$	$2.5 \cdot 10^{-6}$	10^{-6}
	Huber	9.195819 10^{-6}	1.104140 10^{-5}	-8.236337 10^{-7}	6.736898 10^{-6}	-1.050264 10^{-6}
	LS	-2.581611 10^{-3}	1.190665 10^{-2}	-2.041525 10^{-2}	1.552465 10^{-2}	-4.409180 10^{-3}

Table 5.3: Comparison of estimators for simulated data sets.

5.10 Summary

In this study the usability of the Spectral Reconstruction Approach (SPERA), should be evaluated by numerical test experiments simulating the expected error distributions. As the simulated data sets showed, the robust estimators delivered reliable estimates of the initial parameters even under conditions with heavy tailed noise distributions, that set the limit for the wide-spread least squares estimators. The feasibility of the Spectral Reconstruction Approach could therefore be demonstrated in combination with the robust Huber estimator.
Given a suitable fluorophore absorber combination, that does not affect transport, the Spectral Reconstruction Approach delivers reliable estimates of water-sided gas concentration fields in the mass boundary layer.With SPERA a simplified tomographic approach is presented that allows to resolve gas concentrations in more than one single depth layer. Furthermore, SPERA offers arbitrary orientation of the 2D measurement plane for determining water-sided gas concentration profiles. Therefore the technique allows the study of mass transport phenomena in all directions including spanwise direction with respect to main flow. In that way detailed near surface studies of spanwise structures like Langmuir circulations or structures like thermal convection cells seem to come into grasp of experiments for the first time.

Yet, it has to be emphasized again that SPERA so far cannot be used for visualization of concentration fields in the thin boundary layers as the best suited absorber found so far cannot be used in the high concentrations as would be necessary due to its solubility limit. As could be shown, also the dye best suited for these kinds of measurements could not fulfill the demands of the technique for measuring in the extremely thin mass boundary layer under wind-induced turbulence. The fluorophore-absorber dye pair HPTS and Violamine R is just suited for measurements in the mm-range. However, if a better suited pair is found, measurements under wind-induced turbulence are possible.

These experimental aspects are independent of the question whether the inverse problem that has been set up can be solved not only in theory without noise but also under heavy-tailed noise distributions as they were encountered in the test experiments. Numerical simulations of different scenarios were tested in the following section to test the estimators on the SPERA problem without available measurement data sets.

Therefore, the main problem of SPERA is not solving the inverse problem, as demonstrated above, but the physical realization in experiments, especially as emphasized before - the absorber fluorophore combination. Until such a suitable pair is found the Spectral Reconstruction Approach can only be used under conditions of thick mass boundary layers in the mm-range. These conditions can be encountered in the case of natural convection. Therefore, it is planned to use SPERA in a thermal convection tank.

Chapter 6

Novel Extension for Waves: Static Pattern-LIF (SP-LIF)

The Static-Pattern LIF technique is an extension of the classic LIF technique in gas transfer studies that provides information on the local surface slope. With at least an estimate of the local slope, the water surface topology can be identified more robust with a doubled amount of information compared to normal LIF-setups, where the water surface is typically searched for by symmetry filtering, i.e. Münsterer and Jähne [1998] or Herlina and Jirka [2008]. It can therefore be used even under a strongly-wave distorted surface condition.

6.1 Review of Other Approaches for Measuring Concentration Profiles under Wave-Influence Surface Conditions

The novel SP-LIF technique has to compete with several other techniques used for measurements of gas transfer under a wave-influenced surface.
In the following paragraphs these techniques will be presented with respect to their capabilities compared to SP-LIF.

Surface Characteristics Most conventional approaches for surface identification in LIF-images without background pattern try to find the surface using the characteristics of the water surface in invasion experiments: First, in invasion experiments the water surface can be assumed to be the location with the highest gas concentration, at least in average. In invasion experiments with an acidic gaseous tracer in the pH-method the water surface will usually appear as a local minimum in gray value. Second, due to the total reflection at the water surface, the position of the water surface in a LIF-image can be assumed to be a point of highest local symmetry. Examples for this technique are the works of Münsterer and Jähne [1998], Falkenroth [2007] and Herlina and Jirka

[2008]. Third, the water surface shows a tendency to be a horizontal structure. A derivative calculated along the perpendicular line should give a hint on the position of the water surface.
Yet, these characteristics do not suffice to identify the water surface. On the one hand, the topology of the waves at higher wind speeds becomes to complex and the image of the total reflection is strongly distorted that a symmetry cannot be found. On the other hand, under higher turbulence level the mass boundary layer becomes so thin and all dissolved gas is sometimes almost completely transported to the bulk, that the surface is no longer a local minimum in gray value.
So especially under wavy condition these simple characteristics fail.

Suppression of Waves by Surfactant One method to deal with lens effects in a LIF setup with top illumination is to avoid strong surface distortion by suppressing wave formation. Münsterer and Jähne [1998] and Falkenroth [2007] used a surfactant for higher wind speeds. Both determined mean concentration profiles. This is a credit to the measurement technique, as it allows to examine a wider range of conditions, but does not solve the actual scientific task to obtain measurements under a wave-influenced water surface.

Bottom Illumination To avoid lens effects authors like Duke and Hanratty [1995] and Walker and Peirson [2008] illuminated the water surface in a bottom setup for their LIF-measurements - the light sheet illuminates the water probe from the bottom of the flume. For detailed discussion on the illumination setup geometry, see 8.1.2. This is a reasonable approach, as long as the intensity at the surface is high enough. The image processing for extraction of the concentration information seems to be easier as no background pattern has to be removed. However, the water surface has to be detected here, too. Usually, also the characteristics of the water surface as described above are used. Furthermore, total reflection at the water occurs frequently as light is passing from optical dense medium water to optical thin medium air.

Wave Follower Walker and Peirson [2008] used a wave follower to measure transfer velocities with a LIF technique (bottom illumination) at different positions of large gravity waves. Unfortunately, the authors did not mention capillary wave trains or their effect on the sheet. Capillary wave trains riding on the larger waves may be a problem for the wave follower, they might not be individually studied but appear as parts of the larger waves they ride on. Gas transfer combined to such small scale phenomena may therefore be very hard to measure directly.

Summary The general problem of all methods presented before is a bad estimate of the surface and therefore poor knowledge of the local coordinate system attached to it. This leads to wrong estimates of depth-dependent gas concentrations. What is needed is more information on the water surface position especially under waves. The here presented SP-LIF approach allows to study

water-sided gas concentration fields under strong wavy conditions and even under passing capillary wave trains.

6.2 Main Idea of SP-LIF: Discretization of Illumination

The main idea that stands behind the Static-Pattern LIF technique is a discretization of the illuminating light sheet:

A light sheet illuminates the water probe from above in a top setup. In that way it is effected by surface distortion due to waves. In a homogeneous sheet these lens effects are hard to detect if they are overlaid by a decrease of local intensity due to invasion of the tracer gas.

The situation is different, if a single ray is regarded:
A single light ray is bend at the water surface according to the law of refraction. If the thickness of the ray is small enough, which means smaller than the wavelength of the smallest water waves but at least an order of magnitude above the optical resolution of the camera, the form of the ray will be not strongly influenced by lens effects and can be detected by the camera.
The orientation of the diffracted ray is given by the local slope at the surface.

Now, the homogeneous illumination is replaced by a discretized, in more detail by an array of individual rays. This discretized light source allows a suitable approximation of the water surface, based on two characterizing properties of the illumination:
First, an illumination by several light rays with a distance of at least the thickness of the individual rays should create a discretized sheet, in which the orientation of the individual rays is an index of the local wave slope. The rays should lie dense enough to allow a reliable interpolation of the gas concentration between the illuminating rays.
If convergence effects occur due to waves the rays will also converge, sometimes even cross each other, but they will still be individually recognizable. And the orientation of each ray remains the result of the diffraction of each ray at individual positions and individual slopes of the surface. So a discretized knowledge of the surface orientation can be gained. Values in between can be interpolated.
Second, if the incoming angle of the beams is tilted by a certain angle with respect to the perpendicular line, further information on the water surface can be gained: the position of the water surface at the individual beams. The original beam and its total reflection are in that way slightly tilted. So the intersection of both lines marks the position of the water surface - especially at a flat water surface, where it would not possible to detect the surface without a tilted illumination. That bend gets even more pronounced when waves are present, see figure 6.1. So the discretized light sheet gives a significant improve in information especially under the presence of waves - not only an estimate of the surface

position with the bend even if no concentration signal is present but also an estimate of the surface orientation by the refraction of the individual beams. If the orientation angle of the structure γ is known, the surface slope m_s can be determined by and basic consideration of optical refraction. However, the local orientation estimation is not free of noise and so also the surface slope is affected by noise. But the local orientation estimation gives a significant increase - in best case a doubling - in information as it gives an approximation of the first derivative of the surface.

If the position of the surface is known by conventional symmetry methods at least at one point of the image, the information given by the surface slope allows to set up a piecewise linear interpolation of the surface function. This piecewise linear interpolation is a first estimate of the surface and can be used as start point for a spline interpolation to be fitted to the surface.

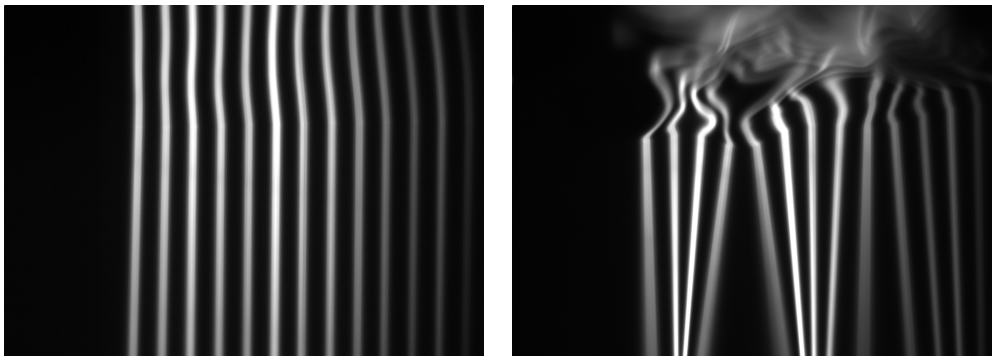

(a) (b)

Figure 6.1: Static-Pattern LIF tested in illumination by 13 individual Laser beams of 1 mm thickness: (a) Discretized sheet at a flat interface and (b) at a wave-influence surface with a mean wind speed of 8 m/s and a fetch of 2.1 m

To refine this still rather coarse illumination grid, a multi-beam splitter should offer a finer discretization. In the search for that a solid state Laser (Nano-250-445-450, manufacturer RGB Lasersysteme GmbH) was found that produces a static pattern when the beam is widened to a sheet by a concave mirror. The pattern is an intrinsic property of the solid-state Laser used. The angle of the stripes with respect to the perpendicular line horizontally varies between 8-1 degrees from left to right and has to be determined separately. For details on the Laser see 8.1.1.

An image of that pattern can be seen in figure 6.2(a). This pattern shows structures over a range of several orders of magnitude in size ranging from a Gaussian like structure the size of the image width to structures the size of 10 pixel in width, that appear as fine vertical stripes in figure 6.2(a). Figure 6.1(b) shows an image of transport of dissolved gas from the surface towards the bulk taken by the SP-LIF setup. The procedure to extract the local wave slope theoretically from the local orientation of the pattern - or in other words

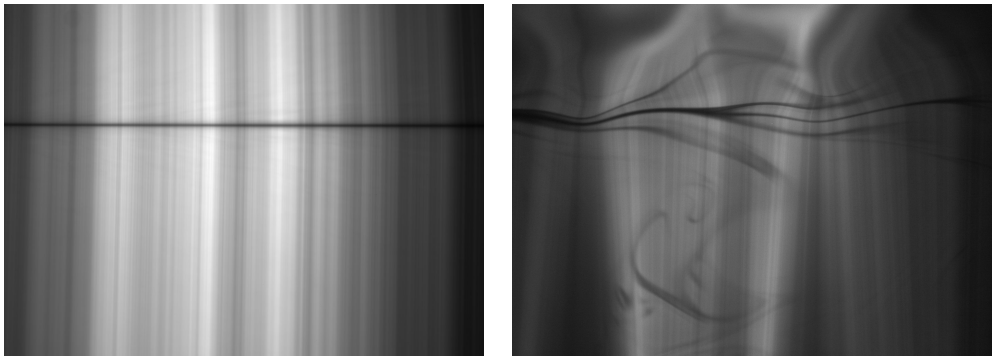

(a) Static pattern at flat interface.

(b) Distortion of static pattern of the Laser sheet by passing wave

Figure 6.2: (a) Static pattern in the local gray values of the Laser sheet; image taken at a flat water surface. (b) Static pattern of the Laser sheet distorted by a passing wave. The dark eddies overlay the pattern and mark locations of higher dissolved concentration of HCl or lower concentration of $R^{-3}O^{-}$, respectively.

the orientation of the vertical stripes - is described in the following section. The first main task in image analysis consists of separating the two signal of pattern orientation and structure of dissolved gas.

In the next section the basic ideas of the image processing routines are presented that allow the separation of both pattern and concentration signal.

6.3 Separating Pattern and Concentration Signal: Basic Ideas of Image Processing

To gain depth dependent gas concentration from an SP-LIF images, the local orientation of the pattern has to be separated from the intensity variations due to varying dissolved gas concentration first (these variations appear as dark eddy structures in the images). This is done in a five step procedure, which is sketched in figure 6.3 and described in the following subsections. Here, only basic concepts are presented while the details of the image processing procedures are described in chapter 9.

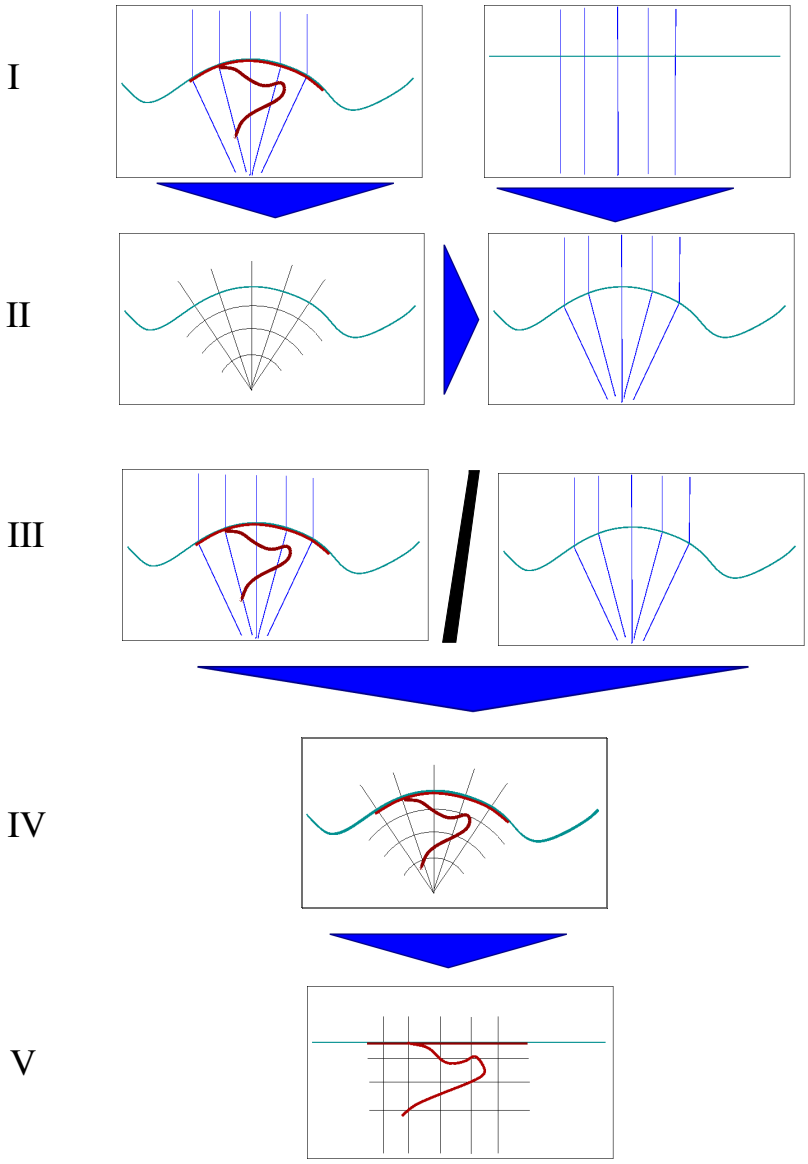

Figure 6.3: Steps of concentration field extraction by image analysis required in Static-Pattern LIF. Red: concentration signal; Lightblue: water surface; Black: local coordinate system Blue: Laser illumination.

Step I: Measurement Values Image and Background Pattern

The actual measurement value, the image showing a snapshot of the tracer concentration field, includes the wave-deformed background pattern. The signal of the background pattern can be measured separately at a flat surface without any disturbances by the overlaid signal of dissolved tracer. Furthermore, this pure pattern signal contains also the Lambert-Beer decay of fluorescence intensity with depth. The images of the background pattern are taken before the start of a measurement series. With an undisturbed background pattern, one of the two signals is known.

Step II: Orientation Extraction and Surface Detection

From the measured SP-LIF image the orientation of the background pattern and the orientation of the surface is extracted. With this knowledge, the ideal background pattern gained in step I can be warped in the pattern produced by the current surface function. The warped ideal background pattern does not contain the eddy structure of dissolved tracer gas, it represents then the pure information of the background signal in the measurement image.

Step III: Removing the Background Pattern

In step III the measured image is divided by the warped background signal gained in step II. In this step the pattern signal including Lambert-Beer decay is removed from the image.

Step IV: Pattern-free Concentration Fields

In step IV the post-processed image contains now only the signal of local dissolved gas concentrations. But the image is still distorted by the influence of the passing waves.

Step V: Transformation on Cartesian Mesh for Concentration Field Analysis

Here the information on the surface topology is used for warping the pure concentration signal image gained in step IV to a Cartesian mesh, see figure 6.4. The warped concentration image contains the actual measurements, the depth-dependent concentrations of the dissolved tracer. All analyzing of concentration fields can now be done on these images.

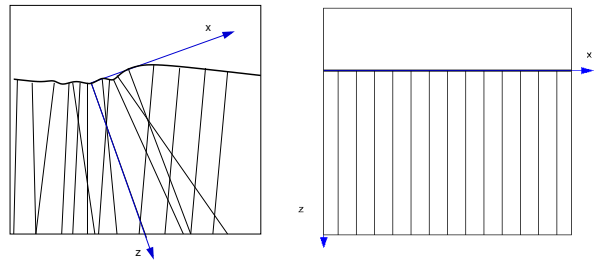

Figure 6.4: Fifth step of image processing: Warping of the surface-dependent local measurement mesh in the left image (a) to the global Cartesian mesh for calculation in the right image (b).

In the following section the trigonometric relations will be given that allow to reconstruct the surface orientation from the extracted pattern signal.

6.4 Surface Topology from Refraction of the Static Laser-Pattern

In this section the theoretical fundamentals from elementary optics are presented that allow to determine the local wave slope from the angle of the refracted individual beams of the background pattern and vice versa. The inverse relation is needed for warping the ideal background pattern into the form of the wave distorted image, see step II.

6.4.1 Surface Orientation from Refraction Angle

In this subsection the surface orientation or slope m_s at a single point is to be calculated from the refraction angle of the incoming beam γ_s. So a function of the form $m_s = m_s(\gamma)$ is needed. In the case of the static Laser pattern, the angles of the incoming pattern beams vary with position between 1-8 °with respect to the perpendicular line, see figure 6.2(a), for an easier detection of the water surface even under flat surface conditions. This has to be regarded in calculating the surface orientation. A sketch of the refraction of an incoming beam at an air-water interface is plotted in figure 6.5.

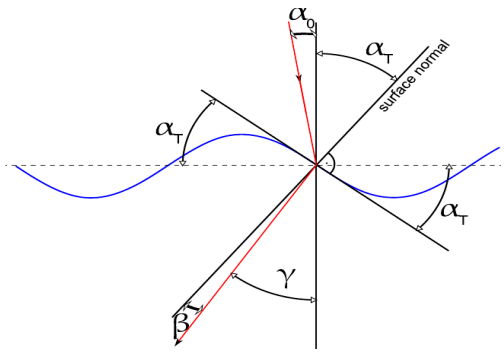

Figure 6.5: Refraction of a light ray at an undulated water surface; Graphic adapted and extended from Jähne [1994]

The notation in figure 6.5 is as follows:

α:	Angle of incoming beam with respect to the surface normal
α_0:	Air-sided angle of incoming beam with respect to the perpendicular line
α_T:	Angle between the perpendicular line and the surface normal
β :	Angle of refracted beam with respect to the surface normal
γ:	Angle of refracted beam with respect to the perpendicular line

Geometric considerations yield the following relations among the six angles:

$$\alpha = \alpha_0 + \alpha_T \tag{6.1}$$

$$\alpha_T = \gamma + \beta \tag{6.2}$$

Air-sided angle of incoming beam α_0 is a constant dependent on position, as it is determined by the sheet pattern. Its value has to be gained experimentally. The local slope m_s of the surface can then be calculated by:

$$m_s = \tan(\alpha_T) \tag{6.3}$$

Now a relation is needed that links α_T to α_0 and γ. Snellius' Law of Refraction states that:

$$n_a \sin(\alpha) = n_w \sin(\beta) \tag{6.4}$$

Here, $n_a = n_a(\lambda_L)$ stands for the refraction index at the Laser wavelength in air and $n_w = n_w(\lambda_L)$ the refraction index of the Laser wavelength in water, while α and β are the corresponding angles.
Together with the geometric relations shown above Snellius' law can be rearranged to achieve a relation to calculate the surface slope dependency on the

angle of the structure in water:

$$\frac{n_w}{n_a} = \frac{\sin(\alpha)}{\sin(\beta)} \tag{6.5}$$

$$\Leftrightarrow \frac{n_w}{n_a} = \frac{\sin(\alpha_T + \alpha_0)}{\sin(\alpha_T - \gamma)} \tag{6.6}$$

$$\Leftrightarrow \frac{n_w}{n_a} = \frac{\sin(\alpha_T)\cos(\alpha_0) + \cos(\alpha_T)\sin(\alpha_0)}{\sin(\alpha_T)\cos(\gamma) - \cos(\alpha_T)\sin(\gamma)} \tag{6.7}$$

$$\Leftrightarrow \sin(\alpha_T)\cos(\gamma) - \cos(\alpha_T)\sin(\gamma) = \frac{n_a}{n_w}\left(\sin(\alpha_T)\cos(\alpha_0) + \cos(\alpha_T)\sin(\alpha_0)\right)$$

$$\Leftrightarrow \tan(\alpha_t)\cos(\gamma) - \sin(\gamma) = \frac{n_a}{n_w}\left(\tan(\alpha_T)\cos(\alpha_0) + \sin(\alpha_0)\right) \tag{6.8}$$

$$\Longrightarrow \tan(\alpha_T) = \frac{\frac{n_a}{n_w}\sin(\alpha_0) + \sin(\gamma)}{\cos(\gamma) - \frac{n_a}{n_w}\cos(\alpha_0)} \tag{6.9}$$

The relation presented above is a generalization of the relation between local wave slope and refracted beam deduced by Lange et al. [1982] that is used for example for wave slope calculations of the imaging slope gauge, Rocholz [2008]. In contrast to their relation, here an arbitrary angle of the incoming beam α_0 with respect to the perpendicular line can be used.

The orientation of an individual pattern line is then given by:

$$y = \tan(\gamma) \cdot x + y_0^g \tag{6.10}$$

$$0 = \cos(\gamma)y - \sin(\gamma)x - \cos(\gamma)y_0^g \tag{6.11}$$

with $y_0^g = y_c + \tan(\gamma)x_c$. (x_c, y_c) is the pixel position at which γ has been calculated. (x,y) are points on the line. This line gives the direction of the local orientation of the pattern. The orientation of the z-axes of the local coordinated system attached to the water surface is given by the sum $\gamma + \beta = \alpha_T$.
The corresponding line is then given by

$$0 = \cos(\alpha_T)y - \sin(\alpha_T)x - \cos(\alpha_T)y_0^a \tag{6.12}$$

with $y_0^a = y_c + \tan(\alpha_T)x_c$ for each pixel (x_c, y_c).

6.4.2 Determination of Local Angle α_0 of Pattern Structure in Air

For the above presented relations the angle of the pattern structure in air α_0 is needed. These angles can be determined in a measurement:
At a flat surface $\alpha_T = 0 \quad \forall x$ the angle of the pattern structure in air can be calculated from Snellius' law of refraction. α_0 dependent on the pixel position

is needed as input parameter.

$$\alpha_0 = \arcsin\left(\frac{n_w}{n_a}\sin(\beta_{flat})\right) \tag{6.13}$$

$$\text{with } \beta_{flat} = -\gamma_{flat} \tag{6.14}$$

Dependent on the current height of the water surface the angle α_0 - as it is non-zero - changes with the position of the row number.
Therefore α_0 has to be calculated for every surface position individually.

6.4.3 Inverse: Angle of Refracted Beam γ Calculated from Surface Slope m_s

In step III the background pattern has to be removed from the acquired image. This image is therefore divided by the ideal background pattern warped into the wave state of the image.
For calculating the warping function, a formula for calculating the angle of the refracted beam from surface slope $m_s = \tan(\alpha_T)$ is needed:

$$\gamma = \alpha_t - \beta \tag{6.15}$$

$$\gamma = \alpha_T - \arcsin\left(\frac{n_a}{n_w}\cdot\sin(\alpha_T + \alpha_0)\right) \tag{6.16}$$

The simple relations presented here provide all theory that is necessary for estimating surface orientation from the pattern orientation used in SP-LIF. Yet, the separation of pattern from the concentration signal is a task of image processing.

6.5 Experimental Realization

The above presented theoretical relations that combine the surface orientation and the orientation of the pattern will be used in the image processing routines. In this section a simple image processing routine for pattern separation with a high contrast illumination is presented, that can be realized with MATLAB image processing toolbox. The corresponding procedures for low contrast illumination like the Laser pattern are not presented here but in chapter 9, as in that case the methods of digital image processing needed for extraction of the local orientation of the pattern separated from the eddy structures are complex and need an extra discussion.

Identification of Individual Orientation of the Illumination Beams As a first discretized illumination source the full illuminating light sheet was replaced by a grid of 13 individual Laser rays by blocking parts of the full sheet. Images taken with that illumination can be found in figure 6.6. If the contrast between illumination beams and background and is large enough, like in this

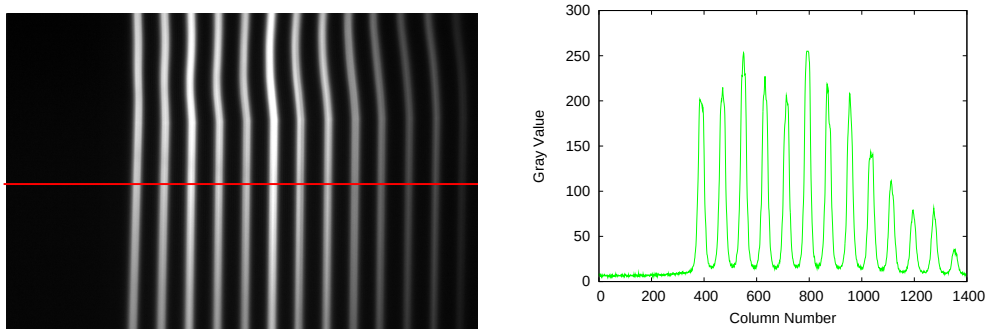

(a) (b)

Figure 6.6: Static-Pattern LIF tested in illumination by 13 individual Laser beams of 1 mm thickness: (a) Discretized sheet at a flat interface in red the orientation of the intensity profile is marked that is plotted in (b). The contrast between beams and background is large enough to allow threshold registration.

rough pattern a simple threshold registration can be done with low effort. With an additional Hough-transform all lines in the image can be captured. This yields the slope of the refracted beams and with knowledge of the individual line parameters the intersection points of these can be calculated yielding the water surface at the supporting positions.
A code to do this has been implemented in MATLAB based on its Hough routine in the image processing toolbox, see the appendix for the detailed algorithm.

In the case of the Laser pattern illumination the situation is quite different: the contrast between the individual striped features is low - so a detection by a simple threshold algorithm is no longer possible, see figure 6.7. Here, a much more complex image processing routine has to be used to extract the desired orientation of the pattern reliably. Details on this procedure will be discussed in chapter 9.

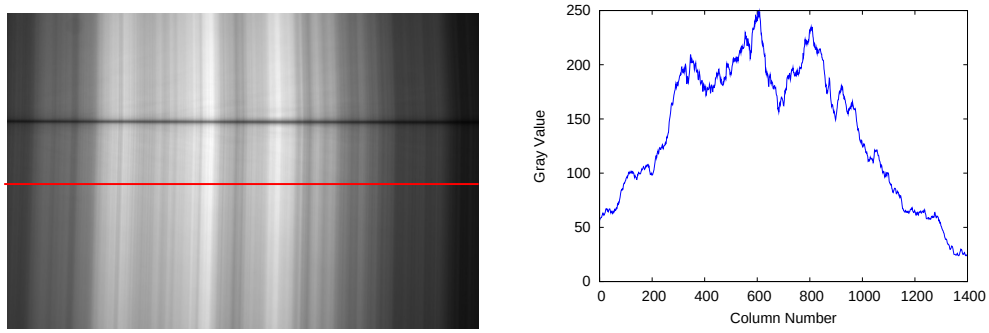

(a) (b)

Figure 6.7: Static-Pattern LIF with Laser pattern illumination sheet: (a) Laser pattern illumination sheet. In red the orientation of the intensity profile is marked that is plotted in (b). The contrast between the stripes of the pattern is extremely low, therefore threshold registration is no longer possible.

6.6 Summary

Static-Pattern LIF is a novel LIF technique that gives additional information on position and orientation of the water surface. Thus allowing a more robust detection of the water surface - the reference level for every water-sided gas concentration profile. Yet, the additional information of the local slope has to be extracted from the images via an extensive orientation analysis. Otherwise, if this extraction was not done the pattern would be just an additional disturbance of the measurement data. This is true especially in the case of a fine discretized illumination sheet. A rough discretization, however, with high contrast can be fairly easy dealt with by Hough transform.
For high-resolution measurements, static-Pattern LIF as measurement technique is bound to an elaborate image processing routine for analysis of the measurement data. Details of the complex image processing are discussed in chapter 9. Nonetheless, SP-LIF is a valuable addition to the techniques known so far. For the first time, with SP-LIF, a LIF technique is presented that allows measurements of water-sided gas concentrations in the top setup at highly wave-distorted surfaces. The additional information of surface slope increases the data on surface topology in best case by a factor of 2, thus leading to more reliable fit results even under conditions where estimates of surface position by symmetry filtering fail.

Part IV

Experimental Setup

Chapter 7

Ocean Simulation: The Wind-Wave Tunnel

All the experiments under wind-induced turbulence performed in this work have been carried out in the new closed circuit linear wind-wave tunnel LIZARD (**LI**near **Z**trong **A**cid **R**estistant **D**evice) built by the author in the first two years of this PhD following the basic construction design of Jähne [2006].
The new wind-wave tunnel is a substitute for an older annular facility built at the Woods Hole Oceanographic Institution that has been used for many years at Heidelberg, for example the works of Degreif [2006] and Falkenroth [2007] have been carried out there.

The effort was made to built a completely new wind-wave tunnel to guarantee best experimental conditions for using highly reactive gases as tracers in combination with an optimized optical access for a side-LIF setup (see chapter 6). This optimized setup forms the base to investigate transfer processes from the gaseous phase into the liquid even under a strongly wave-distorted water surface.

In the present section the characteristics of the wind-wave tunnel LIZARD are described beginning with the criteria for construction 7.1, the reasons for the chosen design in 7.2, and followed by a short technical description in 7.3. In appendix A a more detailed description of the individual tunnel elements as well as the sensor equipment can be found. Furthermore the measured characteristics of flow are given in A.3.

7.1 Main Design Criteria

As indicated above several criteria led to the final construction of the wind-wave tunnel. The most important ones were:

- usability for highly reactive gases
- optimized optical access to diminish distortion/astigmatism effects as far as possible

- best flow properties by realizing a wind-wave tunnel of the Göttingen type
- temperature stabilization

The usability for highly reactive gases is a demand resulting from the pH-indicator method as described in section 3.4. For this reason, the interior of the wind-wave tunnel is completely covered with PTFE-foliage, which is resistant to a wide range of chemicals including strong acids and bases. Additionally, the flume atmosphere can be deposited in the chemical fume deposition system to avoid decontamination of the surrounding room.

To allow the imaging of the near-surface region in the water-phase from beneath the surface, the angle of view has to be tilted against the perpendicular line, see fig.7.1. The reason for this tilt lies in waves that will block the direct line of view of the surface when their amplitude gets pronounced. Furthermore, the optical resolution of a LIF-side setup intended for observations of the water-sided near surface region is strongly sensitive to blurring: Even if a Scheimpflug setup (see section 8.2.1 for details) is used for optimal imaging of a tilted subject to lens plane, the objective remains tilted against the side-window of the wind-wave tunnel, see fig.7.1(a). This leads to astigmatism created by refraction at the tilted phase transition planes (air-glass, glass-water), which creates strong blurring.

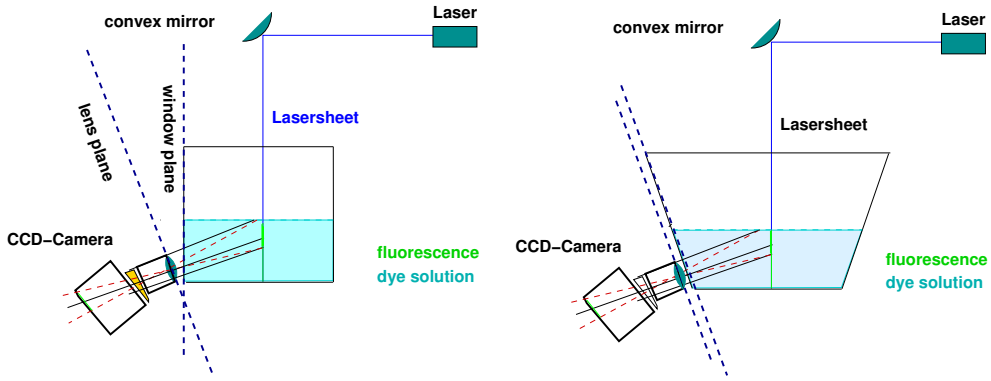

(a) perpendicular observation window

(b) tilted observation window parallel to lens plane to reduce astigmatism

Figure 7.1: Sketch of LIF camera setup at different kinds of observation windows.

For that reason, the new wind-wave tunnel should offer a unique feature for optical access: the observation window alongside the water segment of this new wind-wave tunnel should be tilted, so that camera objective and window plane can be oriented parallel in a side-LIF setup.

Beside the above described special features for LIF-measurements flow properties are demanded to follow the state of the art in wind-wave tunnel design.

For this reason, the basic design of the tunnel is that of the closed circuit Göttingen type introduced by L. Prandtl in the 1930's, see for example Oertel [2004]. Secondary effects on the fluid flow in the middle of the water segment where the LIF illumination is located these effects should be negligible. This had been tested as the tilt of the side-windows may affect the flow properties, see A.3.1.

A stable temperature in air and water phase during LIF experiments is mandatory, as not only fluid properties (see section 2) and Schmidt number vary strongly with temperature but also the chemical reactions used in the pH-method depend strongly on temperature (see section 3.4).
Therefore, temperature variations in the whole tunnel should be stabilized at least to ± 0.5 ℃.

How these criteria can be realized in the best way has to be determined after the general design type is chosen.

7.2 Design Types of Wind-Wave Tunnels or Reasons for a Linear Wind- Wave-Tunnel

For LIF experiments three different types of wind-wave tunnels have been used in the past: A grid-stirred or jet tank, a annular wind-wave tunnel or a linear wind-wave tunnel. The three types will now be discussed with respect to this task.

Grid-stirred/Jet-Tank The first type, the grid-stirred tank, is a model for bottom-induced turbulence like it can be found in rivers. This type was excluded immediately. These tanks are not intended to be used under wind induced shear stress though it has been done for example by Asher and Litchendorf [2009], who placed their tank in a wind-wave tunnel to study effects of waves. The fetch[1] is very low as the maximum fetch available is the diameter of the tank, usually less than 0.7 m. Surfactants can also be a problem without an extensive cleaning as reported by Asher and Pankow [1989].
For LIF experiments however, a grid-stirred tank is well suited as no waves are present, disturbances are in the range of mm, as reported for example by Herlina and Jirka [2008] or Schulz and Janzen [2009] and do not interfere even with a laser light sheet that penetrates the surface from above. Lens effects can be neglected in that way.

Annular Wind-Wave Tunnel As the grid-stirred tank is not an option, the next type is the annular wind-wave tunnel. With its infinite fetch waves with high amplitudes can be generated easily. Here, secondary currents induced by centrifugal forces when forcing the water to follow the curvature of the walls

[1] fetch means the distance the wind has exercised shear stress on the fluid.

can be problem in small facilities with low radii. See for example the work of Ilmberger [1980], where these effects have been thoroughly studied.
An image series taken in a small annular facility by the author, can be seen in figure 7.2, illustrating the rapid movement of the topmost layer in direction of the outer wall, where this layer dives into the bulk, leading in that way to an increased gas transfer.

Figure 7.2: Secondary current effects in the Small Circular Facility at the Heidelberg Aeolotron Lab; images taken in a LIF setup, fluorophore HPTS, tracer HCl, wind speed below 3 m/s.
Laser sheet orientation is spanwise to the flow (sheet width: 10 cm) in the annular wind-wave tunnel. The diagonal arrow mark the direction of time evolution and the arrow labeled as flow marks the direction of the secondary current to the outer wall of the wind-wave tunnel: The dark eddy moves from the inner wall to the outer wall with time.

These effects become negligible at radii of more than 3 m. So a large facility would be needed, however the water volume should not exceed a volume of 0.2 m^3 due to the high costs of the fluorophore. Another problem are the curved walls of the facilities which led to strong optical distortions when trying to image the interior from the outer walls, especially Falkenroth [2007] reported difficulties to get a good optical access on the Small Annular Facility. He had to install an optical adapter filled with water ending in a planar glass plate parallel to the camera objective to reduce part of the distortion of the curved walls. In annular wind-wave tunnels surfactants can also be a problem when the surface is not cleaned before the measurements.

Linear Wind-Wave Tunnel Finally, left is the last type of the wind-wave tunnels: the linear wind-wave tunnel. A wave undulated surface can be achieved here given that the fetch is long enough that waves can be formed. In contrast

to the annular type the wave field depends on the fetch - so the longer the wind has had time to exercise force on the surface the more pronounced waves and turbulence are found. So here the effects of fetch dependency on gas transfer and wave formation can be studied.
In general (as the fetch is lower) the waves in a linear tunnel are much smaller than the waves in a annular facility. Yet, both the linear and the annular facilities generate young steep waves which differ from the old waves found in the oceans. This has to be kept in mind, according to Csanady [2001].
Furthermore, the linearity of the flume also offers the possibility of large observation windows parallel to which optical mounting systems can be easily set up. Wave suppression by surfactants can is usually low as they are blown to the end of the tunnel where they can be removed easily.

Conclusion: Linear Flume Summarizing the last three paragraphs led to the conclusion to build a linear wind-wave tunnel to study the effect of waves in a linear facility due to better optical resolution and less secondary current effects.
In the next subsection a brief technical description of the main properties of the tunnel built is given.

7.3 Short Technical Description

The new low-speed wind-wave tunnel LIZARD at the Institute for Environmental Physics at Heidelberg has a water segment of 4 m total length, with an 0.8 m-long breakwater at the end. Mean water width is 37 cm and mean water depth is 9 cm, with 23 cm height of the air space above. The water used is ultra pure water with a conductivity of less than 0.1 μS/cm.
The tunnel is a closed circuit wind-wave tunnel of the Göttingen type introduced by Prandtl, characterized by the jet inlet before the test section and guide vanes in the four corners of the two flow turning units.
Free cross section area in the water segment for air flow is 966 cm^2. The maximum wind speed is about 15 m/s in the filled water segment, generated by an axial fan by Hürner Funken.
The contraction ratio[2] at the jet inlet is 3.35. To further minimize disturbances a honeycomb of mesh size 3 cm is installed before the inlet.
Water surface area is 1.11 m^2, with a water volume of 0.150 m^3 compared to an air volume of 3 m^3.
Four different water cycles are installed, in the main cycle a centrifugal pump (Schweikert, MPN 101) can induce a counter current flow in the wave tunnel with a maximum volume flow of 80 l/min. The other three water cycles are intended to be used for degassing/gassing, filtering, an additional deionization unit, and water analysis via an absorption spectrometer cell.
Water temperature can be kept constant via heating/cooling units, while the air phase can only be heated with an IR heating unit. Furthermore, the tunnel

[2]largest inner diameter divided by smallest inner diameter at the jet inlet

has an additional outer temperature insulation to simplify temperature stabilization. The measurement section is located within a purity tent, kept at a low overpressure to prevent dust from entering the water unit.
The permanent sensor equipment of the tunnel consists of two Prandtl tubes for wind velocity measurements, four temperature sensors, two in air, two in the water phase, a unit for differential pressure between tunnel and laboratory, a pressure sensor for total pressure, a conductivity sensor, and an absorption spectrometry cell.
A detailed description of the above mentioned features will be given in the appendix together with an overview of the general design, an overview of the individual tunnel elements and finishing with the instrumentation equipment of the tunnel. Here, only the most important part - the water segment is presented.

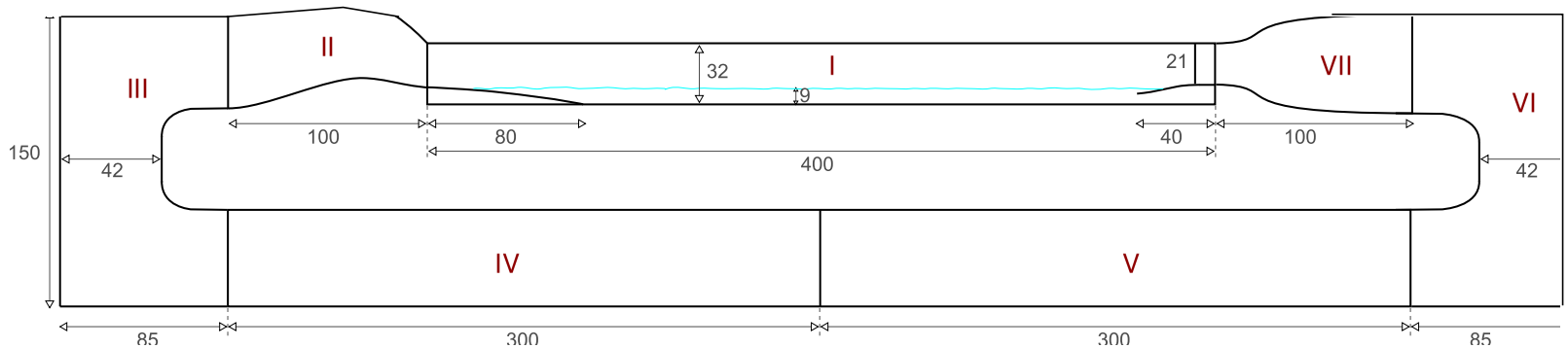

Figure 7.3: Sketch of the wind-wave tunnel LIZARD. The segments are numbered as follows:

Element	Description
I	water segment
II	small diffusor
III	(small) flow bending unit 1
IV	wind generator unit
V	large diffusor
VI	(large) flow bending unit 2
VII	jet inlet with honeycomb

Element 1: The Water Segment

The heart of the new wind-wave tunnel is the design of the water segment. A cross section through the water segment can be found in figure A.2.

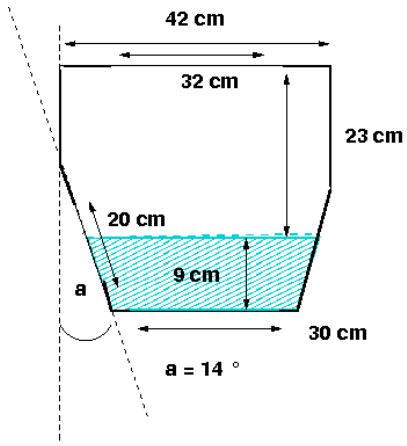

Figure 7.4: Cross Section of the Water Segment of the Wind-Wave Tunnel. The angle of the tilted side window is $\theta = 14.6 \pm 0.3°$.

Three large observation windows allow best optical access from different points of view: from top, bottom and as special feature - the side window with tilting angle of $\theta = 14.6 \pm 0.3°$, which allows parallel orientation of the detector objective to the window in the LIF side-setup as discussed above.
LIZARD is a linear wind wave wind-wave tunnel with a water segment of maximum fetch length of 3.4 meters (observable range: 0.4-2.2 m) by a total length of the water segment of 4 meters and a total of 150 ± 8 water capacity, with 126 ± 8 liters in the tunnel itself and 24 l in the four water cycles with a total air volume of 3 m^3 of the whole tunnel[3]. The maximum water depth is 9 cm while the water surface area is approx. 1.11 m^2 at full water height. The height of the corresponding air space is 23 cm. Free cross section area in the water segment for air flow is 966 cm^2.
A 0.8 m-long breakwater at the end ensures that wave reflection is suppressed. It consists of 11 flexible PTFE half-tubes of 20 mm diameter, that are oriented in that way that the reflected fluid is caught in their arch while the inflowing water is passing the outward arched spheres easily.
Four different water cycles are installed: In the main cycle a centrifugal pump (Schweikert, MPN 101) can induce a counter-current flow in the wave tunnel with a maximum volume flow of 80 l/min. It is used for fast mixing operations for example titrations of the fluorescent pH indicator with HCl or NaOH. In the main cycle three dosing units (Schott Titronic Universal piston burette) are installed which allow precise dosing down to volumes of 0.01 ml/min. They are used for setting up the pH value in the water phase to the desired pH value by

[3]Maximum water capacity has been estimated in a conduction experiment by adding known amounts of 1 M HCl and measuring the changes in conductance.

adding acid (HCl 0.1 M) or base (NaOH 0.1 M). Degassing/gassing, filtering, and water analysis via an absorption spectrometer cell are located in the other three water cycles. The water temperature can be kept constant via a heating/cooling unit with controller (manufacturer Cool Tronic GmbH) consisting of 18 Peltier elements attached to an aluminum plate of 390 mm x 300 mm located at the bottom of the water segment under the wave break.
The tunnel has an additional outer temperature insulation to simplify temperature stabilization. Two PT-100 temperature sensors (manufacturer Greisinger Sensoric) are located in the water phase to measure local temperature, one in the water tunnel itself, one in the main water cycle in combination with an conductivity sensor (manufacturer WTW, type Cond 340i) for monitoring accumulation of ions. One PT-100 sensor is located above the wave break for measurements of air temperature. The second air temperature sensor is mounted in the second adapter of the wind generator unit.

The measurement section is located inside a simple purity tent, kept at a low overpressure to prevent dust from entering and therefore finally entering the water unit. This effort was taken as floating dust on the water surface disturbs LIF measurements by Mie scattering and blocking parts of the Laser sheet, see section 11 for further details.

The wind-wave tunnel water inlet is attached to a deionization unit (manufacturer: KSN-Wassertechnik,type Nowadest 1500 NF) so that the water used is ultra pure water with a conductivity of less than 0.1 μS/cm, see section A.4 for details.

The wind velocity in the water segment is measured via the difference in static and dynamic pressure with two Prandtl tubes located at a fetch of 2.4 m. One is installed as a static sensor for measurements of the mean wind velocity. The second one is mounted on a movable table (manufacturer Owis-Stauffen, type SM 32) to measure with high precision (table position accuracy 0.1 mm) the vertical position of the tip of the tube. It is used for measurements of the vertical velocity profile from which friction velocity is calculated, see A.3 for details. The horizontal position of the second Prandtl tube can be changed to seven equally distributed positions (3.5 cm distance between them, with 10.5 cm distance of the outer points to the tunnel walls).

7.4 Summary

The new wind-wave tunnel LIZARD follows the design of a linear tunnel of the Göttingen type. Its most remarkable feature are the tilted side walls including a large observation window, that allows parallel orientation of camera objective and observation window to reduce astigmatism. In that way the tunnel LIZARD is optimized for best optical resolution for measurements in the LIF side-setup.

Chapter 8

The Optical Setup

In all setups for Laser-induced fluorescence the achieved spatio-temporal resolution plays a key role as it determines the smallest boundary layer thicknesses to examine and the highest wind speed to examine, respectively. So the spatio-temporal resolution that can be achieved and expected is the quantity of interest.

Two optical systems determine the properties and therefore the quality of the optical setup: On the one hand, the illumination or Laser setup and on the other hand the detector or camera setup. While temporal resolution mainly depends on the frame rate of the camera, the spatial resolution depends on a variety of factors describing the illumination and the detector setup.

In this work the spatial resolution could be improved by using a Scheimpflug setup in combination with a tilted observation window of the wind-wave tunnel (see chapter 7.1 for technical details of the tunnel). The used illumination configuration was a static Laser sheet generated by widening a Laser beam by a convex mirror that illuminated the water phase from above the surface, as needed by the Static-Pattern LIF method, that was developed within this work, see 6. The detector system consisted of the CMOS camera 'Falcon' of Dalsa, with a Nikon objective, and an accessory lens.

In this section possible configurations of the optical setup for LIF measurements are presented and compared to each other regarding spatial and temporal resolution and noise. This discussion includes a comparison to setups recently or currently used by other authors.

8.1 Illumination Setup

Besides the used light source, the illumination setup can be characterized both by the orientation of the illumination sheet and the way the sheet is created. In the following three subsections these topics will be discussed.

8.1.1 Light Source

The illumination light source used in this work is a diode laser Nano-250-445-450, manufactured by RGB-Lasersysteme GmbH and distributed by Linos Photonics. According to the manufacturer's data sheet the output power is 450 mW at a wavelength of 445 ± 5nm. The form of the beam is elliptic with a cross section of 1.1x2.8 mm^2. Laser power can be adjusted in a range from 1 mW up to 600 mW, according to own measurements, see 8.1 (corresponding steerage voltage range 1.2-5 V; below the threshold 1.2 V the output power drops by a factor of 10^3 to the μW range). For measurements laser power was in the range 80-96% of maximum to ensure short exposure times. Dye saturation was not reached. For a more detailed discussion see section 11.

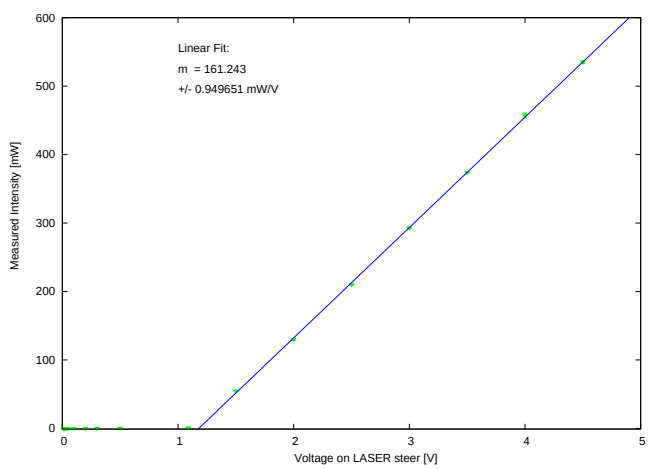

Figure 8.1: Laser output power of the Nano-445-440-450 depending on steering voltage at the controller, with a slope of 161 ±9 mW/Volt.

Discrepancies appeared in measurements of the output power integrated over the whole detectable spectrum to measurements preformed with band pass filters (Measurements were performed with an Optical Power Meter-840C from Newport). This indicated that the Laser light consisted of several individual modes. For this reason the Laser spectrum was measured.

Spectral Analysis of the Laser Modes

The spectral analysis showed that the Laser modes shifted in a range of approximately 4.5 nm [440.5-445 nm] with the adjustment of the Laser power output, see figures 8.2 and 8.3. All measurements were done with an 'Optical Spectral Analyzer' (OSA) from Ando at the Technical University of Darmstadt, Group 'Laser und Quantenoptik' of Prof. Walther. The Laser output was coupled into the analyzer by an optical fiber.

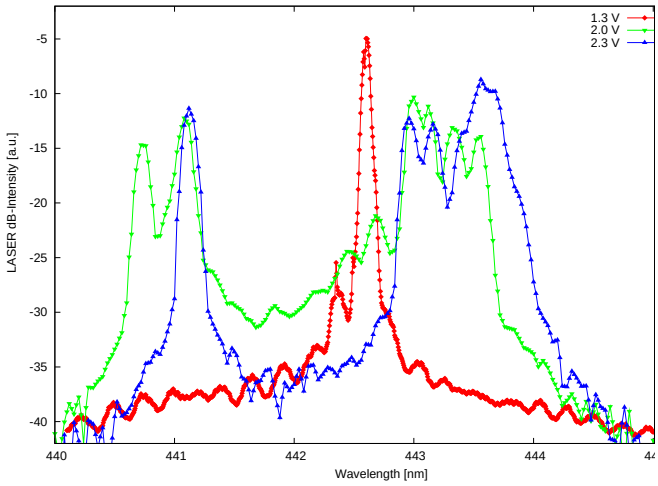

Figure 8.2: Laser modes of the Nano-445-440-450 depending on steering voltage at the controller, 1.3-2.3 V corresponding to 161 ±9 mW/Volt.

A rough simplification indicated that at low output power the modes above 440 nm are active while at higher power the modes tended towards 445 nm.
The used fluorophore HPTS has its maximum emission in the excited anion base component around 455 nm. In the range of 440-450 nm the absorption has a strong gradient. If Laser modes shift even in a small range of 5 nm, the absorption changes from 440 to 445 nm by approximately 8 % and therefore fluorescence emission, see figure 8.4.
This leads to the effect that the absolute power of the fluorescence emission is not directly proportional to the laser power even if saturation excitation of the dye solution is not reached, Tsien et al. [2006].

To prevent the appearance of this nonlinear behavior, measurements should be taken at a fixed laser power.

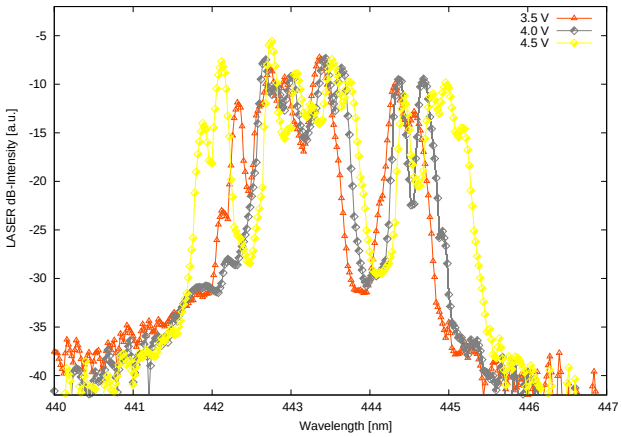

Figure 8.3: Laser modes of the Nano-445-440-450 depending on steering voltage at the controller, 3.5-4.5 V corresponding to 161 ±9 mW/Volt.

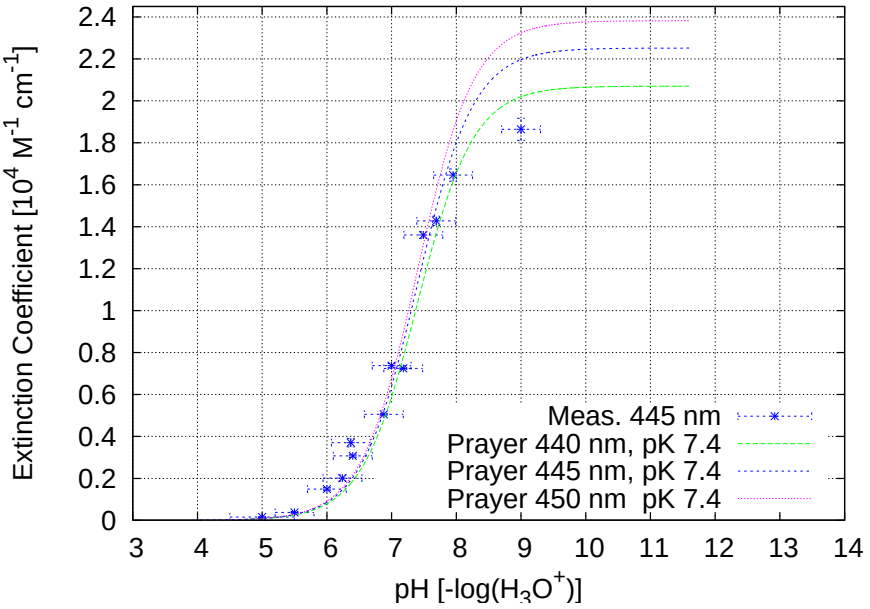

Figure 8.4: pH dependent extinction coefficient around 445 nm of HPTS based on measurements with an optical multichannel analyzer HP 8453 (Temperature = 24.0 ±0.5℃). The curves represent the pH dependence of the extinction coefficients (data from Prayer [1997] calculated for pK = 7.4) at three different excitation wavelengths, 440,445 and 450 nm. Due to the logarithmic nature of the pH scale changes in the lower range only appear to be negligible.

Drift in Laser Output Power

A stable output power of the Laser with variations below the variations in fluorescence intensity due to its Poisson noise is most desirable for LIF measurements. For that reason the stability of the output power was monitored over several hours with an optical power meter. A graphical representation of the results is shown in figure 8.5.

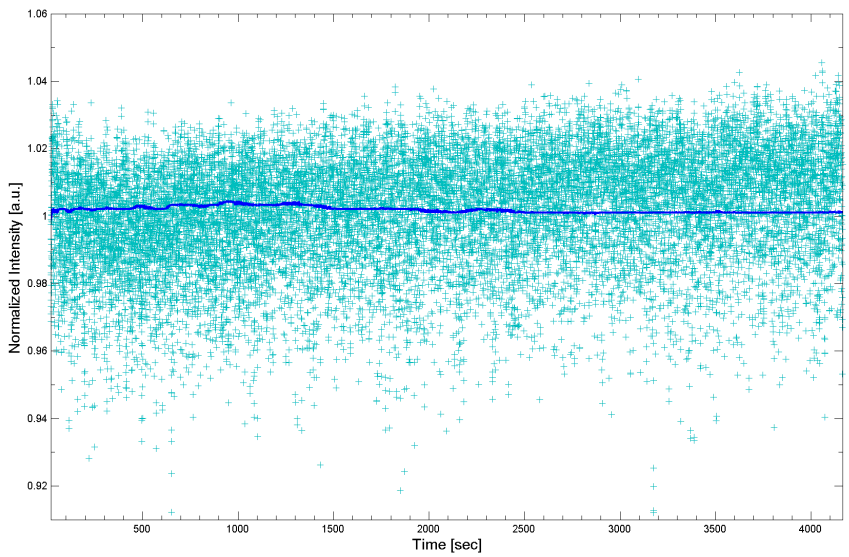

Figure 8.5: Drift in output power of the used laser Nano-440-450, measured by P. Warken. The blue line shows the laser intensity, while the cyan crosses show the fluorescence intensity, the fluctuations of which are one order of magnitude larger than those of the laser.

The measurements by P. Warken showed that the fluctuations of the laser are well below 1% and can therefore be neglected with respect to the fluctuations in fluorescence intensity.

8.1.2 Sheet Optics

The chosen orientation of the light sheet depends on two factors: On the one hand, the optical access offered by the wind-wave tunnel may limit the possible orientations of the light sheet if - for example - a bottom window is not available. On the other hand, some fluorophores react to the presence of dissolved gases with a reduction of fluorescence like PBA or (fluorescein and HPTS in the case of an acid gas). In invasion experiments, the concentration of the gaseous tracer is the highest at the surface and therefore fluorescence intensity is remarkably reduced there, see for example figure 8.6. So at the surface a high illumination

intensity would be required.
In general, three orientations of the illuminating sheet are used: The illumination from the side, illumination from the bottom and illumination from the top. All three show differing advantages and drawbacks.

Orientation of Illuminating Sheet

Illumination from the Side Illumination from the side is only done in experiments in the bulk or if horizontal planes were examined like in the work of Tsumori and Sugihara [2007] and Takehara and Etoh [2002].
If the near surface region is examined waves may block the illumination, so this illumination cannot be used for measurements of the water-sided boundary layer with a wave undulated interface.

Illumination from the Bottom Illumination from a bottom light source is used by various authors i.e. Walker and Peirson [2008], Peirson [1997] and Duke and Hanratty [1995].
Advantage of this orientation is that the light sheet is not altered by movements of the surface, yet the problem is that the light intensity due to Lambert-Beer decay is lowest at the surface, where the boundary layer is to be investigated and gas concentration is highest in invasion experiments. This will be a problem if fluorophores decrease fluorescence intensity under higher dissolved gas concentrations. As signal to noise ratio drops for low intensities due to Poisson-statistics of photon absorption, Jähne [2005], a high laser power or a low water depth is needed to account for these effects, which is done in the experiments of Duke and Hanratty [1995], where a water depth of 11 mm was used. Walker and Peirson [2008] used a higher laser power (exact values not mentioned) and also reduced water depth locally to 9 cm. Furthermore, total reflection of the illumination cannot be neglected under waves, as the surface marks the transition from an optically dense to an optically thin medium.

Illumination from the Top The illumination from the top is used, if a high intensity of the laser light is needed a the surface and cannot be achieved in the bottom configuration. If illumination from the top is used the light sheet is deformed by the changing surface topology due to waves, which lead to convergence and divergence of the light sheet depending on the location. These lens effects cannot be avoided. Therefore, the illumination from the top is mainly used in grid-stirred tanks where the surface remains smooth, i.e. Herlina and Jirka [2008],Schulz and Janzen [2009]. Furthermore, under a wavy interface these convergence and divergence effects lead to a local increase of the intensity that may easily be mistaken for a decrease in the concentration of dissolved gaseous tracer in an automatic detection algorithm, see for example figure 8.6. That is why most authors using this configuration measured before the onset of waves. Münsterer and Jähne [1998] for example suppressed waves by adding a surfactant Triton X to be able to measure at higher wind speeds.

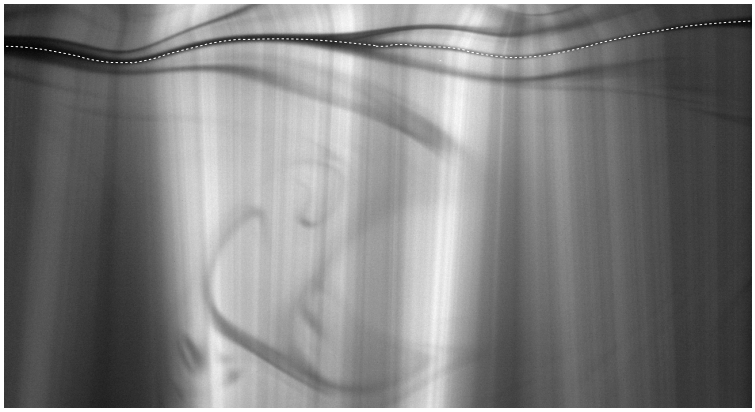

Figure 8.6: Illumination light sheet altered by lens effects caused by a passing wave; mean wind speed is 5 m/s.
Laser sheet orientation is streamwise to the flow in the linear wind-wave tunnel LIZARD. The surface is marked by the white-dashed line. The dark eddies mark a higher concentration of dissolved HCl.

Reasons for Choosing Top Setup In the experiments conducted here, the fluorophore HPTS and an acid gaseous tracer, HCl, is used in invasion experiments. The mean intensity at the surface is therefore expected to be low, so high intensity would be required at the surface. This would already give reason for choosing the top setup. Additionally, in the Static-Pattern LIF setup, see section 6 the drawback of the deformation of the Laser sheet is made to an advantage: The deformation of the Laser sheet pattern is used to calculate the orientation of the surface and therefore to enable measurements at a wavy interface.

Ways of Creating a 2D-sheet Light sheet

The way of generating a 2D laser light-sheet determines the limits of optical resolution by blurring. Crimaldi [2008] distinguished two typical setups: a dynamic and a static light sheet both differently affected by blurring.

Static Sheet A sheet is called static if the sheet is produced by a cylindrical lens or cylindric mirror and is static in time. Here laser intensity is spread to a line of a certain thickness depending on the condensing optics with much less intensity than the original laser.
Blurring is supposed to happen if the distance of movement $\mathbb{R}$ during exposure time $t_{exposure}$ is greater than the smallest structure to be resolved $L_{structure}$.

So blurring should not occur if the following relation is fulfilled:

$$\mathbb{R}_{static} = u \cdot t_{exposure} \,/\, L_{structure} \ll 1. \tag{8.1}$$

Dynamic Sheet A dynamic sheet was called a sheet generated by a rotating mirror or a scanner. Here full laser intensity is used at every vertical line of the sheet. Crimaldi [2008] showed that using a dynamic sheet a higher local resolution can be achieved than using a static sheet, with L_{imaged} as the image length in the streamwise direction:

$$\mathbb{R}_{dynamic} = u \cdot t_{exposure} \,/\, L_{imaged} \ll 1. \tag{8.2}$$

This relation is only valid if the illumination time t_i by the scanning sheet is less than $L_{structure}/t_i \ll 1$.
The obtained image is distorted by the movement of the fluid and has to be postprocessed.
So a dynamic sheet would be preferred if a high intensity was needed.

Choice of Sheet Generation: Static Sheet In a Static-Pattern LIF setup a dynamic sheet cannot be used, as explicitly properties of the intrinsic beam pattern are used that would be destroyed in a dynamic sheet. If intensity of the laser sheet and minimal exposure time fulfill the condition 8.1.2, a static sheet will be not a disadvantage. However, another variation might be possible - a pulsed sheet - in the case that the minimal exposure time of the camera is the limiting factor of the setup.

Most favorable - given that laser intensity is high enough- would be to illuminate the probe instantly (within the time scale of the setup) with a pulsed static laser sheet. So that every sheet appears only in the pulse time of the laser t_{pulse} in a fraction of time of the exposure time of the CMOS-chip:

$$\mathbb{R}_{pulsed} = u \cdot t_{pulse} \,/\, L_{structure} \ll 1 \tag{8.3}$$

This variation of the above mentioned static sheet could be used in a Static-Pattern LIF setup to improve temporal resolution.

Parallelizing the Sheet Beam Paths

For SP-LIF a illumination light sheet is favorable whose beam path angles in air with respect to the perpendicular line are close to zero, see section 6.
For that reason, a confocal lens ($f = 30$ cm) is set at a distance of its focal length f from the convex mirror used for creating the sheet, see figure 8.7. The passing sheet is in that way parallelized. This is a common procedure and is used by various authors, i. e. Van Vliet et al. [2004].

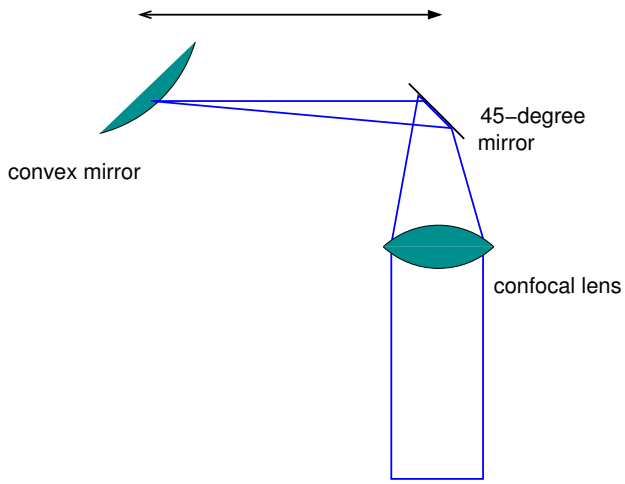

Figure 8.7: Sketch of optical setup for parallelizing illumination sheet by using a confocal lens.

The confocal lens has an additional effect as it also collimates the spanwise depth of the laser light-sheet to approximately 0.1 mm. This collimation leads to an decrease in blurring as the reduced thickness leads to an decreased overlay of different concentration in the sheet of finite width. The reason for this is, that the image taken by the side camera is an integral overlay of the concentrations at different thickness-layers in the sheet, for more details see section 11.1.2.

The generated sheet had a width of 40 mm and a thickness of 0.1 mm, thus leading to a total illuminated area of 0.04 cm^2.
The total laser power per square centimeter is calculated to:

$$P_{lasersheet} = \frac{P_{Laser}(4.9\ \mathrm{V})}{A_{ill}} \tag{8.4}$$

$$\approx 1.25\ \mathrm{W/cm^2} \tag{8.5}$$

which is a rather moderate value.

8.2 Detector Setup: The Imaging System

For all the measurements conducted in this work as CMOS-camera a Falcon, manufacturer Dalsa, was used. This CMOS-camera specifications include a chip size 1024 x 1400, 1023 gray values (10 bit) with pixel size of 7.4μm×7.4μm, a maximum frame rate of 67 Hz when using the full chip-size for recording. For wind speeds below 4.5 m/s this configuration was used.

The frame rate could be increased to 150 Hz by a reduction of the used pixels to an area of interest of 660 x 1400 pixels and a reduction of the gray values to 256 (8 bit). This configuration was used for wind speeds above 4.5 m/s.

The minimal frame rate is 2 Hz and minimal exposure time 0.03 μs. The minimal frame rate was used for acquiring uncorrelated images series for statistical analysis, see section 5.8.1.

The objective was a Nikon, Nikkor with f = 50 mm, minimal f-stop of 1.2. It was used with an accessory lens, Nikon Close-up No.4, with additional 3 diopters. The used Scheimpflug adapter was designed and constructed by B. Jähne.

8.2.1 Scheimpflug Setup: Significant Improvement of Optical Resolution by Scheimpflug-Arrangement

In every LIF-side setup an image is taken of an object with a slightly tilted camera, see section 4.2. Yet, if a tilted object is to be imaged the sharp image plane is no longer parallel to the lens plane: image plane and lens plane intersect in a line at finite distance and no longer at infinity. A sketch of the orientation of the planes is given in figure 8.8.

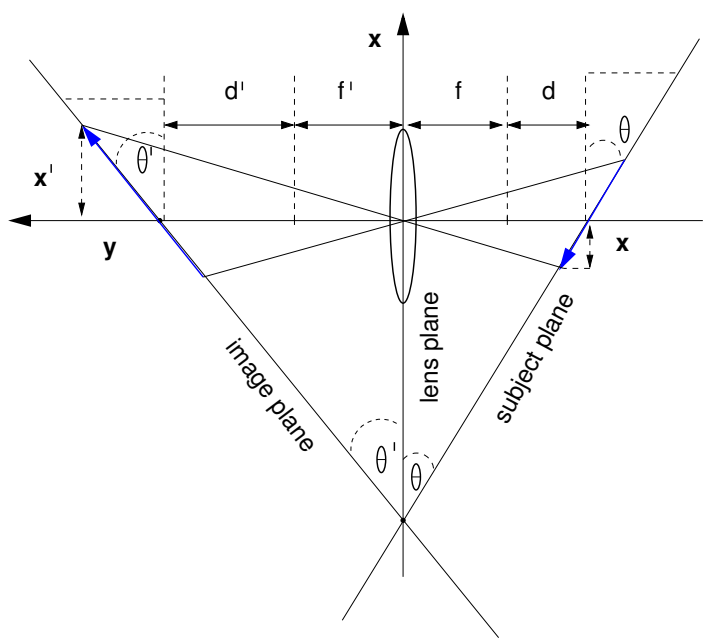

Figure 8.8: Geometry of the Scheimpflug setup.

With a common camera setup, where sensor plane and lens plane are fixed in parallel position, only parts of the image will be sharp. Most authors in LIF studies have tried to reduce these effects by using a lower angle of tilt, see for example Walker and Peirson [2008] with an angle of 1.7 °. To achieve an image that is sharp in every image point (X,Y) the plane of the image sensor must be tilted against the lens plane to come to lie on the true image plane. Such a

setup is named after Scheimpflug [1904], who together with Carpentier [1901] was the first to use such an arrangement for imaging. A comparison of images of a tilted plane with and without Scheimpflug setup is given in figure 8.10. With the Scheimpflug setup and a careful adjustment of the same, the imaged plane is sharp in every pixel.

In fluid dynamics Scheimpflug setups are used for example in angular stereoscopic imaging setups in Particle Image Velocimetry (PIV),McKeon et al. [2007]. Bäumler [2000] used a Scheimpflug setup for imaging of tilted planes in the water phase of a wind-wave tunnel at Heidelberg.

In this work, a Scheimpflug setup is used for the first time for imaging of the vertical plane of emission in a LIF setup in a linear wind-wave tunnel. In figure 8.9 a sketch of the Scheimpflug Setup at the wind-wave tunnel is shown.
The tilt of the object plane θ corresponds here to the angle of tilt of the observation window, as the objective or lens of the camera setup is orientated parallel to the observation window.
In a Scheimpflug setup, though the image is sharp everywhere, a distortion is

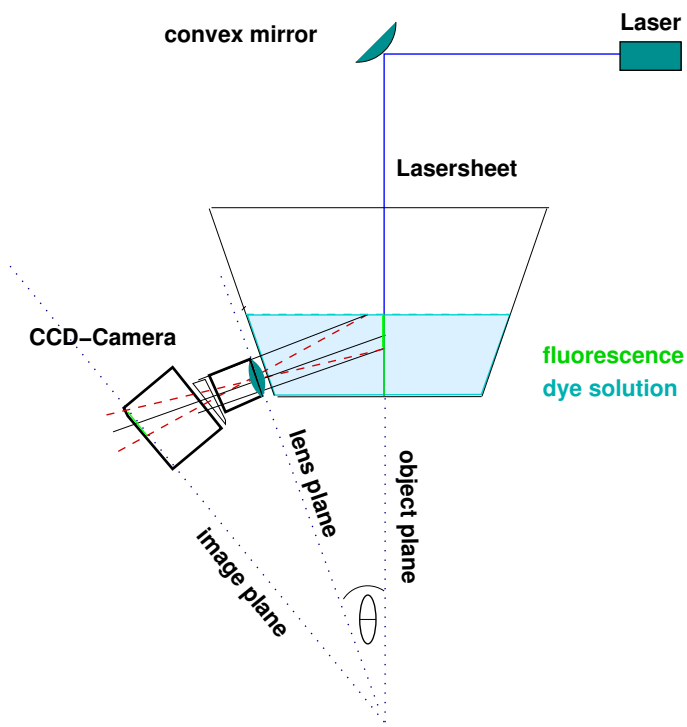

Figure 8.9: Sketch of Scheimpflug arrangement for the LIF camera system at the tilted observation window

generated over the image regarding the distance between equidistant points x_i and x_{i-1} in the original image and the new distances between x'_i and x'_{i-1} in the image. In the subject the point distance between mesh points are assumed

to be constant:

$$\Delta x = x_i - x_{i-1} = \text{constant}. \tag{8.6}$$

The mesh points are imaged via a position dependent lateral magnification function $M_e(x)$:

$$\begin{aligned}
\Delta x' = x'_i - x'_{i-1} &= M_e(x_i) \cdot x_i - M_e(x_{i-1}) \cdot x_{i-1}, && (8.7)\\
&\quad \text{assuming } M_e(x_i) \approx M_e(x_{i-1}),\\
\Delta x'_i &\approx M_e(x_i) \cdot (x_i - x_{i-1}), && (8.8)\\
&\approx M_e(x_i) \cdot \Delta x_i. && (8.9)
\end{aligned}$$

With geometric considerations and basic equations of imaging according to Jähne [2010], these lateral magnification M_e that changes with position of the image plane can be calculated. The used parameters are defined according to figure 8.8:

$$\begin{aligned}
M_e &= \frac{x'}{x} && (8.10)\\
&= \frac{f}{d \cdot \tan(\theta)}\\
&= \frac{f}{d} \cdot \frac{1}{1 + \frac{x}{d}\tan(\theta)}
\end{aligned}$$

With $M_e^0 = \frac{f}{d}$ as the magnification of the central pixel of the image, the magnification equation can be expressed as a function of x

$$M_e(x) = M_e^0 \cdot \frac{d}{d + x \cdot \tan(\theta)}. \tag{8.11}$$

From these considerations it can be seen that $M_e(x_i)$ has to be determined to be able to correct the distortion in the obtained images.

The distortion of the image can be inverted, if the tilting angles of the object plane θ and of the image plane θ' are known. The distortion function $M_e(x)$ can be approximated by a quadratic polynomial as shown by F. Friedl, when expanded in a Taylor series:

$$\begin{aligned}
M_e(x) &= M_e^0 \cdot \frac{d}{d + x \cdot \tan(\theta)}, && (8.12)\\
&= M_e^0 - M_e^0 \cdot \frac{\tan\theta}{d} x + M_e^0 \cdot \frac{2 \cdot \tan^2\theta}{d^2} x^2 + O(x^3). && (8.13)\\
& && (8.14)
\end{aligned}$$

Since $\tan\theta < 1 \; \forall \theta < 45°$, this series converges.
For an estimate of an upper limit of these distortion, it is assumed that $M_e^{max} = 0.5$. Furthermore, typical values for the setup at LIZARD are taken: the tilt-angle of the side window $\theta = 14.6 \pm 0.3°$, $\tan\theta \approx 0.26$ and together with an

image height of $x = 24$ mm and a distance $d \approx 170$ mm. The upper estimate yields then

$$\frac{x \cdot \tan\theta}{d} \approx 0.036 < 4.\% \tag{8.15}$$

So the distortion effects are rather small, but should nevertheless be corrected.

In the present case, a calculation of the scaling function M_e is more complicated as a change in media, here water, glass and air is also Incorporated in the setup. In the given case, it is therefore easier to determine the mapping function by taking images of a calibration target, say a mesh with known grid-size, where the original distances are known. The corresponding coefficients can be determined via a least-squares fit to the data, acquired with the calibration target.

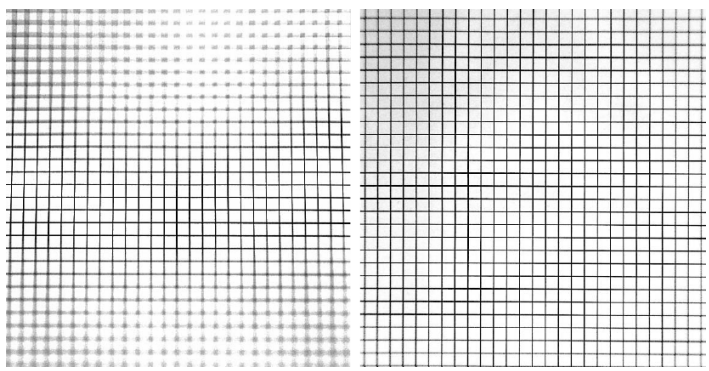

Figure 8.10: Illustration of effect of Scheimpflug on resolution: Images of a plane with 45°slope, image taken (left) without and (right) with Scheimpflug adapter between objective and image sensor; images from Bäumler [2000]

8.3 Summary

The combination of the tilted tunnel observation window and the Scheimpflug arrangement of the detector system has been demonstrated to guaranteed best imaging of the illumination plane even under a high tilt in the observation angle. This highly favorable setup has been used for the first time for a Side-LIF setup. The effort for the post-processing to account for the spatial deformation is worth the price. The correction is discussed in section 9.

Part V

Processing of Experimental Data

Chapter 9

Image Processing

The desired concentration profiles of dissolved hydrogen chloride have to be calculated from the measurement data of the LIF setup. In the case of LIF the data consists of gray value images, so to actually gain the information needed some kind of image analysis has to take place.
The SP-LIF technique presented in chapter 6 as measurement technique is bound to elaborate image processing routines for analysis of the acquired images. In these images the desired signal of the local concentration fields is overlayed by the distorted background pattern.
The two signals, the concentration field and the background pattern have to be separated. In the description of SP-LIF as technique a five-step procedure was presented to achieve this. However, for practical separation of the two images this core-procedure has to be extended. The additional information of surface slope besides surface position increases the data on surface topology in best case by a factor of 2. With more accurate estimates of the surface as initial guess more reliable fit results become possible even under conditions where estimates of surface position by symmetry filtering and local minima analysis fail, e. g. strongly wave-influenced surfaces.

The image processing routines used in this study are either part of the image processing software HEURISKO from Aeon, or are implemented in the VIGRA image processing toolbox of U. Köthe, HCI.

9.1 Relation to Previous Studies

In the former LIF-experiments a homogeneous illuminating light sheet was used. The main problem encountered in these studies is the identification of the water surface. This is usually done by using the characteristics of the water surface:

- In invasion experiments the water surface can be expected to be the region of highest gaseous tracer concentration and therefore **lowest fluorescence intensity** - in the mean. This needs not to be valid in the case of surface renewal events.

- The position of the water surface will most probably be in a range of

several millimeters up to 2 centimeters **around the position of the water surface under flat surface conditions**. This range will become larger under higher wave conditions and will therefore be characteristic for the wind speed in absence of surfactants.

- The water surface must be a continuous line over the whole width of the image. The found positions will most probably form a **smooth continuous curve**; exceptions may be found in capillary wave trains.

- Since the total reflection of the illuminated plane is part of the image, the water surface must be a **region of high local symmetry**.

- In SP-LIF the distortion of the background pattern in the direct vicinity of the water surface must show least deviations from the ideal background pattern. The water surface must therefore be a line of **highest correlation with the ideal background pattern**.

Variano and Cowen [2007] detected the surface by manual selection in their image sequences - an extremely time consuming task. Münsterer and Jähne [1998] and Falkenroth [2007] used symmetry filtering (binomial filters) for detection. Münsterer and Jähne [1998] combined filtering with a fuzzy logic approach testing for two characteristics of the water surface, on the one hand local minima in intensity encountered in HCl invasion experiments and on the other hand a local high symmetry due to total reflection.
Herlina and Jirka [2008] and Walker and Peirson [2008] searched for the local minimum in intensity in their studies of oxygen transfer with PBA. Walker and Peirson [2008] rejected images where the local minimum could not be identified. Summarizing their results, the identification of the water surface with a homogeneous light sheet cannot be guaranteed in every image. But rejecting certain images may lead to a systematic error in the data sets: The images which do not show a minimum in surface concentration may be the images where just strong bursts or sweeps have removed the high gas concentration completely from the mass boundary layer. By deliberately eliminating them from the data sets, especially the images with high turbulence and therefore high transport are excluded. In that way a significant shift in the results may be produced. To avoid such effects the processing of the data has to ensure that almost all data sets can be evaluated.

9.2 Improvement and Contribution by SP-LIF for Surface Detection

In Static Pattern LIF the available information regarding the surface is nearly doubled, as the local orientation of the background pattern allows the determination of the corresponding surface slope. The additional information of the local slope has to be extracted from the images via an orientation analysis that is presented in this chapter. Surface detection with nearly doubled information on the surface becomes therefore more robust.

9.3 Procedures for Analyzing SP-LIF Data

The sketched five-step procedure presented in 6.3 has to be adapted for practical purposes depending on the situation. Preprocessing, as described in 9.3.1 is mandatory for all image sequences. In the second step two cases will be regarded separately: First, the analysis of SP-LIF data gained with the simple 13-beam illumination is shown in 9.3.2. Here the ideal situation of SP-LIF is presented. Second, analysis is shown for the fine pattern produced by the Laser illumination itself in 9.3.3.

9.3.1 Preprocessing: Removal of Dark Current and Scheimpflug Distortion

This preprocessing steps have to be done for all the described cases. The represent the essential preprocessing of data: A correction for dark current of the CMOS-chip and background illumination is done by taking images of the measurement section without laser illumination before the start of each measurement. The average of these images the so called dark image is subtracted from the individual images of the measurement series. In that way the dark current signal is removed.
The correction for the distortion of the image due to the Scheimpflug setup is done by applying the procedure described in section 8.2.1. The determination of the scaling factor of the background target, was done with an adapted form of the algorithm for determination of the MTF-function written by Rocholz [2008].

9.3.2 Simple 13-Beam Illumination: Flat and Wavy Interface

The image processing procedure in this simple case consists of two steps: First the orientation estimation of single beams and second the estimation of the position of the surface on the identified beams.

Orientation Estimation

As the contrast between illuminating beam and background is so high, a simple threshold can be set to register the beams in a binary image. In the binary image all part of the illumination is set to one, the background to zero. Any disturbances by a concentration signal are eliminated by this registration. A Hough-transform applied to the binary image, e.g. from the MATLAB image processing toolbox, gives the line parameters of the single 13 beams.

Surface Position

Due to the bend at the water surface, the position of the water surface can be identified in the binary image as a position of high corner strength.

Using the boundary tensor of Köthe [2003], implemented for example in the VIGRA image processing toolbox, the edge and junction strength for each pixel can be determined. The boundary tensor T is positive semi-definite symmetric

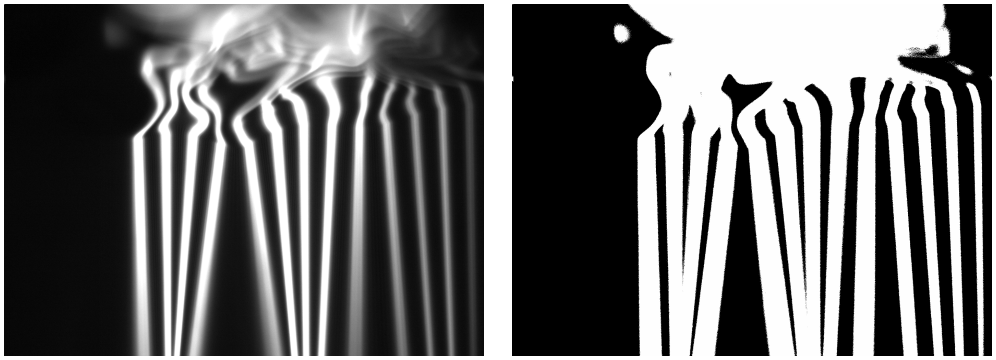

(a) (b)

Figure 9.1: (a) Original image before registration; image taken at wind speed of 8 m/s. (b) Binary Image after registration.

tensor of second order evaluated for each pixel (x,y). It can be decomposed in an edge and junction part:

$$T(x.y) = T_{edge}(x, y) + T_{junction}(x, y) = \tag{9.1}$$

Edge and junction strength can be determined via an analysis of the tensor elements and its trace. For further details see Köthe [2003].

The position of the bend, that appears at the water surface, marks a junction. Therefore the junction strength should show a local maximum, see figure 9.2 as the resulting image of the junction or corner strength determined by applying the boundary tensor. Without a concentration signal the water surface position can be determined with an accuracy of approximately 5 pixel, even under a strongly wavy interface. In the presence of a concentration signal this accuracy can be increased up to 1 pixel. The corner strength gives an estimate of the surface position with an accuracy of 5-pixel. If in the original the neighborhood of the estimated surface position is scanned for the next local minimum in gray value, this local minimum would give the position of the water surface with an accuracy of up to 1 pixel. Once surface orientation and position for the single beams are known, the transformation on a Cartesian mesh can be done. For this the warping algorithm of the HEURISKO image processing toolbox was used.

Summarizing, this single illumination is relatively easy to handle, but gives just a rough estimate of the concentration field.

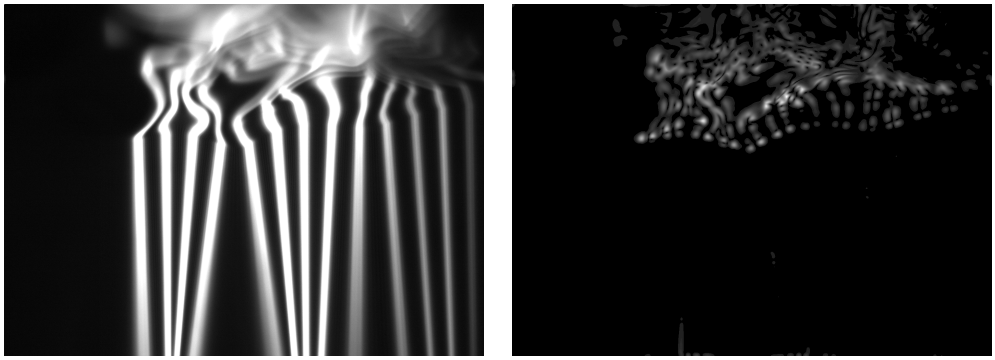

(a) (b)

Figure 9.2: The corner strength determined via the boundary tensor gives an estimate of the surface position. (a) Original image. (b)Corner strength ('cornerness') determined with the boundary tensor. The first maxima in direction from bottom to top of the images mark the position of the water surface with an accuracy of approximately 5 pixel.

9.3.3 Fine Pattern Illumination

In the case of the fine pattern illumination the determination of local orientation and surface position is far more complex than in the case of the simple 13-beam illumination, as background pattern and concentration signal appear as two transparent overlayed signals. The separation of the two transparent signals of background and concentration fields has to be achieved for this case. Image processing of overlayed transparent signals is a very young discipline as Ihrke et al. [2008] discussed in their review paper regarding the state of the art in the analysis of transparent objects. The Optical flow techniques used in that context, for example by Garbe et al. [2006] for analyzing micro flows, are not applicable here, due to the too low upper limit of the frame rate of the camera. Optical flow techniques demand a shift in position in the range of one pixel. However, as the background pattern moves with the phase velocity of the air-water interface and is additionally distorted, the encountered shift of the pattern between the images of a sequences are in the range of 30-200 pixels at a wavy-interface.

In the following paragraphs the cases of a flat and a wavy interface are treated separately due to the differing image processing.

Flat Interface

In the case of a flat interface the background pattern can be simply removed by division of a mean background signal determined before the measurement started in the absence of a concentration signal. What remains is the concentration signal as can be seen in figure 9.3.

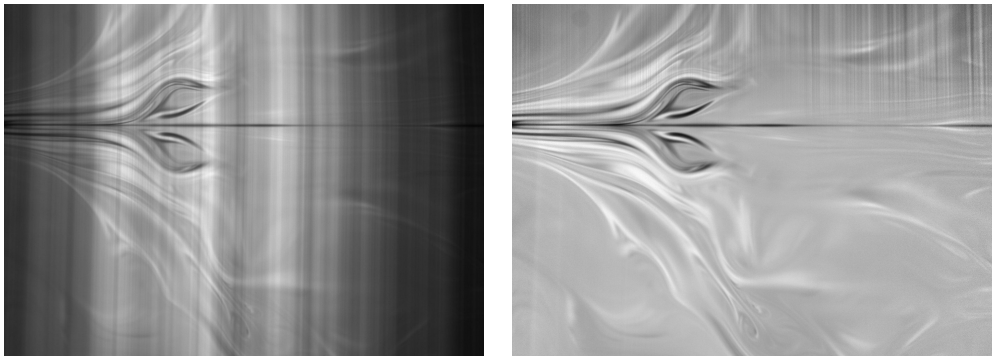

(a) (b)

Figure 9.3: Background correction for fine pattern at a flat surface. (a) Original image before division of the background image; image taken at wind speed of 3 m/s. (b) Background removed image. Except of some noise remainders the pattern could be almost completely removed. In the total reflection above the water surface the pattern remains visible.

Waves

Here, the situation the local orientation of the background pattern has to be determined. Estimation of local orientation is done by a eigenvalue decomposition of symmetric tensors, describing the local orientation by derivatives. These orientations have to be determined for every pixel in the image.
The local orientations are gained as the corresponding eigenvectors. Two different approaches have been tested: The structure tensor and the multiple orientation tensor (MOP). The boundary tensor used in section 9.3.2 is also one example of these tensors. The structure tensor gives the orientation of the strongest structure, while the MOP gives generally two strongest structures per regarded pixel.

Both will be shortly discussed in the following subsections.

The Structure Tensor Approach The structure tensor approach was introduced by Knutsson [1989]. The strongest local orientation is determined by maximizing the following functional:

$$\max_{n} \int_{\Omega} \left(\nabla g(x')^T n\right)^2 d\Omega$$
$$\Longleftrightarrow \max_{\mathbf{a}} \int_{\Omega} \mathbf{n}^T \begin{bmatrix} f_x^2 & f_x f_y \\ f_x f_y & f_y^2 \end{bmatrix} \mathbf{n}\, d\Omega. \tag{9.2}$$

The f_i are the local derivatives with respect to the subscript and $\mathbf{n}$ represents the corresponding eigenvectors that have to be determined. $d\Omega$ stands for a region on which the tensor is calculated, in that way an averaging over the small spatial domain $d\Omega$ is included. The largest eigenvalue of the here defined structure tensor corresponds to the eigenvector of the orientation of largest

strength. In the structure tensor approach it is implicitly assumed that only one local orientation is given. The orientation vector o is defined as

$$\mathbf{o} := \begin{bmatrix} f_y^2 - f_x^2 \\ 2 \cdot f_x f_y \end{bmatrix} \quad . \tag{9.3}$$

Its arguments gives the angle of the orientation, while its absolute value yields a measure for the strength of the single orientation, for more details see Jähne [2005].

In the case of the overlayed signals of background pattern and concentration fields, the structure tensor was applied to the gradient images (images of the derivative of the original image in (a) horizontal and (b) vertical direction). In the horizontal gradient image vertical structures are dominant, while horizontal structures are suppressed. Therefore, here the horizontal eddy components and mainly the water surface with its large horizontal character should appear. In the vertical gradient images it is the other way round. The application of the structure tensor to the vertical gradient image of a moderately wave-influenced image is shown in figure 9.4. The evaluation of the orientation vector gives an

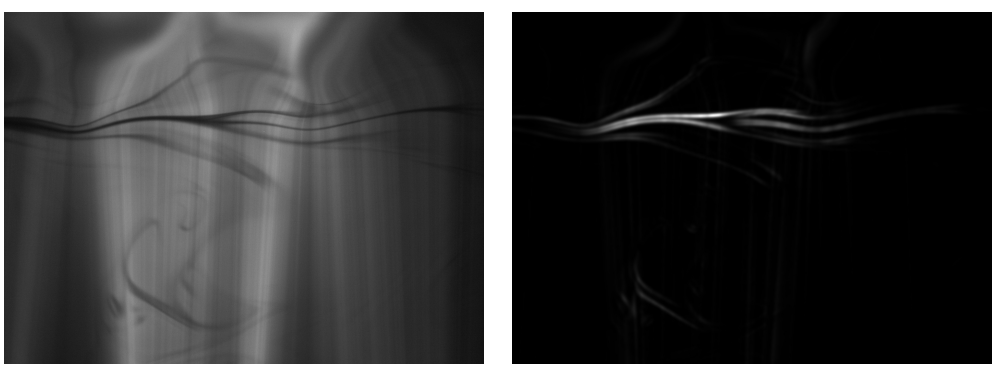

(a) (b)

Figure 9.4: The structure tensor applied to a concentration image: (a) Original image; image taken at a wind speed of 5m/s. (b) Strongest orientation determined by the structure tensor.

estimate of the water surface position. With knowledge of the surface function the background pattern, imaged without a concentration signal as described in section 6.3, is warped to match this surface condition. Division by the warped background pattern gives the concentration signal. The result of this procedure is shown in figure 9.5. This procedure works well once a good estimate of the surface position is available. It works in principle, but the results given by the structure tensor approach had to be revised by a human to achieve good surface estimates.

Summarizing, the method works, but an automatic surface detection without human supervision even at moderate waves could not been achieved so far.

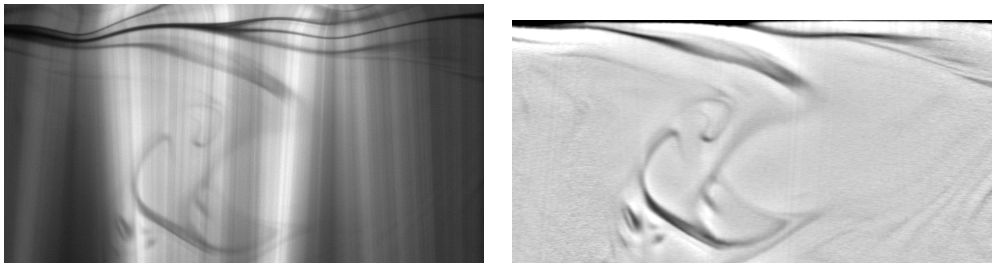

(a) (b)

Figure 9.5: Result of the division of the warped background: (a) Original image; image taken at a wind speed of 5m/s. (b) the remaining concentration signal after division by the warped ideal background signal and warping on a Cartesian mesh.

The Multiple Orientation Tensor For even stronger wave influenced surfaces and high bulk turbulence an additional approach was tested: The multiple orientation tensor was introduced by Aach et al. [2006] for orientation estimation for two overlayed signals and was later extended to multiple local orientations by Aach et al. [2009].
Their approach was to look for the minimum of the the following constraint regarding the two orientation vectors $\mathbf{u}$ and $\mathbf{v}$ on a domain $d\Omega$:

$$\min_{u,v} \int_\Omega \left(\frac{\partial^2}{\partial u \partial v} g(x')^T (u+v) \right)^2 d\Omega$$

$$\Longleftrightarrow \min_{\mathbf{a}} \int_\Omega \mathbf{a}^T \begin{bmatrix} f_{xx}^2 & f_{xx}f_{xy} & f_{xx}f_{yy} \\ f_{xx}f_{xy} & f_{xy}^2 & f_{xy}f_{yy} \\ f_{xx}f_{yy} & f_{xy}f_{yy} & f_{yy}^2 \end{bmatrix} \mathbf{a}\, d\Omega \tag{9.4}$$

Here, the last formulation yields a tensor - the MOP-tensor - for an overlay of two transparent signals with f_{ii} as the corresponding second derivatives evaluated on the area $d\Omega$; $\mathbf{a}$ is the MOP-vector from which the two orientation directions can be determined.

This approach gives two orientations $\mathbf{u}$ and $\mathbf{v}$ in every pixel, but the procedure does not allow to distinguish easily which of the orientations is the dominating one. This lack of a measure for orientation strength is a severe drawback. To determine which of the orientations is the stronger one, the structure tensor has to be evaluated additionally, which increases the computational time. The two orientations were sorted. In figure 9.6 an example image is given. The angle next to 90 degree was counted for orientation one or the vertical pattern (9.6(c)), the other angle was counted for orientation two or the concentration field signal(9.6(d)).

From the image of vertical orientations an estimate of the surface slope can be determined, as the slope is coded in the structure angle. Together with an estimate of the surface position, gained for example by searching for local min-

ima and local symmetry as done by Münsterer and Jähne [1998], fitting of a cubic spline function under the condition of the first derivative matching the determined slopes as a constraint might be an option for the future.

Up to now, the structure tensor image is used for human detection of the water surface. An automatic reconstruction of the water surface failed completely.

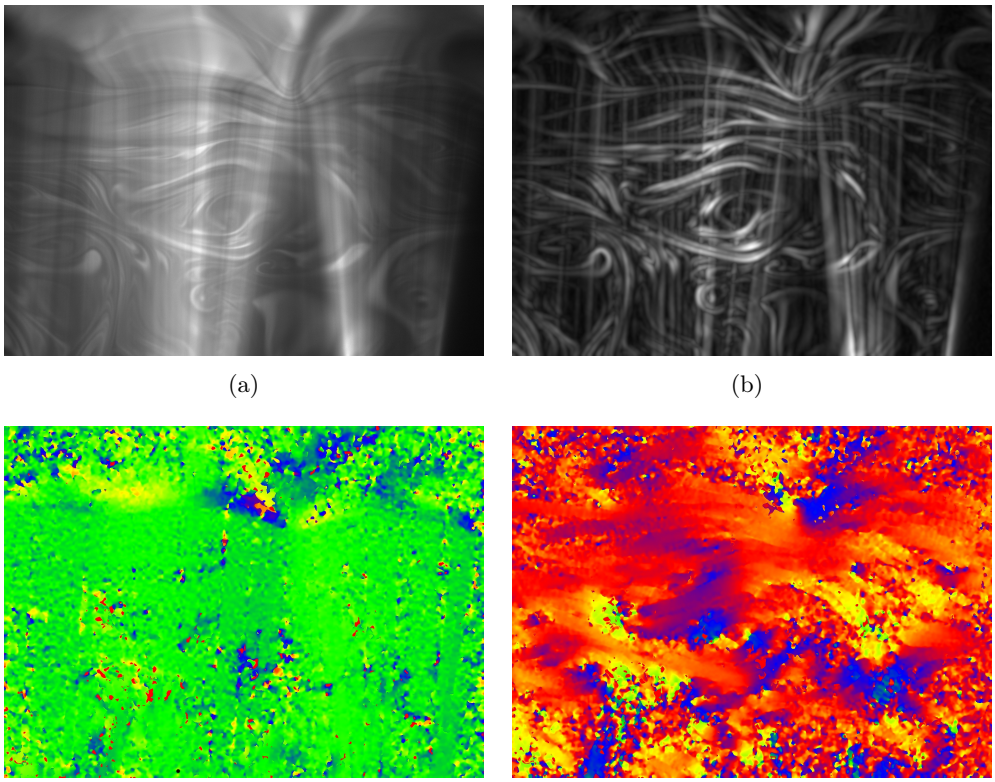

(a) (b) (c) (d)

Figure 9.6: (a) Original image; image taken at wind speed of 6m/s . (b) Strongest orientation determined by the structure tensor. (c) Vertical orientation angle determined by MOP. (d) Horizontal orientation angle determined by MOP. Red represents horizontal structures, green vertical structures. Yellow and blue stand for ± 45 °slope. The noise in both MOP orientation estimations is high.

9.4 Postprocessing

Lambert Beer Correction

The exponential decay term is determined in the concentration signal free background pattern image, that is taken before each measurement. After the transformation of the pattern-freed signal to the Cartesian mesh a correction for

Lamber-Beer decay can be done. The image was then normalized by the average of the exponential decay function to achieve a uniform intensity beside the concentration fluctuations.

Extraction of Dye Concentration from Local Gray Values

The local intensity changes in gray value are directly proportional to the fluorescence intensity and therefore concentration of the anion base component of HPTS the as the buffer point condition was satisfied in all measurements. The following equation gives the relation of the fluorescence intensity to the dye component $R^{-3}OH$, the species that substitutes HCl transport in water:

$$[R^{-3}OH] = C_{t=0} - [R^{-3}O^{-}]. \tag{9.5}$$

9.5 Outlook

As up to now, an automatic reconstruction of the water surface failed completely, here a short outlook is given how this might be achieved. The idea is fitting of a cubic spline function under the condition of the first derivative matching the determined slopes as a constraint.
A spline suitable for this may be the cubic Hermite-spline. A cubic Bezier spline is equivalent to the cubic Hermite spline but is too complex to show here in this outlook.
The intention of a general spline interpolation is to connect given data points by a smooth curve. An introduction to splines is given in Stoer [1994] or Deuflhard and Hohmann [1993], while a detailed presentation can be found in de Boor [1978] including algorithms and FORTRAN-routines.

Spline function is usually defined on an interval $\Delta S = [a, b]$ with a separation:

$$\Delta S := [a = x_0 < x_1 < \cdots < x_n = b]. \tag{9.6}$$

The distance Δx between the individual sub-intervals is assumed to be constant:

$$\Delta x = \text{constant}. \tag{9.7}$$

In an image this would correspond to the given pixel-size. The size of the total interval would be

$$\Delta S = (n+1) \cdot \Delta x. \tag{9.8}$$

Here, both the determined slopes $m_s(x_p, y_p)$ and the estimated positions (x_p, y_p) could be used to set up a two-times continuously differentiable cubic Hermite spline function. The parameters on every sub-interval are given by

$$\begin{aligned} s_i(x) = \quad & y_p + m_s(x_p, y_p) \cdot (x - x_p) + \frac{c_i(y_p, m_s)}{2} \cdot (x - x_p)^2 \\ & + \frac{d_i(y_p, m_s)}{6} \cdot (x - x_p)^3 \end{aligned} \tag{9.9}$$

While the estimates of the second derivatives c_i and third derivatives d_i are calculated from the input m_s and y_p.
The spline has a support of four sub-intervals Δx, meaning that each data point influences the coefficients in four nearest neighbor intervals.

Together with a parameter estimation routine and a rough estimate of the surface positions and slopes this approach can maybe be realized in the future for surface fitting.

9.6 Summary

With the simple 13-beam static pattern illumination that gave a high contrast a fit of the water surface even in the absence of a concentration signal is possible with an accuracy of approximately 5 pixel. In the presence of a concentration signal this could be improved to pixel accuracy.
So promising the results for a high contrast illumination and a rough pattern, the automatic identification of the water surface position with the fine pattern illumination and its low contrast failed up to now. Yet, in the case of high turbulence level, where it was even not possible to identify the water surface even for a human observer in all cases, the static pattern illumination allowed the identification of the water surface by eye, at least after application of the structure tensor.

Chapter 10

Statistical Analysis of the Gained Data Sets

10.1 Statistical Analysis for Controlled-Flux Techniques in Comparison to Constant Concentration Techniques

In contrast to the low-soluble gases CO_2 and O_2, which are subject to a constant concentration at the boundary of the water surface (Henry's law of solubility), the tracer HCl is subject to a flux boundary condition due to its high solubility in water, which can be approximated to be nearing infinity with respect to other gaseous tracers, see section 3.6.
The methods for statistical analysis for the case of a constant flux boundary condition were first presented by Jähne et al. [1995] for the controlled flux-technique in active thermography studies of heat transfer, introduced by Jähne et al. [1989].
These methods are adapted in this study for mass transfer of the tracer HCl, that follows the same boundary condition of the Neumann type.

In the air-phase a constant flux of the tracer is implied. The mean flux density of the gaseous tracer averaged over area A and time τ can be generally described by:

$$\bar{\mathbf{j}} = \frac{1}{A \cdot \tau} \int_{\tau} \int_{A} \mathbf{j}(\mathbf{x}, t) d^2x \, dt. \tag{10.1}$$

As this flux density varies statistically the above formulation is equivalent to the following formulation as the expected value of a continuous probability density function $\mathrm{f}(\mathbf{j})$:

$$\bar{\mathbf{j}} = \int \mathbf{j} \, \mathrm{f}(\mathbf{j}) d\mathbf{j}. \tag{10.2}$$

This probability density function is the true quantity of interest, because it includes the description of transport characteristics. Mean and variance are

just the first moments of this distribution describing center of gravity and spread and contain much less information than the distribution itself, but are readily obtained by measurements.
This flux of the gaseous tracer $\mathbf{j}$ into the water phase characterizes the air-sided transport.
As mass transfer will be mainly studied in the water phase not only the flux $\mathbf{j}$ of the gaseous tracer is of interest but also the water-sided transfer velocity k_w. The following two subsections will present how estimates of the mean transfer velocity k_w can be calculated from measurements depending on the boundary condition encountered at the air-water interface.

10.1.1 Estimation of Water-sided Statistical Quantities for Neumann and Dirichlet-type of Boundary Condition

The transfer velocity depends both on the flux density $\mathbf{j}$ of the gaseous tracer and on the concentration difference Δc according to the definition in section 2.4,

$$k_w = \frac{|\mathbf{j}|}{\Delta c} = \frac{\left|-D\frac{\partial c}{\partial z}|_{z=0}\right|}{\Delta c}.$$

Now an estimate of the transfer velocity k_w has to be calculated for the two cases of

1. a constant concentration difference between bulk and surface $\Delta c = c_{bulk} - c|_{z=0}$ (Dirichlet boundary condition), or
2. a constant flux $\left.\frac{\partial c}{\partial z}\right|_{z=0}$ (Neumann boundary condition).

The flux density can be estimated from a linear fit to the concentration profile within the mass boundary layer, if the diffusion coefficient is known, since Fick's first law yields,

$$\mathbf{j} = -\mathcal{D}\left.\frac{\partial c}{\partial z}\right|_{z=0}. \tag{10.3}$$

The concentration difference can also be extracted from the concentration profiles. In the case of the Dirichlet boundary condition the concentration difference is constant while the flux may vary. In the case of the Neumann boundary condition with a controlled flux, the flux is constant and the concentration difference may vary.
For estimating the mean transfer velocity k_w this has to be taken into account.

Dirichlet Boundary Condition, Δc = constant

$$\begin{aligned} \overline{k_w} &= \overline{\left(\frac{\mathbf{j}}{\Delta c}\right)}, \\ &= \frac{\overline{\mathbf{j}}}{\Delta c} \\ &= \overline{(k_w)_{meas}} \end{aligned} \tag{10.4}$$

With a constant concentration difference the mean transfer velocity can be estimated from averaging the individual transfer velocities at different times t_i. The index *meas* refers to the single measurements.
The time constant of the boundary layer τ^* (see section 2.4.3) is here calculated as

$$\tau^* = \frac{\mathcal{D}}{\overline{k_w}^2}. \tag{10.5}$$

Neumann Boundary Condition, j = constant

$$\begin{aligned} \overline{k_w} &= \overline{\left(\frac{\mathbf{j}}{\Delta c}\right)}, \\ &= \frac{\mathbf{j}}{\overline{\Delta c}}, \\ &= \frac{1}{\overline{(1/k_w)_{meas}}}. \end{aligned} \tag{10.6}$$

In this case, for an unbiased estimate of the mean transfer velocity the mean of the reciprocal transfer velocities at every time t_i has to be calculated. Again the index *meas* refers to the single measurements.
The time constant of the boundary layer τ^* for the Neumann case is calculated as

$$\tau^* = \mathcal{D}\left(\frac{1}{\overline{(1/k_w)_{meas}}^2}\right). \tag{10.7}$$

Summary It is important to choose the corresponding averaging type for each type of boundary condition. This can be shown in a simple example: $k_w^D = \overline{k_w}$ will be the mean of a Dirichlet problem, in which 20% of the registered times the transfer rate will be three-times increased, so $\frac{2}{10}\times$ the single transfer rates, while in 80% of the registered times the transfer rate will be the reduced to the half value, so $\frac{8}{10}\times$ the single transfer rates:
For the Dirichlet type this would correctly lead to

$$\overline{k_w} = \frac{2}{10} \cdot 3k_w^D + \frac{8}{10} \cdot \frac{1}{2}k_w^D = k_w^D. \tag{10.8}$$

If the Neumann type is chosen, but the individual transfer rates still kept as the Dirichlet ones, the obtained mean k_w^N differs significantly as here the reciprocals have to be summarized:

$$\overline{\frac{1}{k_w}} = \frac{2}{10} \cdot \frac{1}{3k_w^D} + \frac{8}{10} \cdot \frac{1}{0.5k_w^D} \tag{10.9}$$

$$\Longrightarrow k_w^N \approx 0.6k_w^D. \tag{10.10}$$

Based on these considerations the quantities that should be obtained from the measurements are chosen.

Chapter 11

Estimation of Systematic Error Sources

Before an evaluation of the measurements can be done an analysis of the expected error sources has to be made. In this chapter the systematic error sources are discussed. Like all measurement techniques Laser-induced fluorescence is biased by various error sources. In the following five subsections these error sources are regarded in with respect to errors affecting the concentration signal in 11.1, errors due to disturbances of the flow regime in section 11.2, followed by the most severe error sources in signal processing 11.3, the errors special for SP-LIF in 11.4 and SPERA in 11.5. The chapter finishes with 11.6 in a summary.

11.1 Errors Affecting the Concentration Signal

In the following subsections error sources of the LIF-technique are discussed individually with respect to their effect on the final concentration estimates and the possibilities to reduce their influence.

11.1.1 Fluorophore

Quenching of Fluorescence by Oxygen or Halogens

Largest reported lifetime of HPTS fluorescence is 5.7 ns by Weller [1958], which is taken as upper limit of the estimates.
Due to the small lifetime quenching effects are rarely encountered. Wolfbeis et al. [1983] reported a fluorescence decreases from saturated nitrogen solute to a saturated oxygen solute by approximately 5%. The fluctuations in oxygen concentration in this setup were smaller by two orders of magnitude, so had no effect. Halogens were not present so their influence could be neglected.

Photobleaching

Every fluorophore is subject to a destruction by intense illumination, this is called photobleaching. Larsen and Crimaldi [2006] formulated a non-dimensional

photobleaching parameter B for planar LIF measurements in aqueous flows. For excitation with a static light-sheet the formulation is the following:

$$B := \frac{Q_p \sigma_a P_{Laser}}{0.5\, h\, \nu\, 2b\, U\, \sqrt{2\pi}} \tag{11.1}$$

with Q_p as number of dye molecules bleached per absorbed photon, σ_a as the absorption cross section of the dye, h as Planck's constant, ν as frequency of the Laser excitation, $2b$ as width of sheet and U as the mean velocity of the water body. If $B < 1.4 \cdot 10^{-2}$ fluorescence intensity variations are less than 1 %.
Wolfbeis et al. [1983] reported HPTS to be less sensitive to photobleaching than fluorescein, but gave no quantitative values for Q_p. For fluorescein $Q_p = 4.6 \cdot 10^{-5}$ is estimated from data of Larsen and Crimaldi [2006] and Tsien et al. [2006]. Using this value for calculations of HPTS and a mean water velocity of 5 cm s^{-1},$\nu = 6.7 \cdot 10^4$Hz, b=0.01 cm and $P_{Laser} = 1.25\, W/cm^2 \cdot 0.02\text{cm}^2$ with a sheet element area size of 0.02 cm^2

$$B \approx 1.0 \cdot 10^{-2} < 1.4 \cdot 10^{-2}. \tag{11.2}$$

According to these estimates photobleaching for the current setup can be neglected for wind speeds greater than 3.5 ms^{-1}. Please note, the water velocity is estimated to be 1-2% of the wind velocity. Better estimates are not available so far, as water velocity has not been measured dependent on wind speed. So photobleaching may have even an higher effect than estimated here.

Optical Heating

Peterman et al. [2003] pointed out that heating effects in water may have non-negligible effects and gave values of the order of 1 K per Watt Laser power.
As Asher and Pankow [1989] reported also an increase of 0.4 K in the illuminated light-sheet of their LIF-application in gas transfer studies, the effect of optical heating in for the given setup was calculated. The specific heat capacity c_v was given as $4.2 \cdot 10^6$J/(m^3 K).

The sheet geometry has been presented in 8.1.2. There the Laser output power was estimated to 1.25 Wm^2 for an illuminated are of 0.04 cm^2. With an quantum yield Φ_q of 0.99 for the anion base maximally 1 % of the Laser power can be transformed to heat.
The extinction coefficient of the dye allows to approximated the volume where 90% of the radiation is absorbed. With a maximal extinction coefficient of the anion base of $\mathfrak{e} = 2.44 \cdot 10^4\text{M}^{-1}\text{cm}^{-1}$[1] (Lamber-Beer decrease in base 10) or $\varepsilon = \mathfrak{e} \cdot \ln(10) = 5.6 \cdot 10^4\text{M}^{-1}\text{cm}^{-1}$ (Lamber-Beer decrease in base e) and a concentration of the anion base of 10^{-5}M the depth of 10 % transmission is

[1] M stands for mol/l.

estimated to:

$$z_{ref} = \frac{-\ln(I/I_0)}{\varepsilon \cdot c_{abase}} \tag{11.3}$$

$$\Rightarrow z_{ref}((10\%)) = \frac{-\ln(0.1)}{\varepsilon \cdot c_{abase}} \tag{11.4}$$

$$z_{ref}((10\%)) \approx 4 \text{ cm.} \tag{11.5}$$

The illuminated volume therefore can be approximated to 0.04 $\text{cm}^2 \times 4\ \text{cm}^2 \approx 0.16\ \text{cm}^3$. In combination with the Laser power that is absorbed in the illuminated volume $P_{Laser} \cdot \Phi_q$ the temperature increase ΔT per second can be estimated to ($c_p = 4.2\ \text{Jg}^{-1}\text{K}^{-1}$; $\rho_{water} \approx 1\, g/cm^3$)

$$\frac{\Delta T}{\Delta t} \approx \frac{\Delta P_{Laser} \cdot \Phi_q}{\rho_{water} \cdot V_{ill} \cdot c_p} \tag{11.6}$$

$$\Rightarrow \frac{\Delta T}{\Delta t} \approx 2 \cdot 10^{-5}\text{Ksec}^{-1}. \tag{11.7}$$

This value can be neglected with respect to heat fluxes due to evaporation. The actual heating effect has to be lower since the fluid flow has not been respected here.

Oversaturation by Laser Excitation

Saturation of fluorescence emission is a severe problem as scattering processes like Raman and Rayleigh scattering are proportional to the excitation power and do not reach a saturation value like fluorescence. An excitation near saturation therefore reduces the signal to noise ration significantly.
Tsien et al. [2006] reported a simple way of estimating a possible oversaturation by the fluorescent dye, that is followed in this subsection: In steady state the depopulation rate constant k_F of the excited state and the rate constant of excitation k_a are linked via the following relation, where x is the fraction of molecules in excited state, and (1-x) the fraction of molecules in ground state:

$$k_F \cdot x = k_a\,(1 - x) \tag{11.8}$$

$$\rightarrow x = \frac{k_a}{(k_a + k_F)}. \tag{11.9}$$

The excited state lifetime τ_F of HPTS anion base is 5.29 ns according to Prayer [1997]. Molecules in the excited state are depopulated with a rate constant k_F including all possible depopulation channels calculated as

$$k_F = \frac{1}{\tau_F} \approx 1.9 \cdot 10^8\text{sec}^{-1}. \tag{11.10}$$

The rate constant of excitation can be estimated to

$$k_a = \sigma_a \cdot E_{Laser}. \tag{11.11}$$

The cross section of absorption σ_a can be estimated with the maximum extinction coefficient at 454 nm $\mathfrak{e}(454\text{nm}) = 2.44 \pm 0.01 \cdot 10^4 \text{M}^{-1}\text{cm}^{-1}$(Prayer [1997]) and the Avogadro number N_a to:

$$\sigma(454\text{nm}) = \frac{\mathfrak{e}(454\text{nm}) \cdot ln(10) \cdot 10^3\, cm^3 l^{-1}}{\text{N}_a} \tag{11.12}$$

$$\approx 9.3 \cdot 10^{-17}\text{cm}^2. \tag{11.13}$$

The irradiance of the Laser in numbers of photons E_{Laser} can be estimated to ($\nu_{ex} \approx 445\text{nm}$)

$$E_{Laser} = \frac{P_{Laser}}{h\nu_{ex}} \tag{11.14}$$

$$\approx 2.8 \cdot 10^{18}\text{photons cm}^{-2}\text{sec}^{-1}. \tag{11.15}$$

Thus leading to a rate constant :

$$k_a \approx 2.61 \cdot 10^2 \text{ sec}^{-1}. \tag{11.16}$$

The fraction of molecules in the excited state is with these values estimated to

$$x = 1.4 \cdot 10^{-6}. \tag{11.17}$$

So saturation is not reached by far.
Furthermore, the maximum rate of output k_{em}^{max} of photons per molecule can be estimated to

$$k_{em}^{max} = \Phi_q \cdot k_F \tag{11.18}$$

$$\approx 2.0 \cdot 10^8 \text{ photons sec}^{-1}. \tag{11.19}$$

The output per molecule in the present setup is then 10^6 times lower.

For a negligible triplet state excitation Tsien et al. [2006] states, that the noise N is found to be proportional

$$N \propto k_a^{0.5}, \tag{11.20}$$

and the signal S proportional to

$$S \propto \frac{k_a}{k_a + k_F}. \tag{11.21}$$

The signal to noise ratio $\frac{S}{N}$ is then proportional to the following ratio:

$$\frac{S}{N} \propto \frac{k_a^{0.5}}{k_a + k_F} \tag{11.22}$$

This expression is maximized for $k_a = k_F$.
So the present configuration is a factor of 10^6 away from best signal to noise ratio with respect to fluorescence. An increase of signal to noise ratio with the current maximal input power of the Laser of 400 mW can only be achieved in a more focused sheet or by using a dynamic sheet configuration. A dynamic sheet however cannot be used in a SP-LIF setup as the static background pattern is needed. But a dynamic sheet can be used in SPERA, which is planned to do in future experiments.
With respect to photobleaching however, a further increase in Laser power is only suitable at higher wind speeds, see section 11.1.1.

Reduction of Laser Excitation by Medium and Reabsorption by Dye Solution

The extinction coefficient of the fluorophore component has been determined in aqueous solution, therefore absorption by the medium is included in this term and should not appear as a additional quantity. The proportion of absorption of the medium with respect to the extinction coefficient at the Laser excitation wavelength is a factor of 10^{-3} and can be neglected: The emitted Laser lines used in this work are in the range of 440-450 nm, here the absorption coefficient of pure water Sogandares and Fry [1997] reported to be below $1.0 \cdot 10^{-4}\mathrm{cm}^{-1}$. Characteristic extinction coefficients of fluorescent dyes are in the range of $3 \cdot 10^4\,\mathrm{M}^{-1}\mathrm{cm}^{-1}$ according to Schmidt [2000]. Together with the typical dye concentrations used for LIF experiments in this work c= 10^{-5}M this leads to an absorption coefficient of $\alpha_{fluorophore} = \varepsilon \cdot c \approx 3.0 \cdot 10^{-1}\mathrm{cm}^{-1}$ so three orders of magnitude higher than the absorption by the aqueous medium.

The reabsorption of fluorescence by the fluorophore itself is more severe. The probability of reabsorption is linked to the Stoke's shift between absorption and emission spectra. The larger the Stokes shift the smaller usually is the overlap of the two spectra and therefore the probability of reabsorption when traversing the dye solution. HPTS offers with 57 nm an extremely large Stokes shift, see section 3.7.4. Spry et al. [2007] reported for concentrations of less than 10^{-4} M negligible reabsorption.

11.1.2 Optical Setup

In this section the influence of the optical setup is presented. This includes variations of the light source, as well as scattering and influence of the sheet thickness on the quality of the concentration signal.

Variations in Laser Intensity

Instabilities in the Laser intensity were encountered by many authors. For that reason Asher and Litchendorf [2009] log the Laser intensity during all measurements separately. Therefore, the stability of excitation of the here used solid-state Laser was examined for these effects. Measurements yield fluctuations less than 1 % of total output power. After a warming phase of 20 minutes, a drift in output power could not be encountered any more. See section 8.1.1 for further details on the Laser.

Scattering

Known problems of LIF are a sensitivity towards scattering of the excitation light as shown by Platt and Stutz [2000]. Fluorescence with typical cross sections of $10^{-14} - 10^{-25}\,\mathrm{cm}^2/sr$ may be overlayed by different kinds of scattering processes:

- Rayleigh scattering,

- Raman scattering, and
- Mie scattering.

Rayleigh scattering occurs if light scatters at particles smaller than the wavelength. In the wind-wave tunnel the dye molecules act as scattering particles. Rayleigh scattering is proportional to the irradiance E and the proportional $\propto \frac{1}{\lambda_L^4}$. Typical scattering cross sections are $10^{-26} - 10^{-29}\,\mathrm{cm}^2/sr$. As Raleigh scattering does not shift the wavelength of the scattered light, it can be prevented from entering the detector by a simple filter.

Mie scattering occurs at particles much larger than the wavelength and is encountered at floating dust particles in a wind-wave tunnel. As it also does not lead to a wavelength shift it can be suppressed by using a bandpass filter. Typical scattering cross sections are $10^{-6} - 10^{-24}\,\mathrm{cm}^2/sr$.

Raman scattering cannot be prevented in the solvent water, yet its peak scattering cross section is $10^{-29} - 10^{-31}\,\mathrm{cm}^2/sr$. Values for typical cross sections have been taken from Kruppa et al. [2001].

The scattering cross section of HPTS anion base absorption has been calculated to be $9.3 \cdot 10^{-17}\mathrm{cm}^2$ in subsection 11.1.1.
The respective cross section for HPTS anion base fluorescence is then with quantum yield $\Phi_q = 0.986$ (Prayer [1997])

$$\sigma(454\mathrm{nm}) = \Phi_q \frac{\varepsilon_{abase}(454\mathrm{nm})}{\mathrm{N}_a} \tag{11.23}$$

$$\approx 9.2 \cdot 10^{-17}\mathrm{cm}^2\text{per molecule.} \tag{11.24}$$

For HPTS the cross section of fluorescence exceeds the Rayleigh scattering cross section by 10 orders of magnitude. So only Mie scattering may disturb the fluorescence signal but can also effectively reduced by using a filter for the excitation wavelength. Mie scattering occurs at dust particles within the solution. With a water filter of several μm pore size the percentage of dust can be strongly reduced. Moreover, the dust protection tent set up around the wind-wave tunnel prevents dust particles from entering the measuring section in the first place, see section 7 for details.

Influence of Sheet Thickness and Angle of View: Blurring In an illuminating sheet of finite thickness surface blurring appears wherever an overlay of two rays exists. Walker and Peirson [2008] gave an estimate for the maximal depth Δz_{b1} where blurring can be expected by the following relation between sheet thickness t and observation angle θ:

$$\tan\theta = \frac{\Delta z_{b1}}{0.5t} \tag{11.25}$$

$$\longrightarrow \Delta z_{b1} = \frac{t\tan\theta}{2}. \tag{11.26}$$

With a configuration of $\theta = 14.6$ °and a sheet thickness of 0.1 mm this yields a mean blurring depth of 13 μm or approximately 0.5 pixel. A thickness of 0.5 mm already 3 pixel would be affected by blurring. A much stronger proportion on blurring may be caused by integration of varying concentrations along the light path trough the sheet. A sketch of this situation is given in figure 11.1. The recorded radiance can be calculated using $l = t/cos(\theta)$

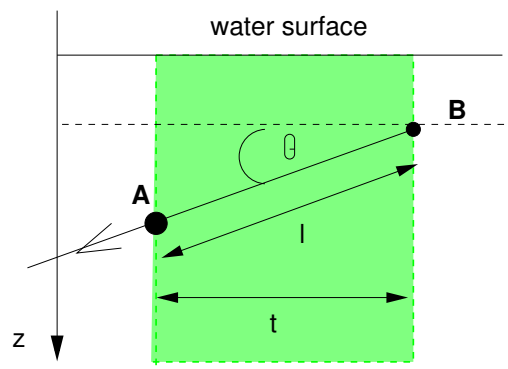

Figure 11.1: Variation of intensity along the path from B to A. The camera integrates the intensity along the light path of length l.

$$L = \int_{s=0}^{s=l} L(s)ds, \tag{11.27}$$

$$L \approx \frac{L(A) - L(B)}{l} \tag{11.28}$$

thus giving a blurring of intensities over a range of

$$\Delta z_{b2} = t \cdot \cos(\theta)\sin(\theta). \tag{11.29}$$

With a configuration of $\theta = 14.6$ °and a sheet thickness of 0.1 mm this yields a range of $\Delta z^{b2} \approx 24\,\mu m$ or 1 pixel. This kind of blurring is present over the whole imaged area and therefore over the whole concentration profile. This would imply that a higher resolution than 25 μm would not improve the resolution in the concentration field.

Blurring due to Extended Exposure Times Another source for blurring are is an extended exposure time. For the static sheet configuration the following condition has to be fulfilled, see (8.1.2)

$$u \cdot t_{exposure} \,/\, L_{structure} < 1. \tag{11.30}$$

As on a camera chip resolution is discretized in pixels the smallest distance that may appear on the digital image would be a movement around a distance of one pixel. With the data of Ültzhöfer [2008] and own data presented in paragraph A.3, the upper limits of exposure time could be calculated for the static sheet configuration. The surface is assumed to move with 2 % of the wind velocity as

upper limit of an estimate of velocity. For an average wind speed of 5 ms^{-1}, a pixel size of 25 μm and an exposure time of usually 0.8 ms at the highest Laser power. The surface blurring would affect,

$$L_{pixel} \approx u_{water} \cdot t_{exposure} \tag{11.31}$$

$$\approx 1.6\,\text{pixel}. \tag{11.32}$$

So a blurring of 2 pixel can be expected at the surface and in the near surface region. Further down, towards the bulk blurring should be drastically reduced as the turbulence elements are more likely to move with velocities of the order of the water-sided friction velocity.

The camera exposure time limit of 0.03 μs sets the minimal value (see section 8.2). For improving the temporal resolution the 'pulsed sheet' configuration presented in section 8.1.2 is needed.

Errors in Detection of the Water Surface

The detection of the water surface especially under waves is a demanding task. In the case of the simple 13-beam illumination the detection of the water surface can be achieved with pixel accuracy. In the case of the fine-pattern illumination under waves the reconstruction achieved an accuracy of 3 pixel under semi-automatic detection. This error in detection influences the whole concentration estimation, as the background pattern orientation will be estimated incorrectly. Parts of the pattern, will remain in the image due to a wrong estimation of its orientation, that cannot be corrected for. So a high background noise of the pattern signal hints a bad estimate of the surface position and orientation. Next to the surface this effect should be least noticeable, but as slopes next to infinity can appear in capillary wave trains, they cannot be neglected. The only possibility is again supervision of the corrected image sequence and a manual removal of images with a too high noise level.

11.1.3 Effects of Temperature Variation

Effects of temperature variations include changes in fluorescence as well as any other chemical reaction taking place in the wind-wave tunnel. Furthermore, chemical reactions themselves like the dissolution of HCl at the water surface may lead to temperature variations thus influencing fluorescence intensity and therefore the concentration signal.

Temperature Dependence of Fluorescence

Coppeta and Rogers [1998] reported a varying temperature dependence in fluorescence of HPTS. For that reason own measurements were conducted and gave a value of $-0.25 \pm 0.03\%$ per Kelvin in the temperature range from 10 - 35 degrees Celsius at an excitation wavelength of 445 nm and pH 8. Measurements were carried out with a Varian Eclipse Carrier Fluorescence Spectrometer with a

Peltier temperature regulation unit[2]. For further details on temperature dependence see section 3.7.4. So changes in fluorescence due to temperature changes can be neglected in the experiments as water temperature was stabilized during measurements with variations of ±0.5K. Under temperature gradients above 3 K between the tunnel water and the air and humidity below 100 % an increase of fluorescence could be detected in the topmost 1mm, thus implying a temperature decrease of -0.75 K in this layer. Evaporative cooling at the surface was assumed to be the cause. Under measurement conditions the tunnel was closed so that relative humidity reached 100 % and such effects could not be detected.

Temperature Dependence of Chemical Constants and Physical Properties of the Flow

All chemical reactions are influenced by changes in temperature, for example the equilibrium constant of the individual reaction according to

$$\ln K = -\frac{\Delta H^0}{RT} + \text{constant}. \tag{11.33}$$

Furthermore, mass diffusion coefficients show a strong temperature dependence and so does viscosity.
As the effect on mass transport of the interaction of all these quantities cannot be estimated without high effort, the temperature during all conducted measurements was stabilized to 20 °C for measurements in the winter term and 22 °C for measurements in the summer term with a variation of ±0.5K. The temperature of the water was adjusted to be 2 degrees below mean room temperature to prevent condensation on the walls of the wind-wave tunnel. Air-temperature in the wind-wave tunnel was 21°C and 23 °C, respectively. The difference between summer and winter temperature results from a maximum temperature difference the heating/cooling units were able to handle.
This temperature gradient was necessary to prevent condensation effects on the tunnel walls, as this would increase the effective water surface for HCl transfer drastically. With a total water surface of approximately 1 m^2 compared to over 54 m^2 total surface of all tunnel elements this is an effect that has to be regarded.

Temperature Increase at the Water Surface by Solution of HCl

If HCl dissolves at the water surface into the ions H^+ and Cl^- Gibb's standard free energy change for ion formation ΔG_F^0 is at a temperature of 20 °C, Riedel [1999]

$$\Delta G_F^0 = -95.4 \text{ kJmol}^{-1}. \tag{11.34}$$

With a typical value of total HCl mass m_{HCl} needed during one measurement in the flume atmosphere of the water segment $10^{-4} \cdot \frac{V^a_{waterSeg}}{V^a_t ot}$ mol $\approx 10^{-4} \cdot \frac{390}{3000} \approx 10^{-3}$ mol, an upper limit can be given for maximum heat production under the assumption that all HCl dissociates in the topmost $d_s = 1\,\mu$m. Münsterer

[2]The spectrometer is property of the AG Herten at Bioquant, Uni. Heidelberg.

[1996] reported this as depth of solution $d_s = 1\,\mu$m, where 99 % of dissolved HCl is dissociated to its ions. These values yield:

$$\Delta T = \frac{m_{HCl}\Delta G_F^0}{\rho_{water}V_{water}} \tag{11.35}$$

$$\approx 0.2 \text{ K.} \tag{11.36}$$

ρ_{water} and $V_{water} = \text{Area}_{waterSurface} \cdot d_s$ meaning density of water and volume of water in which HCl dissolves. As only a fraction of the total amount of HCl is so near the water surface that it can dissolve, this value is expected to be much lower. Furthermore, condensate of water on the tunnel walls can act as a further sink of HCl, as it increases the surface available for dissolution.

11.1.4 Errors due to Illumination Refraction Perpendicular to Observation Plane

As the wave field shows not only variations in wind-direction but also perpendicular to the flow, even if these are less strong (about 20 % less), but these refractions are also a source of errors. The measurement setup does not allow to correct for these effects but in SP-LIF the pattern allows at least to identify the images in which these effects were strong: If the sheet moves out of the focal plane, the fine structures of the pattern vanish. So the decrease in the fine structures is used to identify the disoriented images and remove them manually from the data stack. However, small perturbations cannot be detected and are assumed to be not significant.

11.2 Disturbances of Flow Regime in the Wind-Wave Tunnel

The mean flow in the wind-wave tunnel may be disturbed by temperature flows or secondary currents induced for example by pumps. Furthermore, the air-sided flux of the tracer gas is supposed to be constant in all tunnel elements, however the construction of the inlet of the tracer creates not a perfect homogeneous distribution in the air phase and therefore varying fluxes.

11.2.1 Temperature Flows

Thermal flows that may be overlayed on the mean flow can disturb and should therefore be prevented as far as possible. Though the wind-wave tunnel is well isolated against its surroundings, temperature flows will be present in the wind-wave tunnel not only due to solution processes but also due to the temperature gradient of 1 K between tunnel atmosphere and water, that has been kept up during measurements to prevent the forming of water films on the tunnel surfaces.

According to Garbe [2002] a net heat flux density out of the water can be estimated from the estimated mean temperature change. With a mean temperature increase of 0.5 K per hour of the water, thus $\frac{dT}{dt} < 1.4 \cdot 10^{-4}\,\text{K s}^{-1}$, and with

$c_p = 4.18 \cdot 10^3$ Jkg^{-1}K^{-1}, $\rho = 998$ kgm^{-3} at 20 °C and a water depth of $h_{water} = 9$ cm this net heat flux can be estimated to:

$$\mathbf{j_{net}} = \rho\, c_p\, h_{water} \frac{dT}{dt} \tag{11.37}$$

$$\approx 52\,\mathrm{Wm}^{-2} \tag{11.38}$$

This value is in the range of heat fluxes applied on the surface in active thermography and well below typical flux densities in sensible heat transfer under environmental conditions, Jähne [1991]. In active thermography heat fluxes of this order are neglected.

11.2.2 Secondary Currents

Though a linear wind-wave tunnel is not affected by the typical secondary currents of a annular tunnel, in which a circular fluid motion around the main flow is encountered, other kinds of currents might still be present.
One source of secondary currents are system components. The turbulence induced by the small pumping system that extracts bulk water to measure current mean concentration and concentration of the two components of the fluorophore, may not be neglected at low wind-speeds. For that reason at wind speeds below 4 m/s the pump has been turned off during measurements. Bulk changes where only measured between the single measurements. The geometry of the wind-wave tunnel may influence the measured turbulence structures and concentration fields as well. To avoid disturbances of the flow by the side walls, the illuminated cross section was centered in the tunnel. The wave field measured by Huhn [2008] perpendicular to the main flow, showed a kind of Gaussian distribution around the center. The geometric effects also include the back-flow of fluid at the base of the wind-wave tunnel, which is estimated to affect the lower 2/3 of the depth, Jähne [2006]. According to this assumption the test cross section should not be affected, as only the topmost 25 mm of the total 90 mm are imaged. Yet, this assumption is no guarantee. In the scope of this study the effect of bottom back current has not been tested, but would be worth to do in an additional study. The only possibility at the moment is to compare the results of this study with future studies in different wind-wave tunnels to check for differences in the concentration fields and structures.

11.2.3 Heterogeneous Distribution of HCl Concentration in Air

For the measurements it is necessary that HCl is homogeneously distributed in the air phase when entering the measurement section, the water segment. In this subsection the dispersion of the HCl plume will be estimated when entering the water segment.
A turbulent flow regime can be expected in the wind-wave tunnel at typical measurement speeds greater than 3 ms^{-1}, see section A.3. HCl is added via a tip into the middle of the flow stream directly behind the wind generator, there

turbulent motion is expected to be high and therefore turbulent dispersion. Distance to the water segment is about 8 m, a infinitesimal flow volume would need about $t = 2.7$ sec at a mean wind speed u of 3 ms^{-1}.
A lower limit of dispersion of the HCl plume can be estimated according to Cussler [1997] for flow in a circular tube:
As turbulent flow is assumed, the radial dispersion coefficient can be estimated to

$$E_r \approx \frac{d \cdot u}{600}. \tag{11.39}$$

d is here the cross section of the flow leading elements $d \approx 42$ cm. The mean quadratic displacement σ_q can then be estimated to

$$\sigma_q = \sqrt{2D^a_{HCl}t} \tag{11.40}$$

$$\approx 10\text{cm}. \tag{11.41}$$

So the plume of HCl has already spread to a circle of 20 cm diameter when first entering the water segment with a width of 42 cm.
In reality, the dispersion should be greater as the two 90-degree bends of the bending units together with the rotor turbulence are not regarded in this approximation. An increase by a factor of 2-3 seems to be reasonable.
At least after once cycling trough the tunnel, the plume has spread to the 42 cm of the mean tunnel cross section. The rough estimate made here suggests that the distribution will not be completely homogeneous but next to homogeneous at least in the middle of the wind-wave tunnel. Any variation in the air-sided distribution will appear in the measurements as varying fluxes. A moving of the HCl injection unit before the inlet may increase the distance for mixing, but would increase the danger of damage to the wind generator.

11.3 Error in Signal Processing

11.3.1 Wrong Estimation of Buffer Point

Wrong estimation of the buffer point is the most severe problem of the pH-technique. If measurements are made when the buffer point condition is not fulfilled, the change in fluorescence intensity of the anion base is no longer proportional to the concentration change of the dissolved gaseous tracer. See section 3.4.2 for a detailed discussion of the effects.
The fulfillment of the buffer point condition may vary locally within the water segment. Therefore, besides measuring of the bulk concentration of the two fluorophore species, the experimenter must search the taken individual image sequences of a measurement series at one fetch position for the best contrast, which is the optical hint for reaching the buffer point locally. Usually, only 2-3 sequences out of the 30-40 of the total series showed an equally high contrast. An estimate of the remaining error in identification of the buffer point may be 5-20 %.

11.3.2 Violation of Lambert-Beer Decay by Strong Concentration Variations

Coppeta and Rogers [1998] already mentioned a violation of the Lambert-Beer decay of fluorescence intensity due to strong local concentration variations.
The local concentration of the gaseous tracer HCl under extreme conditions could be so high that the concentration of the fluorescing anion base of HPTS is reduced to a value near zero. Nothing is absorbed at that location and therefore nothing can be emitted and the radiance also drops to zero, see figure 11.2. This means that below such a strongly acid location the intensity of the excitation is higher than it would be expected and without correction by a fit of an exponential decay a higher local concentration would be extracted.

These effects belong also to measurement regimes, where the buffer point

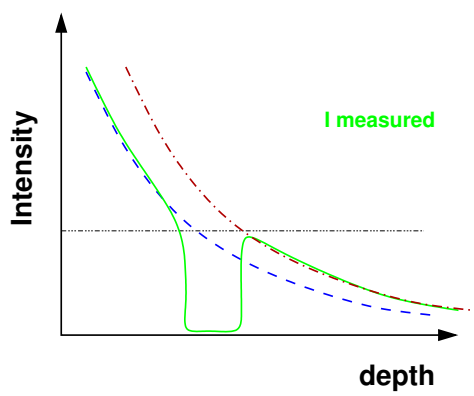

Figure 11.2: Violation of assumption of Lambert-Beer decay of fluorescence intensity due to extreme concentration variations. The dashed lines mark the exponential Lambert-Beer decay. In blue the decay above the location of extreme concentration is marked. The red dashed line lies above the blue line, as in the extreme concentration area nothing has been absorbed and so the intensity in that depth becomes too high for that depth- compared to the undisturbed case.

condition is violated. This will happen if the flux of HCl into the water body is too high, see section 3.4.3.
This has to be prevented by a careful observation of the gradient directly at the water surface: if an extremely low intensity next to the surface can be detected with no visible gradient in gray value the buffer point condition is violated and the tracer flux has to be reduced.

11.3.3 Errors in Diffusivity of Gaseous Tracer

The error in the constant of diffusion or diffusivity is not only an error of the pH-technique but also of every technique using gaseous tracers. The error of the diffusivity $\mathcal{D}$ is quite large. If transfer velocities are to be calculated from

concentration profiles, this error cannot be ignored:

$$\mathbf{k} = \frac{\mathcal{D}\frac{\partial c}{\partial z}\Big|_{z=0}}{c_{z=0} - c_{bulk}}. \tag{11.42}$$

In the case of the coupled diffusivity of the tracer HCl and the dye HPTS the error in diffusivity is approximately 20 %, see section 3.4.3. Compared to the error in the concentration gradient and the concentration difference, this determines the error of the resulting transfer velocity. Yet, the error is a scaling factor given that the Schmidt number exponent is constant. So at least the relative errors between transfer velocities at different wind speeds and fetch conditions are not affected.

11.4 Discussion of Special Error Sources of SP-LIF

The main error source for SP-LIF is the wrong identification of the water surface which is done via image processing. A wrong surface identification has two effects: On the one hand, it leads to a wrong depth reconstruction which again leads to wrong depth-dependent concentration fields. On the other hand, a wrong identification leads to a bad correction of the data with respect to the background pattern, which means that parts of the pattern remain as additional noise in the concentration images.
The error of this wrong identification is hard to estimate with the current number of evaluated images, but seems to be in the order of 2 -10% (after supervision) with an increase with increasing surface roughness, where the surface identification is more demanding.

11.5 Discussion of Special Error Sources of SPERA

Besides the above presented error sources, the spectral approach includes errors resulting from the optimization routines for detecting the global optimal solution of concentrations. The quality of fit is also hard to evaluate.
Errors in reconstruction may be checked for real experimental data by a comparison of the estimated concentrations to the results of a LIF side-setup. Up to now, the intensity of the emitted spectrum was too low for the commercial spectrometer used, so that this test still lacks. A test of the errors in reconstruction have been estimated in noised artificial data sets to be of the order of 1% for non-Gaussian noise and three depth layers. For five depth layers, only one of the test cases gave a solution, there the first two depth layers were estimated with an error of approximately 10%, while the errors towards the deeper layers increased up to 40%.

A further error source special for the spectral reconstruction approach mark the occurrence of singular events, i.e. wave slopes exceeding 85 degrees with respect to the horizontal line, which appear in capillary wave trains. In SPERA measurements in contrast to side-setup measurements these events cannot be

registered easily, at these points the intensity of the emitted integral spectrum would drop to zero. So a pre-analysis of the images for these spots could prevent a wrong reconstruction.

11.6 Summary

The most severe errors of the here used pH-technique are a bad estimate of the diffusivity and the wrong identification of the buffer point. While diffusivity gives a factor with error of about 20 % to transfer rates, the wrong determination of the buffer point is harder to handle. The determination of the local buffer point depends on the experimenters knowledge and practical experience. An error can only be estimated to be of 2-10 percent. The discussion of the other error sources in this section led to the conclusion that from general errors only temperature drifts mark the most severe problems that cannot as easily reduced as Mie scattering by using optical and particle filters.
In spite of all temperature stabilizing efforts, the experimenter has to make sure that if drifts exceed ± 0.5 K the measurements are stopped to prevent inconsistent measurements. In future, if temperature dependencies of system parameters are more readily known it may be able to correct for these drifts but at the present state this is impossible.
The additional error sources for SP-LIF and SPERA are method dependent. The errors in SP-LIF are estimated to be below the errors due to wrong buffer point identification.
The errors of SPERA however are estimated to be of the same order of magnitude as the wrong identification of the buffer point, thus leading to errors in the range of 10-30% in total for three depth layers.

Part VI

Results and Discussion

Chapter 12

Results: Static-Pattern LIF

In this chapter the obtained results of the Static-Pattern LIF technique will be reported in two sections:
In the first section the conditions are described under which measurements were conducted. The second section describes qualitative observations regarding wave slopes and moreover the flow characteristics at different levels of turbulence. These qualitative observations allow to distinguish the different models for gas exchange presented in 2.5, with respect to their assumptions on the turbulence structures. This section will end with a comparison of the gained results with results by qualitative measurements of other authors.
Unfortunately, quantitative results of the measurement technique cannot be presented in this thesis, as the image processing procedures did not work reliably until the handing in of the study.

12.1 Conducted Measurements

Measurements were conducted under wind velocities ranging from 0 to 7.5 ms^{-1} and at five positions with fetch from 67 to 210 cm with a distance of approximately 46 cm (67.4 cm, 103.1 cm, 138.9 cm, 174.6 cm, and 210.2 cm).
As only a small amount of the measurements satisfied the buffer point condition after detailed inspection about 90% of the measurements were rejected see section 3.4. The remaining measurements used for analysis are listed in the table 12.1.

Mean Wind velocity [ms^{-1}]	**fetch: 67.4 cm**	**fetch 2: 103.1 cm**	**fetch 3: 138.9 cm**	**fetch 4: 174.6 cm**	**fetch 5: 210.2 cm**
1	-	-	-	-	-
2	1/374/67 Hz	-	-	-	-
2	1/374/2 Hz	-	-	-	-
3	-	-	-	2/374/67 Hz	1/374/67 Hz
3	-	-	-	1/374/2 Hz	1/374/2 Hz
4	-	-	-	-	-
5	-	-	-	2/374/67 Hz	-
5	-	1/374/2 Hz	-	-	-
6	-	1/374/67 Hz	1/374/67 Hz	1/374/67 Hz	
6	-	1/374/2 Hz	-	-	1/374/2 Hz
6.4	5/1159/150 Hz	-	-	-	5/1159/150 Hz
	2/300/15 Hz	-	-	-	2/300/15 Hz
7.3	5/1159/150 Hz	-	-	-	5/1159/150 Hz

Table 12.1: Measurement conditions regarding wind speed and fetch position. The numbers in the columns stand for: number of series/images per series/frame rate. The used image size in pixels was 1024 x 1400 pixels with 1023 gray values (10 bit) and a total measurement time of 5.6 sec per series in the case of 67 Hz measurements and 660 x 1400 pixels with 255 gray values (8 bit) and a total measurement time of 7.7 sec per series in the case of 150 Hz frame rate. Moreover, measurement series with 2 Hz (367 images/10 bit) and 15 Hz (1500 images/8 bit) were taken to achieve non-correlated images for statistical analysis. Only measurements are listed which were conducted at the buffer point of the dye-solution, so that the pH-measurement method was applicable, see section 3.4 for details.

12.2 Qualitative Results

In this section all qualitative results that have been gained in this study are presented.
First, several characteristic events in turbulent transport, that could be identified in the image series, are described in section 12.2.1. Then their statistical appearance at different wind speeds and two different fetch positions is presented in 12.2.2. Furthermore, the SP-LIF allows to identify (at least for a human observer) the surface location and therefore also the local surface slope, especially in capillary wave trains where measurements of the surface slope are rare. With the knowledge of the surface orientation a relationship between turbulence motion and wave state can be also investigated, which is done in section 12.2.5.

12.2.1 Identified Coherent Structures in the Surface Vicinity under Wind-Induced Turbulence

In this subsection a qualitative description of the observed coherent structures is given. They were classified in five individual groups. For the qualitative characterization data sets recorded with a framerate of 2 Hz have been used, to ensure no correlation between the individual images of the series.
The discussion starts with the two most widely encountered types: 'layering' and 'eddy cascades'. Layering seems to dominate at lower wind speeds, while eddy cascades seem to dominate at higher wind speeds.
More special types of bursts and sweeps will be shown in the following subsections, called jet events, pike-heart events, and jet explosion. The images shown here for characterization correspond to a plane section of 34 $\times$ 24 mm with a resolution of 25 μm per pixel.
In figure 12.1 an example image is shown together with the spatial scale and the wind direction. Scale and wind direction are the same in all following figures.
Finally, a summary of the qualitative findings will be given together with a comparison to the results of other researchers.

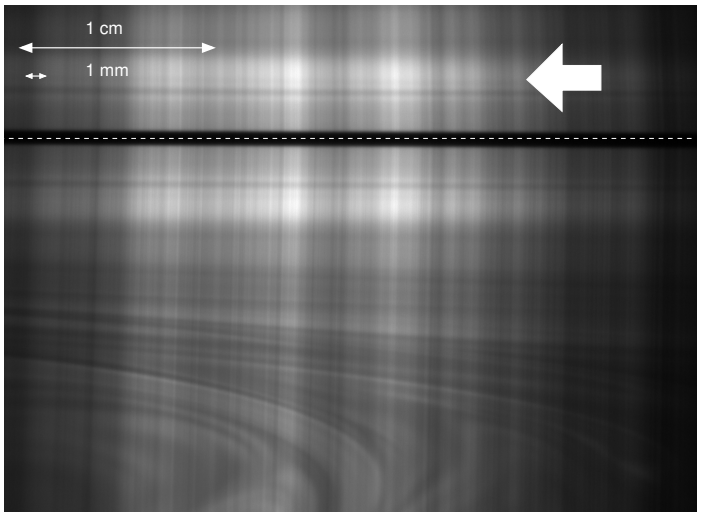

Figure 12.1: Spatial scale of the LIF images plotted in an example image. The water surface is marked by a white-dashed line and the wind direction is marked by the white error. The part of the image above the water surface is the total reflection of the illuminated plane at the water surface. The total reflection appears as the angle of view of the camera is slightly titled.

Layering

The transport phenomenon 'layering' is a kind of turbulent transport where whole layers of several mm-thickness slowly move up- or downwards in the fluid, an image of such an event is shown in figure 12.2.The layers dive as whole slowly in the bulk, where one large bulk eddy is visible. These layers appear to be broadened in time by diffusion. Especially at wind speeds below 3 ms^{-1} these transport by layer movement is encountered most frequently in the direct vicinity of the water surface.
At higher wind speeds the layering events seem to appear with a lower frequency. A kind of layering can sometimes be detected at higher wind speeds in the bulk region of several mm depth (in approximately 8 mm depth in the image shown in figure 12.3). There the mixing between regions nearer to the mass boundary layer with a higher momentum and regions in the bulk with lower momentum seems to be reduced.

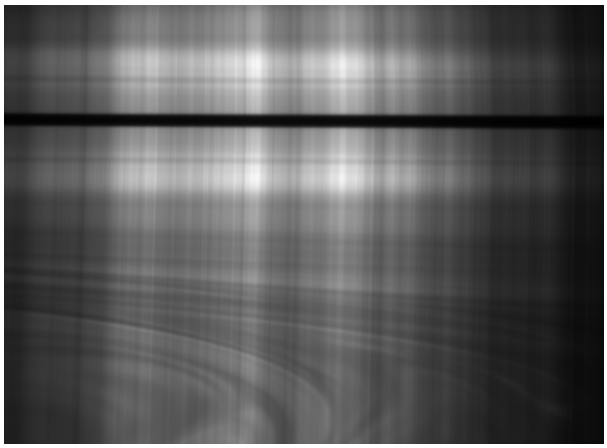

Figure 12.2: Image of 'layering' in lower turbulence: next to the interface evolves a horizontally quick moving layer of higher concentration of dissolved gas, separated from slower moving layers deeper in the bulk with lower gas concentration and therefore higher fluorescence. A kind of band structure of layers of different concentrations is visible. The image is taken at a wind speed of 2 ms^{-1} and a fetch of 67 cm. Wind direction is marked by the white arrow.

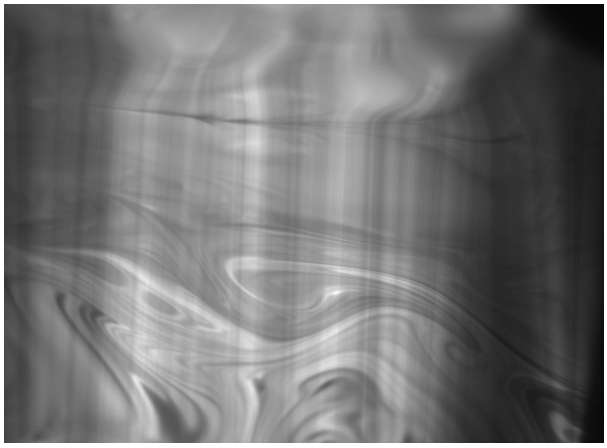

Figure 12.3: Image of 'layering' in high turbulence: next to the interface evolves a quick moving layer of higher concentration of dissolved gas, separated from a slower moving bulk layer with lower gas concentration and therefore higher fluorescence. Eddies at the 'interface' of the layers are responsible for exchange between the layers. The image is taken at a wind speed of 6 ms^{-1} and a fetch of 103 cm.

Eddy Cascade

A variety of turbulent eddies of different sizes can be observed in the experiments with the rotational axis spanwise to the main flow direction.
At lower turbulence motion the diameter of these eddies seems to be larger on average than at higher turbulence levels. i.e. higher wind speeds or higher fetch. The variety of eddy sizes seems to be lower at lower turbulence, very large eddies appear with a diameter of the image width or larger, see for example the bulk region of figure 12.2. They are mainly encountered deep in the bulk (below 15 mm water depth) but they can come near the surface from time to time, see the image of a surface renewal event in figure 12.18.
At higher turbulence levels, i.e. higher wind speeds or higher fetch (see figure 12.4 and 12.17, eddies of intermediate size (7-10 mm) appear more frequently in the bulk, while smaller eddies with a diameter of 3-5 mm often appear near the surface in figure 12.11.
Generally, observations indicate that at higher levels of turbulence, the number of eddies and the variety in eddy sizes seems to be remarkably increased (see figure 12.5 for the case of higher wind speeds and figure 12.4 for higher fetch and lower wind speed). Especially many eddies of the intermediate diameter around 8 mm are encountered more frequently.
In the bottom left corner of figure 12.5 a large eddy complex is visible that closely resembles a Kelvin-Helmholtz structure, see for example Lesieur [2008]. Kelvin-Helmholtz vortices usually indicate the mixing of two layers with counter-current flows.

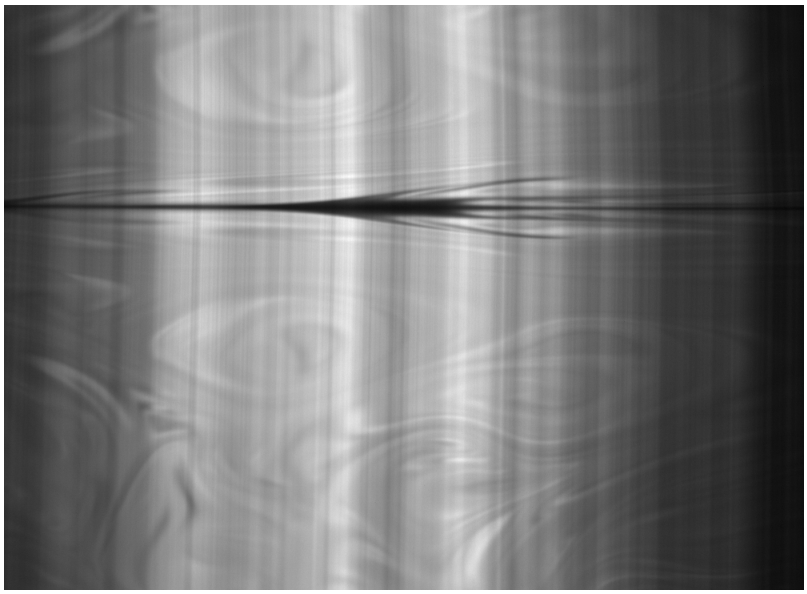

Figure 12.4: Image of a cascade of turbulent eddies of various sizes. Larger eddies are visible in the bulk region, while near the surface only layering and jets are visible. The image is taken at a wind speed of 3 ms^{-1} and fetch 175 cm.

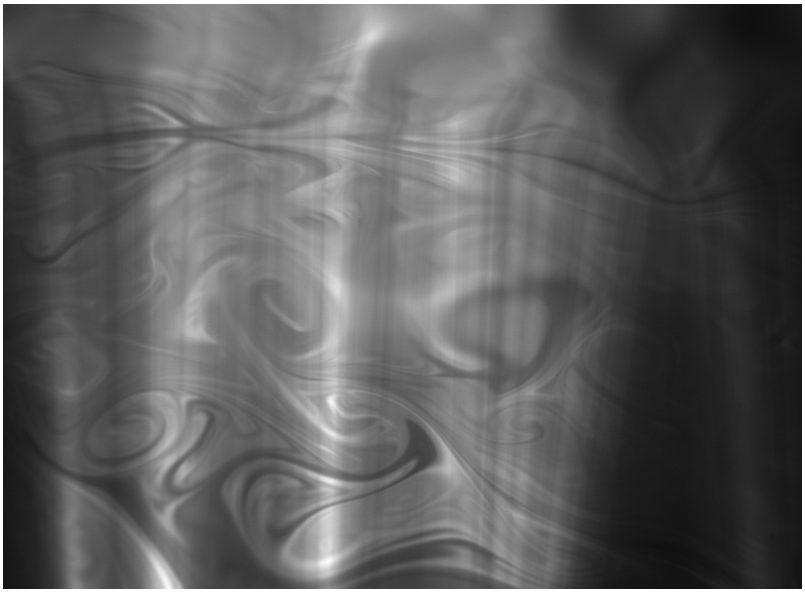

Figure 12.5: Image of a cascade of turbulent eddies of various sizes. The image is taken at a wind speed of 6 ms^{-1} and a fetch of 103 cm.

Streaks and Jet Burst Events

Jet burst turbulence events are encountered at low turbulence levels as well as at large turbulent levels. They are characterized by an upwelling of bulk fluid in front of the jet and a downwelling of the jet wings of higher dissolved gas concentrations towards the bulk.
At lower turbulence levels the downwelling seems to be slower and the wings more pronounced, see figure 12.6 or 12.17. Also the upwelling in front of the jet is clearer, as areas of higher local concentration are included, maybe due to a slower mixing.
At higher turbulence the downwelling jet wings seem to be loosing consistency more rapidly. This might result from a soon contact with the more pronounced bulk eddies that distribute the higher concentration effectively, see figure 12.7.

Such structures were also imaged in near surface turbulence by Münsterer [1996], as shown in figure 12.8. Also in Direct Numerical simulations of turbulent channel flow by Green et al. [2007] such structures were encountered, see figure 12.9. The here encountered jet like structures may be the 2D projection of hairpin vortices. Yet, without a 3D reconstruction such considerations are merely speculation.

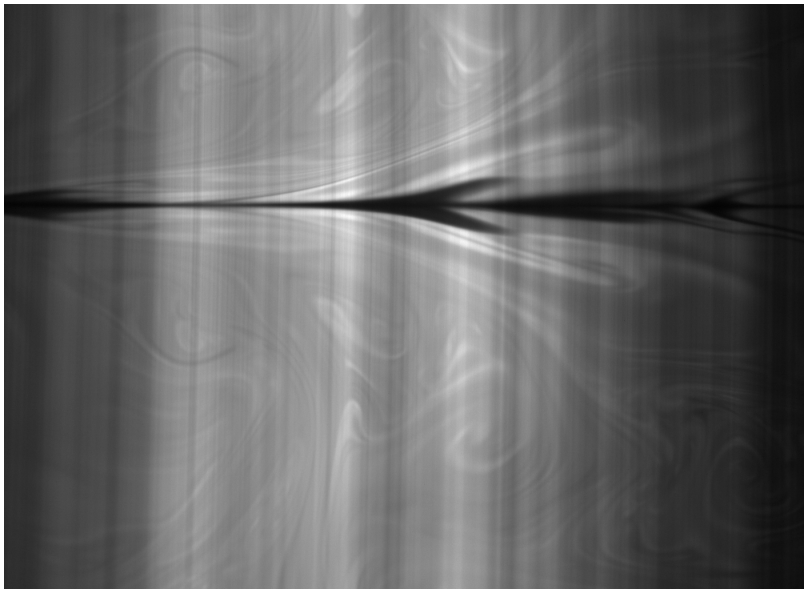

Figure 12.6: Image of a 'Jet' turbulence event: the wings of a diving jet appear as dark region due to higher local gas concentration. In front of the jet wings fluid is streaming towards the surface. The image is taken at a wind speed of 3ms^{-1} and a fetch of 175 cm.

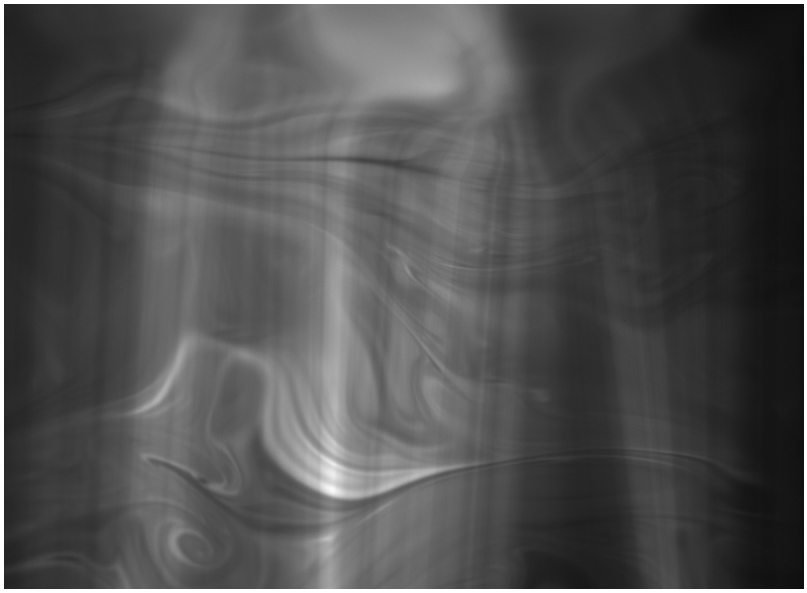

Figure 12.7: Image of a 'Jet' turbulence event: the wings of a diving jet appear as dark region due to higher local gas concentration, they interact with the turbulent eddies in the bulk. In front of the jet wings fluid is streaming towards the surface. The image is taken at a wind speed of 6ms^{-1} and a fetch of 103 cm.

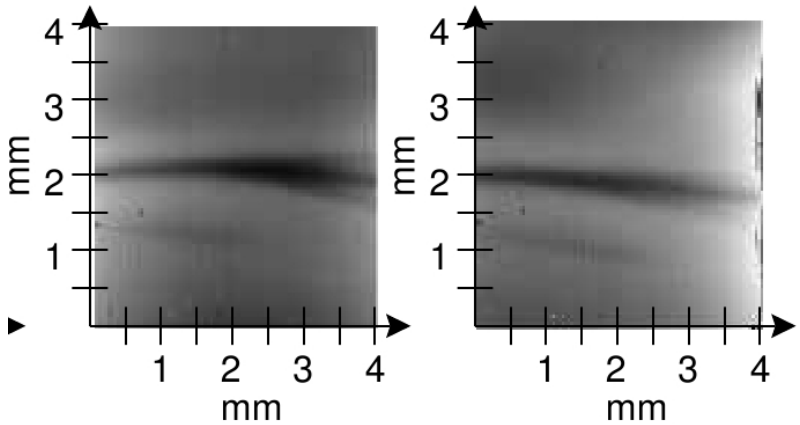

Figure 12.8: Image of near surface turbulence reported by Münsterer [1996]. The image seems to contain a 'Jet' turbulence, though less pronounced event at a friction velocity of $u^* = 0.75$ cms^{-1} in an annular wind wave tunnel.

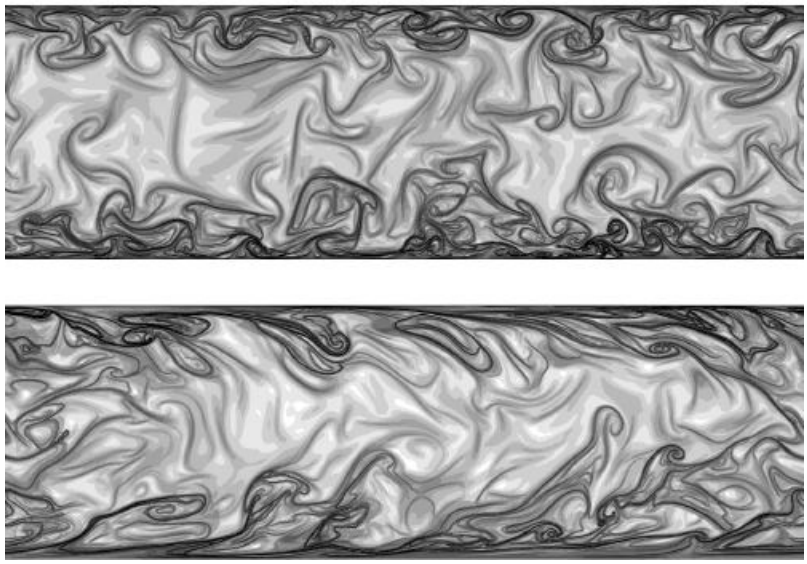

Figure 12.9: Images of coherent structures in turbulent channel flow gained by DNS, Green et al. [2007]. A 2D cross-section parallel to main flow is shown The structures at the top boundary (surface) resemble the here observed jet events and pike heart events of the following subsection.

Pike-Heart Burst-Sweep Events

These burst sweep turbulence structures resemble a pike-heart due to the shape they form together with their total reflection at the water surface.
Pike-heart burst-sweeps are related to jet events: Also upwelling motion occurs in front of its downwelling jet wings, which might be a bit less strong than in the jet event case. Characteristic is here, that the downwelling jet wings meet upwelling bulk fluid. These two motions together form a pronounced eddy near the surface mixing bulk and surface near fluid, see figures 12.10 and 12.11. Sometimes, the pike-heart events follow in a kind of successive family among jet turbulence events, which can also be seen in figure 12.11 and 12.12.
Like the jet turbulence events, the wings of the pike-heart events appear to be more pronounced in low level turbulence and less pronounced in high level turbulence. Pike-heart events seem to occur from low level turbulence up to higher turbulence, yet in higher turbulence they are less frequently encountered as they appear to evolve to jet explosion, which are described in the next paragraph.

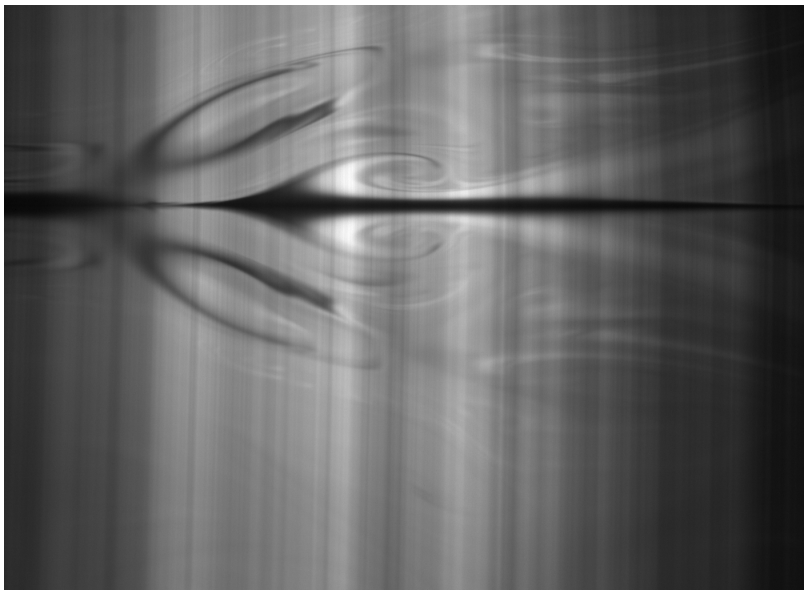

Figure 12.10: Image of 'Pike-Heart' turbulence event: the wings of a diving jet (dark region due to higher local gas concentration) event meet a surface-directed movement (light region due to lower local gas concentration). The overlay of both movements produces the pike-heart shape. The image is taken at a wind speed of 3 ms^{-1} and a fetch of 175 cm.

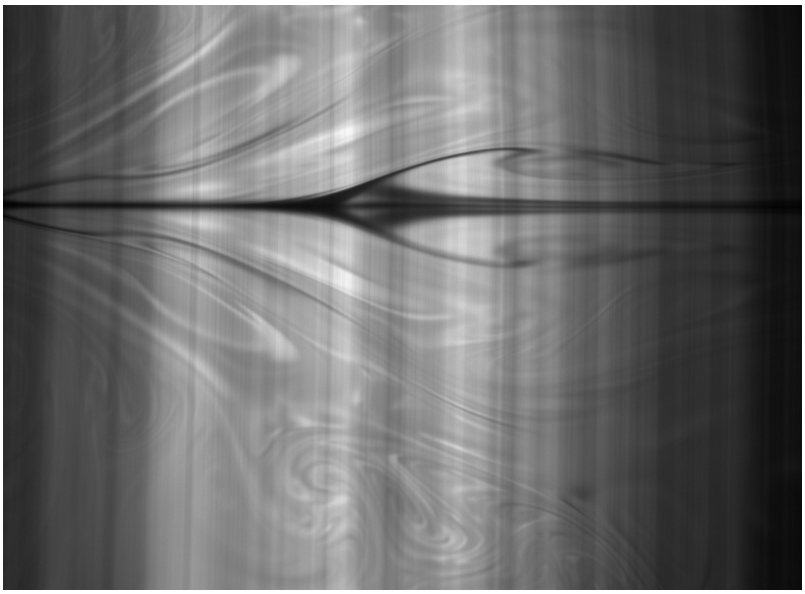

Figure 12.11: Image of a 'Pike-Heart' turbulence event turning into an 'extended jet' event: the wings of a diving jet (dark region due to higher local gas concentration) event meet a surface-directed movement (light region due to lower local gas concentration). The overlay of both movements produces the pike-heart shape. The image is taken at a wind speed of 3ms^{-1} and at a fetch of 175 cm.

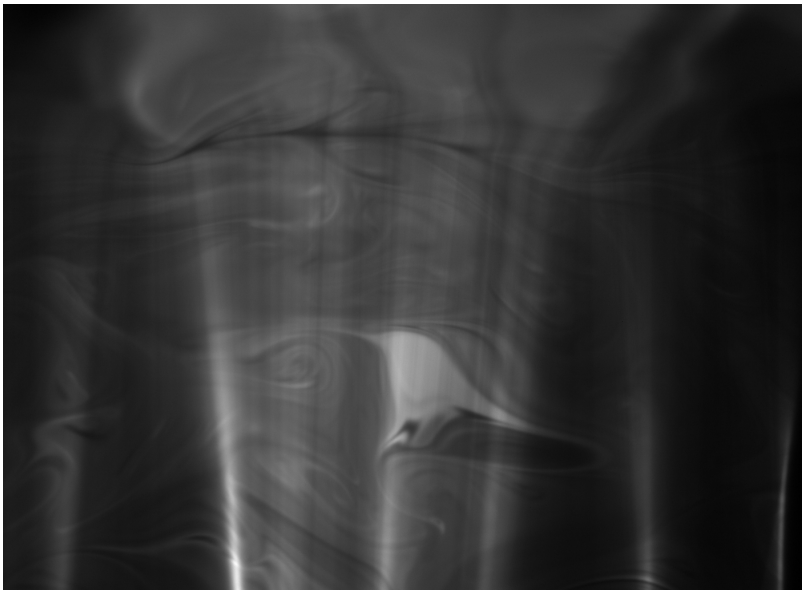

Figure 12.12: Image of a 'Pike-Heart' turbulence event: the wings of a diving jet (dark region due to higher local gas concentration) event meet a surface-directed movement (light region due to lower local gas concentration). The overlay of both movements produces the pike-heart shape. The image is taken at a wind speed of 6 ms^{-1} and a fetch of 103 cm.

Extended Jet Burst-Sweep Events

Extended jet burst-sweep events seem to be the equivalent of pike-heart turbulence events at higher turbulence levels. They were not regarded at wind speeds below 4 ms^{-1} in the experiments conducted here and appear with higher frequency with rising turbulence level, hence higher fetch and higher wind speed. Jet explosions seem to be the result of an interaction of a downwelling jet event with an eddy cascade or high turbulence region near the surface, that effectively mixes downwelling and upwelling fluid. Examples are shown in figures 12.13 and 12.14.

Maybe jet explosion can also be regarded as a family of fast moving jet and pike-heart events in an extremely short distance, an interpretation which image 12.13 may allow.

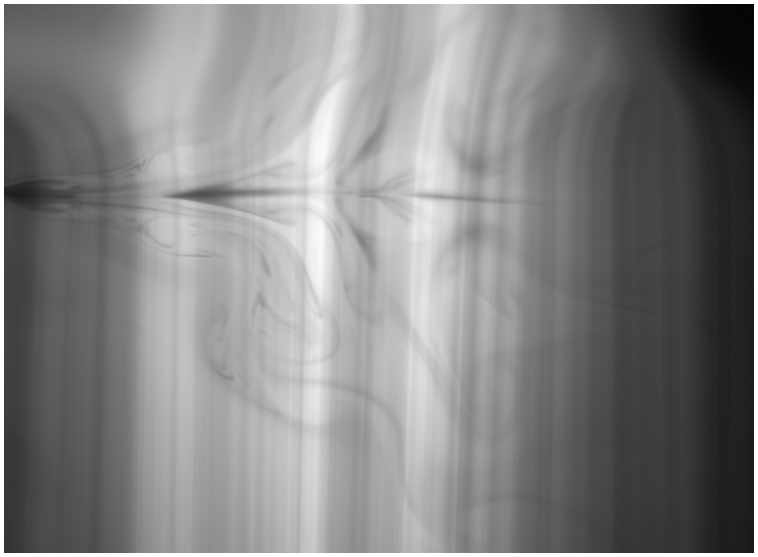

Figure 12.13: Image of an 'extended jet' turbulence event: the wings of a diving jet (dark region due to higher local gas concentration) produce a eddy cascade that interacts with bulk turbulence. The overlay of both movements produces the pike-heart shape. The image is taken at a wind speed of 5 ms^{-1} and a fetch of 103 cm.

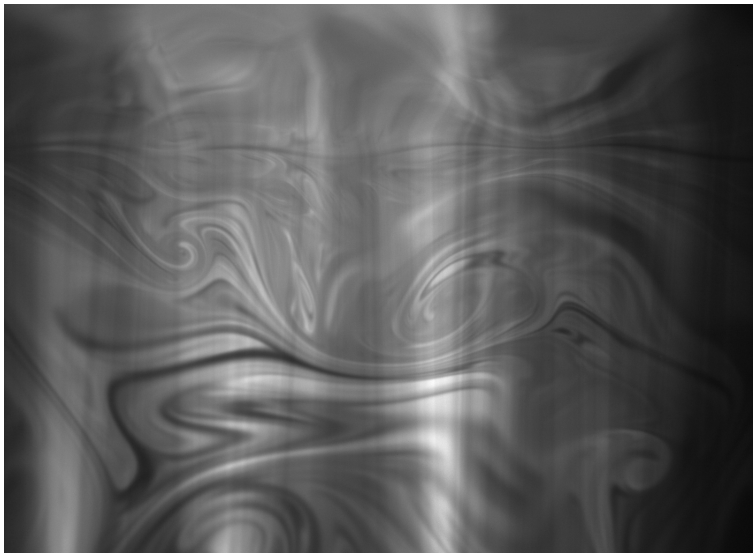

Figure 12.14: Image of an 'extended jet burst-sweep' turbulence event: the wings of the diving jet produce a cascade of eddies that interact with large eddies in the bulk. The eddy cascades shows similarities with a von-Karman eddy wake. The eddy cascades hands fluid with high gas concentration over to the bulk eddies which transport them into the bulk. The image is taken at a wind speed of 6 ms^{-1} and a fetch of 103 cm.

12.2.2 Statistical Appearance of Different Kinds of Turbulence Events at Varying Turbulence Levels

In this subsection the statistical appearance of the above defined near surface turbulence events is estimated by counting their numbers at different wind speeds and at the same fetch position. For this statistical analysis also data sets could be used, that did not satisfy the buffer points condition, see section 3.10, and were therefore rejected for concentration fields measurements. As the three data sets are rather small with 374 images each, the probabilities determined here can give only a rough estimate of the actual values, but they may suffice to indicate a trend. In table 12.15 the determined probabilities are listed for a fetch of 103 cm. Due to that data sets the layering events dominate at low wind speeds of 2 ms^{-1}, where no burst-sweep structures of any kind were encountered. While at medium wind speeds of 3 ms^{-1} the simple burst that look like jet structures are encountered frequently. At wind speeds of 6 ms^{-1} the complex burst-sweep structures of pike-heart events and extended burst-sweeps were encountered in 48 % of the images, while in most of the remaining the eddy structures of various vortices in sizes and forms were so dominating that single coherent events could not be identified or maybe could not be evolved due to the high turbulence level even in the near surface region.

wind speed $< u_{10\,cm} >$ [m/s]	**Layering**	**Jet**	**Pike Burst-Sweep/ Extended B.-S.**
2	**100 %**	0 %	0 %
3	19 %	**54%**	27%
5	5%	47%	**48%**

Figure 12.15: Statistical appearance of turbulent structures at different conditions. The probability is gained by counting the number of images, which show the event divided by the total number of images in the series. Here, a series consisted of 374 images recorded with a low frame rate of 2 Hz to prevent correlation between the single frames. For each wind speed the most frequently occurring events are bold.

12.2.3 Upwelling (Sweeps/Surface Renewal Events) and Downwelling (Bursts) Events and Surface Renewal dependent on Turbulence Level

Though the number of different turbulence events can be given by simple counting, a qualitative evaluation of the number of upwelling and downwelling events is hard to give as all above presented turbulence structures include both upwelling and downwelling of fluid in one single event.
In general, the exchange between bulk fluid and the mass boundary layer seems to be more direct in the case of low turbulence. There, large eddies transport bulk fluid into the mass boundary layer as can be seen for example in figure 12.16 for a pike-heart turbulence event, in 12.17 and 12.18 for a jet turbulence event. Furthermore, layering transport events can also be regarded as a kind of surface renewal, see figure 12.2, and this seems to be the dominating process at low level turbulence.
At higher turbulence levels the number and variety of eddies observed seems to rise. Exchange of fluid appears to be mainly done by these turbulent eddy motions. Therefore, the exchange of bulk fluid and near surface fluid is not as direct as before but achieved by transport trough these cascade of eddies. Direct renewal events were observed very rarely, the case of a renewal of layers between the bulk and the surface layers were encountered more frequently, an image is shown in figure 12.19.

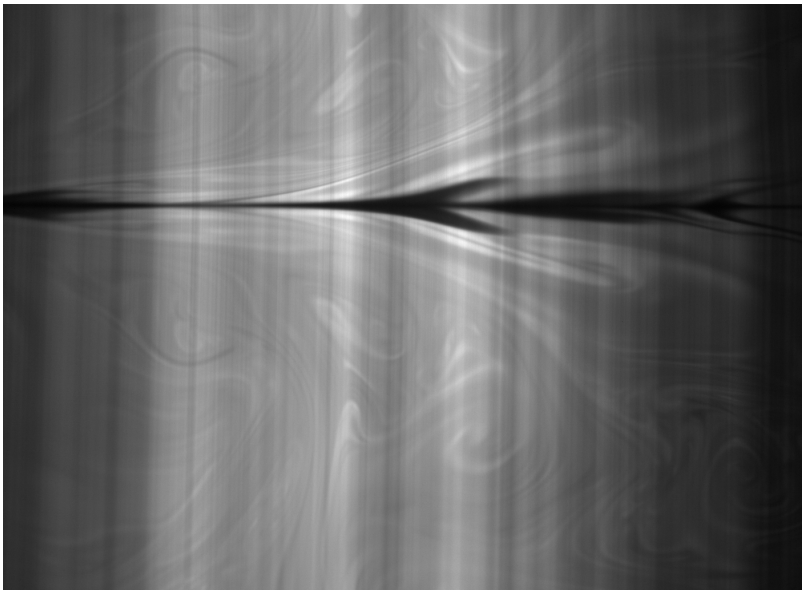

Figure 12.16: Surface renewal event in the context of pike-heart turbulence event. The image is taken at a wind speed of 3 ms^{-1} and a fetch of 175 cm.

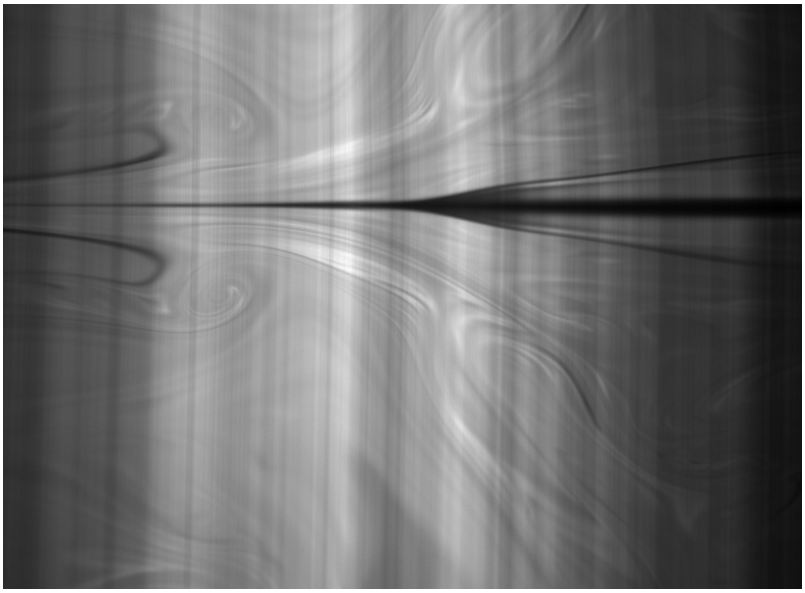

Figure 12.17: Surface Renewal event at low turbulence level in a jet turbulence event. The image is taken at a wind speed of 3 ms^{-1} and a fetch of 175 cm.

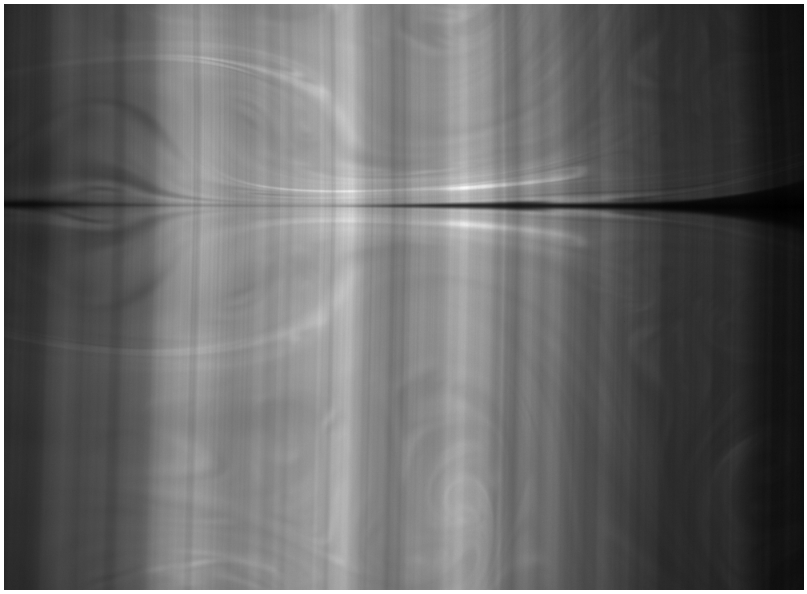

Figure 12.18: Surface Renewal event at low turbulence level. The image is taken at a wind speed of 3 ms^{-1} and a fetch of 175 cm.

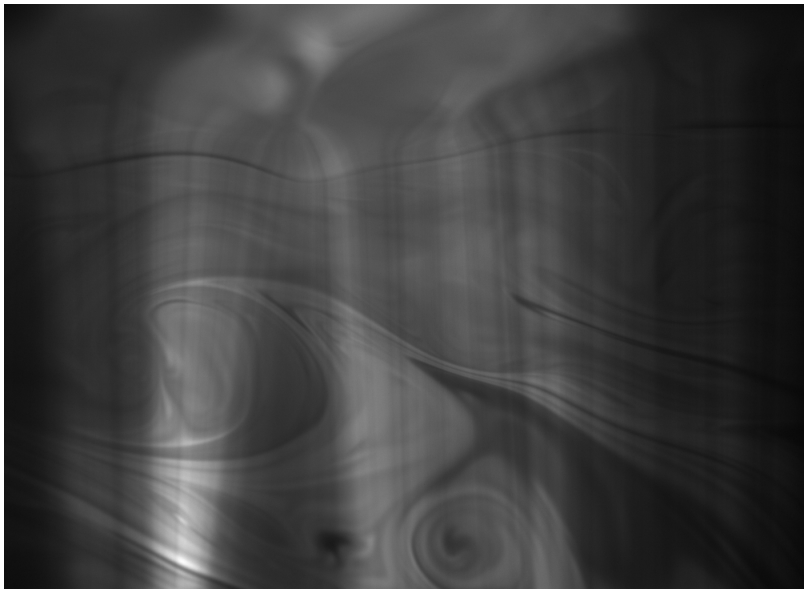

Figure 12.19: Deep Renewal event at more than 8 mm depth at high turbulence level. The image is taken at a wind speed of 6 ms^{-1} and a fetch of 103 cm.

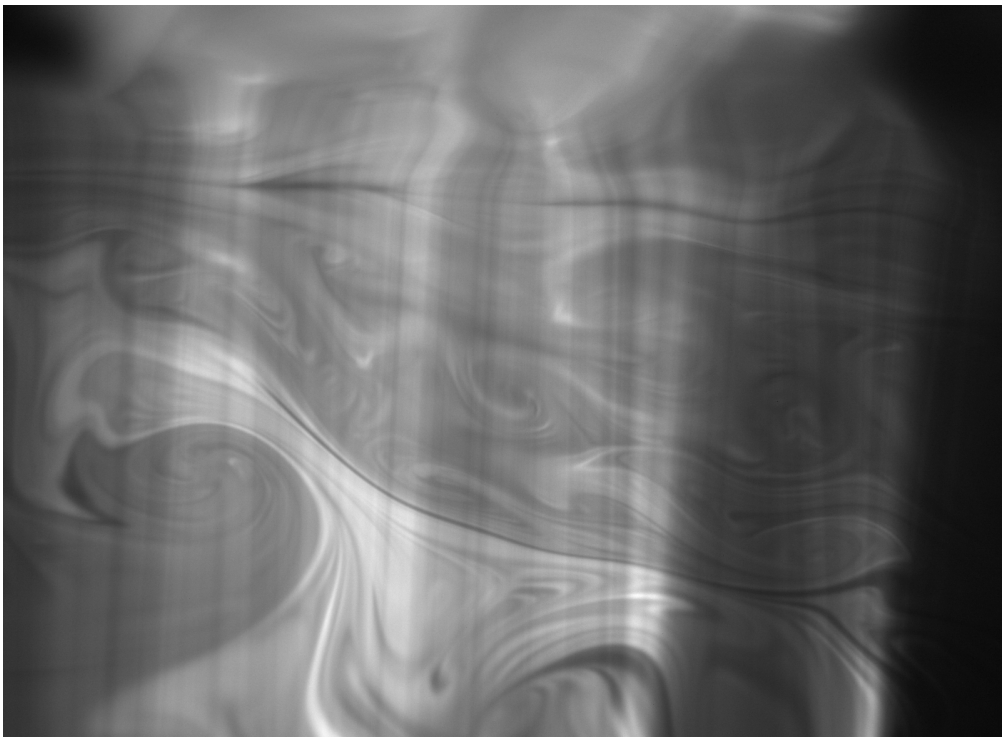

Figure 12.20: Intermediate Renewal event at a wind speed of 6 ms^{-1} and a fetch of 103 cm.

12.2.4 Wave Slope of Capillary Waves

With the SP-LIF technique wave slopes were recorded, when extracting the water surface, in a small cross-section of 34 mm length with a resolution of 25 μm. In capillary wave trains wave slopes near infinity were measured in the SP-LIF setup. An example is shown in figure 12.21.
The achieved resolution is about a 1/40 compared to the resolution of 1 mm of the imaging slope gauge of Rocholz [2008], used for systematic studies of 2D-wave slopes in our research group, which registers wave slopes in a range of $\pm 45\,^{\circ}$ with respect to the horizontal line. SP-LIF is not a substitute of this method, but may deliver additionally information on wave slopes in small capillary waves.

The extreme wave slopes were registered regularly in capillary wave trains with the onset of microscale wave breaking. The probability for these high slopes increased with the probability of microscale wave breaking, therefore, in first approximation also with the wind speed. At wind speeds above 7 ms^{-1} every registered wave with microscale wave breaking showed wave slopes next to infinity directly before the roller, see figure 12.22.
The registered waves were not of a sinusoidal form but resembled more a cycloid.

In future, LIF-measurements in a volume-scan setup are planned, to allow spatial 3D-measurements of concentration fields. These volume-scans could also be used as a new method of the wave slope registration with an improved spatial resolution for a systematic study of highest slopes in capillary wave trains. However, this method will not allow studies of surface areas greater than 3 cm^2, and therefore cannot compete with the imaging slope gauge. Furthermore, it will be limited to laboratory facilities as the possibility of side-view of the illuminated volume is necessary.

12.2.5 Wave State and Gas Exchange

Walker and Peirson [2008] measured transfer velocities with respect to position of the wave. They determined lowest transfer at the crest and highest transfer

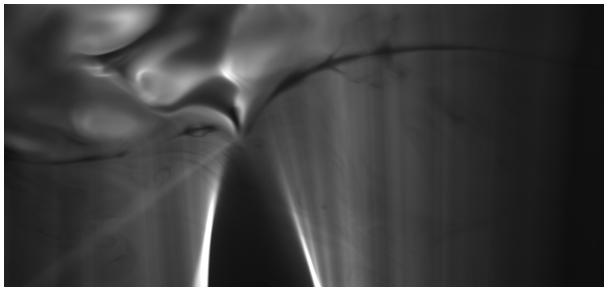

Figure 12.21: Wave slope near infinity (refracted beam: $\gamma \approx 41°$) registered in a passing capillary wave train directly before the roller at the crest.

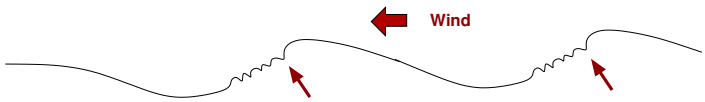

Figure 12.22: Typical position of wave slope next to infinity directly in front of the roller before the wave crest of a wave under microscale wave breaking. The location is marked with the small arrow.

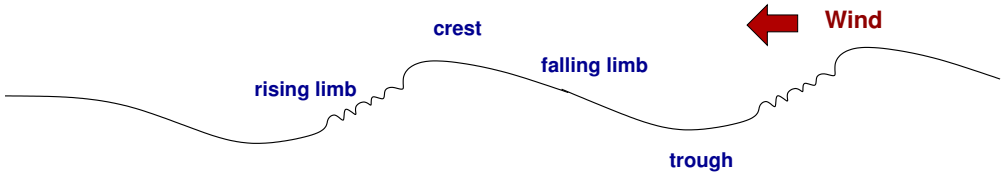

Figure 12.23: Four positions of a wave where Walker and Peirson [2008] measured transfer rates: rising limb, crest, falling limb and trough.

in the trough. This is in contrast to the predictions of the surface divergence model set up by McCready et al. [1986] and others.

Image Series of Microscale -Breaking Wave

In this subsection the influence of microscale wave breaking is qualitatively discussed for four parts of a wave according to Walker and Peirson [2008]: rising limb, crest, falling limb and trough. For illustration a typical microscale wave breaking event is shown in figure 12.24, that has been recorded in the wind-wave tunnel LIZARD.

Rising Limb/Capillary Wave Train In figures 12.24(b) and 12.24(c) images of the rising limb with the capillary train are shown. Jet and pike-heart events occur in the capillary wave train. The induction seems to be linked with the dips in the capillary wave trains. Jet and pike-heart events are downwelling events that occur directly after previous upwelling motion.

Crest and Roller At the crest jet explosion events are recorded. Here the wings of the jet and pike heart events come in contact with a turbulent eddy structure, see figures 12.24(d) and 12.24(e). It could be assumed that these turbulent eddies belong to the roller structure at the top of the wave, a region of high turbulence as stated by Ebuchi et al. [1993]. The boundary layer gets thinner in these areas.

Falling Limb In the falling limb, see figure 12.24(f), the wings of the jet explosion seems to diminished due to mixing with bulk fluid. Whole parts of the boundary layer are not visible any more, while other parts start thickening.

Trough In the trough, see 12.24(a), a few long spread layers of higher concentration are visible towards the bulk, while the boundary layer shows parts with high and low thickness, with a tendency towards higher concentrations towards the rising limb.

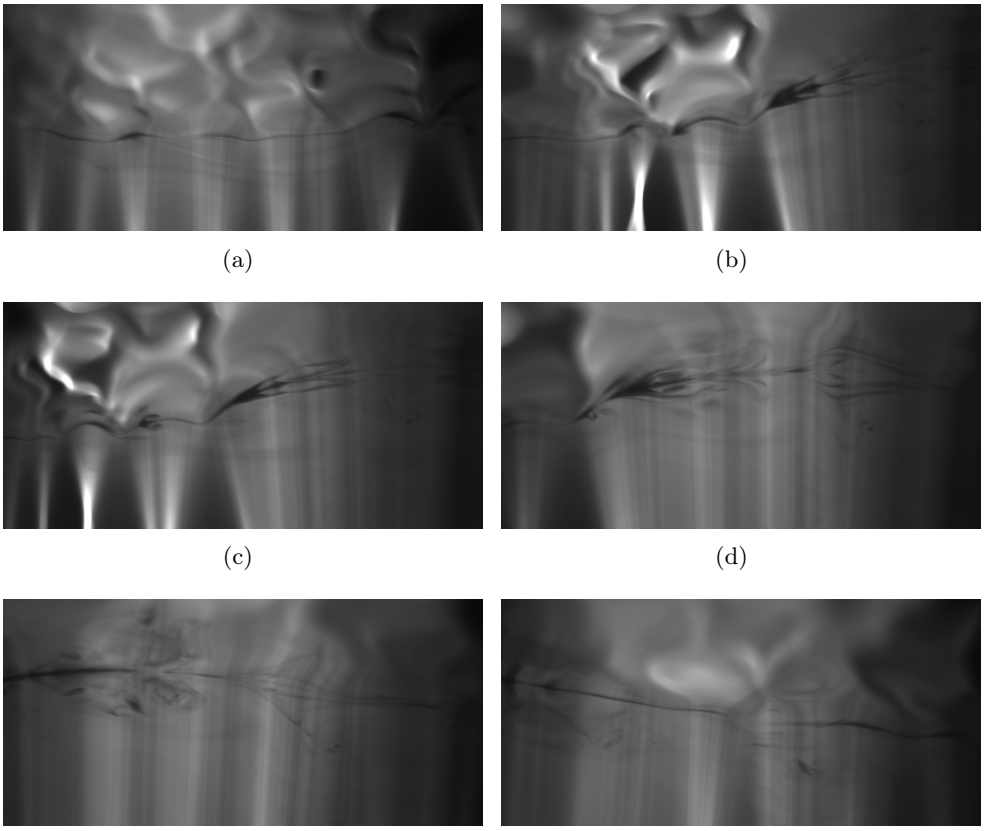

(a) (b) (c) (d) (e) (f)

Figure 12.24: Image series of a microscale wave breaking event taken at a wind speed of 7.3 ms^{-1} with a framerate of 150 Hz and an exposure time of $0.8 \cdot 10^{-3}$s.

Summary The observations presented in this subsection seem to indicate an increased gas transfer in the water-sided mass boundary layer in the capillary wave train and in the roller at the wave crest.

12.2.6 Comparison of Qualitative Results to Model Assumptions and Results of Other Authors

The findings of the last subsection, that a direct exchange between bulk and mass boundary layer seems to appear more frequently at lower turbulence levels would suggest that under these conditions the surface renewal model or the large eddy model would be appropriate.
Under higher turbulence, eddies of various sizes have been observed very fre-

quently. Their diameter seems to shift towards intermediate and small ranges with higher turbulence, as large eddies seem to appear with lower frequency. Therefore, transport seems to be mainly done by interaction of eddy motion. This would imply that the small eddy model might be applicable.

Both these qualitative findings of more frequently appearing surface renewal motions at lower turbulence and more frequently exchange of bulk and near surface fluids by eddy motions support the results of other authors:

Münsterer and Jähne [1998] reported in HCl invasion LIF-measurements that the surface renewal model gave the best fit to the mean concentration profiles obtained in their measurements. As they measured mainly under a flat interface at lower wind speeds and with an additional surfactant at higher wind speeds, it could be concluded that their measurements could be declared as of lower turbulence level compared to a wavy condition.

The classification as low and high turbulence level of low and higher wind speeds is needed if a comparison is tried with measurements in grid-stirred tanks, that simulate bulk turbulence but not wind-induced turbulence.
Herlina and Jirka [2008] measured in a grid-stirred tank at both low and high turbulence levels with a combined PIV-LIF method based on oxygen quenching. They obtained spectra of turbulent mass flux and mean concentration profiles. Their spectral analysis indicated that at low turbulence levels large eddies dominate the flow, while at higher turbulence levels small eddies seem to become more and more dominant.
Furthermore, they reported better correspondence of the surface renewal model at lower turbulence levels and better correspondence of the small eddy model at higher turbulence levels with respect to the mean concentration profiles they have measured.

The comparison of wave state and the turbulence transport phenomenons with the image series shown in figure 12.24 seems to indicate that indeed an increased gas transfer occurs in the water-sided mass boundary layer in the capillary wave train and in the roller at the wave crest, like the surface divergence model suggests, see 2.5.2. This would be in contrast to the findings of Walker and Peirson [2008] who reported the largest transfer rates at the troughs and the lowest at the crest.
Measurements of authors like Tsumori and Sugihara [2007], Xu and Khoo [2006], Herlina and Jirka [2008], and Asher and Litchendorf [2009] supported the surface divergence model as they found that in their measurements the transfer velocity k scaled with the surface divergence β, which is one of the predictions of the surface divergence model.
The discrepancy in the above described observation of turbulent transport under microscale wave breaking to the measurements of Walker and Peirson [2008] cannot be evaluated without a quantitative determination of the gas transfer velocity from the measurements conducted here, which will be done in the near future.

Chapter 13

Discussion and Outlook

Besides the building of an optically optimized wind-wave tunnel for LIF measurements, the main aim of this study was to identify and to develop a measurement technique suitable for measurements under a strongly wave-influenced water surface. In this scope the Spectral Reconstruction Approach (SPERA), that allows to determine arbitrary-oriented cross sections of concentration fields, has been investigated and theoretically analyzed. The technique could not be fully exploited in experiments as no high-soluble absorber dye could be found yet with an extraordinary high extinction coefficient in a thin absorption band, that also lay in the emission band of the fluorophore. Although a few dyes matched the spectral demands, even the most suited dye lacked the higher solubility needed to achieve the desired concentrations for a higher spatial resolution of the technique.
In an extension of the planar side-LIF, the Static Pattern LIF (SP-LIF) setup, a novel measurement technique was developed that allows to determine reliable estimates of the water surface position even under high turbulence levels, where the classic surface detection procedures fail. With a reliable estimate of the surface position the needed reference for the depth for the concentration fields are provided.

13.1 Discussion of the SPERA-Technique

In theory, the SPERA technique could be shown to work, even with extremely high noise level in the data sets. Some problems for practical realization however remained.
At the concentrations of the absorber dye needed for resolving layers with a thickness of 1 mm, all tested dyes show strong surface activity. Unless an absorber dye is found with an even higher extinction coefficient so that lower concentration below the surface activity limit could be used, SPERA is not applicable under high wind-induced turbulence situations and therefore small thicknesses of the corresponding boundary layers.
Summarizing, the aim of developing a technique for measuring spanwise gas concentration profiles under a strongly-wave influenced water surface could not be fully achieved with SPERA yet with the current absorber-fluorophore pair.

13.2 Discussion of Results of the SP-LIF

The SP-LIF technique shows encouraging possibilities towards the study of gas exchange under strong wave-influenced water surface. For the first time this technique allowed the detection of the water surface even in absence of a concentration signal. As strong surface renewal events may remove the dissolved gas concentration in the mass boundary layer completely, detection of the water surface in absence of a concentration signal is necessary to avoid a systematic drift in the statistics of the image sequences that may occur when such events are excluded from evaluation.
The quality of the single images was so high, that coherent structures could be identified under the varying wind and fetch conditions even without the processed image sequences. With this qualitative analysis an evaluation of the assumptions of the different models on turbulence was possible for the first time: These studies suggest that the assumptions of the surface renewal model are accurate at lower wind speeds.
Furthermore, at higher wind speeds (above 5 m/s) the influence of eddies increases, indicating that the small eddy model may be more appropriate here.

A relation of gas transport to the state of a wave under microscale wave breaking seems to be given. In the capillary wave train below the crest an increase in number of jet and pike-heart burst-sweep events could be frequently observed, while at the wave crest extended jet burst-sweeps events could be often observed. This may indicate that here the gas transport velocity is increased according to the predictions of the surface divergence model.

Summarizing, from the here examined measurement techniques SPERA and SP-LIF, SP-LIF currently shows the highest potential for measuring water-sided concentration fields under a highly wave-influenced water surface.

13.3 Outlook

In the near future, a systematic statistical analysis of the SP-LIF measurement series will be performed. To avoid time-consuming human detection of the water surface in the strongly wave influenced image sequences a semi-automatic image processing routine is the aim. That would offer a pre-analysis of the water surface, so that only corrections of the surface estimates have to be done by the user. Maybe the direct combination of the image processing software with routines from parameter estimation under additional constraints will be a step towards this aim. A first concept based on spline interpolation using the estimates of surface position as input parameters and the surface orientation as additional constraints has already been developed.

To improve the temporal resolution of the SP-LIF setup a pulsed static Laser sheet may be used, but this would demand an even more powerful Laser. For a more reliable estimate of the spatial resolution of the detector setup a determi-

nation of the MTF of the camera would be favorable.

Furthermore, the developed SP-LIF technique shows versatile possibilities for extended future experiments:
An extension of SP-LIF to 3D-volume rendering seems realistic, in which the static Laser sheet is used to scan a 3 D volume by combining the sheet configuration with a scanning mirror. Here, full information on the flow and concentration fields could be gained, which might be an important first step of using measurement values for comparison to the results of Direct Numerical Simulations.
Moreover, using the pH-method in combination with another fluorophore for the oxygen quenching technique would be a first step for cross-validation of results of high-soluble and low-soluble gases. A suitable candidate would be the ruthenium complex used by Falkenroth [2007].

The Spectral Reconstruction Approach SPERA may be applicable in low turbulence situations with large mass boundary layer thickness, for example in free convection. Also an application to heat transfer with its higher thicknesses of the boundary layer may be an alternative, with the temperature sensitive fluorophore Rhodamine B and a suitable absorber.

Besides, from these future applications the wind-wave tunnel LIZARD, that has been built in this study, with its unique tilted side observation windows, offers the best basis for the systematic study of 2D concentration profiles under defined wind and fetch conditions. These experiments are already under way and may provide interesting results for the near future for water-sided gas concentration fields and the corresponding transport processes.

Part VII

Appendix

Appendix A

The Wind-Wave Tunnel

Here in the appendix, a more detailed description of the wind wave tunnel LIZARDis given including an overview of general design rules, an overview of the individual tunnel elements and finishing with the instrumentation equipment of the tunnel.

A.1 General Design Rules of a Wind-Wave Flume

A wind-wave tunnel in its simplest form is a laboratory device that simulates the system of atmosphere and ocean. It usually is a closed system with a defined ratio of gaseous to liquid phase, that can be separated from the surroundings. Parameters like mean wind velocity, temperature and composition of the gaseous and the liquid phase can be determined and controlled. Adjustable total pressure could be a further tunable parameter of a tunnel but is not realized in the present setup. Kümmel [2004] formulated three basic rules that have to be fulfilled in optimal channel flow: First, the interior cross section of flow should be as great as possible to reduce losses at a given volumetric flow. Secondly, surface finish quality should be as smooth as possible and thirdly, flow optimized velocity profiles are needed.
The first two demands are easy to understand. The last demand is guaranteed under the conditions:

- The **contour line** should be at least **two-times continuously differentiable**. If contour lines follow the spline approach (see for example [Stoer, 1994])- splines are twice continuously differentiable-, harsh edges are avoided where boundary layer separations and therefore friction losses may occur.

- The flow **velocity** should be kept **constant as far as possible**. To avoid formation of boundary layer separations changes of velocity along main flow direction have to be minimized. Especially changes in velocity perpendicular to main flow may lead to turbulent eddy formation. For this reason guide vanes have to be used in the right-angled bends. A special

problem is the wind rotor, as its rotating blades form a strong unavoidable source of flow disturbance, Goldstein [1965].

- The **acceleration** should be kept **constant as far as possible**.
  Especially changes from acceleration to retardation lead to losses in retardation elements. Furthermore, changes in direction of the main flow - therefore radial accelerations - can lead to losses and unwanted secondary flows. In closed tunnels with circular air phase radial accelerations cannot be avoided but to reduce these effects radii of curvature should be as great as possible. The problem of retardation or diffusor elements can be minimized by a slow expansion over several meters to a larger diameter as that found at the jet inlet.

All the above stated demands can be summarized to one sentence: Avoid production of layer separations and losses as far as possible. Details on boundary layer separation and eddy formation can be found in Prandtl [1952] or Schlichting and Gersten [2006].
All these demands have been tried to be fulfilled in the design of LIZARD.
LIZARD's general construction follows Prandtl's demands on a wind-wave tunnel realized in the so called 'Göttinger wind tunnel' concept characterized by usage of guide-vanes in the right-angled bends and the gradually changing in diameter in contrast to a rapid contraction at the jet inlet directly before the water segment to reduce flow disturbances by convergence of stream lines. For further details see Prandtl [1952].
This was just a brief summary of demands, as details of wind-wave tunnel design are an extensively vast topic. More information on wind tunnel design can be found in Metha and Bradshaw [1979] Kümmel [2004], Goldstein [1965] and Prandtl et al. [2002].
In the following sections you will get a more detailed overview of the individual elements of LIZARD. The author follows in the description the guidelines of the report of Lindgren [2002].

A.2 Design of the Linear Wind-Wave Tunnel LIZARD

A.2.1 General Design Criteria for LIZARD

Besides the above mentioned qualities demanded of LIZARD for LIF measurements (usability for highly reactive substances, temperature stabilization, optimized optical access), several other criteria had to be regarded:

- The setup should be a **closed circuit wind-tunnel** to ensure a closed chemical/exchange system.

- The **quality of flow should be high** (stable mean flow, low wind-velocity variation and others).

- The available **limited space** of 8 m in length and 1.5 m in width sets the limit for the maximum length of water segment.
- The tunnel should consist of **individual coupled elements**, to allow moving of the tunnel to different locations.
- The **weight** of the individual segments should be so **low** that two people could easily handle one.

A.2.2 Material of the Tunnel Elements

Basic Material LIZARD is a wind-wave tunnel of low weight. The backbone of the wind-wave tunnel consists of foamed PVC, manufactured as 'Kömacel' by Kömmerling Plastics. The material shows a low weight, and high stability together with a low temperature conductance.

Every element is covered with PTFE-foliage (Teflon) coating of 0.25 mm thickness (manufactured by Polytetra) to ensure high resistivity against highly reactive substances and a variety of solvents like alcohols and aldehydes. The back of the foliage is specially treated to allow gluing of the backside, while the topside shows the unchanged PTFE surface. The foliage was put on the basic elements in overlapping layers (overlap at least 5 cm). The glue on the topside of the foliage is fixed by adhesion. To ensure that the overlapping comes not loose, a thinner PTFE-foliage of 0.1 mm thickness is fixed on top of the overlap of thick foliage.

The combination of foamed PVC and PTFE-foliage led to high-chemical resistant elements with low weight: Together with the PTFE- coating the elements weight less than 40 kg each (besides the water segment) and are therefore easily movable by two people.

A.2.3 The Individual Elements of the Wind-Wave Tunnel

In this subsection the individual elements of the wind-wave tunnel LIZARD are described in more detail. Figure A.1 shows a sketch of the wind-wave tunnel and its elements in a plane side view. The air exceeds the water volume by approximately a factor of 22.

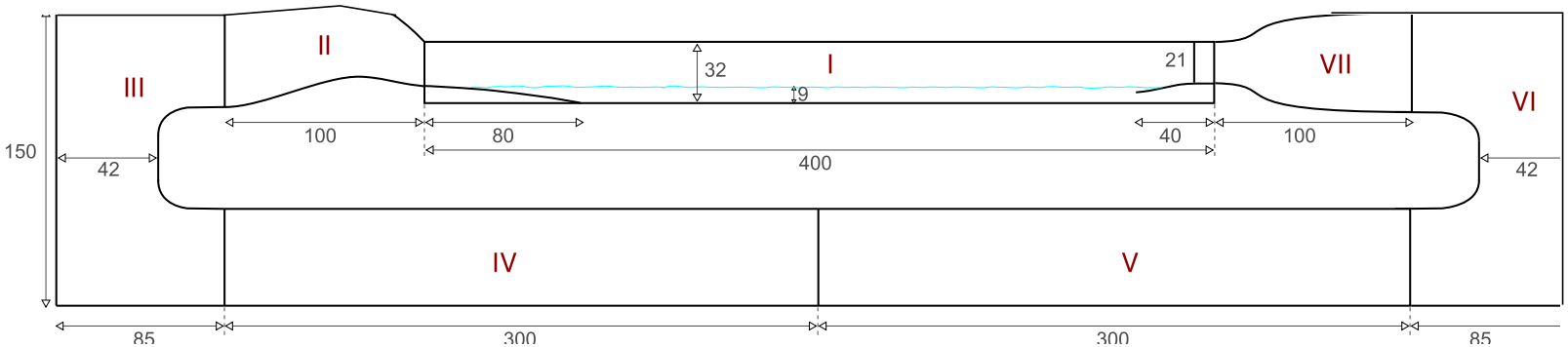

Sketch of the wind-wave tunnel LIZARD

Figure A.1:

Element	**Description**
1	Water Segment
2	Small Diffusor
3	(Small) Flow Bending unit 1
4	Wind generator Unit
5	Large Diffusor
6	(Large) Flow Bending unit 2
7	Jet Inlet with Honeycomb

The total air phase held a volume of approximately $3.3 \pm 0.3\text{m}^3$.
The most remarkable characteristic of the wind-wave tunnel was that its inside was totally covered by PTFE-foliage.Given the reactivity of the used gases, the air phase had to be separated from the surrounding atmosphere. The wind-wave tunnel was therefore constructed as a closed setup. The air volume when contaminated by reactive gases could be deposited via a special air filter system into the chemical hood system of the building.

Element 1: The Water Segment

The heart of the new wind-wave tunnel is the design of the water segment. a cross section through the water segment you find in A.2.

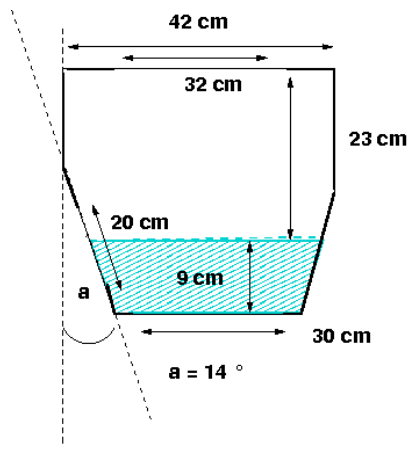

Figure A.2: Cross Section of the Water Segment of the Wind-Wave Tunnel. The angle of the tilted side window is $\theta = 14.6 \pm 0.3°$

Three large observation windows allow best optical access from different points of view: from top, bottom and as special feature - the side window with tilting angle of $\theta = 14.6 \pm 0.3°$, which allows parallel orientation of the detector objective to the window in the LIF side-setup as discussed above.
LIZARD is a linear wind wave wind-wave tunnel with a water segment of maximum fetch length of 3.4 meters by a total length of the water segment of 4 meters and a total of 150 ± 8 water capacity, with 126 ± 8 liters in the tunnel itself and 24 l in the four water cycles with a total air volume of 3 m^3 of the whole tunnel. The maximum water depth is 9 cm. The height of the corresponding air space is 23 cm. Free cross section area in the water segment for air flow is 966 cm^2.
Water surface area is approx. 1.11 m^2 at full water height, with a water volume of 0.150 m^3. Maximum water capacity has been estimated in a conduction experiment by adding known amounts of 1 M HCl and measuring the changes in conductance. A 0.8 m-long breakwater at the end ensures that wave reflection is suppressed. It consists of 11 flexible PTFE half-tubes of 20 mm diameter, that are oriented in that way that the reflected fluid is caught in their arch while the inflowing water is passing the outward arched spheres easily.

Four different water cycles are installed: In the main cycle a centrifugal pump (Schweikert, MPN 101) can induce a counter-current flow in the wave tunnel with a maximum volume flow of 80 l/min. It is used for fast mixing operations for example titrations of the fluorescent pH indicator with HCl or NaOH. In the main cycle three dosing units (Schott Titronic Universal piston burette) are installed which allow precise dosing down to volumes of 0.01 ml/min. They are used for setting up the pH value in the water phase to the desired pH value by adding acid (HCl 0.1 M) or base (NaOH 0.1 M).

The other three water cycles are intended for usage of degassing/gassing, for filtering, for an additional deionization unit, and water analysis via an absorption spectrometer cell. The water temperature can be kept constant via a heating/cooling unit with controller (manufacturer Cool Tronic GmbH) consisting of 18 Peltier elements attached to an aluminum plate of 390 mm x 300 mm located at the bottom of the water segment under the wave break.
The tunnel has an additional outer temperature insulation to simplify temperature stabilization.
Two PT-100 temperature sensors (manufacturer Greisinger Sensoric) are located in the water phase to measure local temperature, two in the water tunnel itself at each end, one in the main water cycle in combination with an conductivity sensor (manufacturer WTW, type Cond 340i) for monitoring accumulation of ions.
One PT-100 sensor is located above the wave break for measurements of air temperature. The second air temperature sensor is mounted in the second adapter of the wind generator unit.

The measurement section is located within a simple purity tent, kept at a low overpressure to prevent dust from entering and therefore finally entering the water unit. These effort was taken as floating dust on the water surface disturbs LIF measurements by Mie scattering and blocking parts of the Laser sheet, see section 11 for further details.

The wind-wave tunnel water inlet is attached to a deionization unit (manufacturer: KSN-Wassertechnik, Nowadest 1500 NF) so that the water used is ultra pure water with a conductivity of less than 0.1 μS/cm, see section A.4 for details.

The wind velocity in the water segment is measured via the difference in static and dynamic pressure with two Prandtl tubes located at a fetch of 2.4 m. One is installed as a static sensor for measurements of the mean wind velocity. The second one is mounted on a movable table (manufacturer Owis-Stauffen, type SM 32) to measure with high precision (table position accuracy 0.1 mm) the vertical position of the tip of the tube. It is used for measurements of the vertical velocity profile from which friction velocity is calculated, see A.3 for details. The horizontal position of the second Prandtl tube can be changed to seven equally distributed positions (3.5 cm distance between them, with 10.5 cm distance of the outer points to the tunnel walls).

Element 2: Small Diffusor

In the three-dimensional diffusor at the end of the water segment the cross section is enlarged from 966 cm^2 to 1764 cm^2 at a total length of 1m.
The small diffusor is slightly bend upward to ensure that wave spray from the break is captured. This small disturbance of the flow was accepted to prevent water from entering the bottom part of the tunnel.

Element 3 & 6: Flow Bending Units

In the flow bending units, see a sketch in figure A.3, the air flow is turned 180 degrees to lead it back towards the wind generator unit where the flow is accelerated again.
The essential parts of the two bending units are the guide vanes in the respective corners: In every corner 8 guide vanes are located (size 342x420 mm^2 in the small and 342x740 mm^2 in the large unit). The distance between the vanes d is chosen to be 0.2 times the corner width follows Zwaaneveld [1950] approach for a homogeneous leaving flow as cited in Kümmel [2004].

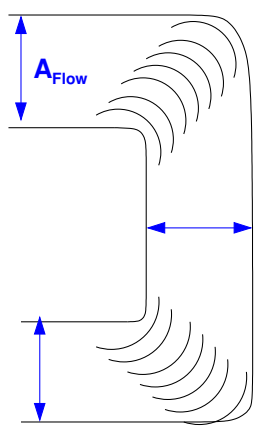

Figure A.3: Sketch of a flow bending unit with the eight guide vanes in each corner.

Element 4: Wind Generator Unit

To induce wind stress on the water surface a seven-blade axial rotor, type HF A 400-D, manufactured by Hürner Funken, is used. The rotor with an inner diameter of 390 mm and an angle of attack of 30° is located in the middle of the wind generator unit. Three additional airfoils behind the airscrew are provided by the manufacturer to suppress the rotation from the flow.
This rotor delivers a maximum wind speed of about 15 m/s (extrapolated from

measurements, see figure A.4)in the filled water segment allowing therefore the study of waves even to the condition of wave breaking with bubble entrainment. The motor is mounted axially behind the rotor encapsulated and therefore separated from the atmosphere in the tunnel with its potentially aggressive gases. For this reason, additional cooling air for the motor is needed from outside.
The frequency of rotation is adjusted via a frequency shifting unit from Siemens, Sinamics G110, type A.
Important to note is that the wind generator itself might act as a source of variations of the flow: Lindgren [2002] warned that axial rotors could create pulsating variations of the streamwise flow component if the work load became to large.

The adaption from the circular axial rotor to the quadratic cross section of the other elements of the flume is done via two adapters manufactured by Beck Kunststoffverformung GmbH. In the adapter before the rotor an IR-lamp is located for heating the atmosphere in the wind-wave tunnel if needed.

In the second adapter directly after the axial rotor - where turbulent motion is expected to be highest - the joint for gaseous tracer injection is located. Another possible position would be directly before the inlet of the axial rotor but is not used to prevent the reactive gases from damaging the polypropylene-surface of the rotor in higher concentrations, especially aromatics that are intended to be used as tracers in future experiments. A cylindrical tube with a length of 20 cm, an outer diameter of 6 mm and an inner diameter of 4 mm leads the gaseous tracer directly into the middle of the flow to ensure best mixing before the flow reaches the water segment.

Furthermore, in this element the joint for adding CO_2-reduced dry air (source: nitrogen generator K-MT-3-LAB from Domnick Hunter/Zander Aufbereitungstechnik) is also located. As a pH indicator is used with HCl as gaseous tracer every gas that can lead to changes in pH by dissolution has to be removed from the air phase. For this reason the flume is flushed with CO_2-reduced dry air before each measurement (CO_2 concentration below 10 ppm).

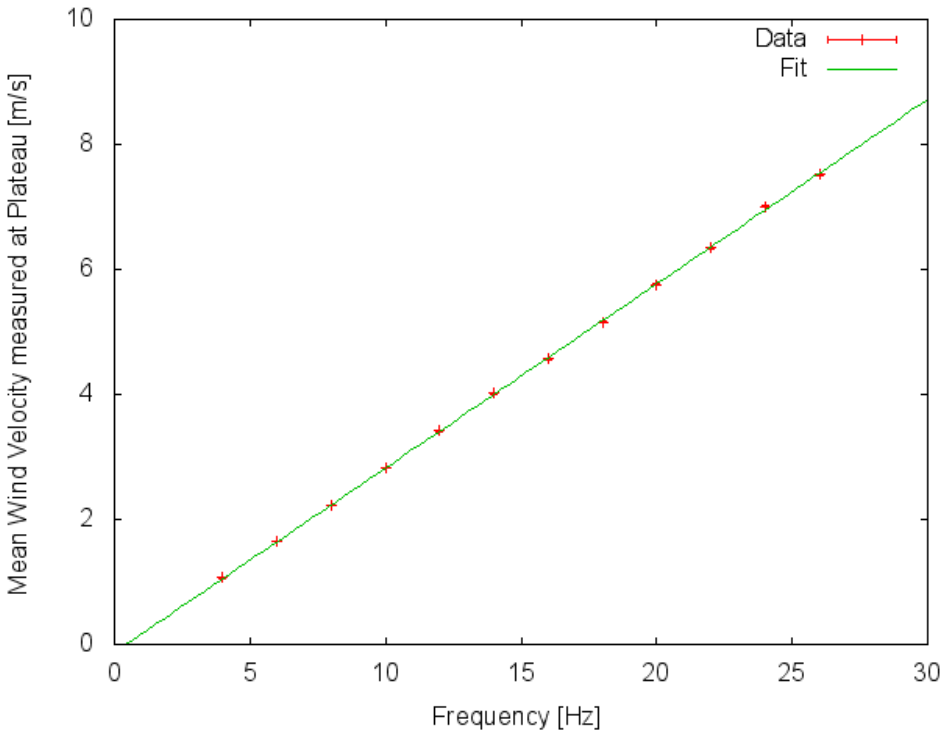

Figure A.4: Mean wind speed measured at the velocity plateau is plotted versus the frequency of the frequency shifting unit. The data for calculation is taken from measurements together with F. Friedl.
Results of the least-squares fit, $v_{wind} = s \cdot \text{freq.} + \text{y-offset}$: slope $s = 0.294764 \pm 0.001\,[\text{ms}^{-1}\text{Hz}^{-1}]$;y-offset $= -0.126221 \pm 0.02\,[\text{ms}^{-1}]$.

Element 5: Large Diffusor

The wind generator unit follows the large diffusor or retardation unit where the cross section diameter of the flow is gradually expanded from 1764 cm^2 to $3276\,\text{cm}^2$.

Element 7: Jet Inlet with Honeycomb

The element contains the stagnation chamber where the honeycomb and the jet inlet is located. This element has the greatest influence on the quality of the flow. The honeycomb is a flow straightening device and is very effective in reducing fluctuations in the unwanted spanwise direction, (Scheiman and Brooks [1981]). Furthermore, eddies larger than the cell diameter (here 3 cm) are effectively damped.
In the jet inlet or contraction element the flow is accelerated, this leads to a large streamwise strain, that reduces non-uniformities in the mean flow before the flow enters the water segment, so non-uniformities are strongly reduced.

The contraction ratio - largest inner diameter A_2 divided by smallest inner diameter A_1 at the jet inlet, see the sketch A.5 - characterizes the quality of the fluctuation reduction in the jet. The higher this value the better. The contraction ratio of LIZARD is 3.35 which is a medium value. Prandtl used a value of approx. 4, see Goldstein [1965]. Sometimes even a ratio of 9 is encountered see for example Lindgren [2002]. Due to a limit space a higher contraction could not be realized.

To further minimize disturbances a honeycomb of mesh size 3 cm is installed before the inlet, where the flow speed is very low due to the large cross section. A screen was not added.

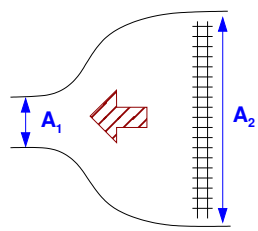

Figure A.5: Sketch of the jet inlet with honeycomb.

A.3 Characterization of Flow Properties

Mean wind velocity and depth dependent wind profiles were measured in a student's project using a Prandtl's tube for determining wind velocities. For further details see [Ültzhöfer, 2008].
Wave statistics were determined in a diploma thesis by Huhn [2008].
Here, only the most important parts of their results are reported.

Logarithmic Wind Profile The wind-wave tunnel showed logarithmic wind profiles over its total width of 420 mm. Measurements were taken in distances of 35 mm beginning from the middle position (210 mm) to the outer walls (point 1: 105 mm, point 7: 315 mm). The horizontal decline from median position to the outer walls were in the range of -7 % of the mean velocity.

Friction Velocity The friction viscosity is determined as the length of the Reynolds stress vector, following the considerations of Weber [1999].
As in this linear wind-wave tunnel the main wind velocity has just components in x- or main flow direction, the second part of Reynolds stress vector can be neglected, and the friction velocity reduced to Prandtl's formulation presented in equation 2.55.

$$u_* = \left(\overline{u'w'}^2\right)^{1/4} \tag{A.1}$$

Air-sided friction velocity is determined via a fit of a logarithmic profile to the measured wind velocity profile at seven positions in y-direction, with a distance of 35 mm each.
Water-sided friction velocity is determined as the ratio of densities of air and water respectively out of the air-sided friction velocities. Results are presented in figure A.6 and A.7.

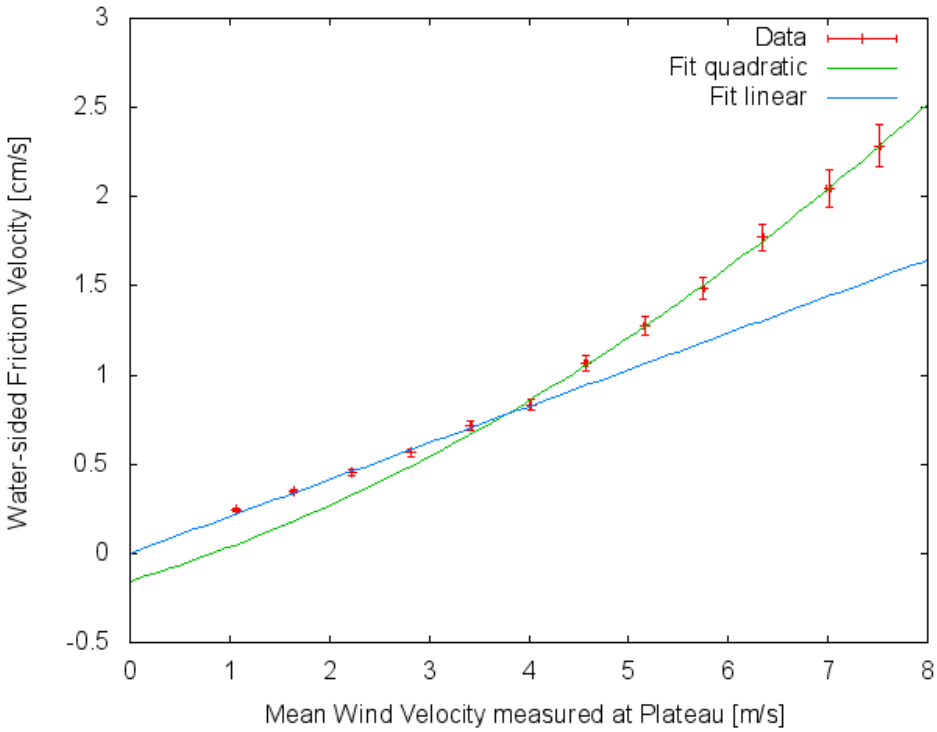

Figure A.6: Air-sided friction velocity in the wind-wave tunnel; data for calculation from measurements together with F. Friedl.
Results of the linear least-squares fit $u_{*a} = s \cdot v_{wind}$ + v-offset: slope $s = 0.294764 \pm 0.001\,[\mathrm{cms}^{-1-1}]$;
v-offset $= -0.126221 \pm 0.02\,[\mathrm{cms}^{-1}]$;reduced chisquare: 0.000302668.

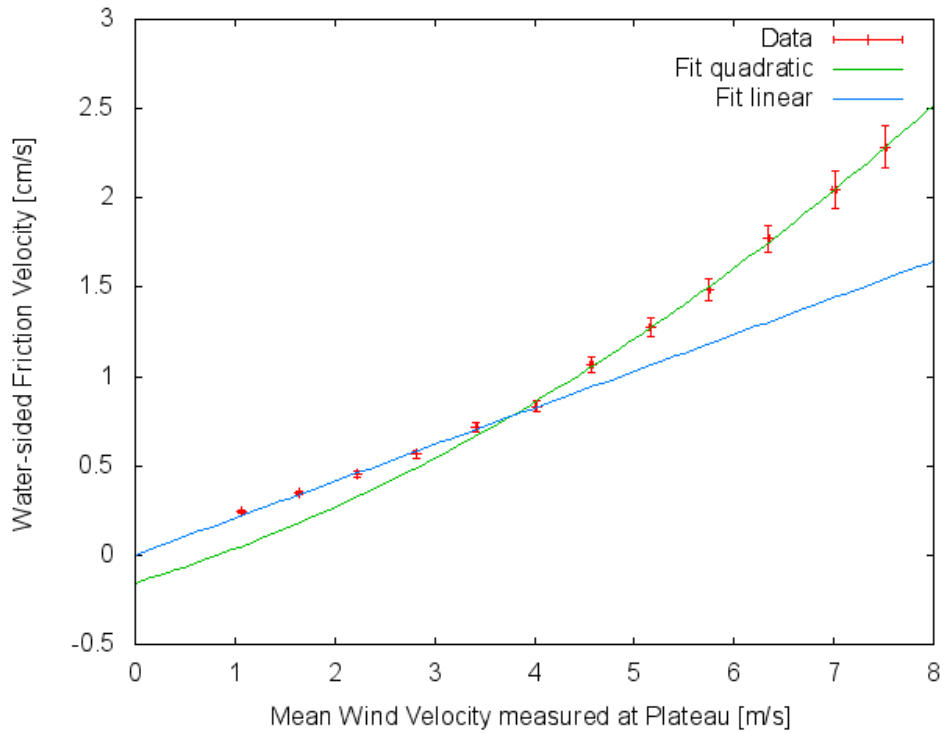

Figure A.7: Water-sided friction velocity in the wind-wave tunnel; data for calculation from measurements together with F. Friedl.
Results of the linear least-squares fit $u_{*w} = s \cdot v_{wind}$ + v-offset:: slope = 0.0596891 ± 0.002 ;
y-offset = 0.0 ± 0.06 ;reduced chisquare: 1.70254e-05; units of air-sided friction velocity [ms^{-1}] .

Time Constant for Injection of Tracer As invasion experiments are to be conducted, a time constant for the transition of the air space of the injected gas tracer in closed-circuit wind-wave tunnel has to be estimated. This is done by assuming a simple box model, with two boxes as model for air and water phase: The water surface of the tunnel is about $A_w \approx 1\mathrm{m}^2$ and the volume of the air space V_a this means that the effective height a gaseous tracer has to traverse is

$$h_{eff} = \frac{V_a}{A_w} \tag{A.2}$$

$$\approx 3\mathrm{m} \tag{A.3}$$

With a mean transfer velocity of the tracer $k_a \approx 1\,\mathrm{cms}^{-1}$ the time constant for transition of these distance becomes

$$\tau = \frac{h_{eff}}{k_a} \tag{A.4}$$

$$\approx 300\mathrm{s} \tag{A.5}$$

$$\approx 5\mathrm{min} \tag{A.6}$$

After this time has passed the tracer should be distributed so far, that at the imaging setup invasion events of the gaseous tracer could be recorded.
In reality, typical values exceed this estimate by a factor of three, which may indicate that an additional sink of HCl may be present. It is assumed that at least on parts of the tunnel walls water condensate is found, that acts as a sink for HCl. To reduce this effect the tunnel walls were kept at a higher temperature than the tunnel air by slightly heating the outer air-space.

A.3.1 Wave Slope Statistics

The statistics of waves regarding mean quadratic slope and wave heights presented in this subsection have been studied in the wind-wave tunnel by Huhn [2008]. Here, only the main results are shown that are relevant to this study. An image of waves under microscale wave breaking taken in the flume is shown in figure A.8.
One of the questions regarding the wave field of the wind-wave tunnel, has been whether a symmetric wave field will be generated though the tunnel walls have a differing tilt. The cross wind distribution of mean surface slope clearly shows that in spite of the asymmetry of the angle of tilt of the flume walls, the slope distribution remains symmetric, see figure A.3.1, so no disturbances are registered. The upwind profile shows a slight skewness towards negative slope, which is typical for capillary wave trains riding on the larger gravity waves, see figure A.3.1.

Furthermore, it would be convenient to know at which wind speed the onset of waves is to be expected. The measurements of Huhn [2008] showed that at a mean wind speed of 3.5 m s^{-1} at the plateau wave slope increases visibly. Therefore the range of 3.5 to 7.5 m s^{-1} seems to be the most interesting range for measurements under waves.

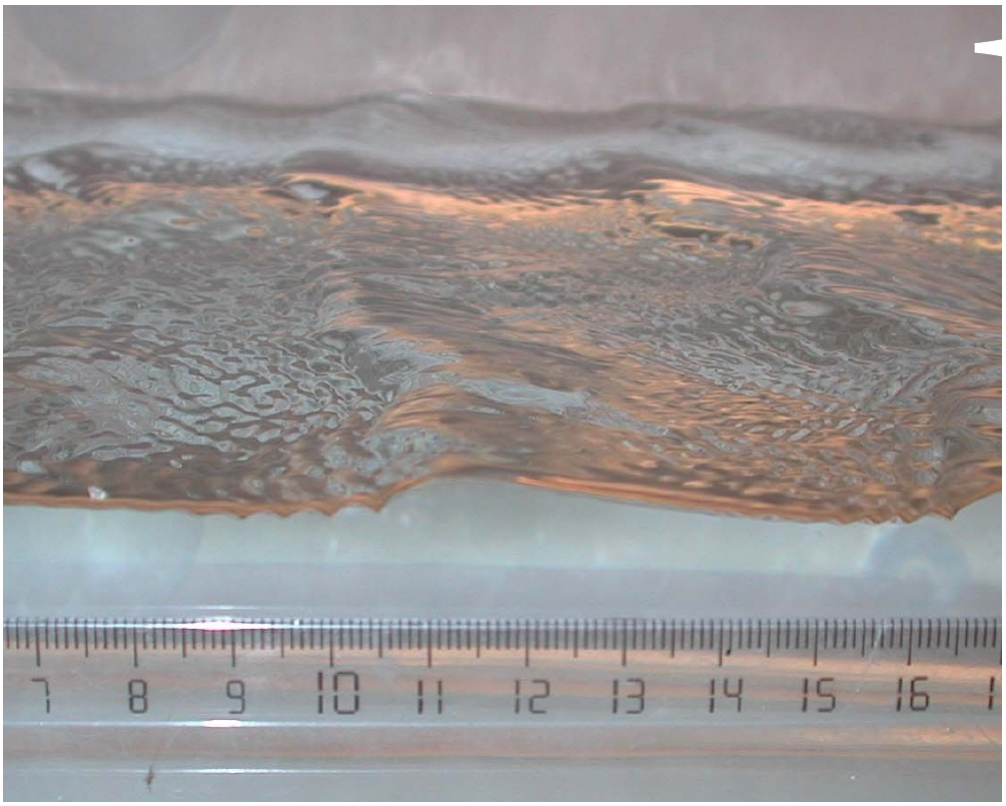

Figure A.8: Typical wave field in the linear wind-wave tunnel at wind speeds of 7.5 m s^{-1}; image taken from [Huhn, 2008].

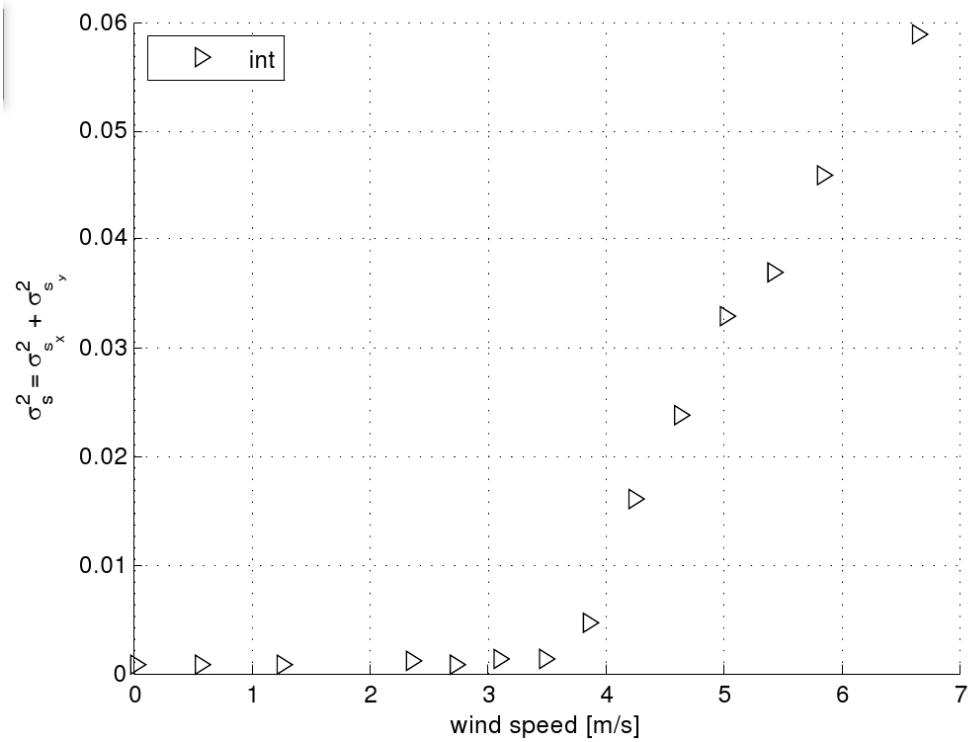

Figure A.9: Evaluation of mean square slope in relation to mean wind velocity; measurements and graphic by Huhn [2008] at a fetch of 2.38 m.

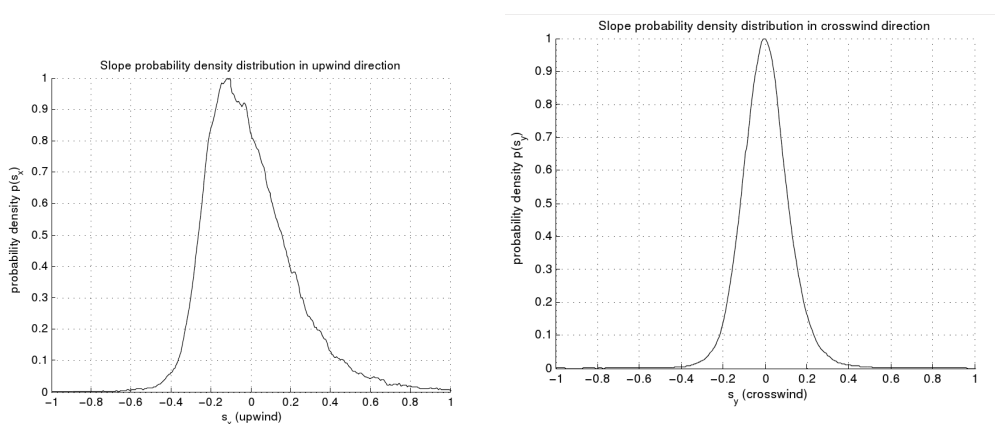

(a) Upwind (b) Crosswind

Figure A.10: Wave slope probability density distribution in the tunnel at a wind speed of 6.7 m s^{-1}; The cross wind distribution shows that in spite of the asymmetry of the angle of tilt of the flume walls, the distribution remains symmetric; measurements and graphic by Huhn [2008].

A.4 Further Technical Characteristics of the Wind-Wave Tunnel

Ultra Pure Water

This wind-wave tunnel is supposed to work as a simulation of the earth's atmosphere-ocean system.
Yet, it has to crudely simplify the actual highly complex system to make the basic processes explorable. For one thing, the water does not have the actual salt composition like sea water but is instead water of lowest conductivity (between $0.01 - 0.1\frac{\mu S}{cm}$) at the start of experiments. The deionization unit used is manufactured by KSN-Wassertechnik, type Nowadest 1500 NF. The actual conductivity is monitored by a conductivity sensor from WTW, type Cond 340i. This is a credit to the LIF experiments to be carried out: High salt concentration can influence the emitted fluorescence of the dye used in the LIF setup described in section 3.4. This is exactly the case for the fluorophore HPTS that is used in this setup, see 3.7 for details.

HCl Vaporization Unit

The HCl vaporization unit has been built to ensure a constant flux of HCl into the wind-wave tunnel. The unit consist of a Teflon container for HCl, 32% in aqueous solution, with a total volume of 300 ml. The volume has been chosen to be rather high to reduce evolving concentration differences in the hydrochloride acid due to the higher partial pressure of HCl with respect to the solvent water. The air volume above the hydrochloride acid is approximately 20 ml, with an area of 100 cm^2 and a height of 2 mm. The unit is mounted in a temperature stabilization unit of manufacturer Huber, a K6-cc, that ensured a temperature of 20 ℃ with an accuracy of ±0.1 ℃.
A controllable flux of dry air is flushing the air space with rates ranging from 1 -100 ml min^{-1}. As mass flux controller a controller of series M (max. flow rate 100 ml min^{-1}), manufacturer Analyt, was used with an accuracy of ±0.2% full scale and additionally ±0.4% of set rate.
The maximum flow rate flushes the air space completely every 12 seconds. This time suffices to ensure that enough HCl is evaporated in the $\sigma = 2$ mm thick air space.Data for vapor pressure of HCl above aqueous solution is taken from Perry and Green [2008].With these data HCl concentration in the air space dependent on flow rate could be estimated.
A gas pressure tank of HCl was not used as no suitable regulation units for constant flux were found for this reactive gas.

Appendix B

Determining Extinction Coefficients

For all the measurement techniques presented in this work, a high-precision knowledge of the extinction coefficients of the selected absorber dye and fluorophore is mandatory.
Unfortunately, these data sets are only very rarely available. For the dyes used here no such data was found except for one extinction coefficient of HPTS at one fixed wavelength.
So the values had to be determined experimentally.
The determination of the extinction coefficient of a dye solution is based one of the most common tasks: determining the absorption spectrum of the dyes to be examined.

B.1 General Description of the Technique

Absorption is described by the Bouguer-Lamber-Beer law as has already been done in 5.5 including its validity limits.

$$E = E_0 \exp\left(-\varepsilon(\lambda) c_A z\right) \tag{B.1}$$

In a logarithmic plot this relation appears as a linear relation in the concentration of the absorbing dye c_A under the assumption of a fixed light path depth of z_f; the measuring cuvettes used here had a $z_f = 1\text{cm}$.

$$\ln\left(\frac{E}{E_0}\right) = -\varepsilon(\lambda) c_A z \tag{B.2}$$

The extinction coefficient of the dye can be experimentally determined by measuring the $\ln\left(\frac{E}{E_0}\right)$ under different concentrations of the dye as the slope of the line fitted to the measured values via a total least squares fit.
For a good line fit at least 5 supporting data points are necessary, as stated for example by Tamhane and D.Dunlop [1999] and Montgomery et al. [2006].

A total least squares fitting algorithm was used to determine the slope, as both $\ln\left(\frac{E}{E_0}\right)$ and the concentrations had non-negligible errors.

E_0 is measured separately with a cuvette filled with pure solvent (water or water/buffer solvent) to account for properties of the solvent. All spectra were dark current corrected.
As the spectrometer gave its result in log to the base of 10, the absorption measured was

$$\text{absorption} = -\log\left(\frac{E_{probe} - E_{darkcurrent}}{E_0 - E_{darkcurrent}}\right) \tag{B.3}$$

Typical extinction coefficient are listed in the following table adapted from Schmidt [2000] and Kleinschmidt [2001]

type of absorption	σ **[cm^2]**	ε **[M^{-1} cm^{-1}]**
electronic - atomic (UV/VIS)	10^{-12}	$3 \cdot 10^8$
electronic - molecular (UV/VIS)	10^{-16}	$3 \cdot 10^4$
rotat./vibr. (IR)	10^{-19}	$3 \cdot 10^1$
Raman (IR)	10^{29}	$3 \cdot 10^{-9}$

Table B.1: Typical value of extinction coefficients for different types of absorption range.

B.2 Typical Error Sources

A typical error is that the validity of the Bouguer-Lambert-Beer law is not given. In that context it has to be checked, whether

- scattering and reflexion have to be insignificant
- homogeneous distribution of dye demanded
- only valid for dilute solutions - relative to the depth regarded not all intensity should be absorbed
- temperature has to be kept constant
- solvent dependent absorption
- absorption spectrometer
- constant pH Value

Temperature The most severe problem in practical measurements is the demanded constant temperature during the measurements. To achieve measurements at a temperature of 20℃the measuring solutions together with the cuvettes had to be kept in a thermostabilized bath otherwise temperature drifts of 1-2 ℃were not unusual.

Spectrometer In the measurements conducted here a Optical Multichannel Analyzer (OMA) from Hewlett Packard (HP 8453) was used. The spectral resolution is done by an optical grating in combination with an array of diodes as detector, which allows instantaneous measurement of all wavelength in the range of the spectrometer setup.
Known error sources of the OMA are (based on Schmidt [2000])

- white light used as the illumination light source:
  this is a severe problem especially when absorption spectra of fluorophores are to be investigated and the part of the illumination is transformed into fluorescent light at a larger wavelength. The absorption appears to be lower than it is as the fluorescence intensity is added up on the transmitted irradiance,

- probe is part of the optical light path:
  It has to be free of scattering particles

- lower sensitivity and lower dynamics of the diode array compared to a CCD-detector

According to Schmidt [2000] an Optical Multi-channel Analyzer is not well suited for high-precision measurements. Typical errors of the extinction coefficients in the measurements conducted here were in the range of 5-20% depending on the dye used and the wavelength range. Especially, at low intensities the OMA results were rather unreliable, though the technical data reported much better values, see

Property	**reported Value**
Accuracy of Wavelength	±0.5nm
Proportion of scattered light	< 0.03 %
Noise	< 0.02 ‰AU
Stability fluctuations	< 0.1 ‰AU

A special problem was the stability of the light source, that needed at least a warming phase of one hour to guarantee stable illumination.

Table B.2: Technical Data of Optical Multichannel Analyzer HP 8453, reported by Manufacturer

Appendix C

Calculation of the pH Value of HPTS in Aqueous Solution

In this paragraph the relation between HPTS components and H_3O^+ will be explicitly derived. Based on the finally derived polynomial, the pH of the solution at a given concentration of HPTS can be calculated as the only positive root of the polynomial.
The calculation is based on four different chemo-physical relations between the concentrations $[Na^+]$,$[R^{-3}OH]$, $[R^{-3}O^-]$, $[OH^-]$,$[H_3O^+]$ of the ions present in the reaction:

1. Mass conservation:

$$\begin{aligned} \left[\mathrm{Na}^+_{t=0}\right] &= 3 \cdot [\mathrm{HPTS}]_{t=0} && \text{(C.1)} \\ \left[\mathrm{R}^{-3}\mathrm{OH}\right] &= [\mathrm{HPTS}]_{t=0} - \left[\mathrm{R}^{-3}\mathrm{O}^-\right] && \text{(C.2)} \\ & && \text{(C.3)} \end{aligned}$$

2. law of mass action

$$\left[\mathrm{R}^{-3}\mathrm{O}^-\right] = K_h/([\mathrm{H}_3\mathrm{O}^+] + K_h) \cdot [HPTS]_{t=0} \qquad \text{(C.4)}$$

3. water ion product

$$[\mathrm{OH}^-] = K_w/[\mathrm{H}_3\mathrm{O}^+] \qquad \text{(C.5)}$$

4. conservation of charge

$$0 = 4 \cdot [\mathrm{R}^{-3}\mathrm{O}^-] + 3 \cdot [\mathrm{R}^{-3}\mathrm{OH}] + [\mathrm{OH}^-] - ([\mathrm{H}_3\mathrm{O}^+] + [\mathrm{Na}^+_{t=0}]) \qquad \text{(C.6)}$$

After reformulation of the conservation of charge the polynomial for finding the concentration of hydronium ions H_3O^+ as its positive root can be given:

$$
\begin{aligned}
0 &= (4 \cdot K_h \cdot [HPTS]_{t=0} \cdot [\mathrm{H_3O^+}] + 3 \cdot [HPTS]_{t=0} \cdot [\mathrm{H_3O^+}]^2 + K_w \cdot [\mathrm{H_3O^+}] \\
&\quad + K_w \cdot K_h - [\mathrm{H_3O^+}]^3 - K_h \cdot [\mathrm{H_3O^+}]^2 - [\mathrm{Na}^+_{t=0}] \cdot [\mathrm{H_3O^+}]^2 \\
&\quad - [\mathrm{Na}^+_{t=0}] \cdot [\mathrm{H_3O^+}] \cdot K_h)/([\mathrm{H_3O^+}] \cdot ([\mathrm{H_3O^+}] + K_h)) \\
&= (-[\mathrm{H_3O^+}]^3 + 3 \cdot [HPTS]_{t=0} \cdot [\mathrm{H_3O^+}]^2 - [\mathrm{Na^+}] \cdot [\mathrm{H_3O^+}]^2 - K_h \cdot [\mathrm{H_3O^+}]^2 \\
&\quad - [\mathrm{Na^+}] \cdot K_h \cdot [\mathrm{H_3O^+}] + 4 \cdot K_h \cdot [HPTS]_{t=0} \cdot [\mathrm{H_3O^+}] + K_w \cdot [\mathrm{H_3O^+}] \qquad \text{(C.7)} \\
&\quad + K_w \cdot K_h)/(([\mathrm{H_3O^+}] + K_h) \cdot [\mathrm{H_3O^+}]) \\
&= -[\mathrm{H_3O^+}]^3 + (3 \cdot [HPTS]_{t=0} - K_h - [\mathrm{Na}^+_{t=0}]) \cdot [\mathrm{H_3O^+}]^2 \\
&\quad + (4 \cdot K_h \cdot [HPTS]_{t=0} + K_w - [\mathrm{Na}^+_{t=0}] \cdot K_h) \cdot [\mathrm{H_3O^+}] \\
&\quad + K_w \cdot K_h \qquad \text{(C.8)}
\end{aligned}
$$

K_h is here the equilibrium constant of HPTS and K_w the self ionization product of water.
If HCl is added additionally, a further law of mass action has to be added and the conservation of charge equation adapted accordingly.

Acknowledgments

Here, I want to thank all the people, who have supported me during the last years in many ways.

First, I want to thank Prof. Dr. Bernd Jähne for giving me the opportunity to do this challenging thesis in his group with this variety of tasks from experimental to theoretical work. Especially, the fruitful discussions with him regarding experimental work and image processing helped me a lot.

Moreover, I want to thank Prof. Ulrich Platt for reviewing this thesis in spite of his full timetable, as well as Prof. Jörg Hüfner and Prof. Hans-Georg Bock I thank for agreeing to be examiners in my defence.

I owe a great deal to the members of the Imaging Processing Group at the HCI and the Institute of Environmental Science (IUP). It has been a pleasure to work with all of them. Their selfless help, patience and good advice even in awkward circumstances - sorry again for the chaos you all had to endure at the Aeolotron laboratory during the building time of the tunnel in 2006/07 - have helped me to hold on even when I was near to giving up the whole thesis.
Especially, I owe a great deal to Günther Balschbach, Tanja Binder, Leila Nagel and Kerstin Richter who have supported me not only in experimental and theoretical problems but have also spent ages in proof-reading of this thesis. Here, I also want to thank Pius Warken and René Winter from the LIF-subgroup for fruitful discussions about LIF-theory and suggestions for presenting it understandable. Also special thanks go to Felix Friedl, who will continue my work on LIF in the Aeolotron group and who was forced to spend the first two years of his PhD thesis as a kind of my diploma student. Roland Rocholz, Martin Schmidt and Pavel Paplov for being my guides to image processing, Uwe Schimpf and Günther Balschbach for strong support in all experimental problems. Björn Voss and Ullrich Köthe I want to thank for their strong support in analyzing my wavy images including endless discussions about software implementation.
Without the help of the student assistants David Appel, Tobias Junginger, Dominik Globig, Jason Teichmann, Anja Fath, Jan Attig, David Kosslar, Simon Murmann, Benjamin Heinzmann and Tina Buchmann building LIZARDand keeping it alive would have been impossible and this thesis would have lasted at least two years longer.

Kai Ueltzhoefer I owe a special deal for choosing 'wind profiles in a linear wind-wave tunnel 'as 'Miniforschung'- project. Furthermore, I thank Felix Friedl, Pius Warken and the whole group for endless proofreading of this thesis. My office colleagues Felix Vogel, Moritz Rosenfeld and Sam Hammer I want thank for their patience especially during the weeks of thesis writing. They did not only born to share an office with me but gave me valuable help and advise in many ways over the last years. And I don't want to forget Phil Stricker who has always been there when my desktop-computer started striking.
From the groups of Prof. Aeschbach-Hertig and Dr. Wagenbach I want to thank Martin Wieser, Tobias Kluge and Barbara May for their help in dealing with

high purity water.
From the group of Prof. Mangingi I want to thank Evelyn Böhmn, Daniela Polag and Dennis Scholz. Working together with them has always been a pleasure. Exchanging ideas about pH-value determination was extremely helpful- and many thanks for letting me use the high precision weighing unit for my Masslösungen. which reduced the errors in the solutions to the purity error of the solid solvent.
From the group of Prof. Roth I thank Klaus Schneider and Cornelius Claussen for help with striking linux comupters and Angelika Gassama for support in drying silica bubbles. Susanne Lindauer, Sabine and Helga Baus from the C14-lab, thanks for support with ice blocks and their help with unknown chemicals, corroded gas bottles, and cleaning murky 'Maßkolben'.

It was great to have Karl Wunderle, Stefan Hunsmann, Tim Klostermann and Pia Heinlein for gaining and interpreting spectra of strange fluorescent dyes and their knowledge in looking for gas leaks.
Thanks to Jessica Balbo and the whole group of Dirk-Peter Herten at Bioquant. All the HPTS pH-spectra shown in this study were taken at their fluorescence spectrometer and allowed me to gain temperature-dependent fluorescence spectra.

Kai Schorstein from the group of Prof. Walther at the TU Darmstadt I owe much for his help in characterizing my Lasers. Examining the spectral composition of the output spectra with the possibilities of their lab has spared me much problems.
Debasish Bannerjee Thanks Nils van Hinsberg from the group of Prof. Tropea for valuable hints in flume construction and data analysis.

Of course, without the skill of the people from the physical workshops at the IUP and the Kirchhoff-Institute of Physics LIZARDwould have become nothing more like a feeble 'let's hope it will last for the measurements' wind-wave tunnel. Especially, I want to thank Siegfried Spiegel, his profound help and advise has often helped me to escape nearing disaster.

From the group of Prof. Reinelt I want to thank Marcus Oswald and Thorsten Bonato for discussing the appropriate formulation of the mathematical models. Catherine Proux-Wieland helped me a lot in getting the French PhD thesis about my fluorophore - without her I would have been at a loss.

Now I come to thank my second family at the IWR, the people from the group of Prof. Hans-Georg Bock:
Especially, I want to thank Hans-Georg Bock and Johannes Schloeder, who showed me that being a physicist did not disqualify one from learning numerical mathematics. I was so fascinated by the possibilities and capabilities of numerical optimization that I decided to do my diploma thesis in the optimization group.
I want to thank the whole group and especially Margret Rothfuss and Stefan

Körkel as well as Mario Mommert, Leo Wirsching, Andreas Sommer, Simon Lenz, Jerko Horvat, and Christian Hoffmann from the PARAMIDE team, for their moral support and friendship since my fifth semester at university when I stumbled as a student assistant in the optimization workgroup.

Especially, I want to thank my cooperation partners with respect to robust optimization, Prof. Ekaterina Kostina and Tanja Binder from the University of Marburg. The work with them has always been a pleasure and I hope this cooperation between them and the image processing workgroups will continue in the future.

Gratefully, I acknowledge the financial support of this interdisciplinary thesis, on the one hand, by the Graduate School 1114 'Physical Measurement Techniques for Transport Processes across Interfaces' of the German Science Foundation (Deutsche Forschungsgemeinschaft) and on the other hand, by the 'Heidelberg Graduate School for Mathematical Method in the Science'.

Last but not least, I thank my family, my parents and my sister, for their never-ending support and love through all my life. This thesis is dedicated to them.

Bibliography

T. Aach, C. Mota, I. Stuke, M. Mühlich, and E. Barth. Analysis of Superimposed Oriented Patterns. *IEEE Transactions on Image Processing*, 15(12):3690–3700, 2006.

T. Aach, C. Mota, I. Stuke, M. Mühlich, and E. Barth. Analysis of Multiple Orientations. *IEEE Transactions on Image Processing*, 18(7):1424–1437, 2009.

W. E. Asher and T. M. Litchendorf. Visualizing near-surface concentration fluctuation using laser-induced fluorescence. *Exp. Fluids*, 46:243–253, 2009.

W. E. Asher and J. F. Pankow. Direct observation of concentration fluctuations close to a gas-liquid interface. *Chemical Engineering Science*, 44:1451–1455, 1989.

M. A. Atmane, W. Asher, and A. T. Jessup. On the use of the active infrared technique to infer heat and gas transfer velocities at the air-water interface. *Journal of Geophysical Research*, 109:C08S14, 2004.

Y. Avnir and Y. Barenholz. pH determination by pyranine: medium-related artifacts and their correction. *Analytical biochemistry*, 347(1):34–41, 2005.

S. Banerjee, D. S. Scott, and E. Rhodes. Mass Transfer to Falling Wavy Liquid Films in Turbulent Flow. *Ind. Eng. Chem. Fundamen.*, 7(1):22–27, 1968.

S. Banerjee, D. Lakehal, and M. Fulgosi. Surface divergence models for scalar exchange between turbulent streams. *International Journal of Multiphase Flow*, 30(7-8):963–977, 2004. J JUL-AUG.

S. Bannerjee and S. MacIntyre. The air-water interface: Turbulence and scalar interchange. In P. L. F. Liu, editor, *Advances in Coastal and Ocean Engineering*, volume 9, pages 181–237, Hackensack, N. J., 2004. World Scientific.

R. Barnadas-Rodríguez and J. Estelrich. Effect of salts on the excited state of pyranine as determined by steady-state fluorescence. *Journal of Photochemistry and Photobiology*, 198:262–267, 2008.

I. Barrodale and F. D. K. Roberts. An improved algorithm for discrete l_1 linear approximation. *SIAM Journal on Numerical Analysis*, 10(5):839–848, 1973.

R. H. Bartels, A. R. Conn, and J. W. Sinclair. Minimization techniques for piecewise differentiable functions: The l_1 solution to an overdetermined linear system. *SIAM Journal on Numerical Analysis*, 15(2):224–241, 1978.

H. P. Bäumler. Entwicklung eines Scheimpflug-Stereo-Systems zur Strömungsvisualisierung in Grenzschichten. Master's thesis, University of Heidelberg, Heidelberg, Germany, 2000.

K. H. Bäumler and K. Mühlfriedl. Mass transfer and concentration profiles near phase boundaries. *Int. J. Therm. Sci*, 40:425–436, 2001.

A. E. Beaton and J. W. Tukey. The fitting of power series, meaning polynomials, illustrated on band-spectroscopic data. *Technometrics*, 16(2):147–185, 1974.

T. Binder, A.G. Herzog, B. Jähne, and E. A. Kostina. Estimating water-sided vertical gas concentration profiles by inverse modeling. In *2. International Conference on Engineering Optimization, Lissbon*, September 2010.

C. Bliefert. *pH-Wert Berechnungen*. Verlag Chemie, 1 edition, 1978.

H. G. Bock. *Randwertproblemmethoden zur Parameteridentifizierung in Systemen Nichtlinearer Differentialgleichungen*. PhD thesis, University of Bonn, 1985.

G. Brethouwer. *Mixing of passive and reactive scalars in turbulent flows: A numerical study*. PhD thesis, Delft University of Technology, 2000.

J. Carpentier. Improvements in Enlarging or like cameras. GB Patents, 1901.

S. L. Clegg and P. Brimblecombe. The dissociation constant and Henry's Law constant of HCl in aqueous solution. *Atmospheric Environment*, 20(12):2483–2485, 1986.

M. Coantic. A model of gas transfer across air–water interfaces with capillary waves. *Journal of Geophysical Research*, 91:3925–3943, 1986.

J. Coppeta and C. Rogers. Dual emission laser induced fluorescence for direct planar scalar behavior measurements. *Experiments in Fluids*, 25:1–15, 1998.

B. D. Cornish and R. J. Speedy. *J. Physic. Chem.*, 88:1888, 1984.

J. P. Crimaldi. Planar laser induced fluorescence in aqueous flows. *Exp. Fluids*, 44:851–863, 2008.

G. T. Csanady. *Air-Sea Interaction: Laws and Mechanisms*. Cambridge University Press, 2001.

E. L. Cussler. *Diffusion - mass transfer in fluid systems*. Cambridge University Press, 1997.

P. V. Danckwerts. Significance of a liquid-film coefficients in gas absorption. *Industrial and Engineering Chemistry*, 43:1460–1467, 1951. doi: 10.1021/ie50498a055.

C. de Boor. *A practical guide to splines*. Applied Mathematical Sciences 27. Springer Verlag, New York, 1978.

E. L. Deacon. Gas transfer to and across an air-water interface. *Tellus*, 29: 363–374, 1977.

K. Degreif. *Untersuchungen zum Gasaustausch - Entwicklung und Applikation eines zeitlich aufgelösten Massenbilanzverfahrens*. PhD thesis, Institut für Umweltphysik, University of Heidelberg, 2006.

P. Deuflhard and A. Hohmann. *Numerische Mathematik I*. de Gruyter, 2 edition, 1993.

N. Dimarcq, V. Giordano, and P. Cerez. Statistical properties of laser-induced fluorescence signals. *Applied Physics B: Lasers and Optics*, 59:135–145, August 1994. doi: 10.1007/BF01081164.

N. A. Dimmock and G. B. Marshall. The Determination of Hydrogen Chloride in Ambient Air with Diffusion/Denuder Tubes. *Analytica Chimica Acta*, 202: 49–59, 1987.

M. A. Donelan and R. Wanninkhof. Gas transfer at water surfaces - conepts and issues. In M. A. Donelan, W. M. Drennan, E. S. Saltzman, and R. Wanninkhof, editors, *Gas Transfer at Water Surfaces*. American Geophysical Union, 2002.

S. R. Duke and T. J. Hanratty. Measurements of the concentration field resulting from oxygen absorption at a wavy air–water interface. In B. Jähne and E. C. Monahan, editors, *Air-water Gas Transfer, Selected Papers from the Third International Symposium on Air-Water Gas Transfer*, Hanau, 1995.

N. Ebuchi, H. Kawamura, and Y. Toba. Bursting phenomena in the turbulent boundary layer beneath the laboratory wind-wave surface. *Natural Physical Sources of Underwater Sound*, pages 263–276, 1993.

S. Eichkorn. Visualisierung und Quantifizierung des CO_2 Gasaustausches mittels laserinduzierter Fluoreszenz. Diplomarbeit, Institut für Umweltphysik, Fakultät für Physik und Astronomie, Univ. Heidelberg, 1997.

A. Falkenroth. *Visualisation of Oxygen Concentration Profiles in the Aqueous Boundary Layer*. PhD thesis, University of Heidelberg Combined Faculties for Natural Sciences and for Mathematics, 2007.

A. Falkenroth, A. Herzog, and B. Jähne. Visualization of air-water gas exchange using novel fluorescent dyes. In *12th Intern. Symp. on Flow Visualization, Göttingen, 10–14. September 2006*, 2006.

A. E. Fick. Über Diffusion. *Annalen der Physik*, 94(4):59–86, 1855.

G. Fischer. *Lineare Algebra*. Vieweg, Wiesbaden, 14. Auflage edition, 2003.

P. Fogg. *Chemicals in the Atmosphere*, chapter 9. Accomodation Coefficients, Uptake Coefficients and Henry's Law Constants of Gases which React with Water or are Unstable. IUPAC, 2003.

O. Forster. *Analysis 1: Differential- und Integralrechnung einer Veränderlichen*. Vieweg, Braunschweig, 6. Auflage edition, 2001.

T. Förster. Die pH-Abhängigkeit der Fluoreszenz von Naphthalinderivaten. *Zeitschrift für Elektrochemie*, 54:40–+, 1950.

G. E. Fortescue and J. R. A. Pearson. On gas absorption into a turbulent liquid. *Chemical Engineering Science*, 22:1163–1176, 1967.

C. S. Garbe. Bestimmung von Wärmeflußdichten aus Analogdaten. Technical Report 5, Universität Heidelberg, 2002.

C. S. Garbe, K. Roetmann, and B. Jähne. An optical flow based technique for the non-invasive measurement of microfluidic flows. In *12th International Symposium on Flow Visualization*, pages 1–10, Göttingen, Germany, 2006.

C. D. Geddes and J. R. Lakowicz, editors. *Topics in Fluorescence Spectroscopy Vol.9 Advanced Concepts in Fluorescence Sensing Part A: Small Molecule Sensing*, volume 9. Springer Science + Business Media, 2005.

S. Y. Goldberg, E. Pines, and D. Huppert. Proton scavenging in photoacid geminate recombination processes. *Chemical Physics Letters*, 192:77–81, April 1992. doi: 10.1016/0009-2614(92)85431-9.

S. Goldstein, editor. *Modern developments in fluid dynamics*. Dover, New York, 1965.

L. Golub and A. van Loan. *Matrix Computations*. Cambridge University Press, 2002.

T. E. Graedel and M. L. Mandich. Kinetic Model Studies of Atmospheric Droplet Chemistry. *Journal of Geophysical Research*, 91:5202–5221, 1986.

F. J. Green. *The Sigma-Aldrich Handbook of Stains, Dyes and Indicators*. Aldrich Chemical Company Inc., Milwaukee, Wisconsin, 1990.

M. A. Green, C. W. Rowley, and G Haller. Detection of lagrangian coherent structures in three-dimensional turbulence. *Journ. Fluid Mech.*, 572:111–120, 2007.

H.-P. Haar, U. K. A. Klein, F. W. Hafner, and M. Hauser. Determination of the rotational diffusion by a picosecond phase fluorometer. *Chemical Physics Letters*, 49(3):563–567, 1977.

H. Haken and H. C. Wolf. *Molekülphysik und Quantenchemie: Eine Einführung in die experimentellen und theoretischen Grundlagen*. Springer, 1 edition, 1992.

C. H. Hamann and W. Vielstich. *Elektrochemie I.* Verlag Chemie, Weinheim, Deutschland, 1975.

H. Haußecker, U. Schimpf, C. S. Garbe, and B. Jähne. Physics from IR image sequences: Quantitative analysis of transport models and parameters of air-sea gas transfer. In E. Saltzman, M. Donelan, W. Drennan, and R. Wanninkhof, editors, *Gas Transfer at Water Surfaces*, volume 127 of *Geophysical Monograph*. American Geophysical Union, 2002.

Herlina and G. H. Jirka. Application of LIF to inverstigate gas transfer near the air–water interface in a grid-stirred tank. *Experiments in Fluids*, 37:341–348, 2004.

I. Herlina and G. H. Jirka. Experiments on gas transfer at the air–water interface induced by oscillating grid turbulence. *J. Fluid. Mech.*, 594:183–208, 2008. doi: 10.1017/S0022112007008968.

J. W. Hiby, D. Braun, and K. H. Eickel. Eine Fluoreszenzmethode zur Untersuchung des Stoffübergangs bei der Gasabsorption im Rieselfilm. *Chemie-Ing.-Techn.*, 39:297–301, 1967.

G. M. Hidy and J. R. Brock. *The Dynamics of Aerocolloidal Systems.* Pergamon, Oxford, 1970.

R. Higbie. The rate of absorption of a pure gas into a still liquid during short periods of exposure. *Trans.Am.Inst.Chem.Eng.*, 31:365–389, 1935.

P. W. Holland and R. E. Welsch. Robust regression using iteratively reweighted least-squares. *Communications in Statistics - Theory and Methods*, 6(9):813–827, 1977.

P. J. Huber. *Robust Statistics.* John Wiley and Sons, New York, 1981.

F. Huhn. A simple instrument for the measurement of the slope and height distributions of small scale wind-driven water waves. Master's thesis, Institute for Environmental Physics, University of Heidelberg, 2008.

L.-P. Hung. Direct numerical simulation of transport processes at a wave-undulated interface. Personal Communication, July 2009.

I. Ihrke, K. N. Kutulakos, H. P.A. Lensch, M. Magnor, and W. Heidrich. State of the Art in Transparent and Specular Object Reconstruction. In *Proceedings of EUROGRAPHICS.* The Eurographics Association, 2008.

J. Ilmberger. Impulsübertrag und Strömungsverhältnisse in einem runden Wind-Wasser Kanal. Diplomarbeit, Institut für Umweltphysik, Fakultät für Physik und Astronomie, Universität Heidelberg, 1980. IUP D-167.

B. Jähne. *Zur Parametrisierung des Gasaustauschs mit Hilfe von Laborexperimenten.* Phd thesis, Institut für Umweltphysik Universität Heidelberg, 1980.

B. Jähne. Transfer across the Free Water Surface. Habilitation Thesis, University of Heidelberg, 1985.

B. Jähne. Motion determination in space-time images. In O. Faugeras, editor, *Proc. Computer Vision – ECCV 90, Lecture Notes in Computer Science 427*, pages 161–173, New York, 1990.

B. Jähne. From mean fluxes to a detailed experimental investigation of the gas transfer process. In *2nd International Symposium on Gas Transfer at Water Surfaces - Air–Water Mass Transfer, Minneapolis 1990*, pages 244–256. ASCE, 1991.

B. Jähne. Analytical studies of low-level motion estimators in space-time images using a unified filter concept. In *Proc. Conference on Computer Vision and Pattern Recognition (CVPR '94), Seattle, 20.-23. June 1994*, pages 229–236, 1994.

B. Jähne. *Digitale Bildverarbeitung, 6. Auflage*. Springer, 2005.

B. Jähne. Principles of Wind-Wave-Tunnel Design. Personal Communication, April 2006.

B. Jähne. Physikalische Chemie der Austauschprozesse an Gas-Flüssigkeits-Grenzflächen. Compact Course, University of Heidelberg, February 2008.

B. Jähne. *Air-Sea Gas Exchange*, chapter Encyclopedia Ocean Sciences. Elsevier, 2009.

B. Jähne. Theory of Scheimpflug-Imaging. Personal Communication, April 2010.

B. Jähne and K. O. Münnich. Momentum induced gas exchange through a smooth water surface, models and experimental results from linear and circular wind-water tunnels. In H. C. Broecker and L. Hasse, editors, *Berichte aus dem Sonderforschungsbereich 94 Meeresforschung*, number 17, pages 55–62. Univ. Hamburg, 1980.

B. Jähne, P. Libner, R. Fischer, T. Billen, and E. J. Plate. Investigating the transfer process across the free aqueous boundary layer by the controlled flux method. *Tellus*, 41B(2):177–195, 1989.

B. Jähne, R. Nielsen, C. Popp, U. Schimpf, and C. Garbe. Air-Sea Gas Transfer: Schmidt Number Dependency and Intermittency. Presentation at the 37th International Liège Colloquium on Ocean Dynamics (2-6 May 2005), Gas Transfer at Water Surface, 1995. Presentation.

H. Jeffreys. On the circulation of aeroplane lift. *Phil. Mag. Series 6*, 50(298): 815–819, 1925.

A. T. Jessup, C. J. Zappa, and H. H. Yeh. Defining and quantifying microscale wave breaking with infrared imagery. *Journal of Geophysical Research*, 102 (C10):23145–23153, 1997.

J. Jiménez and A. A. Wray. On the characteristics of vortex filaments in isotropic turbulence. *J. Fluid Mech.*, 373:255–285, 1998.

G. H. Jirka and A. H.-W. Ho. Measurements of gas concentration fluctuations at water surface. *Journal of Hydraulic Engineering*, 116:835–847, 1990.

H. R. Kermis, Y. Kostov, P. Harms, and G. Rao. Dual excitation ratiometric fluorescent ph sensor for noninvasive bioprocess monitoring: development and application. *Biotechnol. Prog.*, 18:1047–1053, 2002.

J. Kleinschmidt. Spectroscopic Methods in Biochemistry: Principles and Applications. lecture notes, University of Constance?, 2001.

H. Knutsson. Representing local structure using tensor. In *The 6th Scandinavian Conference on Image Analysis*, pages 244–251, 1989.

A. N. Kolmogorov. The local structure of turbulence in compressible turbulence for very large Reynolds numbers. *Compt.Rend.Akad.Nauk SSSR*, 30:301, 1941.

U. Köthe. Edge and junction detection with an improved structure tensor. In B. Michaelis and G. Krell, editors, *Proceedings of the 25th DAGM Symposium on Pattern Recognition*, volume 2781 of *Lecture Notes in Computer Science*, pages 25–32, Magdeburg, 2003. DAGM.

B. Kruppa, G. Strube, and C. Gerlach. *Optical Measurements*, chapter 7, pages 95–112. Heat and Mass Transfer. 2001.

M. Krystek and M. Anton. A weigthed total least-squares algorithm for fitting a straight line. *Meas. Sci. Tech.*, 18(11):348–3442, 2007.

W. Kümmel. *Technische Strömungsmechanik*. B. G. Teubner Verlag, Wiesbaden, 2004.

P. K. Kundu. *Fluid Mechanics*. Academic Press, San Diego, CA, 4th edition, 2007.

J. R. Lakowicz. *Principles of Fluorescence Spectroscopy*. Springer, 3. edition, 2006.

J. C. Lamont and John C. Scott. An eddy cell model of mass transfer into the surface of a turbulent liquid. *AIChE Journal*, 16:513–519, 1970.

P. A. Lange, B. Jähne, J. Tschiersch, and I. Ilmberger. Comparison between an amplitude-measuring wire and a slope-measuring laser water wave gauge. *Rev. Sci. Instrum.*, 53(5):651–655, May 1982.

L. G. Larsen and J. P. Crimaldi. The effect of photobleaching on PLIF. *Exp. Fluids*, 41:803–812, 2006.

P. Leiderman, R. Gepshtein, A. Uritski, L. Genosar, and D. Huppert. Temperature dependence of excited-state proton transfer in water electrolyte solutions and water-methanol solutions. *J. Phys. Chem. A*, 110:9039–9050, 2006.

M. Lesieur. *Turbulence in Fluids*. Springer, 4 edition, 2008.

W. K. Lewis and W. G. Whitman. Principles of gas absorption. *Industrial and Engineering Chemistry*, 16:1215–1220, 1924.

B. Lindgren. *Flow Facility Design and Experimental Studies of Wall-Bounden Turbulent Shear-Flows*. PhD thesis, Royal Institute of Technology, Stockholm, 2002.

P. S. Liss and L. Merlivat. Air-sea gas exchange rates: Introduction and synthesis. In P. Buat-Menard, editor, *The role of air-sea exchange in geochemical cycling*, pages 113–129. Reidel, Boston,MA, 1986.

U. Lode. Tiefenrekonstruktion vertikaler Konzentrationsprofile in der wasserseitigen Grenzschicht mittels spektroskopischer laserinduzierter Fluoreszenz (LIF). Master's thesis, University of Heidelberg, 1998.

G. A. Lutty. The acute intravenous toxicity of biological stains, dyes, and other fluorescent substances. *Toxicology and Applied Pharmacology*, 44:225–249, 1978.

J. Magnaudet and I. Calmet. Turbulent mass transfer through a flat shear-free surface. *J.Fluid Mech.*, 553:155–185, 2006.

M. J. McCready, E. Vassiliadou, and T. J. Hanratty. Computer-simulation of turbulent mass-transfer at a mobile interface. *AIChE J. Chem. Engng Res. Dev.*, 32:1108–1115, 1986. doi: 10.1002/aic.690320707.

B. J. McKeon, G. Comte-Bellot, J. F. Foss, J. Westerweel, F. Scarano, C. Tropea, and J. Meyers et al. Velocity, vorticity and mach number. In C. Tropea, J. Foss, and A. Yarin, editors, *Springer Handbook of Experimental Fluid Dynamics*. Springer, Berlin, Heidelberg, 2007.

R. D. Metha and P. Bradshaw. Design Rules for Small Low Speed Wind Tunnels. *The Aeronautic Journal of the Royal Aeronautic Society*, pages 443–449, 1979.

A. Mills and Q. Chang. Modelled diffusion-controlled response and recovery behaviour of a naked optical film sensor with a hyperbolic-type response to analyte concentration. *Analyst*, 117:1461–1466, 1993.

D.C. Montgomery, E. A. Peck, and G. G. Vinning. *Introduction to Linear Regression Analysis*. Wiley InterScience, 4 edition, 2006.

R. G. Mortimer. *Physical Chemistry*. Elsevier Acadamic Press, 3rd edition edition, 2008.

K. Mühlfriedel and K.-H. Baumann. Concentration measurements during mass transfer across liquid-phase boundaries using planar laser induced fluorescence PLIF. *Experiments in Fluids*, 28:279–281, 2000.

T. Münsterer. *LIF Investigation of the Mechanisms Controlling Air–Water Mass Transfer at a Free Interface*. PhD thesis, University of Heidelberg, 1996.

T. Münsterer and B. Jähne. LIF measurments of concentration profiles in the aqueous mass boundary layer. *Exp Fluids*, 25:190–196, 1998.

M. Navier. Memoire sur les lois du movement des fluides. *Memoires de l'Academie de Science*, 6:389–416, 1827.

R. Nielsen. *Gasaustausch - Entwicklung und Ergebnis eines schnellen Massenbilanzverfahrens zur Messung der Austauschparameter*. PhD thesis, Interdisziplinäres Zentrum für Wissenschaftliches Rechnen & Institut für Umweltphysik, University of Heidelberg, 2004.

NIST Standard Reference Database. Webbook, April 2010.

J. Nocedal and S. J. Wright. *Numerical Optimization*. Springer Series in Operations Research. Springer Verlag Berlin Heidelberg New York, 1999.

H. Oertel, editor. *Prandtl's essentials of fluid mechanics*. Springer, 2004.

M. J. O'Neil, editor. *The Merck index: An encyclopedia of chemicals, drugs, and biologicals*. Merck Research Laboratories, Whitehouse Station, NJ, USA, 14th edition edition, 2006.

J. F. Pankow and W. Asher. Carbon dioxide transfer at the gas/water interface as a function of turbulence. In *Gas Transfer at Water Surfaces*, pages 101–111. D. Reidel Publishing Company, 1984.

W. L. Peirson. Measurement of surface velocities and shears at a wavy air-water interface using particle image velocimetry. *Expt.in Fluids*, 23:427–437, 1997.

R. H. Perry and D. W. Green. *Perry's Chemical Engineers' Handbook*, volume 8. Mcgraw-Hill Professional, 2008.

E. J. G. Peterman, F. Gittes, and C. F. Schmidt. Laser-induced Heating in Optical Traps. *Biophysical Journal*, 84:1308–1316, 2003.

D. Pines and E. Pines. Direct observation of power-law behaviour in the asymptotic relaxation to equilibrium of a reversible bimolecular reaction. *J. Chem. Physics*, 115(2):951–955, 2001.

E. Pines and D. Huppert. Geminate recombination proton-transfer reactions. *Chemical Physics Letters*, 126:88–91, April 1986. doi: 10.1016/0009-2614(86)85121-1.

E. Pines and D. Huppert. Salt effects on steady-state quantum yields of ultrafast, diffusion-influenced reversible photoacid dissociation reactions. *J. Phys. Chem.*, 95:666–674, 1991.

U. Platt and J. Stutz. *Differential Optical Absorption Spectroscopy, Principles and Applications*. Physics of Earth and Space Environments. Springer-Verlag, Berlin, Heidelberg, New York, 2000.

L. Prandtl. *Essentials of Fluid dynamics*. Hafner Publishing Company, New York, 1952.

L. Prandtl, Oswaitisch K., and Wieghardt K. *Führer durch die Strömungslehre*. Vieweg Verlag, 2002.

C. Prayer. *Etude du transfer photoinduit de proton dans un hydroxyarène, la pyranine, competition avec le transfert photo-induit d'électron á un accepteur, le méthylviologen*. PhD thesis, University Paris 6, 1997.

J. Reinmuth. Zwei-Farbstoff-Technik zur Tiefenrekonstruktion von Gaskonzentrationen in der wasserseitigen Grenzschicht. Master's thesis, University of Heidelberg, 2000.

L. F. Richardson. The supply of energy from and to atmospheric eddies. In *Proc. Royal Society London A*, volume 97, page 354, 1920.

E. Riedel. *Anorganische Chemie*. Walter de Gruyter, 1999.

R. Rocholz. *Spatiotemporal Measurement of Short Wind-Driven Water Waves*. PhD thesis, University of Heidelberg, 2008.

W. Roedel. *Physik unserer Umwelt: die Atmosphäre*. Springer-Verlag, 3 edition, 2000.

P. Sagaut, S. Deck, and M. Terracol. *Multiscale and multiresolution approaches in turbulence*. Imperial College Press, 2006.

T. Scheimpflug. Improved method and apparatus for the systematic alteration or distortion of plane pictures and images by means of lenses and mirrors for photography and for other purposes. GB Patents, 1904.

U. Schimpf, C. Garbe, and B. Jähne. Investigation of transport processes across the sea surface microlayer by infrared imagery. *Journal of Geophysical Research-Oceans*, 109(C8):C08S13, 2004. ISSN 0148-0227. doi: doi:10.1029/2003JC001803.

H. Schlichting and K. Gersten. *Grenzschicht-Theorie*. Springer-Verlag, Heidelberg, Germany, 10th edition, 2006.

W. Schmidt. *Optische Spektroskopie*. Wiley-VCH, 2000.

H. E. Schulz and J. Janzen. Concentration fields near air-water interfaces during interfacial mass transport: oxygen transport and random square wave analysis. *Braz. J. Chem. Eng.*, 26(3):527–536, 2009.

S. Schwartz. *Chemicals in the Atmosphere*, chapter 2. Presentation of Solubility Data: Units and Applications. IUPAC, 2003.

T. S. Schwarz. Development of a depth resolving boundary layer visualiziation für gas exchange at free water surfaces. Master's thesis, University of Heidelberg, 2005.

L. Sigg and W. Stumm, editors. *Aquatische Chemie Eine Einführung in die Chemie wässriger Lösungen und natürlicher Gewässer*. B.G. Teubner Verlag Stuttgart, 3 edition, 1994.

Sigma Aldrich. Url: http://www.sigmaaldrich.com. web resource, September 2009.

R. Sjöback, J. Nygren, and M. Kubista. Absorption and fluorescence properties of fluorescein. *Spectrochimica Acta Part A*, 51:L7–L21, 1995.

F. M. Sogandares and E. S. Fry. Absorption spectrum (340 -640 nm) of pure water. I. Photothermal measurements. *Appl Opt*, 36:8699–8709, 1997.

D. B Spry, A. Goun, K. Glusac, D. E. Moilanen, and M. D. Fayer. Proton transport and the water environment in nafion fuel cell membranes and AOT reverse micelles. *Journal of the American Chemical Society*, 129(26):8122–8130, 2007.

J. Stoer. *Numerische Mathematik 1.* Springer Verlag Berlin Heidelberg, 7. edition, 1994.

G. G. Stokes. On the theories of the internal friction of fluids in motion, and of the equilibrium and motion of elastic solids. *Transactions of the Cambridge Philosophical Society*, 9(II):8–106, 1849.

W. Stumm and J. J. Morgan, editors. *Aquatic Chemistry Chemical Equilibria and Rates in Natural Waters.* Wiley Interscience Publication, John Wiley & Sons, Inc., New York, Chichester, Brisbane, Toronto, Singapore, 1996.

K. Takehara and G. T. Etoh. A direct visualization method of CO_2 gas transfer at water surface driven by wind waves. In M. A. Donelan, W. M. Drennan, E. S. Saltzman, and R. Wanninkhof, editors, *Gas Transfer at Water Surfaces*, Geophysical Monograph, 2002.

A. Tamhane and D.Dunlop. *Statistics and Data Analysis.* Prentice-Hall,Inc., 1999.

M. E. Taylor. *Partial Differential Equations III: Nonlinear Equations.* Springer, 1997.

R. Temam. *Infinite Dimensional Dynamical Systems in Mechanics and Physics.* Springer Verlag, 1988.

H. Tennekes and J. L. Lumley. *A First Course in Turbulence.* MIT Press, Cambridge,MA, 14th edition, 1992. First Edition: 1972.

T. G. Theofanus. *Gas Transfer at Water Surfaces*, chapter Conceptual models of Gas Exchange, pages 271–281. Reidel Publishing, 1984.

Y. Toba, M. Tokuda, K. Okuda, and S. Kawai. Forced convection accompanying wind waves. *Journal of the Oceanographical Society of Japan*, 31:192–198, 1975.

T.-H. Tran-Thi, T. Gustavsson, C. Prayer, S. Pommeret, and J. T. Hynes. Primary ultrafast events preceding the photoinduced proton transfer from pyranine to water. *Chemical Physics Letters*, 329:421–430, 2000.

W.-T. Tsai and L.-P. Hung. *A Numerical Study on the Characteristic Flow Structures of a Micro-Breaking Wind Wave*, pages 159–168. Springer-Verlag, 2007.

R. Y. Tsien, L. Ernst, and A. Waggoner. *Fluorophores for Confocal Microscopy: Photophysics and Photochemistry*, chapter 16, pages 338–352. Springer, 2006.

H. Tsumori and Y. Sugihara. Lengthscales of motions that control air-water gas transfer in grid-stirred turbulence. *J. Marine Systems*, 66:6–18, 2007.

K. Ültzhöfer. Windprofilmessung am linearen Wind-Wellen-Kanal. Technical report, University of Heidelberg, 2008. student project.

E. Van Vliet, S. M. Van Bergen, J. J. Derksen, L. M. Portela, and H. E. A. Van den Akker. Time-resolved, 3d, laser-induced fluorescence measurements of fine-structure passive scalar mixing in tubular reactor. *Exp. Fluids*, 37: 1–21, 2004.

E. A. Variano and E. A. Cowen. Quantitative imaging of CO_2 transfer at an unsheared free surface. In *Transport at the Air-Sea Interface: Measurements, Models and Parametrizations*, pages 43–58. Springer-Verlag, 2007.

W. M. Vaughan and G. Weber. Oxygen quenching of pyrenebutyric acid fluorescence in water. A dynamie probe of the microenvironment. *Biochemistry*, 9:464–473, 1970.

J. W. Walker and W. L. Peirson. Measurement of gas transfer across wind-forced wavy air–water interfaces using laser-induced fluorescence. *Exp. Fluids*, 2008. doi: 10.1007/s00348-007-0398-8.

R. Wanninkhof. The impact of different gas exchange formulations and wind speed products on global air-sea CO_2 fluxes. In C. S. Garbe, R. A. Handler, and B. Jähne, editors, *Transport at the Air Sea Interface - Measurements, Models and Parametrizations*, pages 1–23. Springer-Verlag, Berlin, Heidelberg, 2007.

R. Wanninkhof and W. R. McGillis. A cubic relationship between gas transfer and wind speed. *Geophysical Research Letters*, 26:1889–1892, 1999.

R. Wanninkhof, W. E. Asher, D. T. Ho, C. Sweeny, and W. R. McGillis. Advances in Quantifying Air-Sea Gas Exchange and Environmental Forcing. *Ann. Rev. Mar. Sci.*, 1:213–244, 2009.

R. O. Weber. Remarks on the definition and estimation of friction velocity. *Boundary Layer Meterology*, 93:197–209, 1999.

A. Weller. Zur Kinetik der Fluoreszenzumwandlung. *Zeitschrift für physikalische Chemie*, 15:438–453, 1958.

Wikipedia - the Online Reference. Url: http://www.wikipedia.com. web resource, June 2010.

R. Winter. Working title: Visualizing of gas concentration fields in the air-sided boundary layer. in preparation, 2011.

O. S. Wolfbeis, E. Fürlinger, H. Kroneis, and H. Marsoner. Fluorimetric analysis: 1. A Study on Fluorescent Indicators for Measuring near Neutral pH-Values. *Fresenius Z. Analyt. Chem.*, 314:119–124, 1983.

P. T. Woodrow and S. R. Duke. Laser-induced fluorescence studies of oxygen transfer across unsheared flat and wavy air–water interfaces. *Industrial and Engineering Chemical Research*, 40(8):1985–1995, 2001.

D. Wothe. *Messen des Stofftransports durch die Phasengrenze zweier nicht mischbarer Flüssigkeiten.* PhD thesis, University of Hannover, 2006.

Z. F. Xu and B. C. Khoo. Mass transfer across the turbulent gas-water interface. *AIChe Journal*, 52(10):3363–3374, 2006.

T. A. Zang. On the rotation and skew-symmetric forms for incompressible flow simulations. *Applied Numerical Mathematics*, 7:27–40, 1991.

Z. Zhujun and W. R. Seitz. A fluorescence sensor for quantifying the pH in the range of 6.5 to 8.5. *Analytica Chemica Acta*, 160:47 – 55, 1984.

J. Zwaaneveld. Onderzoek aan plaatschoepen voor bochten. Technical Report 1118, Nationaal Luchtvaart Laboratorium, 1950.